UNIVERSITY OF OKLAHOMA

GRADUATE COLLEGE

THE EFFECTS OF WIND SHEAR ON CONVECTIVE BOUNDARY LAYER ENTRAINMENT

A Dissertation

SUBMITTED TO THE GRADUATE FACULTY

In partial fulfillment of the requirements for the

degree of

Doctor of Philosophy

By

ROBERT J. CONZEMIUS

Norman, Oklahoma

2004

Downloaded from SHAREOK. Persistent Handle URL: https://hdl.handle.net/11244/773

UMI Number: 3138958



UMI Microform 3138958

Copyright 2003 by ProQuest Information and Learning Company.

All rights reserved. This microform edition is protected against unauthorized copying under Title 17, United States Code.

ProQuest Information and Learning Company
300 North Zeeb Road
PO Box 1346
Ann Arbor, MI 48106-1346

THE EFFECTS OF WIND SHEAR ON CONVECTIVE BOUNDARY LAYER ENTRAINMENT

A Dissertation APPROVED for the
School of Meteorology

By

Evgeni Fedorovich

Charles A. Doswell III

Brian H. Fiedler

Randall A. Kolar

Douglas K. Lilly

Alan M. Shapiro

© by Robert J. Conzemius 2004
All Rights Reserved.

Acknowledgements

This research was made possible by funding from the National Science Foundation (NSF) under grant ATM-0124068. Funding was also provided by the University of Oklahoma (OU) School of Meteorology

I would like to start by thanking my advisory committee, who guided me through the research process. I particularly appreciated the easygoing manner and open door policy of my primary research advisor Evgeni Fedorovich. The same goes for Alan Shapiro, who was always willing to put everything aside to discuss a derivation (and to take care of Sydney the Cat when I was away at conferences). Brian Fiedler provided the motivation for me to look at applications of the research that went into this dissertation, and it is Chuck Doswell with whom I had some of the most challenging conversations and who motivated me to expand my thinking more than anyone else. Two other committee members – Randy Kolar and Doug Lilly – were a bit more physically remote than the others but were no less helpful. Doug's ideas formed a basic framework for this study.

Thanks also go out to my family, who frequently checked in with me to see how I was doing, particularly during the final stages of writing this dissertation. They also encouraged me to take a break once in a while to freshen up my mind. They helped get things started on the right foot by assisting me in my move to Norman four years ago. Their assistance obviously goes back a long ways before that.

The School of Meteorology office staff deserve particular commendation—Celia, Marcia, Nancy, and Andrea. They are perhaps the most efficient I've worked with.

Finally, I'd also like to thank my weather-weenie friends for being… well… just weather weenie friends. I'd start naming people, but then I'd always feel like I left someone out. I've never moved to a place where I developed so many friendships so quickly, and I hope those friendships continue for some time to come.

Contents

Acknowledgements iv
List of Acronyms ix
List of Symbols x
Abstract xvi
Chapter 1 Introduction 1
1.1 What is the Convective Boundary Layer? 1
1.2 Definition of Entrainment 4
1.3 The Importance of Entrainment 5
1.4 Entrainment Related to CBL Integral Budgets of Energy 7
1.5 Methods to Evaluate Entrainment 13
1.5.1 Atmospheric Measurements 13
1.5.2 Laboratory Models 15
1.5.3 Numerical Techniques 16
1.6 Layout of Remaining Chapters 21
Chapter 2 Background 23
2.1 Early Studies of Entrainment 23
2.2 Evidence of Shear Effects 26
2.3 Conceptual Models with Shear 28
2.4 Continuation of Field Programs 33
2.5 Continuation of Laboratory Experiments 38
2.6 Large Eddy Simulations of Sheared Convective Boundary Layers 42
2.7 Shear Sheltering of Turbulence 47
2.8 Sheared CBLs in Numerical Weather Prediction Models 48
2.9 Goals of this Study 51
Chapter 3 Numerical Simulations and Models 53
3.1 A Hierarchy of Numerical Methods 53
3.2 Simulations 54
3.3 Turbulence Equations for the Horizontally Homogeneous CBL 55
3.4 RANS-Based Closures 62
3.4.1 TKE-Based Closures 62
3.4.2 Other RANS-Based Closures 65
3.4.3 Points of Caution for RANS-Based Closures 67
3.5 Integral Budget Methods 68
3.5.1 Zero Order Model (ZOM) 68
3.5.2 First Order Model (FOM) 83
3.5.3 General Structure Model (GSM) 92
Chapter 4 Evaluations of Integral Budget Models of Entrainment with LES for the Shear-Free CBL 94
4.1 Methods 94
4.1.1 LES Setup 94
4.1.2 Retrieval of Parameters of Entrainment from LES 97

4.2 Results of LES Shear-free Entrainment Experiments 100
4.3 Summary of Shear-Free LES Experiments 111
Chapter 5 114
5.1 ZOM versus LES Entrainment Flux Ratios 114
5.2 Bulk Model Experiments 119
5.2.1 First Order Model 121
5.2.2 Second Order Model 124
5.3 Comparison of Methods of Defining CBL Depth 131
5.4 Summary 134
Chapter 6 Methodology 136
6.1 Large Eddy Simulation Setup 136
6.1.1 LES Domain 136
6.1.2 Selection of the Parameter Space for Sheared CBLs 137
6.1.3 LES Parameters 141
6.1.4 LES Output Evaluation 144
6.1.5 Methods for Finding z_i and Parameters of Entrainment 145
6.2 Tests of RANS-based Turbulence Closures in NWP 147
6.3 Tests of Integral Budget Methods 148
6.3.1 Tests of ZOM and FOM Parameterizations 148
6.3.2 Numerical Integration of the ZOM and FOM Entrainment Equations 149
Chapter 7 Simulated Convective Boundary Layer Cases 150
7.1 CBL Depth and Velocity Profiles 150
7.2 Entrainment of Heat in Relation to Entrainment Zone Depth 160
7.3 Potential Temperature Profiles 163
7.4 Entrainment of Momentum 164
7.5 Ageostrophic Momentum 168
7.6 Velocity Variance Profiles 171
7.7 Entrainment Flux Ratios 177
7.8 Turbulence Kinetic Energy Budgets 181
7.8.1 Profiles of Terms in the Turbulence Kinetic Energy Equation 181
7.8.2 Evolution of the TKE Budgets 183
7.9 Bulk Richardson Numbers 191
7.10 Summarizing Remarks 197
Chapter 8 Turbulence Structure in Sheared Convective Boundary Layers 200
8.1 Motivation 200
8.2 Cross Sections of Temperature and Velocity 201
8.3 Spectra of Turbulence 208
8.4 Vertical Velocity Skewness 217
8.5 Chapter Summary 220
Chapter 9 Comparison of LES with Atmospheric Data 222
9.1 Introduction 222
9.2 Atmospheric Boundary Layer Measurement Methods 223
9.2.1 Discussion of Selected Previous Studies 223
9.2.2 Additional Platforms 226
9.2.3 Data Comparability Issues 230
9.3 Proposed Comparison 231

9.3.1 Methods 231
9.3.2 Selected days for analysis 234
9.4 Simulation of May 22, 2002 Case 234
9.4.1 Motivation 234
9.4.2 Data and Methods 235
9.4.3 Results 241
9.5 Summary and Conclusions 255
Chapter 10 Evaluations of Numerical Models of Entrainment 258
10.1 RANS-Based Closures in NWP 258
10.1.1 ARPS 259
10.1.2 F&K 262
10.2 Integral Budget Parameterizations 266
10.2.1 ZOM and Hybrid Parameterizations 266
10.2.2 FOM-Based Parameterizations 274
10.3 Numerical Integration of Full ZOM and FOM Equations 275
10.4 Chapter Summary 287
Chapter 11 Summary and Conclusions 291
11.1 Summary of Activities 291
11.2 Findings of the Study 294
11.3 Suggestions for Further Research 301
References 305
Appendix A Large Eddy Simulation model equations 321
Basic Model Equations 321
Subgrid closure 325
Lilly-Smagorinsky closure 326
Deardorff Closure 328
Procedure for Integrating the Equations 329
Appendix B Effect of the Asselin Filter on Spectra 331
Amplitude Errors 331
Phase Speed Errors 333
LES Tests 335

List of Acronyms

AERI	Atmospheric Emitted Radiance Interferometer
AMA	Amarillo, Texas radiosonde launch site
ARM	Atmospheric Radiation Measurement program
ARPS	Advanced Regional Prediction System (Xue et al. 2003)
BAO	Boulder Atmospheric Observatory
CASES-99	Cooperative Atmosphere Surface Exchange Study in 1999
CBL	Convective boundary layer
DDC	Dodge City, Kansas radiosonde launch site
DNS	Direct Numerical Simulation
DYCOMS-II	Dynamics and Chemistry of Marine Stratocumulus experiment
EBBR	Energy balance Bowen ratio method of determining heat flux
FM-CW	Frequency modulation-carrier wave radar
FOM	First order model
GC	CBL case with constant geostrophic wind
GCM	Global circulation model or global climate model
GFS	Global Forecast System
GS	CBL case with shear in the geostrophic wind
GSM	General structure model
HARLIE	Holographic Airborne Rotating Lidar Instrument Experiment
HRDL	High resolution Doppler lidar
IHOP	International H_2O Project
ISS	Integrated Sounding System
ISSF	Integrated surface flux facility
K-H	Kelvin-Helmholtz
LES	Large eddy simulation
MAPR	Multiple antenna profiler
NCAR	National Center for Atmospheric Research
NCEP	National Center for Environmental Prediction
NS	No shear case for the CBL
NSF	National Science Foundation
NWP	Numerical weather prediction
OU	University of Oklahoma
OUN	Norman, Oklahoma radiosonde launch site
RANS	Reynolds-averaged Navier-Stokes equations
SGP	Southern Great Plains Facility (ARM)
SODAR	Sound detection and ranging
SOM	Second order model
TKE	Turbulence kinetic energy
VAD	Velocity azimuth display
ZOM	Zero order model

List of Symbols

a	A constant
b	Buoyancy
b_m	Mixed layer buoyancy (in the interior of the CBL) – ZOM
b_{m1}	Mixed layer buoyancy (in the interior of the CBL) – FOM
b_{m2}	Mixed layer buoyancy (in the interior of the CBL) – SOM
b_s	Reference value of buoyancy determined by extrapolating the linear free atmospheric gradient to the surface
b_{sh}	Buoyancy shift in SOM
c	A passive scalar (see Chapter 9) Phase speed (Appendix B)
c_1	Constant in Fairall (1984) entrainment parameterization
c_2	Constant in Fairall (1984) entrainment parameterization
c_{2S}	Constant in Sorbjan (2004) entrainment parameterization
c_a	Phase speed of the analytic solution (Appendix B)
c_d	Phase speed of the finite difference solution (Appendix B)
c_H	Constant in Sorbjan (2004) entrainment parameterization
e	Turbulence kinetic energy (TKE)
e_s	Subgrid turbulence kinetic energy (TKE)
e -l	TKE-based model derived from RANS
f	Coriolis parameter
f_c	Correction factor applied to subgrid dissipation according to distance from wall
g	Gravitational acceleration
i	$\sqrt{-1}$
k	Wavenumber
l	Master length scale of turbulence
l_s	Length scale under stable conditions
l_u	Length scale in unstable conditions
p	Pressure
p_{gh}	Base state hydrostatic pressure (see Appendix A)
r	Constant in Fairall (1984) entrainment parameterization
s	Constant in Fairall (1984) entrainment parameterization
u	u_1
u_g	The x-component of the geostrophic wind
u_{g0}	The x-component of the geostrophic wind at the surface

u_i Instantaneous value of the ith component of momentum

$\tilde{u}_i$ Filtered u_i

$\overline{u_i}$ The ensemble-averaged value of u_i

u_i' The deviation of U_i from its ensemble average or filtered value.

u_l Characteristic velocity u associated with the length scale l

u_m Mixed layer value of u_1 (ZOM)

u_* surface friction velocity

v u_2

v_g The y-component of the geostrophic wind

v_{g0} The y-component of the geostrophic wind at the surface

v_m Mixed layer value of u_2 (ZOM)

w u_3

w_e Entrainment velocity, after separating the mean vertical velocity at the CBL top from the CBL growth rate dz_i / dt

w_m Effective vertical velocity scale used in entrainment parameterizations that include the effects of shear

w_* Deardorff (1974) convective velocity scale

x Cartesian coordinate system: x-coordinate

y Cartesian coordinate system: y-coordinate

z Cartesian coordinate system: z-coordinate

z_i CBL depth

$\hat{z}_i$ Dimensionless CBL depth

$\hat{z}_{i0}$ Constant of integration for the ZOM equilibrium entrainment equation for dimensionless CBL depth

z_w Distance from the lower surface (see Appendix A)

A Constant describing the relative importance of Deardorff (1980) velocity scale and surface friction velocity in the velocity scaling w_m

A_1 Constant in Stull (1976a,c) for the shear-free CBL entrainment flux ratio

A_2 Constant in Stull (1976a,c) for the surface shear term

A_3 Constant in Stull (1976a,c) for the entrainment zone shear term

A_{1K} Constant in Kim (2001)

A_{2K} Constant in Kim (2001)

A_{3K} Constant in Kim (2001)

A_N Negative area of the heat flux profile (vertically integrated heat flux over the depth where the heat flux is less than zero)

A_P Positive area of the heat flux profile (vertically integrated heat flux over the depth where the heat flux is greater than zero)

B Turbulent buoyancy flux

B_{BG} Constant in the entrainment parameterization of Batchvarova and Gryning (1991, 1994)

B_s Surface buoyancy flux

$B_{\Delta x}$ Filter function for LES (see Appendix A)

C_0 Mahrt and Lenschow (1976) transport loss constant for TKE equation

C_1 Ratio of the negative heat flux of entrainment to surface heat flux in the equilibrium entrainment regime in the ZOM

C_e Constant describing scaled integral of the shear-free CBL TKE

C_{eES} Constant describing scaled integral of TKE due to entrainment zone shear

C_{eSS} Constant describing scaled integral of TKE due to surface layer shear

C_D Surface drag coefficient

C_N Constant describing the loss of energy due to gravity wave radiation

C_P Constant describing the fraction of shear-generated TKE available for entrainment

C_S Smagorinsky constant

C_T Constant describing the relative importance of the TKE spin-up term in entrainment parameterizations

C_ε Constant describing scaled integral of the shear-free CBL dissipation

$C_{\varepsilon ES}$ Constant describing scaled integral of dissipation due to entrainment zone shear

$C_{\varepsilon SS}$ Constant describing scaled integral of dissipation due to surface layer shear

E Dimensionless entrainment rate

G Relative stratification in the entrainment zone

K_h Eddy diffusivity of heat

K_m Eddy diffusivity of momentum

L Obukhov length scale

N Brunt-Väisälä frequency

N_i Brunt-Väisälä frequency of the interfacial layer

Pr_t Turbulent Prandtl number

Q_s Surface heat flux (Km/s)

Ri Gradient Richardson number (see Chapter 1)

Ri_1 Gradient Richardson number specific to the FOM entrainment zone

Ri_{crit} Critical value of Ri_1

R_f Fairall (1984) Richardson number

Ri_k Richardson number defined by Kim (2001)

Ri_v Richardson number based on the full velocity and buoyancy jumps across the entrainment zone, the CBL depth, and the surface friction velocity (Deardorff and Willis 1982)

Ri_N Richardson number based on the background stratification, CBL depth, and surface buoyancy flux

Ri_δ Richardson number defined in Sorbjan (2004)

$Ri_{\delta b}$ Entrainment Richardson number based on full entrainment zone depth (GSM)

Ri_{τ} Richardson number based on entrainment zone buoyancy jump and surface friction velocity (Deardorff and Willis 1982)

$Ri_{\Delta b}$ Entrainment Richardson number based on the ZOM

S SOM variable, defined in Equation (5.22)

S_{ij} Rate of strain tensor

T_{num} Numerator in the entrainment parameterization of Kim (2001)

U SOM variable, defined in Equation (5.22)

V SOM variable, defined in Equation (5.22)

X Expression used in Chapter 5 to relate FOM buoyancy profile to ZOM buoyancy profile

X_{BG} Batchvarova and Gryning (1991,1994) ratio of vertical velocity scale to Deardorff (1974) velocity scale

Y Expression also used in Chapter 5 to relate SOM buoyancy profile to ZOM buoyancy profile

Y_{BG} Batchvarova and Gryning (1991,1994)

α_{ε} Constant of dissipation

α_{K} Constant of eddy diffusivity

β Parameter describing the fraction of turbulence kinetic energy in the convective boundary layer that is parameterized by turbulence parameterizations.

δ Entrainment zone thickness [Stull (1976a,c)]

δ_{ij} Kroneker delta (0 for $i \neq j$, 1 for $i = j$)

δb Full change in buoyancy across the entrainment zone

δu Full change in u across the entrainment zone

δv Full change in v across the entrainment zone

δz_i Full depth of entrainment zone, defined by the thickness of the layer where turbulent heat flux is less than zero.

ε Dissipation rate of turbulence kinetic energy (main text, Appendix A)
Asselin filter constant (Appendix B)

ϕ The instantaneous value of any given quantity

$\overline{\phi}$ The ensemble-averaged value of that quantity

ϕ' The deviation from an ensemble average.

$\tilde{\phi}$ The filtered value of that quantity

φ_e Universal function describing the shape of the TKE profile in the shear-free CBL

φ_{ε} Universal function describing the shape of the dissipation profile in the shear-free CBL

η Exponent for the velocity scaling used in entrainment parameterizations

κ von Karman constant

λ Amplitude error (Appendix B)

λ_{up} Height to which a parcel would travel upward from its current position, working against buoyancy forces, until all its turbulence kinetic energy were expended.

λ_{down} Height to which a parcel would travel downward from its current position, working against buoyancy forces, until all its turbulence kinetic energy were expended.

μ Courant number (Appendix B)

ν Kinematic viscosity

ν_H Thermal diffusivity

π Pressure in the LES equations of motion

ω Turbulence frequency (main text)

ω_a Frequency of the analytic solution (Appendix B)

ω_d Frequency of the finite difference solution (Appendix B)

ω_{dR} Frequency of the finite difference solution: real component (Appendix B)

ω_{dI} Frequency of the finite difference solution: imaginary component (Appendix B)

θ Potential temperature

θ_0 Reference value of potential temperature

θ_v Virtual potential temperature

θ_{v0} Reference value of virtual potential temperature

ρ Density

ρ_0 Reference value of density

σ_{ij}^s Subgrid deviatoric stress tensor (Appendix A)

τ_{ij}^s Subgrid stress (see Appendix A)

ζ z / z_i, the dimensionless boundary layer depth, or vertical coordinate scaled by the CBL depth.

Δ_v The grid cell vertical dimension

Δb Zero order model (ZOM) buoyancy jump at the CBL top

$\Delta \hat{b}$ Dimensionless zero order model (ZOM) buoyancy jump

$\Delta \hat{b}_0$ Constant of integration for the ZOM equilibrium entrainment equation for dimensionless buoyancy jump

Δb_1 First order model (FOM) buoyancy jump at the CBL top.

Δb_2 Second order model (SOM) buoyancy jump at the CBL top.

Δt Time scale of relaxation of Ri_1 in the FOM

Δu ZOM jump in u at the CBL top.

Δu_1 FOM jump in u at the CBL top.

Δv ZOM jump in v at the CBL top.

Δv_1 FOM jump in v at the CBL top.

Δz Entrainment zone thickness in the FOM

Δz_2 Initial entrainment zone thickness in the SOM, and before adjustments in the SOM

Δz_l Adjusted lower entrainment zone thickness in the SOM

Δz_{rev} Adjusted upper entrainment zone thickness in the SOM

Δz_w Height of the first grid cell above the lower surface (see Appendix A)

$\Delta\phi$ Change of the quantity across the top of the CBL (ZOM)

$\Delta\phi_1$ Change of the quantity across the entrainment zone (FOM)

$\Delta\phi_2$ Change of the quantity across the entrainment zone (SOM) before adjustments to buoyancy b_{sh}

Φ_i Energy lost from the CBL top (ZOM) due to radiation of internal gravity waves

Φ_u Energy lost from the CBL top (GSM) due to radiation of internal gravity waves

Γ_u Shear in the *x*-component of the geostrophic wind

Γ_v Shear in the *y*-component of the geostrophic wind

Π Pressure in the equations solved in the large eddy simulation code

Abstract

The current study examines the dynamics of entrainment and the evolution of the dry atmospheric convective boundary layer (CBL) when wind shear is present and seeks to make comprehensive tests of existing hypotheses regarding the effects of wind shear on entrainment and the parameterizations that have been developed from them.

24 large eddy simulations (LES) were conducted for CBLs growing under varying conditions of surface buoyancy flux, free atmospheric stratification, and wind shear. With the intent of elucidating the effects of surface layer shear versus shear at the CBL top, the simulations were divided into three categories: a free atmosphere with no mean wind (NS), an atmosphere with a height-constant geostrophic wind of 20 m/s (GC), and a case with strong shear in the geostrophic wind (GS). The entrainment predictions of LES were then compared with predictions from two 1.5-order, *e-l* turbulence models based on the Reynolds-Averaged Navier-Stokes (RANS) and with two bulk models based on integral budgets of CBL buoyancy, momentum, and turbulence kinetic energy (TKE): the zero order model (ZOM) and the first order model (FOM).

In the LES cases, the sheared CBLs grew fastest, relative to the shear-free CBLs when the surface buoyancy flux was weak and the atmospheric stratification was moderate or weak. From the simulations, there are two fundamental findings. The first is that the entrainment zone shear is much more important than the surface shear in enhancing CBL entrainment. The other is the discovery of a layer of constant *Ri* that forms within the entrainment zone when the relative effects of shear stand out strongly enough.

The tests of the ZOM parameterizations using LES data highlighted their mathematical deficiencies, which caused them to fail when shear was strong. When the full FOM equations were integrated using an entrainment zone depth limited by a critical Richardson number (*Ri*), they were able to model some of the sheared CBL cases in which ZOM fails. Based on the FOM and LES results and the results of testing other

parameterizations, any *Ri*-limited entrainment equation would seem to be most suited to model the dynamics of entrainment in sheared CBLs. Despite its shortcomings, the ZOM places the shear-free CBLs in a common framework from which they can be easily compared to sheared CBLs.

Tests of RANS-based *e-l* closures against the LES data show that the *e-l* closures exaggerate the differences between the entrainment rates of shear-free CBLs and sheared CBLs. The entrainment rate predicted by *e-l* closures for sheared CBLs is too large, regardless of whether the modeled entrainment zone TKE is larger or smaller than that in LES. It is possible that the formulation of the master length scale *l* for CBL turbulence needs to be reduced when shear is a significant source of TKE.

The comparisons between LES and the lidar data for the May 22, 2002 sheared CBL case show that CBL depth comparisons can be made relatively easily when a suitable atmospheric sampling strategy is used. However, the observed CBL growth rates differed considerably from LES, underscoring the fact that atmospheric processes not simulated in LES have a significant influence on the CBL depth. Despite these problems, the conclusions based on the simulation results need to be tested more fully against atmospheric data.

Chapter 1

Introduction

1.1 What is the Convective Boundary Layer?

The atmospheric boundary layer is the layer of the atmosphere that is sensitive to fluxes of momentum, temperature, and passive scalars on the time scale of about an hour or less (Stull 1988). By its nature, the atmospheric *convective* boundary layer (CBL) is a turbulent boundary layer, and its turbulence is primarily forced by the heating at the surface below, radiational cooling in clouds at its top, or both. If the CBL has no clouds, it is referred to as a dry CBL, and the main driving mechanism is heating at the lower surface.

The dry atmospheric CBL is the subject of this study. Turbulence in the dry CBLs develops when the heating of the ground becomes strong enough that the buoyancy force exceeds the viscous force by a critical threshold value, creating absolute instability, and convective motions ensue, transporting the heat upward in plumes or thermals. A thermal is defined as "a relatively small-scale, rising current of air produced when the atmosphere is heated enough locally by the earth's surface to produce absolute instability in its lowest layers" (Glickman et al. 2000).

To facilitate discussion throughout the rest of this text, the CBL will be divided into its three sublayers. The *surface layer* is the lowest sublayer that comprises

approximately 10 percent of the CBL depth. The convective motions in the surface layer are limited by the rigid lower surface and thus cannot transport heat away from the surface effectively. This results in a superadiabatic lapse rate (potential temperature decreases with height) in the near-surface layer. In the middle of the CBL is the *mixed layer*, often referred to as the *CBL interior*, in which stronger vertical motions mix momentum, temperature, and other scalars so that their vertical gradients are much smaller than in the surface layer. The mixed layer is usually the thickest sublayer in the CBL. At the CBL top is the *entrainment zone*, where stable stratification inhibits vertical mixing, and vertical gradients of potential temperature, momentum, and other scalars again become large. The entrainment zone is often called the *interfacial layer*. Above the CBL is the *free atmosphere*, which is usually stably stratified.

Since the dry CBL is driven mostly be the surface heating, we will be discussing the flux of the energy coming from the surface heating. Since the meaning of heat is somewhat controversial in science, we can be more precise and speak of enthalpy (Glickman et al. 2000). However, it is often more convenient for discussion to use "heat flux", so "heat flux" is used often in this dissertation, but when so used, its meaning is intended to be the same as the meaning of "flux of enthalpy". With the aid of the gas laws and dividing by mass, we can describe the flux in terms of specific enthalpy (enthalpy per unit mass). Dividing specific enthalpy flux by the specific heat at constant pressure, we have the temperature flux, and when temperature is standardized in terms of a reference pressure, we can speak of the flux of potential temperature. When water vapor is present, we can then speak of the flux of virtual potential temperature. Finally, when discussing the sources and sinks of turbulence kinetic energy in the system, it is

often most convenient to speak of buoyancy flux. Buoyancy is defined traditionally as $b = \frac{g}{\theta_{v0}}\left(\theta_v - \theta_{v0}\right)$, where g is gravitational acceleration, θ_v is virtual potential temperature, and θ_{v0} is the reference value of virtual potential temperature [see Doswell and Markowski (2004) for a more complete description of the meaning of buoyancy]. The terms buoyancy flux, potential temperature flux, virtual potential temperature flux, and heat flux will often be used interchangeably.

Over land, the CBL undergoes a well-known diurnal cycle (Stull 1988), in which vigorous convective motions are initiated by surface heating in the morning, and the CBL grows during the day as the thermals ascend into the free atmosphere. Late in the day, when insolation weakens to the point that the net heat flux convergence at the surface is negative, the mixed layer decouples from the surface and becomes a residual layer of decaying turbulence. The nocturnal boundary layer then forms as the air in contact with the surface cools and becomes stably stratified. Over the oceans, the diurnal cycle is not as pronounced as over land, and CBLs can occur any time of the day.

In this study, the focus is on the mid-to late-morning and afternoon portion of the diurnal cycle, when the CBL growth is forced by shear or heating of the lower surface, or to be more general, any time the CBL, whether over the oceans or land, is growing. This study focuses specifically on the impact of wind shear on CBL growth. Although the CBL growth, in most cases, is primarily driven by heating at the surface, a pure CBL of this type rarely exists, and there are many situations in which the surface heating is weak (such as in the winter or in the early morning) and the shear-production of turbulence is relatively strong. In these cases, the shear effects on entrainment cannot be ignored. To date, many studies of entrainment have focused on the shear-free CBL, and their

hypotheses for shear-free entrainment have been well-tested in laboratory tanks, atmospheric measurements, and numerical simulations. Far fewer studies have been performed on the influence of shear on CBL entrainment, and most of the hypotheses and parameterizations developed so far have not been well tested over a suitably wide range of atmospheric conditions. The goal of the current study is to examine the dynamics of entrainment when wind shear is present in the CBL and to comprehensively test existing hypotheses and parameterizations regarding the effects of wind shear on entrainment and, more generally, on the CBL development.

1.2 Definition of Entrainment

The CBL growth is controlled by three mechanisms.

The first of these (although not necessarily the largest) is mean upward vertical velocity at the CBL top (Lilly 1968). It is associated with horizontal convergence of the flow within the CBL. Such flows can be forced by quasigeostrophic and other processes in the atmosphere (Holton 1992).

The second mechanism of CBL growth is differential temperature advection. When advection changes with height, it can alter the vertical gradients of potential temperature in the atmosphere and thus alter the environment in which the CBL is growing.

Finally, CBL growth can be driven by the process of *entrainment*, in which more highly buoyant air from the free atmosphere is engulfed by, and becomes part of, the growing CBL (Randall and Schubert 2004). This study focuses specifically on entrainment.

Entrainment occurs as thermals, rising from the surface layer, overshoot their equilibrium level in the inversion at the CBL top (Stull 1988). As they sink back into the mixed layer, they pull down air from above, which is non-turbulent and has a higher potential temperature than the mixed layer air. This free atmospheric air air is annexed into the turbulent mixed layer (Randall and Schubert 2004). Entrainment is not a straightforward mixing process. Mixing involves an exchange of particles in both directions across an interface. However, in the entraining CBL, the interface is moving upward with time, allowing free atmospheric air to enter the CBL, but CBL air does not enter the free atmosphere (unless there are cumulus clouds, which are beyond the focus of this study). As such, entrainment is essentially a one-way process. The entrained free atmospheric air usually has lower concentrations of water vapor and pollutants than the mixed layer air, but the positive fluxes of these constituents from the surface counteract the dilution of these constituents by entrainment.

1.3 The Importance of Entrainment

Understanding the entrainment process is critical for numerous reasons. Firstly, entrainment regulates the exchange of momentum, water vapor, pollutants, and other scalars between the boundary layer and the overlying free atmosphere. Since entrainment controls the CBL depth, it regulates how deeply pollutants and water vapor mix upward into the atmosphere. Numerical weather prediction (NWP) modeling relies on the accurate characterization of the horizontal and vertical distributions of water vapor in the atmosphere (Weckwerth et al. 2004), and since the concentration of water vapor is highest in the lower atmosphere, the CBL has a strong influence on its distribution. For

air pollutants, a deeper CBL means greater dilution for pollutants that are released near the ground (Lyons and Scott 1990). This applies to toxic air pollutants such as sulfur oxides, nitrogen oxides, and carbon monoxide, as well as to greenhouse gases such as methane and carbon dioxide (Davis et al. 1997). Understanding boundary layer entrainment and its effects on the distribution of scalars in the atmosphere is, therefore, a necessity when modeling climate, as well as predicting air quality.

Secondly, entrainment is a process that regulates the formation and dissipation of horizontally extensive marine stratocumulus clouds over the large ocean areas off the western coasts of the continents (Lilly 1968, Stevens 2002). These clouds have albedoes that reach 50%, thereby scattering back to space much of the solar radiation that would otherwise heat the ocean below (Randall and Schubert 2004). Thus, the presence of these clouds helps to maintain the relatively low temperature of the water over which they form, and the cool water helps to maintain the clouds. Thus, marine stratocumuli, which are strongly influenced by entrainment, represent a significantly positive feedback mechanism and are an important part of the earth's climate system.

Third, entrainment affects the depth and quality of moisture in the boundary layer, and when wind shear is present, it can have also have a strong influence on the CBL momentum profiles (Stull 1988). The importance of low-level shear on the character of deep, moist convection (Weisman and Klemp 1982, 1984) has generally been agreed upon in the meteorological community (Doswell and Bosart 2001). The low-level momentum profiles have an impact on the nature of deep moist convection once it has developed, but it may also affect the initiation of storms (Ziegler and Rasmussen 1998). Since the CBL occupies most of the layer in which such shear is important, CBL

processes, an important part of which is entrainment, have a strong impact on the character of deep, moist convection.

Finally, wind energy resources assessment also requires some knowledge of entrainment, since entrainment of momentum affects mean wind profiles and the turbulence structures within the CBL. Since the entrainment rate directly affects the CBL dynamics, it directly or indirectly affects a number of other phenomena. It is therefore critically important to understand how entrainment works, both in the shear-free and sheared CBL.

1.4 Entrainment Related to CBL Integral Budgets of Energy

The growth of the CBL through entrainment can be conceptualized most easily within an ensemble-averaged framework. In theory, an ensemble average consists of the average across an infinite number of realizations of the considered flow. In the shear-free, horizontally homogeneous CBL, horizontal averages can substitute for the ensemble averages, and the horizontally averaged buoyancy and turbulence fields can be considered as functions of time and height. Neglecting mean vertical motion at the CBL top, the evolution of the buoyancy profile in the CBL can then be described entirely in terms of its turbulent vertical flux, and the evolution of the turbulence kinetic energy (TKE) profile can be described in terms of the sources (buoyancy flux), transport (by TKE and pressure), and the dissipation (by viscosity) of TKE.

The entrainment rate is essentially determined by a balance among various sources and sinks of energy. In the shear-free dry CBL, the surface buoyancy flux is the only turbulence production mechanism. It begins when heating generates instability in

the surface layer, causing plumes to form and begin rising to the CBL top. In the ensemble-averaged framework, the buoyancy flux profile is approximately linear throughout most of the CBL. The flux describes the rate of production of TKE (where the flux is positive) or destruction of TKE (where the flux is negative). The buoyancy flux is largest near the surface, where the heating is supplied, and it decreases to zero somewhere near the CBL top, where plumes reach their equilibrium level, that is, the level at which their temperature matches the horizontally-averaged temperature. The convergence of the turbulent flux describes the time rate of change of horizontally averaged buoyancy in the CBL interior.

The turbulence fills the entire CBL and it is usually largest within the CBL interior. As the thermals rise from the surface, they carry TKE upward with them, and in so doing, they transport TKE away from the surface layer, where they originate, and towards the CBL top, where that TKE is spent for entrainment, provided it is not dissipated before then. The transport of TKE thereby represents a sink of TKE near the surface and a source of TKE higher in the CBL.

Ultimately, all TKE meets its demise and is converted into some other form of energy. There are two possible outcomes related to its demise. The TKE can go through the energy cascade process associated with three-dimensional turbulence, with energy transferred from larger to smaller scales until it is entirely converted to heat energy through viscous dissipation. Alternatively, if turbulent plumes manage to rise upward past their equilibrium level and penetrate into the stable layer before this process is complete, they can contribute to the entrainment of warmer air from the free atmosphere into the CBL. This process requires work and consumes the TKE, converting it into the

potential energy of the CBL-free atmosphere system. This occurs in the entrainment zone, where the TKE is destroyed by *negative* buoyancy flux. Also, some energy loss can occur out the CBL top due to the radiation of internal gravity waves.

As the CBL grows, the heat supplied at the surface is mixed throughout the CBL interior by the turbulence. The buoyancy in the CBL increases as long as the flux convergence is positive, and the CBL grows as turbulence entrains free atmospheric air from above. The CBL buoyancy profile thereby "climbs" up the background profile of the free atmosphere. If the heating rate at the surface increases, the heating rate of the CBL interior increases and the CBL will grow more quickly. If the free atmosphere stratification strengthens, the heating required for the CBL to "climb" the free atmospheric buoyancy profile also increases, and the CBL grows more slowly. The fraction of TKE that is dissipated versus consumed by entrainment at the CBL top also determines the entrainment rate (Lilly 1968). If 100% of the TKE is dissipated, there is no negative heat flux at the CBL top, and the entrainment rate is relatively slow. If 100% of the TKE is used for entrainment, as was assumed by Ball (1960), the negative area of the heat flux profile in the entrainment zone equals the positive area below, and the CBL grows at its fastest possible rate. Overall, the entrainment rate is governed by the surface buoyancy flux, the free atmospheric stratification, and the dissipation rate of TKE. The dissipation of TKE determines the fraction of buoyancy-produced TKE that becomes available for the negative buoyancy flux of entrainment.

In the shear-free CBL, this fraction is essentially independent of surface buoyancy flux and stratification (Carson 1973; Tennekes 1973; Betts 1973). The CBL top is commonly identified where the buoyancy flux reaches its minimum in the entrainment

zone. The ratio of the negative of this minimum to the surface buoyancy flux is known as the *entrainment flux ratio*.

In the presence of shear, the kinetic energy of the mean flow can become an additional source of energy for the CBL. In this case, the momentum balance must be considered (Fedorovich 1995, Stull 1988) in addition to the buoyancy and TKE balances. Larger scale pressure gradient and Coriolis forces are essential components of the momentum balance. Like buoyancy, momentum is also dependent on its turbulent vertical flux. At the surface, friction slows the flow, and the momentum flux is generally negative (it sign is opposite to the sign of momentum), and since turbulence also mixes momentum in the CBL, it transports the weaker momentum upward (Stull 1988). Therefore, the negative flux often extends throughout the CBL, but if there is large enough shear in the free atmospheric momentum profile, the flux can reverse sign. Where the flux convergence is positive, the momentum increases, and vice versa.

Shear generates TKE when vertical turbulent fluxes of momentum interact with vertical gradients of momentum (Stull 1988). Since turbulent motions in the CBL mix momentum, the wind shear tends to concentrate at the bottom and top of the CBL, and it is in these two places that the shear-generation of turbulence has the potential to be greatest.

The impacts of shear-generated turbulence on entrainment can be understood in the same terms as buoyancy-generated turbulence. Some fraction of the TKE produced by shear is dissipated, and some is used for entrainment. Depending on where the shear-driven TKE is generated, transport is involved in determining this fraction. The shear at the surface is usually strongest, but this shear-generated turbulence must be transported

upward to the CBL top before it can drive entrainment. At the CBL top, shear-generated turbulence is immediately in a location where it can influence entrainment, but shear at the CBL top is, in many instances, weaker than at the surface. The location of stronger shear more distant from the entrainment zone compared to weaker shear immediately in the entrainment zone leaves it unclear which of these two shears has a greater influence on entrainment. The respective roles of the surface and entrainment zone shears in driving entrainment will be examined in this study.

An important aspect of entrainment zone shear is its contribution to the instability at the CBL top. The primary type of instability associated with sheared flows is Kelvin-Helmholtz (K-H) instability. When sufficient shear exists across a density interface or a stably stratified layer, the destabilizing effects of the shear may become larger than the stabilizing effects of the positive vertical buoyancy gradients, and K-H instabilities ensue (Kundu 1990). K-H instability can occur when the Richardson number, defined as

$$Ri = \frac{\dfrac{g}{\theta_{v0}}\dfrac{\partial \theta_v}{\partial z}}{\left(\dfrac{\partial u}{\partial z}\right)^2 + \left(\dfrac{\partial v}{\partial z}\right)^2}, \tag{1.1}$$

is sufficiently low. In (1.1), u and v are the x- and y-components of velocity, respectively. Ri represents the ratio of the buoyant suppression of turbulence to the shear generation of turbulence. The necessary theoretical condition for K-H instability is $Ri \leq 0.25$, but in many flows, this is not a sufficient condition for the instability.

Although the instability analysis, in the strict sense, applies to nonturbulent flow, Kim et al. (2003) have examined K-H type instabilities at the CBL top, examining the turbulence structures there and their qualitative similarity to K-H billows. Entrainment of free atmosphere air can be enhanced during the wave breaking process associated with K-

H type instability at the CBL top. They also analyzed *Ri* in the entrainment zone, finding *Ri*<1 over a significantly deep layer in the upper portion of the CBL, but the study does not answer questions about the development, persistence, and depth of this layer over a variety of different backgrounds of shear and gravitational stability. It is also uncertain whether there is a limit to *Ri* in this layer when the shear becomes strong. The present study seeks to continue the *Ri* analysis in entraining CBLs in a wider variety of background conditions to relate *Ri* to the strength of the shear-enhanced entrainment.

Grabowski and Clark (1991, 1993a,b) studied instabilities on the interface between a cloud and its environment by numerically simulating the development of these instabilities at the top of a rising thermal. Grabowski and Clark (1993b) focused on the effects of environmental shear in the development of these instabilities and found the effects of the environmental shear on the development of instabilities were far secondary to the effects of the baroclinically generated shear at the immediate interface. Their studies have limited applicability to the sheared CBL, because the turbulence in the CBL concentrates shear at the CBL top more than what was modeled in Grabowski and Clark (1993b). Nevertheless, they can explain some instabilities at the top of the CBL thermals in shear-free CBLs. The overall effect of the concentrated shear at the CBL was not addressed.

More fundamentally, there is no consensus on whether mean shear enhances or suppresses entrainment. Shear across the CBL top can deform thermals such that they do not penetrate as readily into the inversion, and this can theoretically interfere with the entrainment process. If thermals are prevented from overshooting their equilibrium level, then the entrainment zone heat flux would be reduced, and the CBL growth would be

slightly slower. If this effect dominates, the shear, in essence, shelters the CBL from the free atmospheric air (Hunt and Durbin 1999). The present study hopes to provide some additional insight that could be useful for answering this fundamental question.

1.5 Methods to Evaluate Entrainment

Entrainment can be studied using three fundamental groups of methods: direct atmospheric measurements, scaled laboratory experiments, and numerical modeling.

1.5.1 Atmospheric Measurements

It would seem most intuitive to test atmospheric entrainment hypotheses using data directly from atmospheric measurements, and the most natural way to do so would be to measure entrainment directly. However, these direct measurements are very difficult to make. In many cases, it is more feasible to measure the evolution of the CBL depth, entrainment zone thickness, and other parameters of entrainment in conjunction with surface heat flux, and free atmospheric stratification measurements. Owing to the fact that it is not possible to control atmospheric motions precisely, atmospheric measurement data reflect all fluid processes that are occurring simultaneously at the point of measurement, and it is very hard to find pure cases in which only the process of interest is present.

In the case of the CBL, one of these competing processes is the organized vertical motion due to larger scale atmospheric flows, such as baroclinic disturbances, deep moist convection, or processes that are related to horizontal variability of the underlying forcing (sea breezes, drylines, etc.). Averaging over areas kilometers or tens of kilometers wide

may still not be enough to remove these vertical motions from the analysis, so the horizontal convergence within the CBL must be measured very precisely. The most recent entrainment-related experiments (Stevens et al. 2003) are beginning to overcome the limitations to estimating divergence.

When strong wind shear is present, the CBL growth is also affected by differential temperature advection, which can change the background profile through which the CBL grows. Also, the CBL depth has considerable local variability. The interface height between the mixed layer air and the free atmospheric air is highly variable both in space and time, so the measurements of CBL depth must be averaged over a considerable area or time so that the mean of these measurements converges to the ensemble mean, which is necessary for comparison with models (see Chapter 3). Many instruments, such as radiosondes, take measurements only above a point or a small area and cannot be used for averaging. Others, such as aircraft (Lenschow 1973; Flamant et al. 1997; Davis et al. 1997), are expensive to operate and typically have only provided CBL measurements during field campaigns. Some of the more promising measurements (lidar, radar, wind profilers) can perform scans or sample the atmosphere continuously at a relatively high resolution, but many of these technologies are relatively new and have not yet provided sufficient data that could be used in entrainment studies.

However, atmospheric CBL measurements have provided useful data for comparison with entrainment theories in near calm conditions, when the effects of advection and mean vertical motion are significantly reduced. The entrainment rate in relatively shear-free conditions has been estimated with these data (Batchvarova and Gryning 1991, 1994; Boers et al. 1984; Garcia et al. 2002). Additionally, more

established methods of measurement, such as balloon soundings, can be used to retrieve profiles of temperature and horizontal components of momentum (Hoxit 1974, Garratt and Wyngaard 1982, LeMone et al. 1999) to evaluate how they are affected by entrainment.

1.5.2 Laboratory Models

If laboratory models are used to study entrainment, the environment of the experiment can be tightly controlled specifically to test the entrainment hypothesis at hand, and the competing effects of other processes can largely be eliminated. Among laboratory approaches, the water tank and wind tunnel model studies have been the most successful so far.

Water tank studies of the CBL have typically used thermal stratification or height-varying salinity. If the appropriate scaling is applied (Deardorff 1980, Fedorovich et al. 2004a), the water tank results can be made comparable with atmospheric measurements. Water tank experiments have been performed for shear-free CBLs (Deardorff et al. 1969; Deardorff et al. 1980, 1985) and for shear-driven boundary layers (Long 1975; Wu 1973; Deardorff and Willis 1982) but never for sheared CBLs. Water tank studies of the CBL were especially popular in the 1970s and 1980s, after which time rapid advancements in computer technology made numerical simulations a less expensive alternative.

Scaled down simulations of the atmospheric CBL can also be conducted in wind tunnels (Fedorovich et al. 2001a, b; Fedorovich and Kaiser 1998). In these experiments, horizontally evolving CBLs are studied. The downwind distance in a horizontally evolving CBL is the analog of time in the temporally evolving, horizontally

homogeneous CBL that is the focus of the current study. A complicating effect of shear on entrainment in the wind tunnels is that turbulent momentum fluxes cause flow divergence in the horizontally evolving CBL, and this effect directly competes with entrainment in influencing the CBL depth.

1.5.3 Numerical Techniques

Entrainment can also be studied numerically using either simulations or models.

1.5.3.1 Simulations

If the TKE-containing turbulent motions are resolved in the numerical study, the study can be considered a simulation (Wyngaard 1998). With grid spacing on the order of a few millimeters, direct numerical simulation (DNS) resolves all turbulent motions because it numerically integrates the Navier-Stokes and thermodynamic equations (Wyngaard 1998; Pope 2000). Because of the limitations of computer power, it can only be used for domains several orders of magnitude shallower than the atmospheric CBL. Also, DNS makes use of finite difference approximations to the equations of motion, which is subject to various artifacts, including phase speed errors, artificial viscosity, and dispersion errors (Durran 1999).

Large eddy simulation (LES—Deardorff 1970a, 1974a, 1974b, 1980; Moeng 1984; Schmidt and Schumann 1989; Sykes and Henn 1989; Moeng and Sullivan 1994; Sorbjan 1996a,b; Lewellen and Lewellen 1998; Sullivan et al. 1998; and Fedorovich et al 2001a,b) is a simulation that integrates the *filtered* Navier-Stokes and thermodynamic equations (see Appendix A) and resolves most of the energy-containing scales of

turbulence. Any motions that are not resolvable are assumed to be only a small fraction of the total TKE and are parameterized with a subgrid TKE scheme.

A rapid increase in computer power over the past one or two decades has made large eddy simulation (LES) a very popular tool for studying CBL processes. In LES, the environmental parameters such as surface heating, stratification, and shear can be precisely controlled. Representation of flows in LES need not depend on the Taylor hypothesis [see Stull (1988)] because the thermodynamic and kinematic properties are known at all points in the grid simultaneously, making it very easy to calculate horizontal averages, and time averages can be calculated as well. In this manner, LES has been a helpful tool in studying the statistics of turbulence (Deardorff 1974a,b; Moeng and Sullivan 1994) and in visualizing the turbulence structures in the CBL (Kanna and Brasseur 1998), leading to a better understanding of the dynamics of entrainment and the behavior of turbulent structures. The inherent drawbacks of LES are the same as those of DNS, except LES also is limited by the ability of the subgrid model to predict the effects of the subgrid motions on the filtered (resolved) fields. This is the price that must be paid in order to simulate turbulence in larger domains. LES, despite its larger domains, often cannot encompass all the heterogeneity that exists in atmospheric CBLs.

1.5.3.2 Models

In NWP, turbulence must also be described numerically, but the available computer power is insufficient to simulate the turbulence over the entire NWP domain. The computational needs can be substantially reduced if the Reynolds-Averaged Navier-Stokes (RANS) equations are used. In RANS for the CBL, ergodicity is assumed—that

is—the horizontal and ensemble averages are assumed to converge to the same mean. The horizontal averaging is used to form prognostic equations that are integrated forward in time to calculate vertical profiles of averaged TKE, momentum, and buoyancy in the CBL. Because of the horizontal averaging, the turbulence is described not in a resolved but in a statistical sense, and the RANS-based techniques are not turbulence *simulations*, but rather, they are referred to as turbulent flow *models* (Wyngaard 1998).

One particular category of these models is *e*-*l* models (Xue et al. 2001; Fiedler and Kong 2003). In *e*-*l* models, a prognostic equation for TKE (*e*) is solved, and the TKE is related to dissipation and the subgrid eddy diffusivities of momentum and heat through some turbulence integral length scale (*l*). The *e*-*l* models and other RANS-based techniques are common in numerical weather prediction (NWP) models or in other situations where grid cell sizes are not sufficiently small to resolve the principal CBL-scale turbulent motions. The effect of those turbulent motions on the resolved fields needs to be predicted correctly.

To simplify the equations even further, one can integrate the TKE, momentum, and buoyancy balance equations over the depth of the CBL, forming equations that describe the CBL integral budgets of TKE, momentum, and buoyancy (Lilly 1968, Zilitinkevitch 1991, Fedorovich 1995). In this case, all parameters of the flow become time-dependent only. These equations can provide insight into the mechanisms responsible for entrainment, and in some cases, they can be solved analytically to yield prognostic equations for CBL depth. Such models are often used in air quality models to predict the mixing depth, and they are sometimes used in global circulation models (GCMs) as well (Stevens et al. 2002).

In order to enable the vertical integration that leads to these equations, a simplified CBL structure is assumed. These simplified profiles underlie the conceptual models of the CBL, and the degree of simplification of the CBL vertical structure separates these models from one another.

The simplest model is the zero order model (ZOM) [Lilly (1968)] in which the CBL is represented as a slab mixed layer with height-constant buoyancy and a linear buoyancy flux profile. At the CBL top, there is a finite discontinuity, or jump, in both the buoyancy and the buoyancy flux, with buoyancy changing to its free atmospheric value (usually a linear profile) and buoyancy flux jumping from a negative value just below the CBL top to zero. The ZOM gets its name because the discontinuities are in the zero order derivatives of the buoyancy and momentum profiles (i.e. the profiles themselves). These equations have been used to a limited extent to describe CBLs with shear (Zeman and Tennekes 1977; Tennekes and Driedonks 1981; Driedonks 1982; Boers et al. 1984; Fedorovich 1995; Pino et al. 2003) and have also been solved analytically (Zilitinkevitch 1991; Fedorovich et al. 2004a). It will be shown in Chapters 3 and 10 that for CBLs with shear, ZOM entrainment equations suffer from deficiencies that make their usage problematic. The deficiencies may be of a physical origin, but they reveal themselves in a mathematical form in the equations.

The first order model (FOM) [Betts (1974)] has a constant-buoyancy mixed layer just as the ZOM does, but it includes an entrainment layer of finite thickness at the top of the mixed layer, so that the discontinuities in the buoyancy and momentum profiles are in their first derivatives. For the shear-free CBLs, some argue that it is necessary for a finite entrainment zone thickness to be taken into account, as in the FOM, in order for any

conceptual model to capture the true essence of the entrainment process (Sullivan et al. 1998; Van Zanten et al. 1999). Others (Fedorovich et al. 2004a) find the zero order model description of entrainment to be sufficient. For sheared CBLs, the matter may become more important, but it has certainly not been resolved. Studies using the FOM for sheared CBLs (Mahrt and Lenschow 1976; Kim 2001) have made assumptions that neglect some of the effects of the entrainment zone finite thickness. These issues will be addressed in Chapter 10.

Higher order models, such as the general structure model (GSM; Deardorff 1979; Fedorovich and Mironov 1995) have so far been used only for shear-free CBLs. These models have smoother profiles that match the actual horizontally averaged profiles in the CBL a bit more closely. Prognostic entrainment equations from these more complex models are solved numerically. To be true to its definition, the GSM can be reduced to lower order models like the FOM as particular cases of the GSM. The GSM requires the specification of a polynomial function describing the buoyancy profile in the entrainment zone. Since the FOM profile is a first order polynomial, it can fall within the general framework of the GSM.

Because of the demonstrated utility of LES to study CBLs of different types without the large expense of atmospheric field measurement programs, it will be used as the primary tool to investigate sheared CBLs in this study. Since it is relatively straightforward to revise the LES code into a one-dimensional *e-l* model, and because *e-l* models are so commonly used in regional NWP models, it is very worthwhile to examine how these models represent entrainment in sheared CBLs. The results can be widely applied to weather prediction, so the ability of these models to reproduce the entrainment

rates in LES will be examined. Finally, to answer some questions revolving around the ZOM versus the FOM and the importance of entrainment zone thickness, this study will compare entrainment predictions of those models with each other and with LES predictions.

1.6 Layout of Remaining Chapters

The remaining body of this dissertation is divided into the following chapters. Chapter 2 will provide a more detailed review of previous work focusing on sheared CBLs. Chapter 3 will describe the theoretical and numerical techniques that are used to study the sheared CBL and will present them as a hierarchy of numerical techniques, ranging from LES through the RANS-based closures to the ZOM. Chapter 4 is dedicated to resolving some issues surrounding the shear-free CBL dynamics. It shows that shear-free CBLs growing through atmospheres of different stratification fall into a common regime of entrainment. This feature will be used later to directly compare the shear-free and sheared CBL evolution. Chapter 5 develops this framework further and explains some of the differences among the entrainment flux ratios of the ZOM, higher order models, and LES. The goal is to understand which conceptual model framework is best for comparison between sheared and shear-free CBLs and why their entrainment flux ratios are so different. Chapter 6 describes the methods that are used in the numerical experiments performed.

Chapters 7 through 10 present results of the numerical experiments. Chapter 7 contains a detailed analysis of the vertical profiles of mean flow and turbulence statistics from the simulations, and Chapter 8 focuses on the turbulence structure. Chapter 9

presents some considerations for comparing simulations with atmospheric data and then describes a case study comparing simulated CBL growth rates with measured atmospheric CBL growth rates. Chapter 10 shows comparisons of entrainment predictions by LES and the RANS-based and integral budget-based (bulk) models (ZOM and FOM).

Finally, Chapter 11 summarizes the results and presents the overall findings of the numerical experiments.

Chapter 2

Background

2.1 Early Studies of Entrainment

By definition, the dominant turbulence production mechanism in the convective boundary layer is buoyancy flux. In dry convective boundary layers, entrainment is governed mostly by the surface buoyancy flux, which produces TKE, and the overlying atmosphere's hydrostatic stability, which destroys TKE. With this in mind, early studies of entrainment (Ball 1960, Lilly 1968, Betts 1973, Carson 1973, and Tennekes 1973) took the shear generation term in the TKE balance equation to be negligible. Ball's approach was based on the conservation of energy, with heat energy from the surface being converted into the kinetic energy of thermals, then to potential energy by entrainment. Arguing that viscous dissipation was negligible on the CBL scale, he did not include dissipation of TKE in the calculations, and the entrainment flux ratio was unity. Lilly (1968) allowed for some dissipation of the buoyancy-generated TKE within the mixed layer and, not knowing how much dissipation occurred, allowed the entrainment flux ratio to have a value between 0 and 1. Betts (1973), Carson (1973), and Tennekes (1973) then followed up with papers proposing the entrainment flux ratio to be approximately 0.2—a number that has essentially been agreed upon (Fedorovich et al. 2004a). Additionally, Stull (1973) provided a detailed analysis of the structure of

overshooting thermals in the entrainment zone and developed a theory of entrainment based upon that structure.

Laboratory water tank entrainment experiments proceeded concurrently with the theoretical studies. Many of the laboratory studies were motivated by the desire to understand the rate of deepening of the ocean thermocline forced by wind stress (Wu 1973, Long 1975), while others were intended as models of the atmospheric CBL (Deardorff et al. 1969, 1980), but all provided relevant data toward the entrainment problem. Turner (1965) studied the turbulent transport of heat and salinity across a density interface between warm, fresh water and cold, salt water with turbulence forced by heating from below, and then (Turner 1968) studied the transport with turbulence forcing provided by mechanical agitation (but not mean shear). Kato and Phillips (1969) explored the shear-forced turbulent entrainment in a laboratory experiment that was carefully designed to apply a constant stress at the upper surface. The intent was to study the ocean equivalent of mechanical turbulence generated by wind stress at the surface. Wu (1973) applied the wind stress more directly, setting a wind tunnel atop the water tank and studying the rate of deepening of the thermocline in the tank. Long (1975) made further analyses of these and other experiments, in which the mechanical forcing was by agitation (Turner 1968) or shear (Kato and Phillips 1969, Wu 1973) and reconciled some of the differences in those studies.

However, Deardorff et al. (1969) were first to design their experiments to simulate the growth of the atmospheric CBL forced by heating of the ground and to directly test the theories set forth in Lilly (1968). Their data showed that the entrainment flux ratio was much less than unity, which is an important result in understanding the fate

of buoyancy-produced TKE in the CBL (dissipation versus entrainment). Willis and Deardorff (1974) focused more on turbulent statistics in their water tank CBL and demonstrated the comparability of those statistics with atmospheric data when they are normalized by the convective velocity and temperature scales proposed by Deardorff (1970b). Unfortunately, some differences between the atmospheric and water tank CBLs stood out, such as the smaller scaled variance of the horizontal velocity in the water tank than in the atmosphere. This was believed to happen because of the confined horizontal dimension of the water tank and the consequently low width to depth aspect ratio of the CBL. Additionally, the study provided measurements of the buoyant production, turbulent transport, and dissipation of TKE.

Deardorff (1970a; 1972a; 1974a,b; 1980) made the first three-dimensional numerical simulations of the atmospheric CBL. In these simulated flows, the turbulence statistics could be calculated simultaneously everywhere on the grid without sensors contaminating the flow, so these numerical simulations, which came to be known as large eddy simulation (LES), served as a useful tool in understanding the dynamics of turbulence and entrainment in the CBL, despite the relatively coarse resolution that was possible at that time. These early studies concentrated on the turbulence statistics and the turbulence structure in the simulated horizontally quasi-homogeneous CBL. Since the simulations were conducted under typical atmospheric conditions, some showed effects of shear, with the convection organizing into horizontal roll structures (Deardorff 1972a). Because of numerical limitations, the CBL spanned the entire vertical domain of the model grid in these first simulations and therefore was non-entraining.

Deardorff (1974a,b) used a grid large enough to simulate both a CBL and the free atmosphere above it, so this study was the first to simulate entrainment. The changes in the mean profiles of temperature, humidity, and wind as the boundary layer grew were numerically simulated, and the effects of entrainment could be seen in the turbulence statistics. These simulations provided further tests of the entrainment hypotheses of the early conceptual models. Deardorff (1974b) looked at the structures, the TKE budgets, temperature variance and other second moment budgets, as well as the spectra of velocity fluctuations in the numerical simulation of the CBL initialized with sounding data from Day 33 of the Wangara experiment (conducted in Australia in the 1960s). The LES output data were compared with the atmospheric data from the experiment, and the study represents the first LES-atmospheric data comparison.

2.2 Evidence of Shear Effects

While many of the theoretical and observational studies of atmospheric CBL growth were focused on shear-free entrainment, atmospheric studies were finding effects of wind shear on the development of the CBL and turbulence structure within it. Lenschow (1970) studied the CBL turbulence structure and TKE budgets and identified shear production of turbulence in the surface layer. Lemone (1973) studied the structure of CBL rolls using aircraft and instrumented tower data. Pennell and Lemone (1974) also studied the turbulence structure and vertical profiles of the terms in the TKE budget in a trade wind boundary layer, finding significant input by shear throughout the CBL below cloud base. Finally, Lenschow (1974) looked further into the TKE budgets and developed a model for the height variation thereof. These studies provided some quantification of the shear

generation of TKE in the surface layer but not at the CBL top. Nonetheless, their analyses indicated a significant shear contribution to the TKE budget in the lower CBL for rather typical atmospheric wind speeds on the order of 10 m/s. Their estimates of dissipation, however, showed that most of the shear generation near the surface was probably balanced by dissipation. At the CBL top, measurements were not sufficient to address shear generation of TKE.

Evidence for shear effects on boundary layer structure has been well-documented in radiosonde data as well. Hoxit (1974) performed a study analyzing radiosonde data over four consecutive cold seasons (November through March), finding evidence for some downward turbulent transport of horizontal momentum associated with the vertical shear of the geostrophic wind. The velocity profiles were found to be dependent on the orientation of the thermal wind vector (shear in the geostrophic wind) relative to the surface geostrophic wind vector. The data are not presented in a format in which the boundary layer top can be precisely identified, but the vertical profiles provide some evidence of the deepening of and mixing by a turbulent boundary layer between morning (12 UTC) and evening (00 UTC). Arya and Wyngaard (1975) developed a physical model of the baroclinic CBL and used it to predict wind profiles in the CBL. The model profiles agreed reasonably well with profiles from atmospheric measurements.

Kaimal et al. (1976) analyzed data from a field experiment in northwestern Minnesota and found unexpectedly large turbulent stress in the CBL, which was taken as evidence of significant heat and momentum entrainment into the CBL. The data in the upper 40 percent of the CBL were fairly sparse, so the entrainment of momentum and heat had to be inferred from extrapolation of the lower level measurements. To estimate

these fluxes in the upper CBL better, an experiment at Ashchurch, Worcestershire was conducted a couple years later, and the data, presented by Caughy and Palmer (1979), complemented the Minnesota data fairly well, confirming the effects of entrainment in heat flux and momentum profiles in the CBL. Some entrainment flux ratios higher than the shear-free predictions of 0.2 were observed, indicating some possible enhancement of entrainment beyond what would theoretically be found in a shear-free case. Unfortunately, there was some uncertainty in the estimate of the entrainment flux ratio since the surface heat flux was not directly measured (it can be inferred by extrapolating the mixed layer heat flux profile to the surface). These studies were focused on the second moments of turbulence and did not present much data on mean wind profiles, which would have been helpful in relating the entrainment of momentum and heat to shear in the CBL.

Price et al. (1978) performed a study of oceanic mixed layer deepening, with the intention of finding whether the relevant velocity scale for shear-induced mixed layer deepening was the surface friction velocity u_* or the velocity change across the bottom of the mixed layer δu. Their data indicated that the observed deepening rate scaled best with δu. This result has particular relevance for the current study, which also seeks to quantify the relative contributions of surface and entrainment zone shear on CBL entrainment.

2.3 Conceptual Models with Shear

With evidence for shear effects on entrainment building in the mid 1970s, the CBL conceptual models were extended to include the effects of shear on TKE production. The

very first attempt to include any shear effects in the CBL growth equation was by Tennekes (1973), who developed a hybrid velocity scale that combined the Deardorff (1970b) convective velocity scale and surface friction velocity. However, the first true theoretical analyses of the shear influence on atmospheric CBL entrainment were by Mahrt and Lenschow (1976) and Stull (1976a,c). Mahrt and Lenschow worked with the FOM and, although the equation they proposed was not tested against atmospheric, LES, or laboratory data, they did, nonetheless, make an effort to quantify the effects of shear on entrainment. Stull (1976a,c) derived a ZOM-based entrainment rate formula that distinguished four separate processes affecting entrainment: 1) buoyancy generation and consumption of TKE, 2) mechanical generation of TKE due to surface shear, 3) shear generation of TKE at the CBL top, and 4) radiation of energy by vertically propagating gravity waves (Stull 1976b). His parameterization of the shear term at the CBL top includes a finite entrainment zone thickness and thereby departs from the ZOM methodology, leaving his proposed equation an outlier from later ZOM-based entrainment equations, but this inconsistency winds up being somewhat fortuitous since it avoids the most characteristic problem of the shear-inclusive ZOM-based entrainment equations. This problem is discussed later in this section and in Chapter 3.

Zeman and Tennekes (1977) adhered more strictly to the ZOM assumptions and independently derived parameterizations of CBL growth that included the effects of shear at the surface, and they also attempted to take into account the effects of shear at the CBL top. Given lack of experimental data regarding the portion of the shear-generated TKE that was dissipated rather than used for entrainment at the CBL top, they could only suggest a general form for the entrainment zone shear term in their equations, and they

could formally parameterize only the surface shear. However, armed with the ocean studies of Price et al. (1978), Tennekes and Driedonks (1981) were able to resolve this issue and proposed an entrainment equation that parameterized the effects of the velocity jump at the CBL top. The parameterization, however, becomes unbounded and predicts infinite entrainment when the shear becomes strong enough. Tennekes and Driedonks (1981) made reference to the atmospheric measurements of Caughy and Palmer (1979), which probably was the first time the motivation for the extension of the ZOM equations was directly provided by atmospheric data.

Driedonks (1982) proposed a parameterization similar to that of Tennekes and Driedonks but found that using a velocity scaling like that of Tennekes (1973), which accounted only for the effects of surface shear on entrainment, worked best against his limited atmospheric dataset. The number of cases with shear is very small, and the results really could not be generalized. Boers et al. (1984) were able to propose their own, very similar parameterization and test it against lidar measurements of atmospheric CBL depth. At about the same time, Fairall (1984), motivated to understand the effect of CBL entrainment on the refractive index structure parameter, derived an independent, quite different expression for CBL growth forced by buoyancy and shear. It was never tested. Batchvarova and Gryning (1991, 1994) also have a parameterization much like the classic ZOM form, except the surface friction velocity is used to parameterize the shear effects on entrainment. They tested it against their own balloon-borne atmospheric measurements and found reasonably good agreement with the atmospheric data. Pino et al. (2003) proposed the most recent parameterization, which they compared with atmospheric data for one case of CBL growth on a day that had strong surface winds and

some shear above the CBL. Most recently, Sorbjan (2004) developed a parameterization for the buoyancy flux at the top of the entrainment zone. The parameterization is formulated in terms of the Richardson number in the entrainment zone and, like the Stull (1976a,c) formula, it deviates from the ZOM methodology and does not become unbounded with finite shear as do the more strict ZOM parameterizations such as Tennekes and Driedonks (1981) or Boers et al. (1984).

The derivation of the ZOM and FOM equations describing shear- and buoyancy-induced entrainment will be detailed in Chapter 3. However, an important feature of the entrainment equations, if they are derived using strict adherence to the ZOM methodology, should be pointed out here: the effects of shear are represented by a negative sign term in the denominator of the entrainment (dz_i / dt) equation. If the shear term becomes large enough, the denominator goes to zero and the expression becomes unbounded, and if the shear term continues to increase, the entrainment flux ratio changes sign. Both conditions are physically unrealistic. The entrainment flux ratio should become infinitely large as the surface heat flux approaches zero (from the positive side) and the boundary layer becomes purely shear-driven, but the ZOM parameterizations can become unbounded simply with large shear, regardless of the buoyancy flux. The FOM equations include terms that may offset the entrainment zone shear term, but the FOM equations are not fundamentally different from the ZOM equations in their mathematical structure, and they have some of the same undesirable behavior when shear is strong. The complete set of FOM equations has not been derived by any of the authors mentioned above, but the complete set of equations will be derived in Chapter 3 and their effectiveness at modeling CBL entrainment when shear is strong will be tested in Chapter

10. The FOM may be more realistic than the ZOM in that the FOM entrainment zone thickness can be adjusted to limit the bulk Richardson number to some critical value, thereby limiting the size of the shear term. The true behavior of the FOM equations will be explored in Chapters 3 and 10.

In order to develop equations within the ZOM or FOM framework, it is necessary to make a number of assumptions about the integrals of TKE in the CBL, as well as the fraction of buoyancy- or shear-produced turbulence that is available for entrainment, rather than being dissipated. Many of these assumptions are based on very limited atmospheric or laboratory measurements, while others appear to be based solely on intuition. On a more fundamental level, the ZOM and FOM may be too simplified to capture the most important aspects of sheared CBL entrainment.

To summarize the above papers describing entrainment in sheared CBLs, the expressions of Zeman and Tennekes (1977), Tennekes and Driedonks (1981), Boers et al. (1984), Fairall (1984), and Pino (2003) all essentially follow the ZOM methodology, and the expressions of Mahrt and Lenschow (1976) and Kim (2001) are based on the FOM. The parameterizations of Tennekes (1973), Driedonks (1982), and Batchvarova and Gryning (1991, 1994) only use the surface friction velocity to model the effects of shear on CBL entrainment. The expressions of Stull (1976a,b) and Sorbjan (2004) deviate from the strict ZOM and FOM methodologies and cannot become unbounded with finite shear.

2.4 Continuation of Field Programs

Atmospheric boundary layer field programs continued in the 1980s and onward, but the data provided on entrainment in the presence of shear were still very limited, and the experiments mostly provided evidence (without formal quantification) of the enhancement of entrainment by shear. Lenschow et al. (1980) analyzed the mean field and second order turbulence statistics budgets in a baroclinic CBL. In their study, they found that the mean momentum and temperature budgets were affected by the horizontal temperature gradients, but the second moments of turbulence were not greatly affected. Garratt and Wyngaard (1982) analyzed data from three experiments and did an analysis of wind profiles similar to that of Hoxit (1974), finding significant effects of entrainment on the profiles. This finding was supported by Lemone et al (1999) who found significantly "non-mixed" momentum profiles in the CBL when rapid entrainment occurred on a day with strong winds. Brost et al. (1982a,b) studied marine, stratocumulus-topped CBLs, some of which had some strong shear. Their Part I paper analyzed the mean profiles of humidity, potential temperature, and actual and geostrophic wind. In some cases, the shear in both the measured and geostrophic wind was rather substantial, reaching values on the order of 0.01 s^{-1}. In their Part II paper, they examined the turbulent fluxes and TKE budgets and found substantial shear production of TKE at the top of the CBL.

Several authors who developed the entrainment equations mentioned above tested their equations against atmospheric data. Boers et al. (1984) used six atmospheric case studies of daytime CBL growth from sunrise, finding some effects of shear on the entrainment rate. Although their equation parameterized entrainment zone shear, it did

not perform as well in sheared CBL cases as it did with shear-free CBLs. Batchvarova and Gryning (1991) tested their equation against an encroachment model for seven atmospheric CBL growth cases in field experiments in Germany in 1989 and 1990. They used a tethersonde (temperature and humidity sensors tied to a retractable balloon) to measure the CBL depth and temperature and, to estimate the effects of shear, they measured the surface friction velocity with sonic anemometers. In two of their cases, their parameterization clearly outperformed the encroachment model, suggesting the necessity to include shear in the entrainment equation. However, their strongest case only had surface winds of about 5 m/s. Batchvarova and Gryning (1994) combined their ZOM prognostic entrainment model (Batchvarova and Gryning 1991) with their entrainment zone thickness parameterization (Gryning and Batchvarova 1994) and tested it against four central Illinois CBL growth cases, using the same lidar data as Boers et al. (1984), but no evaluation was made on the impact of shear on the results.

Chou et al. (1986) measured the turbulence in a horizontally evolving CBL during a cold air outbreak over the Atlantic ocean off the east coast of the United States. Their analysis of the TKE budgets derived from the aircraft data showed that shear was a significant term in the turbulence production in the CBL, not only near the surface where it was largest, but at the CBL top as well. The vertical resolution of the momentum profile (there are only two points) was not good, and the authors acknowledged some uncertainty in the estimate of the local shear at the CBL top since the vertical spacing of flight legs was large. Nevertheless, the data provided evidence that shear production was a significant contributor to the TKE in that particular CBL.

The First International Satellite Land Surface Climatology Project Field Experiment took place in 1987 and provided data from which entrainment flux ratios could be estimated (Grossman 1992; Betts et al. 1992; Betts and Ball 1994; Betts and Barr 1996; Margulis and Entekhabi 2004). In most of these studies, some rather large entrainment flux ratios were observed, suggesting some shear enhancement of entrainment may have occurred during the experiment. However, the correlation between shear and entrainment flux ratios was, overall, relatively weak, indicating that factors other than the shear itself (i.e., stratification) probably affect the shear enhancement of entrainment.

Barr and Strong (1996) used heat budget methods to analyze data from soundings released from Kenaston and Saskatoon, Canada in June and July 1991 and found some relatively large entrainment flux ratios (on the order of 0.5 rather than the commonly accepted 0.2). Similar methods were used by Angevine (1999), who also found some rather high entrainment flux ratios. Angevine additionally made some association between large entrainment flux ratios and entrainment zone Richardson number, finding ratios of nearly 0.9 when $0<Ri<0.5$ and more typical shear-free ratios of 0.2 or 0.3 when $Ri>0.5$. Additionally, Davis et al. (1997) associated high entrainment flux ratios with large entrainment zone velocity jumps in their aircraft and sounding data from a field experiment over the boreal forests of Saskatchewan and Manitoba, Canada in 1994.

Flamant et al (1997) made atmospheric measurements just south of the Pyrenees in the vicinity of the Mediterranean coast. They measured the CBL depth and entrainment zone thickness with an aircraft-mounted, downward-looking lidar and made turbulent heat flux measurements at three levels in the CBL using aircraft-mounted

sensors. Assuming a linear heat flux profile from the surface to the CBL top, the three-point heat flux profile was extrapolated to the lidar-estimated height of the CBL top. With this extrapolation, the surface heat flux and the entrainment zone heat flux were estimated. They found the entrainment flux ratio varied from 0.1 in shear-free conditions to about 0.3 when the entrainment zone shear was stronger, and they tested the entrainment flux ratio parameterizations of Stull (1976a) and Driedonks (1982) for their cases with shear. They found qualitatively good results with the Stull and Driedonks parameterizations for the cases with shear, and the Tennekes and Driedonks (1981) parameterization worked reasonably well against atmospheric measurements when the shear was weak. Interestingly, they found that the ZOM parameterization of Driedonks (1982) became unbounded when they attempted to compare it with the LES data of Moeng and Sullivan (1994). Since it is not known exactly how the lidar determination of the CBL top compares to the level of the heat flux minimum (the heat flux minimum is the traditional method of determining CBL top and the one that works best within the ZOM framework), and because of the fact that most of the entrainment zone and surface heat flux estimates were extrapolated from measurements within the CBL, the actual values of the entrainment flux ratio may have considerable error, but the authors indicated their results provided evidence for the direct effects of shear on entrainment. Plotting the entrainment flux ratio as a function of entrainment zone velocity jumps, however, does not reveal an obvious association between shear and entrainment flux ratio.

Haegeli et al. (2000) described a technique of fitting idealized profiles of backscatter to actual lidar backscatter profiles to determine local CBL depth and entrainment zone thickness. From these depths, one can determine the entrainment flux

ratio theoretically by the following formula (Nelson et al. 1989), assuming a linear heat flux profile:

$$-\frac{B_i}{B_s} = \frac{z_i}{z_{il}} - 1 = \frac{\delta z_i}{2z_i - \delta z_i} \tag{2.1}$$

where z_i is the CBL depth, z_{il} is the height where the buoyancy flux profile crosses zero, B_S is the surface buoyancy flux, B_i is the buoyancy flux at z_i, and δz_i is the entrainment zone thickness, which is assumed to be twice the distance between z_i and z_{il}. For this assumption to hold, z_i must be exactly halfway between z_{il} and $z_i + \delta z_i$. The experimental results of Fedorovich et al. (2004a) show that this is not the case. Also, lidar-detected z_i is not necessarily the same level as the level of the heat flux minimum, as it is traditionally defined in the ZOM and FOM.

Haegeli et al. (2000) measure relatively high entrainment flux ratios using this method during the rapid growth phase of the CBL in the morning, but Fedorovich et al. (2004a) results show that the entrainment flux ratios should be relatively low when the CBL grows through weak stratification, as it does in the late morning hours.

Angevine et al. (2001) made observations of the initial development of the CBL during the morning in the Flatland96 experiment in central Illinois and the Tropospheric Energy Budget Experiment in 1995 and 1996 at the Cabauw tower in the Netherlands. Wind and temperature readings at several heights up to 200 meters on the tower were used, as were surface heat flux measurements (to determine when the flux became positive in the morning) and a 1290 MHz profiler was used to detect the onset of turbulence at 200 meters above ground level. They integrated an equation for CBL growth given by Garratt (1992) using surface heat flux data and showed that the equation,

along with its assumption that the heat flux of entrainment is a small fraction of the surface heat flux, does not hold during the morning transition. They concluded that mechanically produced turbulence, which is not accounted for by this equation, must be a contributing factor to the TKE and the downward heat flux that is commonly observed during the morning transition. The experimental data of Angevine et al. (1999, 2001) probably provide the most solid atmospheric evidence of shear-enhanced entrainment.

Otherwise, the atmospheric data do provide general evidence of the shear enhancement of entrainment, but little quantification of those effects has been made from those data.

2.5 Continuation of Laboratory Experiments

Laboratory experiments continued in the 1980s and onward as well. During the first half of the 1980s, laboratory water tanks were still widely used for experiments on CBL entrainment. They have been used a lot less since then, because increasing computer power of the last two decades has made numerical simulations a much less expensive alternative to study the CBL. The laboratory tanks can still be useful for testing the theories and the results of numerical simulations.

Deardorff et al (1980) examined, in more detail, the entrainment rate and the entrainment zone thickness in a shear-free laboratory experiment with heating applied at the lower surface. They performed a larger number of experiments and examined the parameter space of stratification more thoroughly than had been done before, using an upgraded version of the Willis and Deardorff (1974) tank. Fedorovich et al. (2004a) found agreement among these water tank data, numerical simulations of atmospheric

CBLs, and the theory of Zilitinkevitch (1991) for the particular CBL regime of equilibrium entrainment (the equilibrium regime will be explained in Chapter 3).

Deardorff and Willis (1985) repeated their 1974 experiments with a shallower CBL to improve the CBL depth to tank width aspect ratio that they blamed for the relative lack of horizontal velocity variance in their 1974 data. With this change, the variance in the laboratory tank matched the atmospheric data much more closely. Additionally, they reexamined the TKE budgets and found that pressure transport term, which they had neglected earlier, could be a significant component of the TKE budget.

Deardorff and Willis (1982) also performed their own version of the rotating annulus experiments of Kato and Phillips (1969). While many earlier studies examining the entrainment rate in sheared boundary layers were focused on the effects of the shear forcing at the surface layer, rather than directly at the density interface where entrainment was occurring, Deardorff and Willis decided to look at both of these. They found an entrainment rate formula of $\frac{dz_i}{dt} / u_* = 0.33 Ri_\tau^{1/2} Ri_v^{-1.4}$, where dz_i / dt is the entrainment rate, and u_* is the friction velocity, to fit their data best. The Richardson numbers in this relation have the following definitions: $Ri_\tau = \delta b z_i / u_*^2$ and $Ri_v = \delta b z_i / \delta u^2$, where δb and δu are the buoyancy and velocity jumps across the entrainment zone. In analyzing the water tank experiments, one must be careful to distinguish between the effects being studied (the turbulence forced by vertical shear in the horizontal velocity) and the side effects (side wall turbulence and centripetal acceleration in the annulus). The Deardorff and Willis study indicated plans to follow up with an experiment combining shear and buoyancy forcing, but no such publication ever followed. Perhaps the most significant outcome of Deardorff and Willis (1982) with regard to the current study can be seen in

their statement on the dependence of entrainment on surface shear and entrainment zone shear: "Together, the dependence indicates that both u_* and δu promote [entrainment], with the δu being the stronger."

Fernando (1991) wrote a review article of numerous laboratory water tank studies of entrainment in the absence of mean shear (forcing by buoyancy or mechanical agitation) and entrainment in cases when shear produced the bulk of the turbulence.

Most recently, McGrath et al. (1997) conducted further laboratory water tank studies of mixing at shear-free density interfaces, with turbulence generated by mechanical agitation. They examined, in detail, the structures related to the mixing process and the different processes that led to the development of these structures. They found that different mechanisms (i.e., "engulfment", generation of linear internal waves, and wave breaking and K-H instability) played roles in mixing at the interface at the top of the boundary layer over different ranges of a bulk Richardson number they defined. They also found results consistent with the hypothesis (Fernando and Hunt 1997) that, at high values of the bulk Richardson number, the density interface consists of both linear internal waves at high frequencies and breaking waves at low frequencies.

Most recently, the temporally homogeneous, horizontally evolving atmospheric CBL was studied in a wind tunnel model (Fedorovich et al. 1996; Fedorovich and Kaiser 1998; Kaiser and Fedorovich 1998; Fedorovich et al. 2001a, 2001b; and Fedorovich and Thaeter 2001). Fedorovich et al. (1996) studied the statistics of turbulent velocity and temperature fluctuations in the wind tunnel and compared them to atmospheric, water tank, and LES data, noting similarities and differences among the datasets. In particular, the horizontal velocity variances were found to be greater in the wind tunnel than in the

shear-free LES and water tank experiments, an effect which was attributed to surface shear. This provided evidence that the surface shear was enhancing turbulence production, but the effects of this shear-generated turbulence on entrainment were still not clear.

Fedorovich et al. (2001a) studied the development of turbulence in the wind tunnel of Fedorovich et al. (1996) and compared the wind tunnel data with LES of the wind tunnel to explore the effects of initial velocity and temperature disturbances on the development of turbulent regimes downstream from the velocity inlet. The corresponding LES/wind tunnel model intercomparison study, Fedorovich et al. (2001b), looked at the effects of shear and surface roughness on the horizontal CBL development and found the effects of shear to depend on the sign of the shear. In cases when the wind speed increased above the horizontally evolving CBL, the downwind development of the CBL was slower than in the basic case with no wind shear at the CBL top. When the sign of the shear was negative, the CBL developed faster than in the basic case. The positive case appeared to provide experimental evidence supporting the theory of shear sheltering of turbulence proposed by Hunt and Durbin (1999), but the negative shear case, which had a faster CBL growth than the basic case, contradicted this evidence. The difference was believed to be due to the upright tilting of thermals in the negative shear case, such that they were able to penetrate the inversion more easily and speed the entrainment process.

It was later discovered that the primary effect of the sign of the shear on the growth of the CBL was due to the CBL divergence resulting from the turbulent momentum flux in the horizontally evolving CBL (Fedorovich and Thaeter 2001). In the

positive shear case, greater momentum from above the entraining CBL was transported downward by the turbulent momentum flux, making the *x*-component of CBL momentum greater at the outlet of the tunnel than at the inlet. The divergence in the CBL thereby became positive, and a net sinking motion developed at the CBL top. This sinking motion suppressed CBL growth. When shear was negative, slower momentum was transported into the CBL, causing convergence and rising motion at the CBL top. The results are specific to the horizontally evolving CBL in the wind tunnel, and because this *x*-dependent momentum transport is absent in horizontally homogeneous CBLs, the wind tunnel model results cannot be generalized to the horizontally homogeneous atmospheric CBL. Nevertheless, the vertical turbulent kinematic temperature flux profiles appeared qualitatively similar between the positive and negative shear cases, indicating the entrainment effects of the absolute value of the shear across the CBL top were similar between the two cases. Fedorovich and Thaeter (2001) also provided an analysis of the entrainment of momentum and heat across the interface. Kaiser and Fedorovich (1998) studied the turbulence spectra in the wind tunnel CBL.

2.6 Large Eddy Simulations of Sheared Convective Boundary Layers

LES has become a much more popular tool for investigating CBL flow regimes, owing to the rapid increase of computer power and the decrease in computer costs. These changes have made computing a more attractive alternative than laboratory experiments. Still, it must be taken into account that numerical methods have their limitations, depending on the schemes in use in any particular model. For these reasons, the LES-atmospheric data

intercomparison studies of Deardorff (1974b) and Pino et al. (2003) and the LES-wind tunnel intercomparison of Fedorovich et al. (2001a,b) are vital in showing that LES can simulate realistic CBL structures, turbulence statistics, and entrainment.

A few other notable LES studies of CBL statistics and turbulent transport from the 1980s were Moeng (1984), Wyngaard and Brost (1984), Nieuwstadt and Brost (1986), Moeng and Wyngaard (1988), Schmidt and Schumann (1989), and Mason (1989). These studies focused on the turbulence statistics and structure within the CBL. The simulations had the utility of providing data on these structures with a resolution that was very difficult to achieve with atmospheric measurements and so, LES became an important tool for understanding the dynamics of the CBL.

The earliest LES study dedicated to the sheared CBL was that of Sykes and Henn (1989), who studied the idealized case of a boundary layer between two flat plates, comparing sheared and shear-free simulations. These data were compared with the laboratory studies of Deardorff et al. (1969), and it was shown that the profiles of turbulence statistics were qualitatively similar. The most significant finding of Sykes and Henn was that the convection organized into roll-type disturbances when the ratio of the friction velocity to the Deardorff (1980) convective velocity scale, u_* / w_* was around 0.35.

Moeng and Rotunno (1990) compared the vertical velocity skewness in LES with the skewness calculated from atmospheric CBL data, noting the differences in the profiles of vertical velocity skewness. The LES showed positive skewness that increased with height to near the CBL top and then decreased rapidly in the entrainment zone. Atmospheric data, however, showed skewness to be only slightly positive throughout

most of the depth of the mixed layer, decreasing only gradually near the CBL top, where it approached zero (Kaimal et al. 1976). Numerical constraints in LES were suggested as the reason for the discrepancy in the profiles, but it could be that shear had an effect as well, as will be seen in later sections.

Moeng and Sullivan (1994) demonstrated the effects of the shear on the CBL profiles of velocity variances. They focused on the structures and the TKE budgets of four different CBL types ranging from a purely convective boundary layer to a relatively highly shear-driven boundary layer, with two intermediate cases. With their results, they verified a velocity scaling that is applicable to intermediate boundary layers with combined shear and buoyancy forcing. They found roll structures when the ratio u_* / w_* was around 0.65 or greater, which is nearly twice as large as what Sykes and Henn (1989) found. Their analysis focused on the dynamics of turbulence in the CBL and did not directly address entrainment rates.

Brown (1996) performed large eddy simulations of the baroclinic boundary layer and compared the resulting velocity variance profiles with predictions from one-dimensional closure models. In an effort to eliminate the effects of entrainment on the results, rigid lid boundary conditions were imposed at the top and bottom of the domain. The author acknowledged that entrainment effects would need to be taken into effect before generalizing the results to the atmosphere, and that baroclinic CBL growth might lead to increased shear across the CBL top, which would enhance the entrainment there.

Kanna and Brasseur (1998) made a detailed examination of the structure of CBL rolls and their dependence on the relative forcing by shear and buoyancy, looking most closely at the mechanisms for the development of low-speed streaks in sheared

convective boundary layers. They suggested that the basis of the formation of the horizontal convective rolls is shear at the surface. Warm air from the heated surface accumulates in these low-speed streaks and helps to organize their ascent. Kim and Park (2003) examined the vortical nature of these structures near the surface. While these studies describe the dynamical origins the horizontal convective rolls, they did not specifically address the entrainment rate in sheared CBLs.

Kim et al. (2003) performed an LES study examining the effects of Kelvin-Helmholtz-like instabilities at the top of the CBL under strong wind conditions, examining the shear-driven processes that might enhance CBL entrainment. They found that the Kelvin-Helmholtz type instabilities developed along the top of horizontal CBL rolls as the Richardson number approached the critical value of 0.25 for the onset of Kelvin-Helmholtz instability. They also concluded that any parameterization used to compute CBL entrainment must take into account the shear across the CBL top since these studies were done under typical atmospheric wind speeds and shear. Their study made a rather thorough analysis of the entrainment mechanism at the CBL top but did not quantify what the enhancement might be or what the relative effects of surface shear versus entrainment zone shear might be.

Pino et al. (2003) addressed the subject of the current study rather directly, looking at the effects of shear on the entrainment rate in a CBL using atmospheric data and three LES runs. The LES runs used the same atmospheric temperature profile as on the morning of the particular atmospheric case they studied, and the runs were divided into a shear-free case, a case of height-constant wind, and a case using the wind profile of the morning sounding, which had height-dependent wind. The LES case with the height-

dependent wind had the fastest CBL growth rate and was best able to reproduce the observed CBL growth rate. The agreement of the LES CBL growth with the atmospheric CBL growth and also with the predictions of the ZOM-based entrainment equation they developed was taken as a general result for CBL types with varying shear and buoyancy forcing. Their entrainment equation worked well for their particular case study but was not tested against a larger variety of atmospheric conditions.

Although not directly addressing sheared CBLs, the LES experiments of Fedorovich et al (2004a) directly addressed the entrainment rate of shear-free CBLs developing against a background of varying atmospheric stratification and provided a framework for comparison between shear-free and sheared CBLs. In particular, the study evaluated the ZOM equations and solutions detailed in Zilitinkevitch (1991) and the general structure model (GSM) of Fedorovich and Mironov (1995). The CBLs examined in Fedorovich et al. (2004a) were a subset of the CBL types examined in Zilitinkevitch (1991), namely, those falling within the equilibrium entrainment regime. In this regime, the nonstationarity (time rate of change of TKE) term can be neglected, and the entrainment flux ratio is a constant. This study will be examined in greater detail in Chapter 4.

Finally, Sorbjan (2004) used LES to test the effects of baroclinity on the entrainment flux ratio of the CBL. He also made efforts to quantify the effects of advection on the potential temperature profiles in the simulation domain. His results showed that shear that developed at the CBL top, due to the effects of baroclinity, enhanced the entrainment flux ratio, and he compared the results to the entrainment parameterization he developed (see Section 2.3)

Other notable LES studies of entrainment during the 1990s include Lewellen and Lewellen (1998), who considered the size of the eddies that are most important in controlling entrainment. Sorbjan (1996a,b) looked at the effects of stratification, and Sullivan et al. (1998) focused on entrainment zone structure. More recently, Otte and Wyngaard (2001) performed high-resolution LES found the entrainment zone to be fairly similar to the nocturnal boundary layer in terms of spectral peaks, eddy diffusivities, variances, and dissipation rates.

2.7 Shear Sheltering of Turbulence

Interestingly, opposing points of view have been formulated, such as the theory of shear sheltering of turbulence proposed by Hunt and Durbin (1999), in which shear across the CBL top prevents thermals from penetrating into the stably stratified air above the mixed layer. As a result, the downward heat flux at the CBL top is reduced, and CBL growth is slowed. The wind tunnel study of Fedorovich et al. (2001b) addressed this theory to some degree, but given the divergence effects in the wind tunnel CBL, they were unable to fully assess the validity of this theory. Most other studies reviewed in this section have suggested shear to be an entrainment-enhancing mechanism rather than an entrainment-suppressing mechanism. A basic understanding of TKE generation processes leads one to believe that shear, as a generator of TKE, should lead to larger entrainment in CBLs. It may be possible that some entrainment suppression effects may occur due to shear sheltering, but any effects may be compensated, partially or fully, by the entrainment-enhancing effects of the TKE shear generation term.

2.8 Sheared CBLs in Numerical Weather Prediction Models

Finally, it would be good to review the history of the turbulence closure models in numerical weather prediction (NWP) and global circulation models (GCMs). Early planetary boundary layer parameterization schemes relied on prognostic equations of boundary layer depth based on conceptual models such as the ZOM. Deardorff (1972b) describes one example of such a scheme. Numerical resolution has since improved, and NWP codes are moving to subgrid turbulence closure schemes that do not require a prognostic prediction for z_i. Rather, the turbulent diffusion is able to produce a fairly well-mixed CBL structure, since the vertical resolution is sufficient to simulate the vertical structure of CBLs whose depths are about a kilometer or more.

Some of the more popular schemes use a prognostic form of the TKE equation. Deardorff (1980) developed a 1.5 order scheme that is commonly used as a subgrid turbulence model in LES and is also used as a turbulence model in some NWP models, such as the Advanced Regional Prediction System (ARPS—Xue et al. 2001) developed at the Center for Analysis and Prediction of Storms at the University of Oklahoma. It computes the TKE at each time step of the model run, and the eddy diffusivities for momentum and heat are calculated using a master length scale of turbulence. In LES of the CBL, this length scale is usually the same as the grid cell length in unstable conditions and less than that in stable conditions. In NWP, the CBL turbulence cannot be explicitly resolved, and the master length scale is much larger. In most models, this length scale is a function of height relative to the CBL depth, which is diagnosed (Xue et al. 2001). The length scale can also be calculated as the root mean square of the

distances a parcel would travel upward and downward until it expended all its TKE on work against buoyancy forces or until it hits the lower surface (Fiedler and Kong 2003).

Mellor (1973) and Mellor and Yamada (1974, 1982) developed a hierarchy of turbulence closure schemes that have become popular in regional models, including the National Center for Environmental Prediction's (NCEP) Eta model (Janjic 1990, 1994; Black 1994). The version in use in the Eta models is the so-called Level 2.5 closure with Level 2 closure applied in the surface layer. This scheme also contains, at its core, a prognostic equation for TKE but also contains equations relating the individual velocity variances to the mean vertical gradients of horizontal velocity, a relevant length scale, and the eddy diffusivity. The CBL structure predicted by Level 2.5 closure was evaluated against LES data by Ayotte et al. (1996), who found that most RANS-based schemes used in NWP have considerable problems modeling entrainment.

Troen and Mahrt (1986) described the basic scheme that has been used in the NCEP Global Forecast System (GFS) model. This system specifies a profile of the eddy diffusivities of momentum in the boundary layer as a function of height relative to the boundary layer depth (z / z_i) and the dimensionless shear. The boundary layer depth is diagnosed according to the profile of temperature and is dependent on a bulk Richardson number, which is dependent, in turn, on the wind speed at the boundary layer top and the temperature excess in the surface layer, relative to the mixed layer temperature. The surface layer excess temperature is proportional to the surface heat flux. Countergradient transport of heat is also introduced.

There is a precedent for testing some of these schemes against LES. LES resolves the CBL turbulence and can provide idealized tests that isolate the effects of shear on

entrainment. Moeng and Wyngaard (1989) examined the turbulence statistics predicted by turbulence closure in large scale meteorological models and compared the entrainment rates of those schemes against LES entrainment. They found a number of problems with the closure schemes, among the most basic of which were the countergradient diffusion of potential temperature, which is seen in LES profiles but does not occur in profiles produced by the turbulence closure schemes. Ayotte et al. (1996) performed a variety of tests of neutral and convective planetary boundary layer parameterizations used in GCMs and NWP models to see how they compared against LES for a variety of boundary layer types, ranging from a neutral boundary layer with shear-forced turbulence to boundary layers with a strong surface heat flux. The primary finding of their tests indicated most of the schemes had some difficulty representing entrainment at the CBL top, although some of the models were able to model entrainment rather well over a limited range of conditions.

Lenderink et al. (1999) performed an analysis to see if a 1.5 order, TKE-based turbulence closures were able to simulate entrainment in stratocumulus-topped boundary layers, where radiative cooling at the cloud top forces the CBL turbulence. The results indicate that the evaluated closure did not predict entrainment in the same manner as LES. The LES showed that entrainment was best understood in terms of a conceptual model of *process partitioning*, which partitions the buoyancy flux into a TKE-consuming part and a TKE-producing part, with these parts further partitioned according to the *process* generating the buoyancy flux. The TKE-based turbulence closure scheme, on the other hand, behaved according to a conceptual model of *Eulerian partitioning*, which only makes the partition between the TKE-consuming and a TKE-producing buoyancy flux.

For the dry CBLs to be simulated in the current study, these two conceptual models were essentially similar, as was seen in Van Zanten et al. (1999).

Lenderink and Holtslag (2000) looked at the effects of grid resolution on TKE-based turbulence model predictions of stratocumulus-topped CBL entrainment and found that coarser resolution detracted from the model's ability to correctly predict entrainment. Fiedler (2002) then evaluated the utility of using an adaptive grid at the CBL top that would provide finer resolution around the inversion level. His results indicated that it would be more productive to use a higher order differencing scheme to represent the sharp gradients at the CBL top than to use an adaptive grid there. Fiedler and Kong (2003) examined the dependence of the TKE-based scheme's performance on the horizontal grid resolution in a nonhydrostatic model.

2.9 Goals of this Study

Some of the preceding studies have examined entrainment in the presence of shear, but they have done so within a limited range of atmospheric conditions. Many have looked at the effects of shear, but only Kim (2001), Pino et al. (2003), and Sorbjan (2004) have addressed entrainment directly. Neither of these has tested the turbulence closures that are found in regional and global NWP models. With regard to the results of the aforementioned studies, the goals of this study are to anser the following four questions:

1. What are the effects of shear on entrainment across a wider variety of atmospheric conditions?
2. How well would the zero- and first-order model parameterizations proposed in the studies work under such conditions?

3. Given that these parameterizations are not used, *per se*, in current NWP models, what would the parameterizations in use in those models predict for entrainment under such conditions?
4. What is the role of shear at the surface versus shear at the CBL top?

Thus, the current study seeks to examine further the growth of the convective boundary layer when both shear and buoyancy forcing exist. The aim of the study is to address the above four questions using a more comprehensive set of cases and to analyze these cases in terms of our previous understanding of entrainment when shear and heat flux are both present. Our previous understanding comes from the following:

1. Conceptual models of CBL entrainment (zero order, first order models)
2. Turbulence closure schemes used in numerical weather prediction and global circulation models.
3. Atmospheric and laboratory studies (a much more limited set).
4. LES studies.

To address the above four questions, the theoretical framework of the models and simulations must be developed, as will now be done in Chapter 3.

Chapter 3

Numerical Simulations and Models

3.1 A Hierarchy of Numerical Methods

As an alternative to using data directly from atmospheric measurements, the influence of shear on atmospheric CBL entrainment can be studied using numerical methods. These methods vary widely in their computational cost and can be conceptually organized into a hierarchy of numerical techniques for studying of the horizontally homogeneous CBL. According to Wyngaard (1998), if the method resolves the CBL turbulence, it is a numerical *simulation*, it lies at the top of the hierarchy, and its computational costs are the greatest. If it does not resolve the turbulence, it is a *model* and is computationally much less expensive.

The models are formed by some sort of integration across the CBL. The integration can be in terms of horizontal averaging, or it can combine these horizontal averages with a vertical integration over the depth of the CBL to form a bulk model. The former method lies in the middle of the hierarchy, and the latter method requires the least computational resources and has the simplest structure. Although the bulk models lie at the bottom of the hierarchy of complexity, their relative simplicity may make them the best tools for providing a conceptual understanding of CBL entrainment.

3.2 Simulations

The top of the numerical hierarchy is occupied by simulations (Wyngaard 1998). The most expensive of these are direct numerical simulations (DNS). DNS resolves all turbulent motions, but it must be done on a very fine grid, and because of the limitations of computer power, it can only be used for domains several orders of magnitude smaller than the atmospheric CBL. To model CBLs, LES is needed.

LES is designed to resolve the principal energy-containing motions in the CBL and models the non-resolvable, smaller-scale motions using a subgrid turbulence closure scheme. The grid spacing in LES must be fine enough that motions in the energy production region of the 3-D turbulence cascade are well-resolved, and the grid should also be able to resolve some motions in the Kolmogorov inertial subrange [see Wyngaard (1998), Pope (2000), and Piomelli and Chasnov (1996) for a description of LES methodology]. LES has been used extensively to study the CBL since it was first developed by Deardorff (1970) and others. Because of computer power limitations, these first simulations were on a very coarse grid that did not really meet the requirements listed above, but computer power has increased enough over the past 30 years that LES has become a very well-accepted and widely used technique for the study of CBL turbulence. LES can simulate CBLs of almost any size, and because the peak in energy is at length scales approximately equal to the CBL depth scale (Caughy et al. 1979), LES is ideally suited for the study of the atmospheric CBL. Because it is a commonly used technique, the derivation of the LES equations will be left to Appendix A.

3.3 Turbulence Equations for the Horizontally Homogeneous CBL

When simulations are too computationally expensive, we can *model* the turbulence to reduce the computational cost. The first step in *modeling* the CBL turbulence is to develop the governing equations for the CBL type considered in this study. Since entrainment equations must be formulated using first principles (conservation of energy), the horizontally homogeneous, temporally evolving CBL is considered a system in which heat energy is input into the system, and a portion of this energy is converted into kinetic energy. Some of this kinetic energy is then dissipated by viscosity via the three dimensional turbulence cascade, and the rest is converted into potential energy by the work involved in the entrainment process.

Entrainment transports low θ_v air upward and high θ_v air downward, resulting in an increase in the potential energy of the system. Shear instabilities at the CBL top generate additional TKE that can also be dissipated or consumed by the negative buoyancy flux of entrainment. To some extent, local shear can exist at the interface between the CBL and the free atmosphere, even when shear in the mean wind is zero, owing to the variance of horizontal velocity in the turbulent fluid at the lower side of the interface (Stull 1988). As the mean wind and/or the shear in the mean wind increase, shear generation of TKE becomes more significant owing to the presence of surface shear, entrainment zone shear, or shear within the mixed layer. This is particularly true if the bulk Richardson number of the mean flow is low enough to support the generation of turbulence through the K-H instability mechanism (Kundu 1990, Kim et al. 2003), but

one must also keep in mind the Ri<0.25 criterion in K-H stability analysis applies to nonturbulent flows.

Because the CBL is turbulent, we look specifically at the equations governing turbulent flow, which are developed using the RANS equations. We define the average to be an ensemble average, which is the average of an infinite number of realizations. In all practicality, this averaging cannot be performed for atmospheric CBLs, so some approximations must be made. In the horizontally homogeneous, temporally evolving CBL in the current study, the ensemble averages can be represented by averages across horizontal planes of infinite extent. For the atmospheric quasi-homogeneous CBL, the ensemble average has to be approximated by averages across finite horizontal planes, which should be chosen large enough that the averaging is representative of the ensemble average. The method of deciding what constitutes a suitable approximation of the ensemble average is subjective, and it is often determined by the limits of the domain being sampled, such as the horizontal extent of a radar or lidar scan, or the horizontal area of the domain in numerical simulations of the atmospheric CBL. Three-dimensional turbulence structures exist everywhere within the atmospheric CBL, so the CBL can only be quasi-homogeneous in the statistical sense. With these considerations in mind, we develop the RANS-based equations describing the CBL that is statistically horizontally homogeneous.

The CBL is generally shallow enough that the changes of density with respect to its mean value can be ignored (except in the gravity term) and the Boussinesq approximation can be made. Also, the ensemble averaged vertical velocity is assumed to be zero.

Let ϕ be any variable describing the state of the fluid, $\overline{\phi}$ its ensemble average, and ϕ' the deviation of ϕ from its ensemble average. For the horizontally homogeneous CBL type considered in this study, any ensemble averaged variable is assumed to be a function of height and time [$\overline{\phi} = \overline{\phi}(z,t)$]. The fluctuating components are functions of x and y, height, and time. The total instantaneous variable is therefore $\phi(x,y,z,t) = \overline{\phi}(z,t) + \phi'(x,y,z,t)$. In the following equations, we adhere to Einstein notation, where u_i is the ith component of velocity, δ_{ij} is the Kroneker delta, and ε_{ijk} is the alternating tensor, as defined in Kundu (1990).

The separated form $\phi = \overline{\phi} + \phi'$ is substituted into the Navier-Stokes and thermodynamic equations, yielding the following equations.

$$\begin{aligned}
&\frac{\partial}{\partial t}\left(\overline{u_i} + u_i'\right) + \left(\overline{u_j} + u_j'\right)\frac{\partial}{\partial x_j}\left(\overline{u_i} + u_i'\right) \\
&= -\frac{1}{\rho_0}\frac{\partial}{\partial x_i}\left(\overline{p} + p'\right) + f\left(\overline{u_j} + u_j'\right)\varepsilon_{ij3} \\
&+ \frac{g}{\theta_0}\left(\overline{\theta} + \theta' - \theta_0\right)\delta_{i3} + \nu\frac{\partial^2}{\partial x_j^2}\left(\overline{u_i} + u_i'\right)
\end{aligned} \tag{3.1}$$

$$\frac{\partial}{\partial t}\left(\overline{\theta} + \theta'\right) + \left(\overline{u_j} + u_j'\right)\frac{\partial}{\partial x_j}\left(\overline{\theta} + \theta'\right) = \nu_H\frac{\partial^2}{\partial x_j^2}\left(\overline{\theta} + \theta'\right) \tag{3.2}$$

In (3.1), we have made the approximation $-(\rho - \rho_0)/\rho_0 \cong (\theta - \theta_0)/\theta_0$, and mass conservation is expressed by $\partial\overline{u_i}/\partial x_i = 0$ and $\partial u_i'/\partial x_i = 0$. In the above equations, p is pressure, ρ_0 is the reference value of density, f is the Coriolis parameter, g is the gravitational acceleration, θ is potential temperature (θ_0 is its reference value), ν is kinematic viscosity, and ν_H is the thermal diffusivity. Next, (3.1) and (3.2) are ensemble

averaged. Following the rules of averaging, which state $\overline{\phi'} = \overline{\phi'}\,\overline{\phi} = 0$, $\overline{\partial\phi / \partial x} = \partial\overline{\phi} / \partial x$, and $\overline{a\phi_i} = a\overline{\phi_i}$ (a is a constant), the RANS equations and thermodynamic equation are derived:

$$\frac{\partial \overline{u_i}}{\partial t} + \frac{\partial\left(\overline{u_i}\,\overline{u_j}\right)}{\partial x_j} + \frac{\partial \overline{u_i' u_j'}}{\partial x_j} = -\frac{1}{\rho_0}\frac{\partial \overline{p}}{\partial x_i} + f\overline{u_j}\varepsilon_{ij3} + \frac{g}{\theta_0}\left(\overline{\theta} - \theta_0\right)\delta_{i3} + \nu\frac{\partial^2 \overline{u_i}}{\partial x_j^2} \tag{3.3}$$

$$\frac{\partial \overline{\theta}}{\partial t} + \frac{\partial\left(\overline{u_j}\,\overline{\theta}\right)}{\partial x_j} + \frac{\partial \overline{u_j'\theta'}}{\partial x_j} = \nu_H \frac{\partial^2 \overline{\theta}}{\partial x_j^2} \tag{3.4}$$

Subtracting these equations from (3.1) and (3.2) yields the equations describing the fluctuating quantities of the flow:

$$\frac{\partial u_i'}{\partial t} + \frac{\partial}{\partial x_j}\left(u_i'u_j' + \overline{u_i}u_j' + u_i'\overline{u_j} - \overline{u_i'u_j'}\right) = -\frac{1}{\rho_0}\frac{\partial p'}{\partial x_i} + fu_j'\varepsilon_{ij3} + \frac{g}{\theta_0}\theta'\delta_{i3} + \nu\frac{\partial^2 u_i'}{\partial x_j^2} \tag{3.5}$$

$$\frac{\partial \theta'}{\partial t} + \frac{\partial}{\partial x_j}\left(u_j'\theta' + \overline{u_j}\theta' + u_j'\overline{\theta} - \overline{u_j'\theta'}\right) = \nu\frac{\partial^2 \theta'}{\partial x_j^2} \tag{3.6}$$

The equations for the time rate of change of the velocity variances and covariances can then be formulated by performing further mathematical manipulations of (3.5). One can copy the equation for the ith component of momentum and replace the index i with the index k. Next, the equation for u_i' is multiplied by u_k', and the equation for u_k' is multiplied by u_i'. Adding these two equations and performing Reynolds averaging on the result gives the following budget equation for Reynolds stresses:

$$\begin{aligned}\frac{\partial}{\partial t}\overline{u_i'u_k'} = &-\frac{\partial}{\partial x_j}\overline{u_j'u_i'u_k'} - \overline{u_j}\frac{\partial}{\partial x_j}\overline{u_i'u_k'} - \overline{u_k'u_j'}\frac{\partial \overline{u_i}}{\partial x_j} - \overline{u_i'u_j'}\frac{\partial \overline{u_k}}{\partial x_j} \\ &-\frac{1}{\rho_0}\left(\frac{\partial}{\partial x_i}\overline{u_k'p'} + \frac{\partial}{\partial x_k}\overline{u_i'p'}\right) + \frac{1}{\rho_0}\left(\overline{p'\frac{\partial u_k'}{\partial x_i}} + \overline{p'\frac{\partial u_i'}{\partial x_k}}\right) \\ &+f\left(\overline{u_k'u_j'}\varepsilon_{ij3} + \overline{u_i'u_j'}\varepsilon_{kj3}\right) + \frac{g}{\theta_0}\left(\overline{u_k'\theta'}\delta_{i3} + \overline{u_i'\theta'}\delta_{k3}\right) \\ &+\nu\frac{\partial^2}{\partial x_j^2}\overline{u_i'u_k'} - 2\nu\overline{\frac{\partial u_i'}{\partial x_j}\frac{\partial u_k'}{\partial x_j}}\end{aligned} \tag{3.7}$$

The TKE equation is derived by taking one half the sum of the equations for $i=k$. The TKE equation is:

$$\begin{aligned}\frac{\partial \overline{e}}{\partial t} = &-\overline{u_j}\frac{\partial \overline{e}}{\partial x_j} - \overline{u_i'u_j'}\frac{\partial \overline{u_i}}{\partial x_j} + \frac{g}{\theta_0}\overline{u_i'\theta'}\delta_{i3} - \frac{\partial}{\partial x_j}\left(\overline{u_j'e} - \frac{1}{\rho_0}\overline{u_j'p'}\right) \\ &+f\overline{u_i'u_j'}\varepsilon_{ij3} + \nu\frac{\partial^2}{\partial x_j^2}\overline{e} - 2\nu\overline{\frac{\partial u_i'}{\partial x_j}\frac{\partial u_i'}{\partial x_j}},\end{aligned} \tag{3.8}$$

where e is the TKE. The first term on the right hand side represents the advection of horizontally averaged TKE by the mean wind. The next two terms represent the source terms for TKE, the first of which describes the interaction between the turbulent fluxes and the shear in the mean wind. Since $\partial\overline{u_i}/\partial x_j$ and $\overline{u_i'u_j'}$ usually have opposite signs, the term is usually a source of TKE. The second source term is the buoyancy generation of turbulence, which consists only of the vertical turbulent flux of buoyancy. The next term is the transport of TKE by the fluctuating part of the velocity field ($\overline{u_j'e}$) and by pressure ($\overline{u_j'p'}$). The fifth and sixth terms represent the Coriolis forces acting on the turbulent velocity fluxes and the viscous diffusion of TKE. These terms can be neglected for the CBL because the time scale of turbulence (~10^3 s for the largest eddies) is much shorter than the Coriolis time scale (nearly 10^5 s), and because the turbulent transport is

several orders of magnitude larger than the viscous transport in the CBL. The final term represents the viscous dissipation of TKE.

The TKE equation can be simplified further for the horizontally homogeneous CBL. Because the horizontal derivatives ($\partial/\partial x$ and $\partial/\partial y$) of all averaged quantities are zero, the horizontal advection terms disappear. Although vertical gradients can still be strong, vertical advection is also zero because the mean vertical velocity $\overline{u_3}$ is zero. For the shear production term, only the *i*=1,2 and *j*=3 terms will contribute because horizontal gradients (*j*=1,2) in the mean horizontal wind (*i*=1,2) are zero. For the transport terms, only the *j*=3 will remain because only vertical gradients exist. The resulting TKE equation for the horizontally homogeneous CBL is:

$$\frac{\partial \bar{e}}{\partial t} = -\overline{w'u'}\frac{\partial \bar{u}}{\partial z} - \overline{w'v'}\frac{\partial \bar{v}}{\partial z} + \frac{g}{\theta_0}\overline{w'\theta'} - \frac{\partial}{\partial z}\left(\overline{w'e'} - \frac{1}{\rho_0}\overline{w'p'}\right) - \varepsilon, \tag{3.9}$$

where $u = u_1$, $v = u_2$, and $w = u_3$. One can also make the same simplifications to the RANS equations for the horizontally homogeneous CBL (3.3). All horizontal gradients are zero in the ensemble averaged horizontally homogeneous CBL, and the equation for *i*=3 disappears because $\overline{w} = 0$. Again, only the terms with *i*=1,2 and *j*=3 contribute. If the geostrophic component of the wind is subtracted from the equations by subtracting the terms $fu_g = -\frac{1}{\rho_0}\frac{\partial p}{\partial y}$ and $fv_g = \frac{1}{\rho_0}\frac{\partial p}{\partial x}$, the pressure gradient and Coriolis terms can be combined to represent the accelerations of the Coriolis force on the ageostrophic component of the wind. Finally, the viscous diffusion of mean momentum is negligible for a turbulent CBL, and the buoyancy term does not contribute to the mean horizontal

momentum. The resulting equations for momentum in the horizontally homogeneous CBL are:

$$\frac{\partial \bar{u}}{\partial t} = -\frac{\partial \overline{u'w'}}{\partial z} + f\left(\bar{v} - v_g\right) \tag{3.10}$$

$$\frac{\partial \bar{v}}{\partial t} = -\frac{\partial \overline{v'w'}}{\partial z} - f\left(\bar{u} - u_g\right) \tag{3.11}$$

Likewise, the thermodynamic equation (3.4) is simplified to:

$$\frac{\partial \bar{\theta}}{\partial t} = -\frac{\partial \overline{w'\theta_v'}}{\partial z}. \tag{3.12}$$

Equations (3.9) through (3.12) can be used in two ways to model the CBL turbulence. First, the full set of differential equations can be used mostly in the above form, except that the second order moments of turbulence are parameterized in terms of eddy diffusivities and vertical gradients. The diffusivities are proportional to the kinetic energy $\bar{e}$ and a master length scale *l*, so the turbulence closure scheme is known as *e-l* closure. This is the fundamental basis of many of the RANS-based turbulence models used in Numerical Weather Prediction (NWP). The NWP grid can typically resolve some of the CBL vertical structure of potential temperature and velocity but must parameterize the turbulence in terms of eddy diffusivities. Through these eddy diffusivities, the effects of CBL turbulent motions on the resolved velocity in the NWP model are accounted for.

Alternatively, one can integrate (3.9) through (3.12) over the depth of the CBL to formulate equations describing the integral budgets of momentum, buoyancy, and TKE. The integration removes the height-dependence of momentum, buoyancy, and TKE, and the resulting equations can be solved analytically or numerically to find the CBL depth

and other parameters of entrainment as a function only of time. This integral budget approach is widely used in applied atmospheric dispersion studies as well as a few GCMs.

Both of these methods are now discussed.

3.4 RANS-Based Closures

3.4.1 TKE-Based Closures

Equations (3.9) through (3.12) contain second order moments of turbulence, which are still unknowns in the problem. These turbulent fluxes are parameterized according to the following hypotheses, which state that the turbulent moments can be specified in terms of eddy diffusivities and mean gradients:

$$\overline{w'e'} + \frac{1}{\rho_0}\overline{w'p'} = -2K_m \frac{\partial \bar{e}}{\partial z}, \tag{3.13}$$

$$\overline{w'u'} = -K_m \frac{\partial \bar{u}}{\partial z}, \tag{3.14}$$

$$\overline{w'v'} = -K_m \frac{\partial \bar{v}}{\partial z}, \text{ and} \tag{3.15}$$

$$\overline{w'\theta'} = -K_h \frac{\partial \bar{\theta}}{\partial z}, \tag{3.16}$$

where K_m and K_h are the eddy diffusivities of momentum and heat, respectively. Since K_m and K_h are themselves unknown, one more assumption is required to relate these quantities to other variables in the system. The eddy diffusivities are written as the product of a master length scale l and some velocity scale. The choice of the master

length scale is somewhat arbitrary, but it must represent the length scales of the turbulence being modeled. The most obvious turbulence velocity scale is $\sqrt{\bar{e}}$.

The eddy diffusivity of momentum, therefore, has the following general form:

$$K_m = \alpha_K \left(\bar{e}\right)^{1/2} l \tag{3.17}$$

where α_K is a constant of proportionality. The eddy diffusivity for heat is related to the eddy diffusivity for momentum through the turbulent Prandtl number, which generally ranges from one third to one under unstable conditions. Dissipation is parameterized by the expression

$$\varepsilon = \alpha_\varepsilon \frac{\left(\bar{e}\right)^{3/2}}{l}, \tag{3.18}$$

where α_ε is a constant. The values of α_K, α_ε, l, and the turbulent Prandtl number are dependent on the particular scheme being used for turbulence modeling. We highlight two particular schemes in this study.

The first scheme is that of Xue et al. (2001). The turbulence length scale in this closure is dependent on the hydrostatic stability. In stable conditions, the length scale is

$$l = l_s = 0.76\left(\bar{e}\right)^{1/2} N^{-1}, \tag{3.19}$$

where *N* is the Brunt-Väisälä frequency. In neutral or unstable conditions (the boundary layer portion of the flow), the length scale is

$$l = l_u = l_0 \left\{ 1.8 z_i \left[\begin{array}{l} 1 - \exp\left(-4z / z_i\right) \\ -0.0003 \exp\left(8z / z_i\right) \end{array} \right] \right\} \tag{3.20}$$

where z is the height, z_i is the boundary layer depth, and $l_0 = 0.25$. The profile of mixing length (3.20) was determined from atmospheric data as described in Caughy et al.

(1979). The boundary layer depth is defined as the level at which a parcel, lifted from the lowest model grid level above ground, becomes neutrally buoyant. Because l_u doesn't become small until $z > z_i$, where the atmosphere is stable, the maximum of l_s and l_u is taken in the region to facilitate a smooth transition. The turbulent Prandtl number is

$$\mathrm{Pr}_t = \max\left[\frac{1}{3}, \left(1 + \frac{2l}{\Delta_v}\right)^{-1}\right], \tag{3.21}$$

where Δ_v is the vertical dimension of the grid cell. The constants in (3.17) and (3.18) are $\alpha_K = 0.1$ and $\alpha_\varepsilon = 0.93$, except $\alpha_\varepsilon = 3.9$ at the first grid level above ground.

The scheme of Fiedler and Kong (2003), hereafter referred to as F&K, does not depend on the determination of the CBL depth to determine *l*. Rather, it defines the length scale as the geometric mean of an upward length scale and a downward length scale, as in Bougeault and Lacarrere (1989). The upward and downward length scales are defined as the vertical distance an air parcel would travel from its original height, working against buoyancy forces, until all its TKE were expended. Mathematically, these length scales are defined through the following integrals:

$$e(z) = \int_z^{z+\lambda_{up}(z)} \frac{g}{\overline{\theta_v}(z')}\left[\overline{\theta_v}(z') - \overline{\theta_v^*}(z,z')\right]dz', \text{ and} \tag{3.22}$$

$$e(z) = \int_z^{z-\lambda_{down}(z)} \frac{g}{\overline{\theta_v}(z')}\left[\overline{\theta_v}(z') - \overline{\theta_v^*}(z,z')\right]dz', \tag{3.23}$$

where λ_{up} and λ_{down} are the vertical distances of parcel travel and θ_v^* is the virtual potential temperature a parcel would have if it ascended or descended from its starting level z to a new level z'. Once λ_{up} and λ_{down} are determined, the mixing length is the

geometric mean: $l = \left(\lambda_{up}\lambda_{down}\right)^{1/2}$. The specifications for the constants are $\alpha_K = 0.35$, $\alpha_\varepsilon = 0.5$, and $\mathrm{Pr}_t = 1$.

The TKE-based schemes [Xue et al. (2001), Fiedler and Kong (2003)] presented here will be tested against LES data in Chapter 10.

3.4.2 Other RANS-Based Closures

In this section, we have looked specifically at 1.5 order, TKE-based, *e-l* closure schemes within the framework of the horizontally homogeneous CBL, but there are numerous other ways to model turbulence within the RANS framework. It is worthwhile to identify these methods to understand where the *e-l* schemes fit within the larger realm of turbulence closure models.

The first manner in which RANS-based turbulence models may differ is with regard to the order of the closure. The order of closure is defined as the highest order turbulent moments that are explicitly contained in the model's prognostic equations. The *e-l* schemes described above are formally considered 1.5-order turbulence closure because they contain a prognostic equation for TKE, which by definition, contains some of the second order moments—namely, the velocity variances—but not all of them, and it does not account for any turbulence anisotropy. In other words, $\overline{u'^2} = \overline{v'^2} = \overline{w'^2} = \frac{2}{3}\bar{e}$. 1.5-order closure is rather typical in NWP codes, but higher and lower order closures are also found.

First order closure schemes do not contain a prognostic equation for TKE, and the assumption (3.17) is not made. Rather, the eddy viscosity is related to a length scale and

to the rate of strain, i.e. $K_m \sim l^2 \partial \overline{U} / \partial z$. The most well-known of these closures is the Lilly-Smagorinsky (1967) closure, which includes the assumption that the TKE is in a balanced state and the rate of production is exactly equal to the rate of dissipation, which is exactly what is needed to relate the eddy viscosity directly to the strain rates and a length scale. The Lilly-Smagorinsky closure can also be described in terms of 1.5-order closure, since it is derived from the TKE equation with shear production in balance with dissipation of TKE, but it does not carry a TKE equation and is, therefore, first order. Other closure schemes, such as O'Brien (1970), simply use an assumed profile of eddy viscosity in the boundary layer and are therefore purely first order.

Alternatively, one can proceed upward in complexity and derive a second order turbulence closure scheme, based on Equation (3.7), which describes the rate of change of all the Reynolds stresses. The most commonly used higher order schemes for modeling atmospheric turbulence are the Mellor-Yamada hierarchy of turbulence closures (Mellor 1973; Mellor and Yamada 1974, 1982), which are formally derived from a non-Boussinesq version of Equation (3.7). The level of turbulence closure is based on the degree of simplification from the starting equation. The so-called Level 4 model (the top of the heirarchy) can be considered a full second-order closure, because it parameterizes only the third order moment term and retains prognostic equations for all Reynolds stresses. All other levels have an increasing number of simplifications that reduce the formal order of the closure to something between 1.5 and 2. The Level 2.5 scheme used in the NCEP Eta model (Janjic 1994) and several other NWP models contains a prognostic equation only for TKE, and it parameterizes the remaining

Reynolds stress terms through simpler equations describing the anisotropy of turbulence, so the scheme is not a 2.5-order closure as its name might lead one to believe.

Rather than changing the order of the closure, one can replace the master length scale of *e-l* closure with a prognostic equation for dissipation, making the scheme an *e-ε* closure. In *e-ε* closure, the prognostic equation for the dissipation ε is formed by assuming the turbulence frequency, defined as $\omega = \varepsilon / e$, is constant. The equations for TKE and dissipation are then solved. Such approaches are not commonly used to model atmospheric turbulence and will not be further considered here.

3.4.3 Points of Caution for RANS-Based Closures

Sometimes, different length scales l might be used in the horizontal and vertical dimensions. The use of more than one length scale departs from the basic assumptions about *e-l* closure, which only requires a single master length scale to close the problem. Xue et al. (2001) make use of separate horizontal and vertical length scales.

Additionally, with the increasing resolution of regional NWP models, the horizontal grid cell size is becoming small enough that the implied horizontal averaging within the grid cell may differ considerably from an ensemble average, and some of the turbulence might start to become resolved. As such, the assumptions implicit in the RANS-based NWP turbulence closures may not hold, putting these RANS-based schemes in a very awkward position. Because they are modeling only part of the CBL turbulence, they depart from their RANS-based origin, and because the grid cell (or filter) width lies in the energy production range of the turbulence spectrum and not within the inertial subrange, they are also not subgrid TKE-based schemes (see Appendix A). This

is a particularly important problem in contemporary NWP, and it is addressed, to some extent, by Fiedler and Kong (2003). However, in this study, it is assumed that the grid cell sizes are large enough that the implied horizontal averaging *can* be considered representative of an ensemble average, and the assumptions of a RANS-based scheme will still hold; we make the assumption that the grid cells are infinitely wide.

Fiedler and Kong (2003) introduce a tunable parameter β in to their model in order to account for some turbulence resolution on the grid. If the horizontal grid cell becomes small enough, β is reduced in order to avoid "double-counting" the turbulence. Fiedler and Kong (2003) experimented with $\beta = 1.0$ for grid cells of 72 km and $\beta = 0.3$ for grid cells of 2 km. Their paper represents the first effort to adjust the turbulence parameterization scheme for fine grids.

3.5 Integral Budget Methods

In order to further simplify the equations for the CBL growth, one can integrate the buoyancy, momentum, and TKE balance equations over the depth of the CBL. To simplify these integrations, the overall CBL structure can be represented in a schematic form, as long as the schematic profiles capture the essential features of the CBL.

3.5.1 Zero Order Model (ZOM)

The greatest possible simplification is to use the zero order model (ZOM) profiles of buoyancy and TKE. Fedorovich (1995) derived ZOM equations for many types of CBLs, including the CBL with surface wind shear and shear in the geostrophic wind. In the

ZOM, the surface layer and entrainment zone, being only a small fraction of the overall CBL depth, are assumed to be infinitesimally shallow. The CBL is therefore schematically represented as a mixed layer in which all scalars are independent of height.

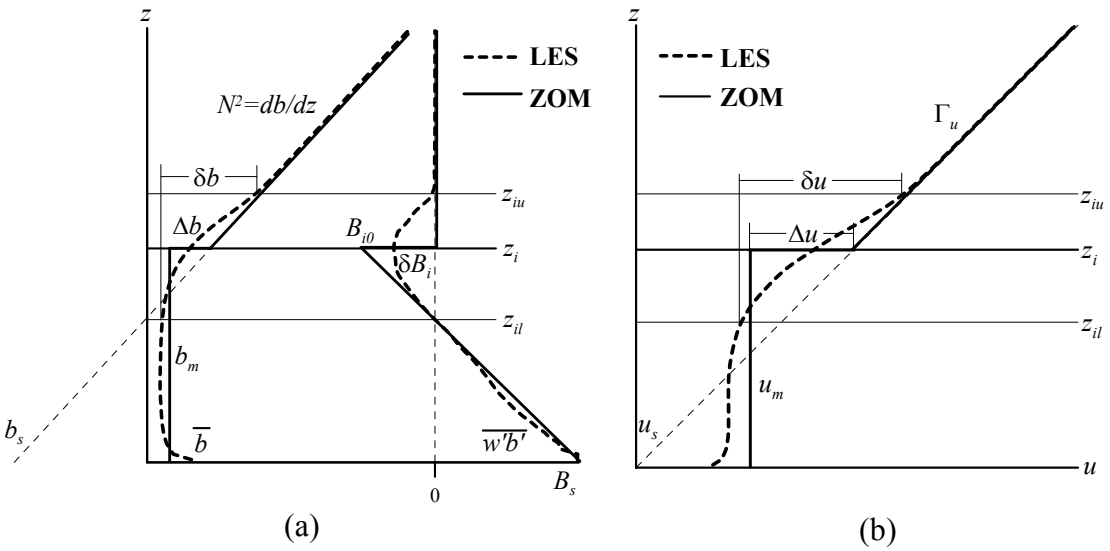

Figure 3.1: Profiles of (a) buoyancy and buoyancy flux and (b) velocity in the horizontally homogeneous CBL. Solid lines indicate LES or atmospheric horizontally averaged profiles, and heavy dashed lines indicate their representation in the ZOM. Lighter dashed lines are the lower (z_{il}) and upper (z_{iu}) limits of the entrainment zone. The diagonal dashed line in (b) represents the profile of geostrophic wind. For changes of any variable ϕ across the entrainment zone, $\delta\phi$ refers to the change of that variable across the entire entrainment zone, and $\Delta\phi$ refers to the change of that variable in the ZOM.

At the CBL top, the scalar quantities jump to their free atmospheric values and therefore have finite discontinuities (Δu, Δv, and $\Delta\theta$) in their zero order derivatives—hence the name zero order model. Figure 3.1 clarifies the differences between these jumps, which are specific to the ZOM, and the total changes of momentum and potential temperature across the entrainment zone. Zero order velocity jumps also occur at the surface, where $\bar{u}$ and $\bar{v}$ change from zero to their mixed layer values u_m and v_m. Above

the entrainment zone, the profiles of momentum and temperature are assumed to be linear and independent of time. The surface buoyancy flux B_s is assumed to be an independent variable.

3.5.1.1 ZOM Equations

The notation in the ZOM equations is made simpler by expressing (3.12) in terms of the traditional definition of buoyancy, $(g/\theta_{v0})(\theta_v - \theta_{v0})$. With Equations 3.9-3.11 unchanged, and the momentum, buoyancy, and turbulence kinetic energy in the horizontally homogeneous CBL are:

$$\frac{\partial \bar{u}}{\partial t} = f\left(\bar{v} - v_g\right) - \frac{\partial \overline{u'w'}}{\partial z}, \tag{3.24}$$

$$\frac{\partial \bar{v}}{\partial t} = -f\left(\bar{u} - u_g\right) - \frac{\partial \overline{v'w'}}{\partial z}, \tag{3.25}$$

$$\frac{\partial \bar{b}}{\partial t} = -\frac{\partial B}{\partial z} = -\frac{g}{\theta_0}\frac{\partial \overline{w'b'}}{\partial z}, \text{ and} \tag{3.26}$$

$$\frac{\partial e}{\partial t} = -\overline{u'w'}\frac{\partial \bar{u}}{\partial z} - \overline{v'w'}\frac{\partial \bar{v}}{\partial z} + \overline{w'b'} - \frac{\partial}{\partial z}\left(\overline{w'e'} + \frac{1}{\rho_0}\overline{w'p'}\right) - \varepsilon\,. \tag{3.27}$$

Since the geostrophic wind profiles in the ZOM are linear, the geostrophic wind can be written as $u_g = u_{g0} + \Gamma_u z$ and $v_g = v_{g0} + \Gamma_v z$, where u_{g0} and v_{g0} are the surface wind components, $\Gamma_u = \partial u_g / \partial z$, and $\Gamma_v = \partial v_g / \partial z$.

Integral budgets of momentum, buoyancy, and TKE are formed by integrating (3.24) through (3.27) over the depth of the ZOM CBL structure. The upper limit of integration is taken an infinitesimally small distance past z_i to incorporate the

discontinuities at z_i. Leibniz' rule is used at the upper interface (z_i) because this level changes with respect to time. The flow is assumed to be non-turbulent at the upper limit of integration. The integrated equations are:

$$z_i \frac{du_m}{dt} = \overline{w'u'}_s + \Delta u \frac{dz_i}{dt} + f\left(v_m - v_{g0} - \frac{\Gamma_v}{2} z_i \right) z_i , \tag{3.28}$$

$$z_i \frac{dv_m}{dt} = \overline{w'v'}_s + \Delta v \frac{dz_i}{dt} - f\left(u_m - u_{g0} - \frac{\Gamma_u}{2} z_i \right) z_i , \text{ and} \tag{3.29}$$

$$z_i \frac{db_m}{dt} = \overline{w'b'}_s + \Delta b \frac{dz_i}{dt} . \tag{3.30}$$

The first two equations describe the integral momentum budget in the ZOM CBL. On the left hand side of each of these equations is the integrated mixed layer momentum. The first term on the right hand side is the turbulent surface flux of momentum. In most cases, this term removes momentum from the CBL because it is of opposite sign to the momentum. Strictly, this term can only be used in the surface layer above the viscous sublayer because w' reaches zero at the ground (z=0). The second term on the right hand side represents the entrainment of momentum at the CBL top as the CBL grows. The last terms in the integral momentum equations represent the integral effects of the Coriolis force on the ageostrophic flow in the mixed layer. In the integral buoyancy budget equation (3.30), the change of mixed layer buoyancy (left side of the equations) depends on the fluxes from the surface (first term on the right hand side) and the entrainment of buoyancy that occurs as the CBL grows (second term on the right hand side).

To make the budget equations for momentum and buoyancy somewhat more concise, we can relate the mixed layer scalars to their free atmospheric profiles by the relation: $\phi_m = \phi_s + \Gamma_\phi z_i - \Delta\phi$ (Γ_ϕ is the free atmospheric gradient of ϕ with $\Gamma_b = N^2$,

and ϕ_s is the surface value if the free atmospheric profile is extrapolated there). With this change, the integral budget equations are rewritten:

$$\frac{d}{dt}\left(\frac{\Gamma_u}{2}z_i^2 - \Delta u z_i\right) = \overline{u'w'}_s + f\left(\frac{\Gamma_v}{2}z_i^2 - \Delta v z_i\right) \tag{3.31}$$

$$\frac{d}{dt}\left(\frac{\Gamma_v}{2}z_i^2 - \Delta v z_i\right) = \overline{u'w'}_s - f\left(\frac{\Gamma_u}{2}z_i^2 - \Delta u z_i\right) \tag{3.32}$$

$$\frac{d}{dt}\left(\frac{N^2 z_i^2}{2} - \Delta b z_i\right) = \overline{w'b'}_s = B_s \tag{3.33}$$

One can obtain profiles for the turbulent fluxes of momentum and buoyancy in the CBL by integrating (3.24) through (3.26) from the surface up to some arbitrary level z. In so doing, we realize that $\partial\bar{u}/\partial t = du_m/dt$ in the mixed layer, allowing us to use the expression $\phi_m = \phi_s + \Gamma_\phi z_i - \Delta\phi$ as was done for (3.31)-(3.33). The flux profiles are

$$\overline{w'u'}(z) = \overline{w'u'}_s - z\left(\Gamma_u \frac{dz_i}{dt} - \frac{d\Delta u}{dt}\right) + f\left\{\left[\Gamma_v z_i - \Delta v\right]z - \Gamma_v \frac{z^2}{2}\right\}, \tag{3.31}$$

$$\overline{w'v'}(z) = \overline{w'v'}_s - z\left(\Gamma_v \frac{dz_i}{dt} - \frac{d\Delta v}{dt}\right) - f\left\{\left[\Gamma_u z_i - \Delta u\right]z - \Gamma_u \frac{z^2}{2}\right\}, \text{ and} \tag{3.32}$$

$$\overline{w'b'}(z) = \overline{w'b'}_s - z\left(N^2 \frac{dz_i}{dt} - \frac{d\Delta b}{dt}\right). \tag{3.33}$$

The flux profiles are all linear if the Coriolis effects are neglected. If not, the momentum flux profiles are quadratic, but because f is relatively small, they are nearly linear in most cases. Evaluating (3.31) through (3.33) at $z = z_i$ and making use of (3.31) through (3.33), we find the following identities:

$$\overline{w'u'}(z_i) = -\Delta u \frac{dz_i}{dt}, \tag{3.34}$$

$$\overline{w'v'}(z_i) = -\Delta v \frac{dz_i}{dt}, \text{ and} \tag{3.35}$$

$$\overline{w'b'}(z_i) = -\Delta b \frac{dz_i}{dt} \equiv B_i . \tag{3.36}$$

With the use of (3.36), the linear buoyancy flux profile in the ZOM CBL can be written

$$\overline{w'b'}(z) = B_s \left(1 - \frac{z}{z_i}\right) - \Delta b \frac{dz_i}{dt} \frac{z}{z_i}. \tag{3.37}$$

The integral TKE budget is derived by taking the integral of (3.27), using (3.31) through (3.33) for the turbulent fluxes. We begin by integrating the shear terms. Because the momentum is constant with height in the ZOM mixed layer, the shear generation of TKE is limited to the surface layer and the entrainment zone. Because these layers in the ZOM are infinitesimally thin, the shear becomes infinitely large, making the integration a bit more complicated.

For the integration across the surface layer, one assumes $\bar{u}$ changes smoothly from 0 to u_m (the velocity profile is logarithmic or nearly so), and the turbulent flux can be assumed constant, which is generally true in the surface layer. Evaluating $\lim_{\Delta \to 0} \int_0^{\Delta} \frac{1}{\Delta} \overline{w'u'}_s \bar{u}(z) dz$ yields the *x*-component surface shear contribution to the TKE integral budget, $-u_m \overline{w'u'}_s$. The same applies to the *y*-component.

At the CBL top, one can handle the integration by isolating a layer of finite thickness Δ, over which $\bar{u}$ and $\overline{w'u'}$ are assumed to change linearly. $\partial \bar{u} / \partial z$ has a constant value of $\Delta u / \Delta$, and because of (3.34), $\overline{w'u'}$ changes linearly from $-\Delta u dz_i / dt$ to zero. Evaluating the integral, taking its limit as $\Delta \to 0$, and doing the same for the *y*-

component yields the entrainment zone shear contribution to the TKE integral budget: $\frac{1}{2}\left(\Delta u^2 + \Delta v^2\right)\frac{dz_i}{dt}$.

The contribution of buoyancy flux to the TKE integral can be found simply by integrating (3.37) from the surface to the CBL top. Because of the rigid lower surface, the vertical velocity fluctuations are zero there, and the TKE transport is zero. At the CBL top, we parameterize the transport by Φ_i. For now, we do not yet specify any form for the integrals of $\partial\bar{e}/\partial t$ and dissipation, but using Leibniz' rule in combination with the assumption that $\bar{e}(z_{i+}) = 0$, the time derivative can be brought outside the integral of TKE. The resulting TKE integral budget is

$$\begin{aligned}\frac{d}{dt}\int_0^{z_i}\bar{e}dz = &-u_m\overline{w'u'}_s - v_m\overline{w'v'}_s + \frac{1}{2}\left(\Delta u^2 + \Delta v^2\right)\frac{dz_i}{dt} \\ &+ \frac{z_i}{2}\left(B_s - \Delta b\frac{dz_i}{dt}\right) - \Phi_i - \int_0^{z_i}\varepsilon dz.\end{aligned} \tag{3.38}$$

Since the signs of u_m and v_m are generally opposite those of $\overline{w'u'}_s$ and $\overline{w'u'}_s$, the surface shear is a source of TKE. The entrainment zone shear term can also be described as the generation of TKE owing to entrainment of momentum into the CBL. This term is always positive as long as the entrainment, dz_i/dt, is positive. The fourth term describes the generation and destruction of TKE by buoyancy forces in the CBL. If the surface flux of buoyancy B_s is positive, it is a source of TKE. As long as Δb and dz_i/dt are both positive, the other part of the buoyancy term represents the TKE consumption by entrainment. Φ_i is usually small enough in atmospheric applications that it can be neglected (Stull 1976b, Fedorovich et al. 2004).

Equations (3.31)-(3.33) and (3.38) do not form a closed set, since the surface momentum fluxes and the integrals of TKE and dissipation are still unknown. Some assumptions about these quantities must be made before the system of equations can be solved.

3.5.1.2 ZOM Analytic Solutions for Shear-Free Equilibrium Entrainment

If the mean wind components throughout the depth of the considered layer are identically zero, the momentum equations (3.31) and (3.32) drop out, and the integral TKE equation simplifies to

$$\frac{d}{dt}\int_0^{z_i} \overline{e}dz = \frac{1}{2}\left(B_s - \Delta b \frac{dz_i}{dt}\right) z_i - \int_0^{z_i} \varepsilon dz \,. \tag{3.39}$$

The integrals of TKE and dissipation in their current form remain unknowns in the equation, but simplifications can be made. Zilitinkevitch (1991) applied the Deardorff (1980) scaling hypothesis, which assumes that the profiles of TKE and dissipation in the CBL are self-similar and can be scaled by the Deardorff (1970) velocity scale, $w_* = \left(B_s z_i\right)^{\frac{1}{3}}$. The profiles of TKE and dissipation are therefore described in terms of the dimensionless height:

$$e = w_*^2 \varphi_e(\zeta), \quad \varepsilon = \frac{w_*^3}{z_i}\varphi_\varepsilon(\zeta), \quad \zeta = \frac{z}{z_i}, \tag{3.40}$$

where φ_e and φ_ε are universal functions of dimensionless height ζ. Applying this assumption, the scaled integrals of TKE and dissipation become constants:

$$\frac{1}{w_*^2 z_i}\int_0^{z_i} e dz = \int_0^1 \varphi_e(\zeta) d\zeta = C_e, \quad \frac{1}{w_*^3}\int_0^{z_i} \varepsilon dz = \int_0^1 \varphi_\varepsilon(\zeta) d\zeta = C_\varepsilon \quad . \tag{3.41}$$

Making these substitutions, we have:

$$\frac{d}{dt}\left(w_*^2 z_i\right) C_e = \frac{1}{2}\left(B_s - \Delta b \frac{dz_i}{dt}\right) z_i - w_*^3 C_\varepsilon . \tag{3.42}$$

With $\frac{d}{dt}\left(w_*^2 z_i\right) = \frac{5}{3} w_*^2 \frac{dz_i}{dt}$ and dividing by w_*^3 (i.e., normalizing by B_s and z_i), we have:

$$\frac{10}{3} C_e B_s^{-\frac{1}{3}} z_i^{-\frac{1}{3}} \frac{dz_i}{dt} = 1 - \frac{\Delta b \frac{dz_i}{dt}}{B_s} - 2C_\varepsilon . \tag{3.43}$$

(3.43) is simplified for a final time by assuming that the entrainment is in an equilibrium regime. In *equilibrium entrainment*, the CBL turbulence is sufficiently developed that the buoyancy production of TKE (the "1" in the above equation) is no longer used to fill the reservoir of TKE in the CBL, so the left hand side of (3.43), the Zilitinkevitch (1975) "spin-up" term, can be neglected. (A scale analysis for typically well-developed CBLs shows that the left hand side term of Equation 3.43 is nearly an order of magnitude smaller than the middle term on the right hand side, which is the next smallest.) The buoyant production of TKE is then balanced only by dissipation and the buoyancy flux of entrainment ($-\Delta b dz_i / dt$), with the latter being a constant fraction of the surface buoyancy flux, B_s. We therefore, define a constant $C_1 = 1 - 2C_\varepsilon$, which brings the TKE equation to the following form:

$$\frac{\Delta b \frac{dz_i}{dt}}{B_s} = C_1 \tag{3.44}$$

C_1 is the ZOM entrainment flux ratio, $-B_{i0} / B_s$, in the shear-free CBL that is in the equilibrium regime of entrainment. C_1 represents the portion of buoyancy-produced TKE that is used for entrainment, as opposed to being dissipated.

(3.33) and (3.44) form a closed set of equations whose dependent variables can be put into a dimensionless form. Because time forms the independent variable in the problem and B_s and N are also considered independent variables, we may choose t, B_s, and N to normalize the dependent variables in the equation. We define $\hat{t} = tN$, $\hat{z}_i = z_i B_s^{-1/2} N^{3/2}$, and $\Delta\hat{b} = \Delta b B_s^{-1/2} N^{-1/2}$. Making these substitutions, we have:

$$\frac{d}{d\hat{t}}\left(\frac{\hat{z}_i^2}{2} - \hat{z}_i \Delta\hat{b}\right) = 1, \text{ and} \tag{3.45}$$

$$\Delta\hat{b}\frac{d\hat{z}_i}{d\hat{t}} = C_1. \tag{3.46}$$

(3.45) and (3.46) are then combined into a single, first-order, ordinary differential equation that can be solved by inverting the equation and using an integrating factor. Taking the constants of integration for the problem $\hat{z}_{i0} = 0$ and $\Delta\hat{b}_0 = 0$ at $\hat{t} = 0$, the solutions are

$$\hat{z}_i = \left[2\left(2C_1 + 1\right)\hat{t}\right]^{\frac{1}{2}}, \text{ and} \tag{3.47}$$

$$\Delta\hat{b} = C_1\left[\frac{2\hat{t}}{\left(1 + 2C_1\right)}\right]^{\frac{1}{2}}. \tag{3.48}$$

The CBL depth and the buoyancy jump across the entrainment zone both increase at a rate proportional to the square root of time.

Fedorovich et al. (2004a) examined this regime of entrainment using LES and found excellent agreement between the LES data and the above solutions. These results will be discussed more extensively in Chapter 4.

3.5.1.3 ZOM Entrainment Parameterizations

The entrainment rate for the full set of sheared CBL ZOM equations (3.31-3.33, 3.38) can be found by parameterizing individual terms in the TKE equation and solving for the entrainment rate, dz_i / dt. We begin by making the same scaling assumptions of (3.41) for the sheared CBL.

$$\frac{10}{3} C_e w_*^2 \frac{dz_i}{dt} = -2\left(u_m \overline{w'u'}_s + v_m \overline{w'v'}_s\right) + \left(\Delta u^2 + \Delta v^2\right)\frac{dz_i}{dt} + B_s z_i - \Delta b z_i \frac{dz_i}{dt} - 2w_*^3 C_\varepsilon \tag{3.49}$$

This scaling assumption may not be valid for the sheared CBL, but the intent here is to merely to show the derivations of the entrainment equations as they have been done before. Other assumptions will be evaluated in Chapter 10.

Collecting the terms involving dz_i / dt on the left hand side, we have

$$\left[\frac{10}{3} C_e w_*^2 + \Delta b z_i - \left(\Delta u^2 + \Delta v^2\right)\right]\frac{dz_i}{dt} = -2\left(u_m \overline{w'u'}_s + v_m \overline{w'v'}_s\right) + B_s z_i - 2w_*^3 C_\varepsilon. \tag{3.51}$$

Since the entrainment is conveniently expressed by the entrainment flux ratio, $\frac{\Delta b dz_i / dt}{B_s}$, we bring out Δb on the left hand side of the equation, then normalize by $w_*^3 = B_s z_i$, the cube of the convective velocity scale.

$$\left[1 + \frac{10}{3} C_e \frac{w_*^2}{\Delta b z_i} - \frac{\left(\Delta u^2 + \Delta v^2\right)}{\Delta b z_i}\right]\frac{\Delta b \frac{dz_i}{dt}}{B_s} = -\frac{2}{w_*^3}\left(u_m \overline{w'u'}_s + v_m \overline{w'v'}_s\right) + 1 - 2C_\varepsilon \tag{3.52}$$

In the surface layer, the hypothesis of Tennekes (1973) is applied. The Deardorff (1970b) velocity scale in the CBL is $w_*^3 = B_s z_i$, and because the heat flux at the CBL top

is $-B_i \sim B_s = w_*^3 / z_i$ for the shear-free CBL, Tennekes hypothesized that the surface shear-generated turbulence contributed proportionally to the velocity scale in the CBL and therefore, the buoyancy flux scales by a linear combination of w_*^3 and u_*^3. Therefore, with $1 - 2C_\varepsilon = C_1$ in the shear-free case, and, given the velocity scaling by $w_m^3 = w_*^3 + Au_*^3$, the right hand side of (3.52) can be rewritten as $C_1 + C_s u_*^3 / w_*^3$, where $C_s = AC_1$. Solving for the negative of the entrainment flux ratio yields the following form:

$$-\frac{B_i}{B_s} = \frac{\Delta b \frac{dz_i}{dt}}{B_s} = \frac{C_S \frac{u_*^3}{w_*^3} + C_1}{\left[1 + C_T \frac{w_*^2}{\Delta b z_i} - C_P \frac{\left(\Delta u^2 + \Delta v^2\right)}{\Delta b z_i}\right]}. \tag{3.53}$$

The constant C_S indicates the relative contribution of surface shear to the buoyancy flux at the CBL top. The constant C_T parameterizes the uptake of TKE by the reservoir that exists within the CBL, making it temporarily unavailable for entrainment (Zilitinkevitch 1975), and C_P represents the portion of the shear-generated TKE at the CBL top that is not dissipated. The constant C_P implies that the integral dissipation of entrainment zone shear-produced TKE can be scaled by $\left(\Delta u^2 + \Delta v^2\right) dz_i / dt$, so the net contribution of entrainment zone shear production to the buoyancy flux at the CBL top is a fraction of the shear generation of TKE. Rewriting (3.53) using the velocity scale w_m, we have

$$-\frac{B_i}{B_s} = \frac{\Delta b \frac{dz_i}{dt}}{B_s} = \frac{w_m^3}{w_*^3} \frac{C_1}{\left[1 + C_T \frac{w_*^2}{\Delta b z_i} - C_P \frac{\left(\Delta u^2 + \Delta v^2\right)}{\Delta b z_i}\right]}. \tag{3.54}$$

More generally, the effective velocity scale is $w_m^\eta = w_*^\eta + Au_*^\eta$, with $\eta = 3$ in this case [Tennekes and Driedonks (1981) and Driedonks (1982) use $\eta = 2$]. We can further define the following Richardson numbers, remembering that $\Delta b = \frac{g}{\theta_0}\Delta\theta$:

$$Ri_t = \frac{gz_i\Delta\theta}{\theta_0 w_m^2} \quad Ri_{\Delta b} = \frac{gz_i\Delta\theta}{\theta_0 w_*^2} \quad Ri_{GS} = \frac{gz_i\Delta\theta}{\theta_0\left(\Delta u^2 + \Delta v^2\right)} \quad Ri_u = \frac{gz_i\Delta\theta}{\theta_0 u_*^2}. \tag{3.55}$$

Since the uptake of TKE by the reservior of the CBL affects both the shear- and buoyancy-generated TKE, most authors scale the nonstationary term (in the denominator of 3.54) by w_m^2 rather than w_*^2. This term could also scale by some fraction of the entrainment zone shear-generated TKE, but for reasons unknown, the authors do not include such a scaling. The final form of the entrainment parameterization is

$$-\frac{B_i}{B_s} = \frac{\Delta b\frac{dz_i}{dt}}{B_s} = \frac{w_m^3}{w_*^3}\frac{C_1}{\left[1 + C_T Ri_t^{-1} - C_P Ri_{GS}^{-1}\right]}. \tag{3.56}$$

This is a very popular form of the ZOM parameterization proposed by most authors. As mentioned in Chapter 2, one potential mathematical problem with (3.56) can be seen immediately. If the shear term in the denominator ($C_P Ri_{GS}^{-1}$) is large enough, it can grow to a size equal to the other terms, and the ZOM entrainment flux ratio becomes unbounded. If the shear increases further, the sign of the expression changes, and detrainment is predicted. While an infinitely large entrainment flux ratio seems reasonable for a boundary layer that is driven only by shear, (3.56) can become unbounded when $B_s > 0$.

The first attempts to parameterize the effects of shear on the entrainment equation were by Tennekes (1973), who noted that when significant surface shear exists in CBLs,

the net production of TKE is larger and the effective velocity scale w_m should be introduced to account for this. Tennekes' parameterization reads:

$$-\frac{B_i}{B_s} = C_1\left(1 + A\frac{u_*^3}{w_*^3}\right). \tag{3.57}$$

This expression reverts back to the shear-free case when $u_* = 0$.

Zeman and Tennekes (1977) did not include the effects of the shear across the inversion because they did not know what to assume for the fraction of shear-generated TKE at the inversion base that would be available for entrainment. Tennekes and Driedonks (1981) used the experimental results of Price et al. (1978) to estimate this fraction, and their entrainment equation (3.56) forms the basis of the subsequent ZOM-based parameterizations (Driedonks 1982, Boers et al. 1984, Pino et al. 2003). Table 3.1 lists the constants that are used in these parameterizations.

Three parameterizations that are essentially tied to the ZOM, but their approaches differ from the strict ZOM methodology. They are Stull (1976a,b), Fairall (1984), and Batchvarova and Gryning (1990, 1994).

Stull (1976a, 1976c) used a ZOM for the most part but deviated from that model slightly when parameterizing shear across the inversion base. His hypothesis regarding the mechanical generation of TKE at the inversion base was that $\overline{w'u'}$ scaled by $\Delta u dz_i / dt$ as is typical in the ZOM, but the scaling for $\partial u / \partial z$ is $\partial u / \partial z \sim \Delta u^2 / \left(\delta dz_i / dt\right)$, where $\delta = z_i - z_{il}$. Stull used the equation

$$-\frac{B_i}{B_s} = \frac{z_i}{z_i - \delta} - 1. \tag{3.58}$$

Stull's hypothesis has the fortuitous result that the problems characteristic of the more typical ZOM-based entrainment equations (i.e. the shear production being a term of negative sign in the denominator) are avoided. His entrainment equation is:

$$-\frac{B_i}{B_s} = A_1 + A_2 \frac{z_i}{\delta} \frac{u_*^2 |u_m|}{w_*^3} + A_3 \frac{z_i}{\delta} \frac{\Delta u^3}{w_*^3}, \tag{3.59}$$

where $A_1 = C_F = 0.1 \pm 0.05$, $A_2 = 0.05 \pm 0.025$, and $A_3 = 0.001 \pm 0.0005$, based on the best fits of this expression with atmospheric data analyzed by Stull (1976c). In this equation, the dependence on surface shear appears to be somewhat greater than the dependence on entrainment zone shear, which is contrary to the water tank data of Willis and Deardorff (1982). The third term on the right hand side of the equation is also problematic to interpret. Δu^3 can have a positive sign or a negative sign, which would mean the shear across the entrainment zone would depend on the sign of Δu. Such a result does not seem to make sense based on physical reasoning. The expression would predict opposite effects of shear on entrainment if a coordinate transformation is made by rotating 180 degrees about the *z*-axis.

Fairall (1984), motivated to find the effects of entrainment on the refraction of electromagnetic waves (for atmospheric remote sensing), developed an independent parameterization, which reads:

$$-\frac{Q_i}{Q_0} = C_F \frac{w_m^3}{w_*^3} \left[\frac{r R_f^{-1} \left(2 + r R_f^{-1}\right)}{1 + 2\left(1 + r R_f^{-1}\right)\left(s - r R_f^{-1}\right)} + 1 \right], \tag{3.60}$$

where $C_F = 0.2$, $w_m^3 = w_*^3 + 8u_*^3$, and the other constants are:

$$R_f^{-1} = \frac{7\left(\delta u^2 + \delta v^2\right)\Gamma}{6\left(g/\theta_0\right)\delta\theta^2}, \quad r = \frac{c_1 - 2}{2\left(c_1 + 2c_2 - 5\right)}, \quad s = \frac{c_1 - 4c_2 + 4}{2\left(c_1 + 2c_2 - 5\right)}, \tag{3.61}$$

where $c_1 = 11$, and $c_2 = 3/14$ (the value of c_2 is not perfectly clear in the paper).

Table 3.1. Values of Constants in Entrainment Equations

Author	A	η	C_1	C_T	C_P
Tennekes (1973)	12.5	3	0.2	0	0
Zeman and Tennekes (1977)	4.6*	3	$0.5 - 0.024\frac{Nz_i}{w_m}$	3.55	0
Tennekes and Driedonks (1981)	4*	2	$0.6 - 0.03\frac{Nz_i}{w_m}$	4.3	0.7
Driedonks (1982)	25	3	0.2	0	0
Boers (1984)	23	3	0.32	0.75	1
Batchvarova and Gryning (1990,1994)	12.5	3	0.2	0	0
Pino et al. (2003)	8	3	0.2	4	0.7

* Expression uses $w_m^2 = w_*^2 + Au_*^2$ rather than $w_m^3 = w_*^3 + Au_*^3$

Batchvarova and Gryning (1990, 1994) use a somewhat different derivation that involves the elimination of $\Delta\theta$, a dependent variable, from the entrainment equation by substituting a diagnostic equation that relates $\Delta\theta$ to surface friction velocity, heat flux (both of which can be calculated from measured surface quantities), and boundary layer depth. The Batchvarova and Gryning formula is:

$$-\frac{B_i}{B_s} = \frac{X_{BG}(1+X_{BG})}{1+X_{BG}+Y_{BG}\left(1+2X_{BG}\right)}, \tag{3.62}$$

where $X_{BG} = w_m^3 / w_*^3 = C_F(1 + Au_*^3 / w_*^3)$, and $Y_{BG} = B_{BG}u_*^2 /(N^2 z_i^2)$.

3.5.2 First Order Model (FOM)

Some relaxation of the degree of simplification of CBL structure may be necessary to retain features of the CBL that may be important for entrainment. In particular, entrainment usually occurs over a layer of finite thickness that might play an important

role in regulating the entrainment rate, particularly for the case when mean shear exists across the entrainment zone. The first order model (FOM), described by Betts (1974), represents the entrainment zone using a layer of finite thickness Δz, and all scalars change linearly with height within this layer, so there are no zero-order discontinuities (jumps) in the scalar profiles. The discontinuities are all in their first derivatives with respect to height. The FOM profiles are shown in Figure 3.2. The parameters of entrainment, where they differ from the ZOM, bear the added subscript "1".

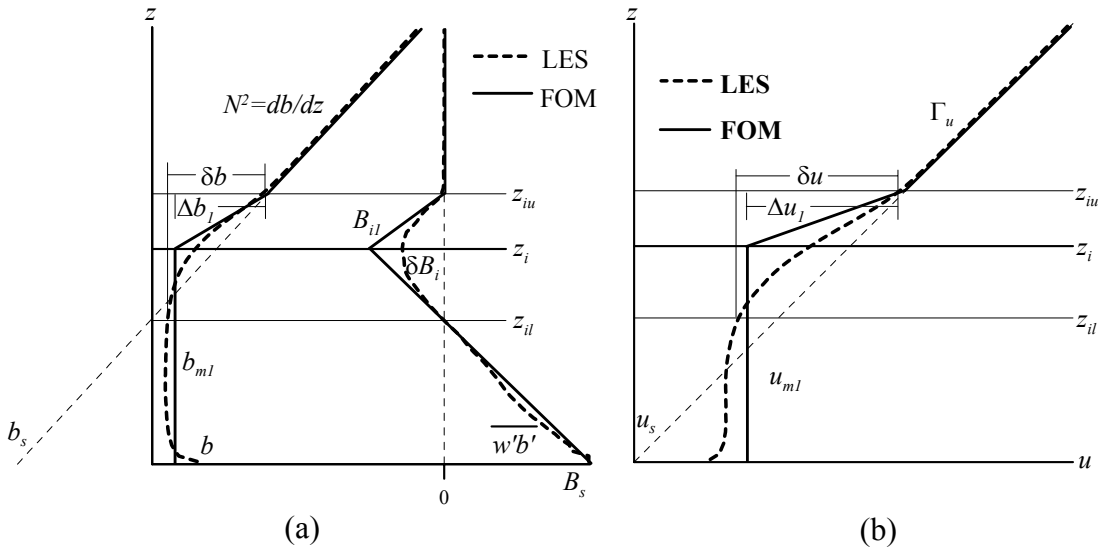

Figure 3.2: Profiles of (a) buoyancy and buoyancy flux and (b) velocity in the horizontally homogeneous CBL. Dashed black lines indicate LES and atmospheric horizontally averaged profiles, and thin solid lines indicate their representation in the FOM. Thin horizontal lines are the lower (z_{il}) and upper (z_{iu}) limits of the entrainment zone. The diagonal dashed lines represent the background profiles of buoyancy in (a) and geostrophic wind in (b). For changes of any variable ϕ across the entrainment zone, $\delta\phi$ refers to the change of that variable across the full depth of the entrainment zone in the atmospheric or LES profile, and $\Delta\phi_1$ refers to the change of that variable in the FOM entrainment zone.

3.5.2.1 FOM Equations

The FOM integral budgets of momentum, buoyancy, and TKE are obtained in the same manner as the ZOM budgets, by integrating over the depth of the CBL and the

entrainment zone. The mixed layer budgets in the FOM are very similar to their ZOM counterparts, but in the entrainment zone, the equations become a bit more complex. To find the flux profiles for momentum and buoyancy there, the linear profiles of buoyancy and momentum must be integrated, yielding quadratic equations. These quadratic equations for the buoyancy and momentum fluxes must then be integrated to form the TKE integral budgets, which are cubic. The resulting set of equations is a bit more complicated than in the ZOM, and their linear terms, which they share with the ZOM and have the same basic meaning, can become obscured by a large number of higher order terms, which might not be the most significant terms in the equations. For this reason, most authors (Mahrt and Lenschow 1976, Kim 2001) chose to make simplifying assumptions that result in the absence of the higher order terms in the flux profiles. Chapter 10 will analyze the validity of these assumptions.

The equations describing the buoyancy and momentum budgets of the FOM CBL, in their mathematically concise form, are:

$$\frac{d}{dt}\left[\frac{N^2\left(z_i+\Delta z\right)^2}{2}-\Delta b_1\left(z_i+\frac{\Delta z}{2}\right)\right]=B_s\,, \tag{3.63}$$

$$\begin{aligned}\frac{d}{dt}\left[\frac{\Gamma_u\left(z_i+\Delta z\right)^2}{2}-\Delta u_1\left(z_i+\frac{\Delta z}{2}\right)\right]&=\overline{w'u'}_s\\ &\quad+f\left[\frac{\Gamma_v\left(z_i+\Delta z\right)^2}{2}-\Delta v_1\left(z_i+\frac{\Delta z}{2}\right)\right],\end{aligned} \tag{3.64}$$

$$\begin{aligned}\frac{d}{dt}\left[\frac{\Gamma_v\left(z_i+\Delta z\right)^2}{2}-\Delta v_1\left(z_i+\frac{\Delta z}{2}\right)\right]&=\overline{w'v'}_s\\ &\quad-f\left[\frac{\Gamma_u\left(z_i+\Delta z\right)^2}{2}-\Delta u_1\left(z_i+\frac{\Delta z}{2}\right)\right].\end{aligned} \tag{3.65}$$

In these equations, the subscript "1" is added to represent FOM parameters of entrainment when they differ from the ZOM parameters. Otherwise, the notation is the same.

It is more convenient for understanding to write these equations in terms of the time rate of change of mixed layer scalars:

$$z_i \frac{db_{m1}}{dt} = B_s + \Delta b_1 \frac{dz_i}{dt} - \Delta z N^2 \frac{d}{dt}\left(z_i + \Delta z\right) + \frac{1}{2}\frac{d}{dt}\left(\Delta b_1 \Delta z\right) \tag{3.66}$$

$$\begin{aligned} z_i \frac{du_{m1}}{dt} = {} & \overline{w'u'}_s + \Delta u_1 \frac{dz_i}{dt} - \Delta z \Gamma_u \frac{d}{dt}\left(z_i + \Delta z\right) + \frac{1}{2}\frac{d}{dt}\left(\Delta u_1 \Delta z\right) \\ & + f\left[\frac{\Gamma_v \left(z_i + \Delta z\right)^2}{2} - \Delta v_1 \left(z_i + \frac{\Delta z}{2}\right)\right] \end{aligned} \tag{3.67}$$

$$\begin{aligned} z_i \frac{dv_{m1}}{dt} = {} & \overline{w'v'}_s + \Delta v_1 \frac{dz_i}{dt} - \Delta z \Gamma_v \frac{d}{dt}\left(z_i + \Delta z\right) + \frac{1}{2}\frac{d}{dt}\left(\Delta v_1 \Delta z\right) \\ & - f\left[\frac{\Gamma_{ug} \left(z_i + \Delta z\right)^2}{2} - \Delta u_1 \left(z_i + \frac{\Delta z}{2}\right)\right] \end{aligned} \tag{3.68}$$

As in the ZOM equations, the first term on the right hand side represents the contribution from the surface flux, and the second term describes the change of mixed layer scalars due to the entrainment of these scalars from the free atmosphere into the CBL. The third and fourth terms exist because, unlike the ZOM, the identities (3.34)-(3.36) do not hold in the FOM. The right hand-most term in both the momentum equations represents the change in integral mixed layer momentum due to the Coriolis force acting on the ageostrophic component of the wind.

If (3.24) through (3.26) are instead integrated not over the entire CBL depth but only to some arbitrary level z, equations for the profiles of buoyancy and momentum fluxes can be obtained. In the mixed layer, these profiles have the form:

$$\overline{w'b'}(z) = B_s - z\frac{db_{m1}}{dt} \tag{3.67}$$

$$\overline{w'u'}(z) = \overline{w'u'}_s - z\frac{du_{m1}}{dt} + f\left\{\left[\Gamma_v\left(z_i + \Delta z\right) - \Delta v_1\right]z - \Gamma_v\frac{z^2}{2}\right\} \tag{3.69}$$

$$\overline{w'v'}(z) = \overline{w'v'}_s - z\frac{dv_{m1}}{dt} - f\left\{\left[\Gamma_u\left(z_i + \Delta z\right) - \Delta u_1\right]z - \Gamma_u\frac{z^2}{2}\right\} \tag{3.70}$$

In the entrainment zone, the profiles are:

$$\overline{w'b'}(z) = B_s - z\frac{db_{m1}}{dt} - \frac{d}{dt}\left[\frac{\Delta b_1}{\Delta z}\frac{\left(z - z_i\right)^2}{2}\right], \tag{3.71}$$

$$\begin{aligned}\overline{w'u'}(z) = \overline{w'u'}_s - z\frac{du_{m1}}{dt} - \frac{d}{dt}\left[\frac{\Delta u_1}{\Delta z}\frac{\left(z - z_i\right)^2}{2}\right] \\ + f\left\{\left[\Gamma_v\left(z_i + \delta\right) - \Delta v_1\right]z - \Gamma_v\frac{z^2}{2}\right\} + f\frac{\Delta v_1}{\Delta z}\frac{\left(z - z_i\right)^2}{2},\end{aligned} \tag{3.72}$$

$$\begin{aligned}\overline{w'v'}(z) = \overline{w'v'}_s - z\frac{dv_{m1}}{dt} - \frac{d}{dt}\left[\frac{\Delta v_1}{\Delta z}\frac{\left(z - z_i\right)^2}{2}\right] \\ - f\left\{\left[\Gamma_u\left(z_i + \delta\right) - \Delta u_1\right]z - \Gamma_u\frac{z^2}{2}\right\} + f\frac{\Delta u_1}{\Delta z}\frac{\left(z - z_i\right)^2}{2}.\end{aligned} \tag{3.73}$$

The TKE equation (3.9) can then be integrated over the depth of the CBL and entrainment zone using (3.67) through (3.73). The buoyancy flux profile is straightforward to integrate, since there are no zero order discontinuities in the buoyancy flux profile.

The vertical gradients of momentum are zero in the mixed layer, so there is no shear contribution to TKE in the FOM mixed layer. Again, special care must be taken to integrate the shear source term at the surface. This integration can be handled in the same manner as it is done in the ZOM. Across the FOM entrainment zone, the

integration of the shear term is more straightforward, since the shear is constant there (i.e. $\Delta u/\Delta z$ and $\Delta v/\Delta z$), and the flux profiles are given by (3.71)-(3.73), which have no zero order discontinuities.

Once the integrations of the individual terms are carried out, $\phi_{m1} = \phi_s + \Gamma_\phi z_i - \Delta\phi_1$ is substituted for the mixed layer scalars ϕ_{m1}. The resulting integral TKE budget is:

$$\int_0^{z_i+\Delta z} \frac{\partial e}{\partial t} dz = \int_0^{z_i+\Delta z} S_x dz + \int_0^{z_i+\Delta z} S_y dz + \int_0^{z_i+\Delta z} B dz + \Phi_{z_i+\Delta z} - \int_0^{z_i+\Delta z} \varepsilon dz \tag{3.74}$$

The individual terms are written as follows:

$$\begin{aligned}\int_0^{z_i+\Delta z} S_x dz = {} & -u_m \overline{w'u'}_s + \frac{1}{2}\Delta u_1^2 \frac{dz_i}{dt} - \frac{\Delta z \Delta u_1}{2}\frac{d}{dt}\left[\Gamma_u\left(z_i+\Delta z\right) - \frac{\Delta u_1}{3}\right] \\ & + \frac{\Delta u_1^2}{6}\frac{d\Delta z}{dt} + \frac{\Delta u_1 f \Gamma_v \Delta z^2}{6} - \frac{f\Delta u_1 \Delta v_1 \Delta z}{6},\end{aligned} \tag{3.75}$$

$$\begin{aligned}\int_0^{z_i+\Delta z} S_y dz = {} & -v_{m1} \overline{w'v'}_s + \frac{1}{2}\Delta v_1^2 \frac{dz_i}{dt} - \frac{\Delta z \Delta v_1}{2}\frac{d}{dt}\left[\Gamma_v\left(z_i+\Delta z\right) - \frac{\Delta v_1}{3}\right] \\ & + \frac{\Delta v_1^2}{6}\frac{d\Delta z}{dt} - \frac{\Delta v_1 f \Gamma_u \Delta z^2}{6} + \frac{f\Delta v_1 \Delta u_1 \Delta z}{6},\end{aligned} \tag{3.76}$$

$$\begin{aligned}\int_0^{z_i+\Delta z} \overline{w'b'} dz = {} & \frac{1}{2} B_s\left(z_i+\Delta z\right) - \frac{1}{2} z_i \Delta b_1 \frac{dz_i}{dt} \\ & + \frac{1}{4}\left(z_i + \frac{\Delta z}{3}\right)\left(\Delta b_1 \frac{d\Delta z}{dt} - \Delta z \frac{d\Delta b_1}{dt}\right)\end{aligned} \tag{3.77}$$

The first term on the right hand sides of the source integrals represent the contribution to TKE from surface fluxes. In the surface layer, these terms are generally source terms as they are in the ZOM.

The second terms on the right hand sides of the integrals represent the contributions from changes across the entrainment zone and are the same in form and

meaning as their ZOM counterparts. The remaining terms result from the finite entrainment zone depth.

(3.63)-(3.65) and (3.74) form a set of equations for the integral budgets of buoyancy, momentum, and TKE for the FOM CBL. Most authors simplify these equations a fair bit. Such simplifications will be seen in the next two sections.

3.5.2.2 FOM Entrainment Parameterizations

Mahrt and Lenschow (1976) developed a FOM set of equations for the entraining CBL with wind shear and bottom heating. They made three assumptions in order for the equations to maintain some degree of simplicity. The first of these assumptions was that the entrainment zone thickness is much smaller than the CBL depth. This allowed them to neglect terms of order (Δz) in the momentum and buoyancy balance equations (3.66)-(3.68), simplifying them to the following forms:

$$z_i \frac{db_{m1}}{dt} = \overline{w'b'}_s + \Delta b_1 \frac{dz_i}{dt}, \tag{3.78}$$

$$z_i \frac{du_{m1}}{dt} = \overline{w'u'}_s + \Delta u_1 \frac{dz_i}{dt} + fz_i \left[\frac{\Gamma_v z_i}{2} - \Delta v_1 \right], \text{ and} \tag{3.79}$$

$$z_i \frac{dv_{m1}}{dt} = \overline{w'v'}_s + \Delta v_1 \frac{dz_i}{dt} - fz_i \left[\frac{\Gamma_u z_i}{2} - \Delta u_1 \right]. \tag{3.80}$$

For the TKE equation, they expected the terms of order (Δz) to still be relatively large, but to simplify the TKE equation, they made their second assumption, which is that the turbulent fluxes of momentum and buoyancy were linear in the entrainment zone. Thirdly, the fluxes at z_i were approximated by $\overline{w'\phi'}_i = -\Delta\phi_1 dz_i / dt$, which is not an exact expression in the FOM. The resulting TKE equation is

$$\int_0^{z_i+\Delta z} \frac{\partial e}{\partial t}\,dz = \frac{1}{2}\left(\Delta u_1^2 + \Delta v_1^2\right)\frac{dz_i}{dt} + \frac{z_i}{2}\left[B_s - \frac{dz_i}{dt}\Delta b_1\left(1+\frac{\Delta z}{z_i}\right)\right] + \left[\overline{w'\left(\frac{p'}{\rho_0}+e'\right)}\right]_0 - \varepsilon z_i\left(1+\frac{\Delta z}{2z_i}\right), \tag{3.81}$$

which is very similar to the ZOM TKE equation. Solving this equation for dz_i/dt and rearranging it to describe $-B_i/B_s$ yields

$$\frac{-B_i}{B_s} = \frac{\Delta b_1 \frac{dz_i}{dt}}{B_s} = \frac{\left[1+2C_0-2C_\varepsilon\left(1+\frac{\Delta z}{2z_i}\right)\right]}{\left(1+\frac{\Delta z}{z_i}\right)-\frac{\Delta u_1^2+\Delta v_1^2}{\Delta b_1 z_i}}, \tag{3.82}$$

where C_0 is the constant specifying the loss of TKE due to transport out of the CBL by gravity waves.

Kim (2001) also worked with the first order model in developing an entrainment parameterization for CBLs with wind shear. She assumed dissipation to be a linear combination of production mechanisms and also made the approximation that the turbulent flux profiles in the entrainment zone were linear. This is inconsistent with the strict FOM methodology, which specifies quadratic buoyancy flux profiles in the entrainment zone. She assumed $d\Delta z/dt \simeq 0$ and, based on her evaluation of the integrals of TKE budget terms using LES data, this approximation seems somewhat reasonable for her LES cases. Her definition of the CBL depth by the level of maximum potential temperature gradient is somewhat inconsistent with FOM, which clearly defines z_i to be at the buoyancy flux minimum. The FOM has a constant potential temperature gradient in the entrainment zone, so a unique absolute maximum does not exist, and it is therefore

not possible to identify a unique height in the FOM where the potential temperature gradient is largest.

Kim's parameterization reads:

$$\frac{-Q_i}{Q_s} = \frac{T_{num}}{1 - \dfrac{\Delta u_1^2}{2\left(g/\theta_0\right)\left(\Delta\theta_1 - \Gamma_\theta \Delta z/2\right)\left(z_i + \Delta z\right)} A_{3K}}, \tag{3.83}$$

where

$$\begin{aligned} T_{num} &= A_{1K}\frac{1}{1+\Delta z/z_i} + A_{2K}\frac{u_*^3}{w_*^3} \\ &\quad + A_{3K}\frac{1}{w_*^3}\frac{\Delta z}{\left(4z_i + 2\Delta z\right)}\left[u_*^2\Delta u_1 + \frac{\overline{w'\theta'}_s}{\left(\Delta\theta - \Gamma_\theta \Delta z/2\right)}\Delta u_1^2\right]. \end{aligned} \tag{3.84}$$

In these expressions, $A_{1K} = 0.2$, $A_{2K} = 0.26$, and $A_{3K} = 1.44$. It is unclear what entrainment zone thickness (Δz) to use when evaluating the parameterization. The thickness is parameterized by the following formula that she proposes:

$$\Delta z = z_i\left(1.12 Ri_k^{-1} + 0.08\right) \quad Ri_k = \frac{\Delta b_1 z_i}{w_*^2 + 4u_*^2 + 0.1\left(\Delta u_1^2 + \Delta v_1^2\right)}. \tag{3.85}$$

These equations, along with the FOM equations for buoyancy and momentum listed in the previous section, provide a complete set of equations that can be integrated forward in time to predict the entrainment rate.

More recently, Sorbjan (2004) developed a parameterization specifically to parameterize the heat flux at the sheared CBL top. This parameterization takes into account the Richardson number of the entrainment zone and therefore requires a finite entrainment zone thickness. The Sorbjan parameterization is

$$B_i = c_H w_*^2 N_i \frac{\left(1 + c_{2S}/Ri_\delta\right)}{\left(1 + 1/Ri_\delta\right)^{1/2}} \tag{3.86}$$

with $c_H = 0.015$ and $c_{2S} = 1.5$. N_i is the Brunt-Väisälä frequency of the interfacial layer, and the Richardson number is the interfacial Richardson number $Ri_\delta = \delta b \delta z_i / \left(\delta u^2 + \delta v^2 \right)$, where the velocity and buoyancy jumps are interpreted as their changes across the full entrainment zone δz_i. This approach is more consistent with the FOM than the ZOM, so it is grouped here with the FOM parameterizations.

3.5.3 General Structure Model (GSM)

Fedorovich and Mironov (1995) describe the general structure model (GSM) for the shear-free convective boundary layer. In the GSM, which originated with Deardorff (1979), higher order polynomials can be used to describe horizontally averaged entrainment zone structure in a more realistic manner than with the ZOM or FOM. The model is based on the idea of the self-similarity of the buoyancy profile in the entrainment zone. For the shear-free case, the basic method for solving the entrainment equation with the GSM equations is the same as with the ZOM and FOM. The buoyancy balance equation is integrated over the depth of the mixed layer and the buoyancy flux profile is derived. The buoyancy flux is then used in the integral of the TKE balance equation, and the TKE balance equation serves as the cornerstone for the CBL depth versus time. The two parameters that are specified in the GSM are the polynomial function describing the buoyancy profile in the entrainment zone, as a function of the depth relative to the entrainment zone thickness, and the relative entrainment ratio *G*, which describes the overall stratification in the entrainment zone, as a ratio of the free atmospheric stratification. Fedorovich et al. (2004a) found $G \approx 1.2$. In order for the GSM to work well in describing entrainment, the buoyancy profile must remain self-

similar, meaning that its shape, after application of appropriate scaling, must not change with time. Fedorovich et al. (2004a) evaluated this assumption. Details of the evaluation will be provided in Chapter 4.

Chapter 4

Evaluations of Integral Budget Models of Entrainment with LES for the Shear-Free CBL

4.1 Methods

This chapter represents a summary of the findings of Fedorovich et al. (2004a), in which entrainment prediction of the ZOM and GSM were tested against LES data for shear-free CBLs. In particular, the shear-free, ZOM equilibrium entrainment equations (3.47, 3.48) of Zilitinkevitch (1991) were evaluated in detail, and the GSM of Fedorovich and Mironov (1995), mentioned in Section 3.5.3, was also evaluated.

4.1.1 LES Setup

The LES runs were designed to test the predictions of CBL growth in the equilibrium entrainment regime. Details of the LES code used in the study can be found in Wyngaard and Brost (1984), Nieuwstadt and Brost (1986), and Fedorovich et al. (2001a), and in Appendix A. The Boussinesq equations of motion and the thermodynamic equation were solved numerically using centered, second order finite difference methods on a staggered Cartesian grid. Pressure was from a diagnostic (Poisson) equation solved using a fast Fourier transform in the horizontal directions and a tridiagonal matrix factorization in the

vertical. The boundary conditions were periodic in the horizontal directions. At the top, the Neumann boundary conditions were specified, with gradients the same as their free-atmospheric values, and at the bottom, Monin-Obukhov similarity functions were applied locally for velocity and temperature, along with a no-slip condition for velocity. Mathematical details of the LES equations are included in Appendix A.

The LES settings for the equilibrium entrainment studies are listed in Table 4.1. The simulation domain was $X \times Y \times Z = 5 \times 5 \times 4$ km^3 on a $50 \times 50 \times 200$ grid. No vertical grid stretching was applied.

The grid cells were 100 meters across in the horizontal direction and 20 meters tall. To test the effects of grid anisotropy on the simulation results, an additional run was conducted on a $100 \times 100 \times 200$ grid. Results of the testing on the finer grid showed that the means and second order statistics on both the finer and coarser grids differed by no more than five percent, indicating the runs can be performed on a coarser grid without significantly affecting the results of the tests.

The initial domain state was a fluid at rest with a two-layer temperature structure. The lower layer extended up to 400 meters and had a potential temperature that was constant with height. Within this layer, a random temperature perturbation with a standard deviation of 2 K was applied to initiate convection. Above this layer was the free atmospheric layer, whose potential temperature increased linearly with height. In order to test the equilibrium entrainment solutions over a wide range of atmospheric stratification, the vertical potential temperature gradient ranged from 0.001 K/m to 0.010 K/m, which is a range that is considered representative of its variability in the atmosphere.

Table 4.1. Parameters of LES for Test of Equilibrium Entrainment Regime

Parameter	**Setting**
Domain size	$5\times5\times4$ km^3
Grid	$50\times50\times200$ ($100\times100\times200$) also used for testing
Surface temperature flux	Q_s=0.3 Km/s (B_s=9.8×10^{-3} m^{2}s^{-2})
Temperature stratification above the CBL	$\partial\theta_v/\partial z$ varying in 0.001 K/m increments, ranging from 0.001 K/m to 0.010 K/m. (N ranging from 6×10^{-3} s^{-1} to 1.8×10^{-2} s^{-1})
Time step	Determined from a numerical stability constrant and was typical about 2 s.
Lateral boundary conditions	Periodic for all prognostic variables and pressure
Upper boundary conditions	Neumann with zero gradient. A sponge layer was imposed on the upper 20% of the model domain
Lower boundary conditions	No slip for velocity with local application of Monin-Obukhov similarity functions according to Fedorovich et al. (2001a), Neumann conditions for pressure, subgrid energy, and temperature.
Subgrid turbulence closure	1.5-order, TKE-based as per Deardorff (1980)

The simulation was started with a constant temperature flux through the bottom boundary, and the CBL was allowed to grow until the depth reached 2400 meters, or 60 percent of the model domain, at which point it was terminated in order to avoid effects from the entrainment zone impinging upon the sponge layer. Turbulence statistics were calculated every 200 time steps, with averaging performed over horizontal planes and over 100 time steps. Table 4.2 lists the statistics that were calculated in LES. These statistics were used to derive the ZOM and GSM parameters of entrainment.

Table 4.2. Statistics Calculated in LES

Order of Statistics	**Quantities calculated**
First order	$\overline{u}, \overline{v}, \overline{\theta}, \overline{E}$ (subgrid energy)
Second order	$\overline{u'^2}, \overline{v'^2}, \overline{w'^2}, \overline{\theta'^2}, \overline{E'^2}, \overline{w'\theta'}, \overline{w'u'}, \overline{w'v'}$
Third order	$\overline{w'w'w'}, \overline{\theta'\theta'\theta'}$

4.1.2 Retrieval of Parameters of Entrainment from LES

In order to make comparisons between LES data and the ZOM and GSM, the parameters of entrainment must be retrieved from LES in a manner consistent with their definitions within the model of study. In particular, the ZOM entrainment zone thickness is zero and, therefore, the jumps of buoyancy across the entrainment zone will be different from the full buoyancy change across the LES entrainment zone, which has a finite depth. This difference is a result of the smoothing of the upper interface, which could be due to the variability of the interface height or turbulent diffusion of the interface. Lilly (2002a) addressed the variability of the upper interface height, and his proposed coordinate transformation will be discussed further in Chapter 5.

Examples of LES profiles of potential temperature and heat flux, as well as the method of deriving the ZOM buoyancy jumps from them, are shown in Figure 4.1. The ZOM jump in potential temperature, $\Delta\theta_v$ is smaller than the change in potential temperature across the whole entrainment zone, $\delta\theta_v$. In order to retrieve $\Delta\theta_v$ from the LES data, the lower limit of the entrainment zone was identified by finding the lowest level at which the heat flux profile crosses zero (this height is defined as the lower limit of the entrainment zone, z_{il}), and the temperature at this level was taken as the mixed layer temperature. Then, the linear free atmosphere profile of θ_v was extrapolated down

to the level z_i to identify the potential temperature at the upper edge of the interface. The difference between these two temperatures was defined as $\Delta\theta_v$, and Δb is related to $\Delta\theta_v$ by the relation $\Delta b = \left(g/\theta_{v0}\right)\Delta\theta_v$.

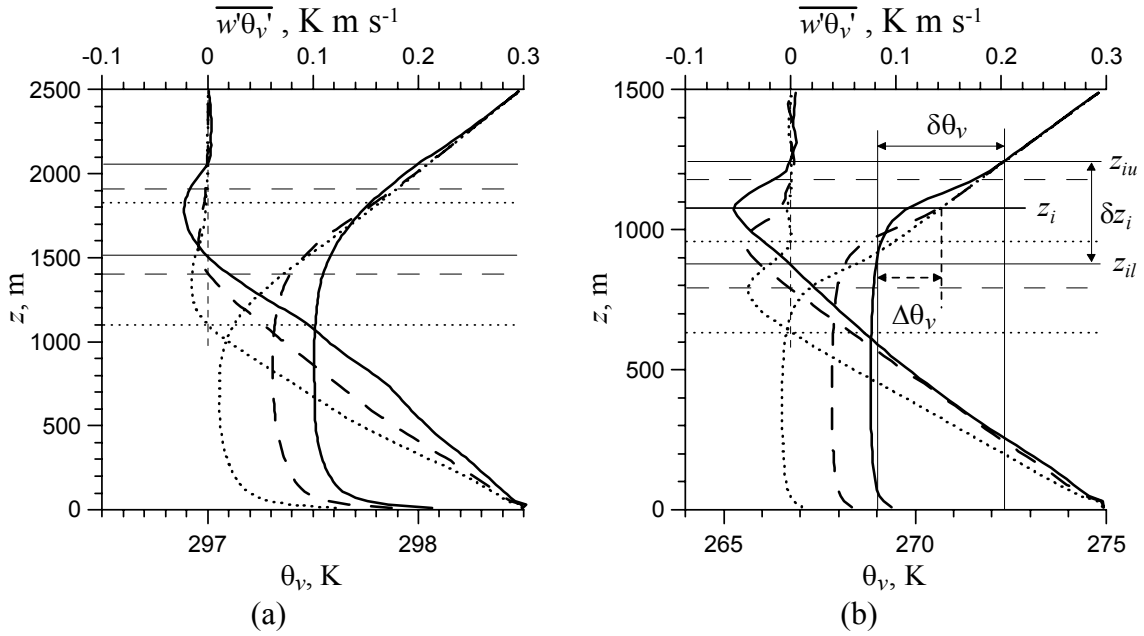

Figure 4.1: Examples of the turbulent heat flux and virtual potential temperature profiles obtained with LES for the cases of weak (a, $d\theta_v/dz = 0.001$ K m^{-1}) and strong (b, $d\theta_v/dz = 0.01$ K m^{-1}) free-atmosphere stratification. The order of profiles in time: dotted, dashed, and solid. Upper and lower interfaces of the entrainment zones are shown for each CBL evolution stage by straight lines of the corresponding style. The elapsed time between the profiles is of the order of 500 s in (a) and 25000 s in (b). Evaluation of bulk model variables from the simulated temperature and heat flux distributions is illustrated in (b) for profiles given by solid curves. See the text for notation.

The CBL depth z_i is defined as the vertical distance between the surface and the height at which the buoyancy flux reaches its minimum. Other methods also exist for finding z_i, such as finding the maximum temperature gradient at the top of the CBL, or lifting a parcel from the surface layer to its level of neutral buoyancy. However, Fedorovich et al. (2004a) find that the minimum heat flux is the most dynamically

relevant parameter, and it is consistent with the definition of CBL depth in the ZOM. The disadvantage of using the heat flux minimum is that it is highly variable in time for any finite LES domain. The maximum potential temperature gradient might be a suitable alternative definition, since its height varies much less, and it would also correspond with the level of the potential temperature jump in the ZOM (which is the same as the heat flux minimum), but the minimum heat flux and maximum temperature gradient do not correspond in LES. It also is inconsistent with the FOM. Although the FOM is not being evaluated here, the models can be evaluated in the most consistent manner by using a definition of z_i that works equally well within all models.

With the ZOM jumps and CBL depth defined in such a manner, the ZOM Richardson numbers can be calculated as $Ri_{\Delta b} = \Delta b z_i / w_*^2$ and $Ri_N = N^2 z_i^2 / w_*^2$. Also, the CBL depth and the buoyancy jump can be put in their dimensionless forms $\hat{z}_i$ and $\Delta\hat{b}$ using the definitions defined in Chapter 3 (Equations 3.45 and 3.46). Finally, the ZOM heat flux of entrainment was obtained by extrapolating the linear LES mixed layer heat flux profile upward from z_{il} to z_i. This was done because the LES profile curved smoothly in the entrainment zone, whereas the ZOM profile is linear between z_{il} and z_i, then jumps back to zero.

The GSM parameters of entrainment were retrieved using the full depth of the entrainment zone. The upper limit of the entrainment zone is typically defined as the level, above z_i, at which the heat flux profile first returns to zero or becomes reasonably close to zero. Because the value of zero was not always reached within the LES domain, the upper limit of the entrainment zone z_{iu} was defined as the level at which the heat flux

increased back to 10 percent of its minimum in the entrainment zone. For the GSM, the entrainment zone thickness was defined as $\delta z_i = z_{iu} - z_{il}$, the potential temperature jump was defined as $\delta\theta_v = \theta_v(z_{iu}) - \theta_v(z_{il})$, and the buoyancy jump was defined as $\delta b = \left(g / \theta_{v0}\right)\delta\theta_v$. The GSM Richardson number $Ri_{\delta b}$ was defined as $Ri_{\delta b} = \delta b z_i / w_*^2$.

4.2 Results of LES Shear-free Entrainment Experiments

Figure 4.2 shows the time dependency of the CBL depth. For $\hat{t} > 100$, the $\hat{z}_i$ values collapse to the predicted $\hat{t}^{1/2}$ relationship. Before $\hat{t} = 100$, the relationship is slightly different because the CBL is still sensitive to the initial conditions, such as the absence of TKE in the 400 meter mixed layer at the start of the run. Once these conditions are forgotten and the TKE has spun up, the values of CBL depth collapse to the ½ power law curve.

The value of C_1 is determined using (3.47), resulting in $C_1 = 0.17$, which is quite close to the commonly accepted value of 0.2. C_1 can also be determined using (3.44), which involves a direct estimation of $\Delta b\left(dz_i / dt\right) / B_s$ directly from LES data. Fedorovich and Conzemius (2001) obtained the same value using this method. It should be noted that there is a significant scatter in the estimates of Δb because of the variability of the CBL depth with time. These two methods provide the best estimate of the ZOM entrainment flux ratio, which, according to the LES data, is independent of *N*. This confirms the predicted constancy of the entrainment flux ratio in the simulated range of free atmospheric stratification.

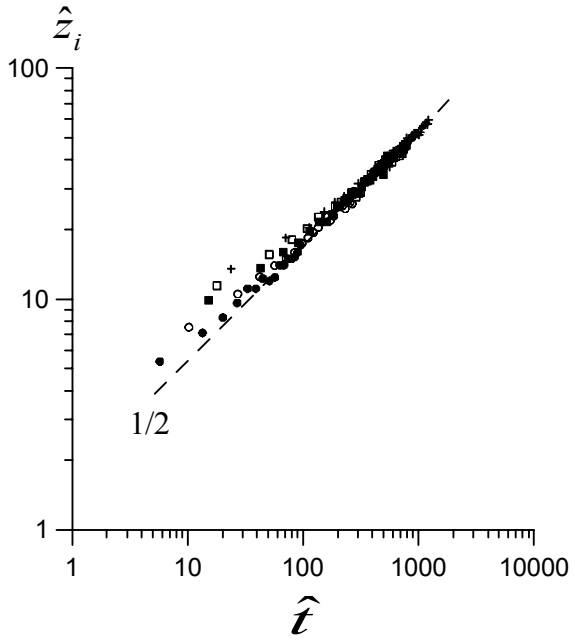

Figure 4.2: Dimensionless CBL depth as a function of dimensionless time. Different symbols correspond to different thermal stratifications in the free atmosphere: $d\theta_v / dz = 0.002$ K m^{-1} (N=0.008s^{-1}) - filled circles, $d\theta_v / dz = 0.004$ K m^{-1} (N=0.011s^{-1}) - open circles, $d\theta_v / dz = 0.006$ K m^{-1} (N=0.014s^{-1}) - filled squares, $d\theta_v / dz = 0.008$ K m^{-1} (N=0.016s^{-1}) - open squares, $d\theta_v / dz = 0.01$ K m^{-1} (N=0.018s^{-1}) - crosses. The dashed straight line indicates the universal ZOM solution for the constant-ratio entrainment regime, $\hat{z}_i = [2(1+2C_1)\hat{t}]^{1/2}$.

The actual ratio $\delta B_i / B_s$ from LES data, as seen in Figure 4.3, is somewhat different from the ZOM ratio and is dependent on N. For weaker stratification, the ratio is smaller, and for the strongest stratification studied, the ratio approaches the ZOM entrainment flux ratio of 0.2. These results are similar to those of Sorbjan (1996), who also performed an LES study on the effects of stratification on the parameters of entrainment, using a larger range of stratification than in the current study. Sorbjan found that the heat flux profiles were sharper when the stratification was stronger, and as is seen in the current study, the shapes of the heat flux profiles resemble the ZOM profile (see Fig. 3.1) more closely at stronger stratification. The differences between the ZOM

profile and the actual LES profiles have important implications for studying the effects of shear on CBL entrainment. Since entrainment of heat is common to both sheared and non-sheared CBLs, measuring the heat flux of entrainment may be the best way to compare the two. Therefore, it is critical to measure the heat flux of entrainment precisely and to fully understand its meaning with the framework of the model that is used for comparison. In particular, the discrepancy between the ZOM and LES entrainment flux ratios needs to be understood fully before a meaningful comparison can be made. This topic will be discussed further in Chapter 5.

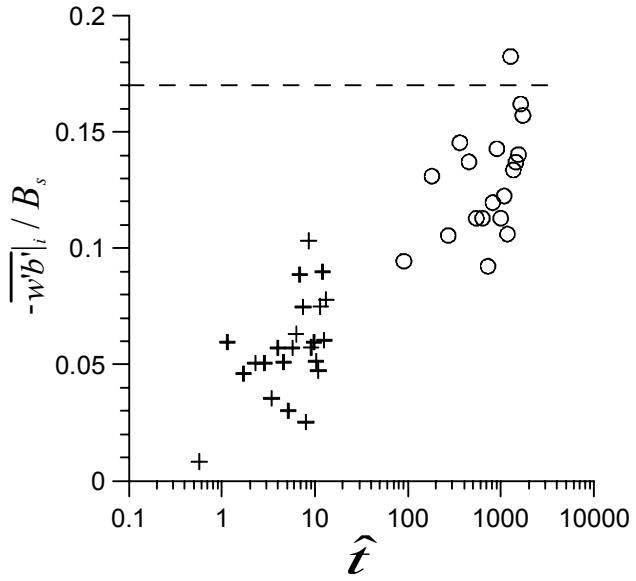

Figure 4.3: Ratio of the buoyancy flux, $\overline{w'b'}$, at $z=z_i$ to the surface buoyancy flux, B_s, as function of dimensionless time $\hat{t} = tN$ for two stratifications in the free atmosphere: weak, $d\theta_v / dz = 0.001$ K m^{-1} (N=0.006 s^{-1}), crosses, and strong, $d\theta_v / dz = 0.01$ K m^{-1} (N=0.018 s^{-1}), circles. The straight line corresponds to the ZOM estimate of the entrainment ratio $C_1 = \Delta b(dz_i / dt) / B_s$, (see Fig. 3.1).

The ZOM Richardson numbers $Ri_{\Delta b}$ and Ri_N can be written in terms of their dependence on time. Given the definition of $w_* = \left(B_s z_i\right)^{1/3}$ and the dependencies for z_i and Δb (3.47 and 3.48), it is easy to find that $Ri_{\Delta b} \sim Ri_N \sim \hat{t}^{2/3}$. These Richardson numbers then allow for an additional comparison between the ZOM predictions and the LES data.

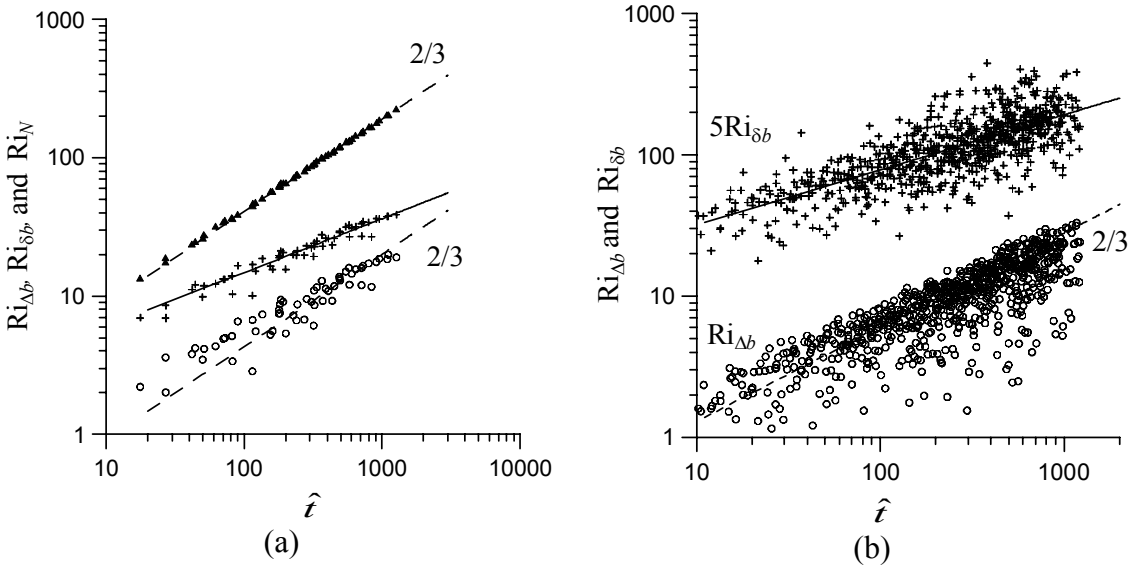

Figure 4.4: Richardson numbers $\mathrm{Ri}_{\Delta b}$ (circles), $\mathrm{Ri}_{\delta b}$ (crosses), and Ri_N (triangles) as functions of dimensionless time $\hat{t} = tN$ for $0.006\ \mathrm{s}^{-1} \le N \le 0.018\ \mathrm{s}^{-1}$ ($0.001\ \mathrm{K\ m}^{-1} \le d\theta_v / dz \le 0.01\ \mathrm{K\ m}^{-1}$) retrieved using approximated $z_i(t)$ curves (a) and original $z_i(t)$ data (b, only $\mathrm{Ri}_{\Delta b}$ and $\mathrm{Ri}_{\delta b}$ are shown). The dashed lines depict ZOM power-law predictions for $\mathrm{Ri}_{\Delta b}(\hat{t})$ and $\mathrm{Ri}_N(\hat{t})$. The solid lines correspond to the 0.39 exponent, which is the best fit for the $\mathrm{Ri}_{\delta b}(\hat{t})$ data in (b).

Additionally, the GSM Richardson number, $Ri_{\delta b}$, allows for easy comparison with the water tank data of Deardorff et al. (1969, 1980) and Deardorff and Willis (1985) since $Ri_{\delta b}$ calculations were also performed on those data. All three Richardson numbers retrieved from LES data are shown in Figure 4.4. Because of the large scatter of the z_i,

Δb, and δb estimates (due to the variability of the heat flux profile) that are used for the Richardson number determinations, the plots of these variables as a function of time were subjected to a polynomial fit before being presented in Figure 4.4a. These fitted data correspond very well to the 2/3 power law predicted by the ZOM for $Ri_{\Delta b}$ and Ri_N. The raw, unfitted data are shown in Figure 4.4b for comparison, and these data also roughly follow the 2/3 power law.

The GSM Richardson number is dependent on the determination of the upper and lower limits of the entrainment zone as well as the CBL top, and the ZOM Richardson numbers are dependent on the determination of CBL top and the lower limit of the entrainment zone. The time dependencies of z_{il}, z_i, and z_{iu} are plotted Figure 4.5. It is remarkable that both z_{il} and z_i vary quite synchronously in time. The zero crossing and the minimum of the heat flux both grow according to $\hat{t}^{1/2}$, as would be expected for a ZOM profile that remains linear with a constant entrainment flux ratio. It is not necessarily expected for the more curved entrainment zone heat flux profiles of LES. Unlike z_{il} and z_i, the upper entrainment zone limit z_{iu} grows a little more slowly than $\hat{t}^{1/2}$. In many of the simulations, the heat flux profile is seen to start out with a very deep area of weakly negative heat flux, but it becomes more ZOM-like in time. In order for this to happen, z_{iu} must grow more slowly than z_i and z_{il}, as seen in the data. As the CBL grows, the strengthening stratification in the entrainment zone appears to retard the penetration of thermals into the upper limits of the entrainment zone. When the free atmospheric stratification is stronger, the entrainment zone is also shallower with a more ZOM-like heat flux profile. This result implies that the buoyancy profile in the entrainment zone is not always self-similar, as is assumed in the GSM, but it depends on

N and t. Since the ZOM $Ri_{\Delta b}$ is independent of z_{iu}, it has exactly the predicted $\hat{t}^{2/3}$ dependence. Because z_{iu} grows more slowly, $Ri_{\delta b}$ has a smaller exponent in its time dependence of $Ri_{\delta b} \sim \hat{t}^{0.39}$.

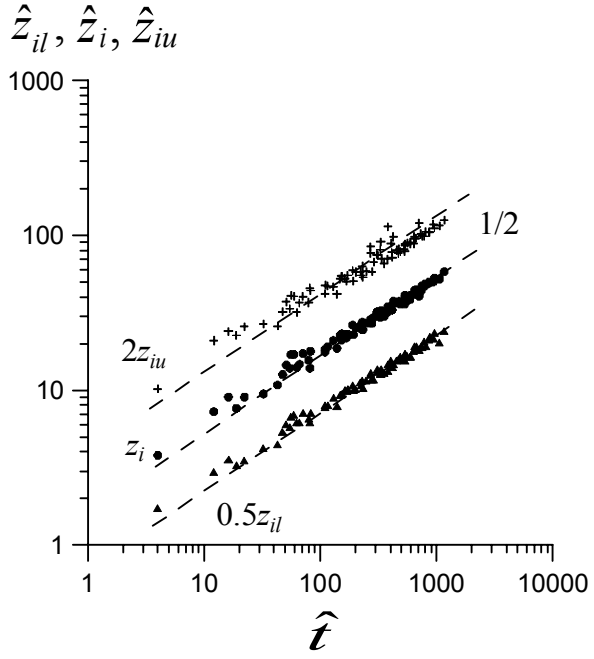

Figure 4.5: Normalized heights of the lower ($\hat{z}_{il} = z_{il} B_s^{-1/2} N^{3/2}$, triangles) and upper ($\hat{z}_{iu} = z_{iu} B_s^{-1/2} N^{3/2}$, crosses) interfaces of the entrainment zone, and the CBL depths $\hat{z}_i = z_i B_s^{-1/2} N^{3/2}$ (circles) as functions of dimensionless time $\hat{t} = tN$ for $0.006\ \text{s}^{-1} \le N \le 0.018\ \text{s}^{-1}$ ($0.001\ \text{K m}^{-1} \le d\theta_v / dz \le 0.01\ \text{K m}^{-1}$). Straight lines correspond to 1/2 power laws.

If the entrainment rate dz_i / dt is scaled by w_*, we have the nondimensional entrainment rate:

$$E = \frac{1}{w_*} \frac{dz_i}{dt} \tag{4.1}$$

Direct comparisons with the water tank data of Deardorff et al. (1980) and the atmospheric data of Nelson et al. (1989) can be made if E and $Ri_{\delta b}$ are calculated.

Additionally, the data from LES runs with different free atmosphere stratification and surface heat flux can be put on the same curve when the nondimensional numbers E and $Ri_{\delta b}$ are found. The GSM-based dependencies $\delta z_i / z_i$ versus E, $\delta z_i / z_i$ versus $Ri_{\delta b}$, and E versus $Ri_{\delta b}$ can be found and compared to water tank and atmospheric data. Additionally, the dependences E versus Ri_N and $Ri_{\Delta b}$ can be tested against their ZOM-predicted relationships.

Using the definitions of the Richardson numbers and the dimensionless entrainment rate, we have:

$$E = \frac{1}{w_*}\frac{dz_i}{dt} = \hat{z}_i^{-1/3}\frac{d\hat{z}_i}{dt} \propto \hat{t}^{-2/3} \tag{4.2}$$

$$Ri_{\Delta b} = \frac{\Delta b z_i}{w_*^2} = \Delta\hat{b}\hat{z}_i^{1/3} \propto \hat{t}^{2/3} \tag{4.3}$$

$$Ri_N = \frac{N^2 z_i^2}{w_*^2} = \hat{z}_i^{4/3} \propto \hat{t}^{2/3} \tag{4.4}$$

Given these relationships, we have the following ZOM-predicted relationships:

$$E \propto Ri_{\Delta b}^{-1} \propto Ri_N^{-1} \tag{4.5}$$

Figure 4.6 shows the dependencies of E on the three Richardson numbers. E has the ZOM-predicted dependency on $Ri_{\Delta b}$ and Ri_N. Some noise appears in the dependency on $Ri_{\Delta b}$ since the relationship requires the retrieval of Δb and z_i, both of which exhibit some scatter. The E dependency on $Ri_{\delta b}$ is somewhat different because of the aforementioned departure of z_{iu} from the $\hat{t}^{1/2}$ curve.

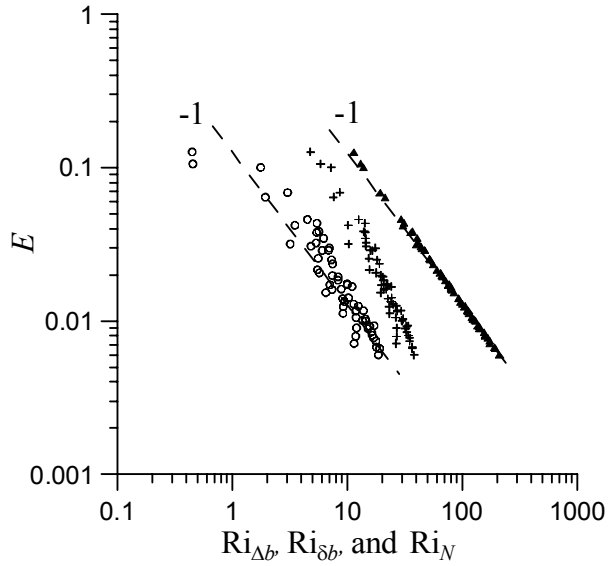

Figure 4.6: Relationships between the dimensionless entrainment rate E and Richardson numbers $\mathrm{Ri}_{\Delta b}$ (circles), $\mathrm{Ri}_{\delta b}$ (crosses), and Ri_N (triangles) derived from LES for $0.006\ \mathrm{s}^{-1} \le N \le 0.018\ \mathrm{s}^{-1}$ ($0.001\ \mathrm{K\ m}^{-1} \le d\theta_v / dz \le 0.01\ \mathrm{K\ m}^{-1}$). The -1 power-law lines show ZOM relationships (see Equation 4.5) between E, $\mathrm{Ri}_{\Delta b}$, and Ri_N.

The relationship between E and $Ri_{\delta b}$ in all ten LES cases is explored further and compared with the water tank data of Deardorff et al. (1980) in Figure 4.7. In doing so, the parameters δz_i and δb have been defined in this study as closely as possible to their definitions in Deardorff et al. (1980). The GSM predictions of this dependency are also plotted on Fig. 4.7 for five different values of the free atmospheric buoyancy gradient used in LES: $N = 0.008 s^{-1}$, $N = 0.011 s^{-1}$, $N = 0.014 s^{-1}$, $N = 0.016 s^{-1}$, and $N = 0.018 s^{-1}$. All five GSM predictions collapse onto the same curve for $Ri_{\delta b} > 4$. The LES data also show quite good agreement with the GSM predictions, showing an approximate $E \propto Ri_{\delta b}^{-3/2}$ relationship.

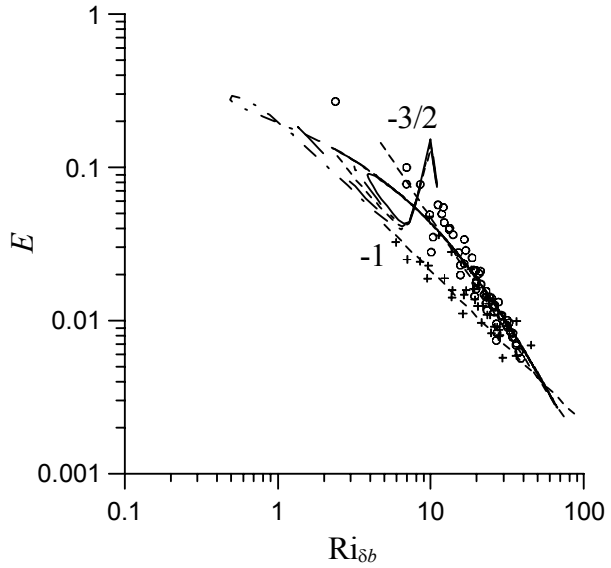

Figure 4.7: Dimensionless entrainment rate E as a function of $\mathrm{Ri}_{\delta b}$. Curves present calculations based on the GSM model of Fedorovich and Mironov (1995) with C_N=0.007 for different N values in the free atmosphere: N=0.008s^{-1} - dashed and dotted line, N=0.011s^{-1} - long-dash line, N=0.014s^{-1} - short-dash line, N=0.016s^{-1} - dashed and double dotted lone, and N=0.018s^{-1} - solid line. The LES data for the stratification range 0.006 s^{-1}≤N≤0.018 s^{-1} ($0.001\ \mathrm{K\ m^{-1}} \le d\theta_v/dz \le 0.01\ \mathrm{K\ m^{-1}}$) are shown by circles. Water tank data of Deardorff et al. (1980) are presented by crosses. Short-dash straight lines present the -1 and $-3/2$ power laws discussed in Deardorff et al. (1980) and Zilitinkevich (1991).

In the GSM, a parameterization is included to model the effects of energy loss due to gravity waves radiating from the CBL top. In particular, the parameterization of Zilitinkevitch $2\Phi_i/(B_s z_i) = C_N Ri_N^{3/2}(\delta z_i/z_{il})^3$ was used. It must be noted with regard to this figure that the value of C_N had to be taken unrealistically small for the GSM to fit the LES data as shown in the figure. This suggests a weakness in the GSM.

Although the LES-derived relationship between E and $Ri_{\delta b}$ is $E \propto Ri_{\delta b}^{-3/2}$, the water tank data appears to match the $E \propto Ri_{\delta b}^{-1}$ relationship more closely. Interestingly Deardorff et al. (1980) also considered the $E \propto Ri_{\delta b}^{-3/2}$ relationship, and the same

relationship was also observed and discussed by Turner (1968, 1973). Zilitinkevitch (1991) suggested that the relationship follows $E \propto Ri_{\delta b}^{-1}$ in more weakly stratified fluids and is closer to $E \propto Ri_{\delta b}^{-2}$ in very strongly stratified fluids. Given the LES results are in this range, and given the scatter that exists in both the LES and water tank data, it can be said that LES and water tank data agree reasonably well in general, although the apparent power law discrepancy is of some concern. It may be mostly due to the scatter in the estimates of these dimensionless quantities.

An additional comparison between LES, the GSM, and atmospheric data can be found by plotting $\delta z_i / z_i$ versus E and $\delta z_i / z_i$ versus $Ri_{\delta b}$ (Fig. 4.8). The GSM shows a dependence that changes with time and ends up between the -1/2 and -1 power law. The LES and water tank data overlap to a considerable extent and show a dependence somewhere between the -1/2 power law suggested by Boers (1989), based on atmospheric data, and the -1 dependence suggested by Deardorff et al. (1980) and predicted by the Zilitinkevitch and Mironov (1992) model. The most significant difference between the LES and laboratory data is that the laboratory $\delta z_i / z_i$ values are a little smaller than those of LES. It is likely that this difference is due to the uncertainty in the estimate of the upper limit of the entrainment zone. In the water tank study of Deardorff (1980), the upper limit was defined as the level "beyond which the buoyancy flux and its vertical derivative remain vanishingly small". In the LES data, we took the upper limit to be the level at which the heat flux dropped to 10 percent of the heat flux minimum. Given that the heat flux minimum returned very slowly to zero in some cases, it is evident that the determination of $\delta z_i / z_i$ vs highly sensitive to the precise definition

of the upper interface height. In this particular case, there is a fair bit of room for subjectivity between the LES and Deardorff et al. (1980) definitions.

The same discrepancy is noted in Figure 4.9. Both the LES and water tank data, however, follow the same trend and are follow a $\delta z_i / z_i \propto E^m$ relationship, where m is fairly close to ¼. This lies within the range of m values considered by Nelson et al. (1989) in their analysis of atmospheric lidar data. Thus, within the range of uncertainty, the agreement among LES, atmospheric, and laboratory data seems to be reasonably good.

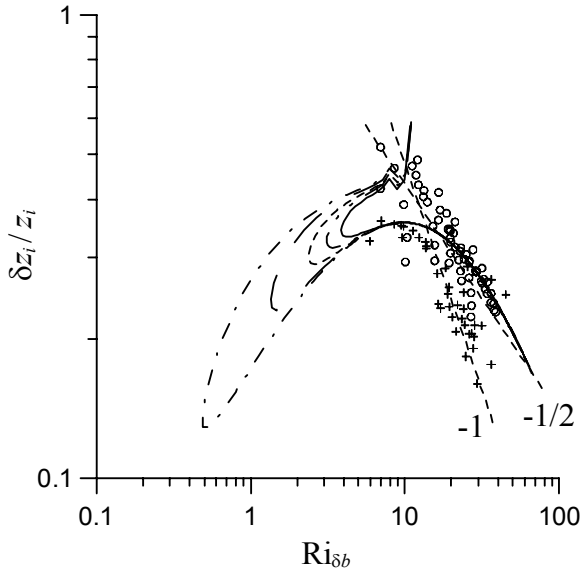

Figure 4.8: Relative entrainment layer depth $\delta z_i / z_i = (z_{iu} - z_{il}) / z_i$ as a function of $\mathrm{Ri}_{\delta b}$. For notation, see Fig. 4.7. Short-dash straight lines present the $-1/2$ power law obtained by Boers (1989) from the analysis of atmospheric data and the -1 power law suggested by Deardorff et al. (1980) based on the laboratory data and predicted by the Zilitinkevich and Mironov (1992) model.

Finally, one important GSM parameter that may be of potential use in the analysis of sheared CBL data is the relative stratification, defined as

$$G = N^2 \frac{\delta z_i}{\delta b},$$

or, the ratio of the free atmospheric buoyancy gradient to the entrainment zone bulk buoyancy gradient. Evaluation of this parameter from LES data show that for the equilibrium entrainment regime, the value of the parameter approaches $G = 1.2$ at large $\hat{t}$.

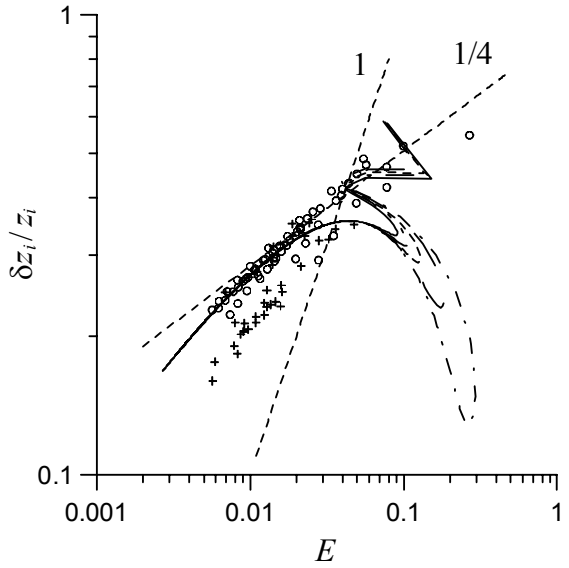

Figure 4.9: Relative entrainment layer depth $\delta z_i / z_i = (z_{iu} - z_{il}) / z_i$ as a function of the dimensionless entrainment rate E. For notation, see Fig. 4.7. Short-dash straight lines correspond to the smallest, $1/4$, and largest, 1, values from the exponent range considered in Nelson et al. (1989) for conditions of equilibrium entrainment in the atmosphere.

4.3 Summary of Shear-Free LES Experiments

In summary, the study of Fedorovich et al. (2004a) reached several important conclusions with regard to the current study, which will look more specifically at sheared CBLs:

1) Fedorovich et al. established LES as a reasonable tool for the study of entrainment, as the LES results are generally comparable with water tank and atmospheric data.
2) The ZOM-based entrainment equations work reasonably well to predict the Δb and z_i dependencies on time in the entraining, shear-free CBL, despite the differences between LES and ZOM profiles of heat flux. The time-dependency of

Δb was seen via the $Ri_{\Delta b}$ dependency that was analyzed. The analyzed dependencies are a rather interesting result and a testament to the robustness of the ZOM in the shear-free case, making it a potential tool for the study of the sheared CBL.

3) The GSM entrainment predictions also work reasonably well, but for the GSM, some discrepancies are encountered in the upper portion of the entrainment zone between LES data and the GSM. The upper limit of the LES entrainment zone z_{iu} grows more slowly, relative to the CBL depth z_i and the lower limit of the entrainment zone z_{il}, as time proceeds in the simulations, and the buoyancy flux profile becomes more ZOM-like as the simulation proceeds. This contradicts the assertion of Haegeli et al. (2000), which states that $-B_i / B_s = \delta z_i /(2z_i - \delta z_i)$. Since the value of C_N in the gravity wave loss parameterization had to be taken very small for the GSM to be agreeable with the LES results, it appears the slow growth of z_{iu} relative to z_i may be more the result of damping of entrainment zone growth by the strong stratification later in any LES run rather than being the result of a loss of energy due to the radiation by gravity waves. In this regard, the CBL entrainment may be slower to forget initial conditions than earlier thought. The simpler ZOM does not include z_{iu} and is therefore unaffected by this problem. However, because of the need to be very careful about evaluating the ZOM-defined buoyancy jump at the CBL top (Δb), the ZOM does not lend itself as easily to comparison with water tank and atmospheric data as does the GSM.

4) Finally, the study of Fedorovich et al. (2004a) established a solid reference for the values and dependencies of parameters of entrainment in the shear-free case and can serve as a good basis for comparison with LES of sheared CBLs. In particular, the ZOM-defined entrainment flux ratio is consistently around 0.2, regardless of atmospheric stratification. This ratio may therefore provide the most direct comparison between sheared and shear-free CBLs, since the entrainment of heat, unlike the entrainment of momentum, is common to both CBL types. Also, the interdependencies of the Richardson numbers $Ri_{\delta b}$, $Ri_{\Delta b}$, and Ri_N, the relative entrainment zone thickness $\delta z_i / z_i$, dimensionless entrainment E, and dimensionless time $\hat{t}$ may serve as a basis for comparison with sheared CBLs, although there is some uncertainty with the exact interdependencies among $\delta z_i / z_i$, $Ri_{\delta b}$, and $\hat{t}$ (GSM). The most direct comparison is with the entrainment flux ratio.

Since the entrainment flux ratio is most critical to the comparison between sheared and shear-free CBLs, it is necessary to examine its meaning a bit further since the reasons for its difference between ZOM and LES are still not perfectly clear. Chapter 5 will make further efforts to resolve this issue.

Chapter 5

Entrainment Flux Ratios

5.1 ZOM versus LES Entrainment Flux Ratios

The entrainment flux ratio was defined in Chapter 1 as the ratio of the negative of the buoyancy flux minimum in the entrainment zone to the surface buoyancy flux. As discussed in Chapter 4 and in Lilly (2002a), the entrainment flux ratio is a bit different between the ZOM and LES. In the ZOM, (3.36) and (3.46) show that $C_1 = \Delta b(dz_i/dt)/B_s$, but if the ratio is evaluated directly from the LES profiles, it is $-\delta B_i / B_s$. These differences are shown in Fig. 3.1.

Chapter 4 also noted that there are two methods for retrieving the ZOM entrainment flux ratio from LES data, one of which is to directly evaluate $\Delta b(dz_i/dt)/B_s$, with Δb retrieved from LES data in a manner consistent with its definition in the ZOM and dz_i/dt estimated from the plots of z_i versus t from LES, and the other was to use (3.47). Another method evaluated in that study, but not mentioned in Chapter 4 or Fedorovich (2004a), is to extrapolate the LES buoyancy flux profile from the surface, through its heat flux zero-crossing, to the level of the buoyancy flux minimum.

The first of these two retrievals is the most consistent with (3.36) and (3.46), but it is complicated by the variability of the heat flux profile, which makes a direct estimate of

the CBL growth rate (dz_i / dt) from LES data rather difficult. (This can be seen by looking ahead to Figure 5.4, which shows that $dz_i / dt < 0$ locally.) In order to separate the effects of this variability from the CBL growth, it is usually necessary to perform a local linear least squares fit on the z_i versus t plot from LES, particularly when statistics are calculated on time intervals less than the convective time scale (on the order of 1000s for typical CBLs). If the CBL is not in an equilibrium entrainment regime, which may well be the case with shear, it is important to see how the entrainment flux ratio varies during the simulation, but the least squares technique filters some of this variability. This fact provides motivation for finding another technique to retrieve the ZOM entrainment flux ratio from LES data, and it also makes it tempting to define z_i by some other method, such as the maximum temperature gradient.

The extrapolation technique of finding C_1 seems to work rather well, but the direct relationship between the extrapolated buoyancy flux profile and $\Delta b(dz_i / dt) / B_s$ is more tenuous. Indeed, the technique retrieves a sharp, ZOM-like entrainment heat flux from LES, but it seems to be more graphical than quantitative. Quantitative and more defendable methods are needed to compare sheared CBLs with shear-free CBLs.

Using the ZOM to analyze shear-free CBLs places them in a framework that allows them to be more easily compared with sheared CBLs, precisely because it shows the entrainment flux ratio to consistently be 0.2 for entraining shear-free CBLs, regardless of atmospheric stratification. This provides motivation for remaining within the ZOM framework. However, the difference between the ZOM and LES entrainment flux ratios raises the following questions:

1) What is the meaning of the entrainment flux ratio of 0.2?

2) If the entrainment flux ratio, evaluated directly from the heat flux minimum and surface heat flux in LES, is almost always less than 0.2, then how does the ZOM solution with $C_1 = 0.2$ work so well for modeling shear-free CBL growth in LES? It seems that it should overpredict the entrainment rate of simulated CBLs.
3) Can either of these be considered the *better* entrainment flux ratio (i.e. which is more relevant with regard to the fate of TKE in terms of dissipation versus consumption by entrainment)?
4) Can the same ratio be retrieved when using a smoother method of z_i retrieval, such as the maximum temperature gradient?

These questions have been around for some time (e.g. Manins and Turner 1978). Lilly (2002a) has tried to explain the ZOM/LES discrepancy by proposing that the horizontally averaged heat flux profiles from LES and atmospheric data are actually a result of the local variability of the height of the interface between the CBL and the free atmosphere. *Locally*, this interface should be sharp, and the profiles of buoyancy and buoyancy flux should resemble their ZOM counterparts. If this is true, the profiles of LES can then be modeled using the ZOM profile, combined with a probability distribution function of the upper interface height, assuming the level of the interface height has a Gaussian distribution. Within any CBL with this type of variable interface height, the ZOM profiles should be retrievable if a coordinate transformation is first performed by normalizing the height coordinate by the local interface height and then performing the horizontal averaging in this new coordinate system, which he uses in a new CBL closure (Lilly 2002b).

Unfortunately, testing these ideas with the LES data was not terribly fruitful. When the coordinate transformation was attempted, the heat flux profile appeared to sharpen slightly for LES runs with the largest stratification in the free atmosphere, but the profiles were still not very ZOM-like, and some numerical artifacts were also seen in the heat flux profile. Lilly (personal communication) suggested that the inability of LES to reproduce the ZOM profiles might have to do with numerical artifacts of LES: the finite grid cell size and the mixing effects of the subgrid model limit the ability of LES to resolve a sharp interface. Lilly (2002a) mentions the idea of performing LES within the normalized coordinate system, but this would require a considerable modification of the current code. Additionally, atmospheric lidar data (Kiemle et al. 1995; Davis et al. 2000) show that the upper interface height isn't necessarily sharp everywhere. At the tops of plumes, where local deformation enhances gradients of water vapor, potential temperature, and aerosols, the interface appears sharp on the lidar data, but in between rising plumes, where the air is slowly descending, the interface becomes considerably more diffuse. Additionally, one might not expect such a sharp interface in the presence of shear, which would likely generate Kelvin-Helmholtz type instabilities that would turbulently diffuse the interface.

It seems worthwhile to test some other ideas to retrieve the ZOM entrainment heat flux from LES data. One idea is to use the ratio of the negative and positive areas of the heat flux profile. For the ZOM with an entrainment flux ratio of C_1, the zero crossing height of the heat flux profile occurs at $z = z_i/(1+C_1)$. Therefore, the z_i-normalized heat flux profile is:

$$\frac{\overline{w'b'}(z)}{B_s} = \left(1 - \frac{z}{z_i}\right) - \frac{\Delta b \frac{dz_i}{dt}}{B_s} \frac{z}{z_i} = 1 - \left(1 + C_1\right) \frac{z}{z_i} . \tag{5.1}$$

Integrating this over the depth of positive heat flux yields the positive area:

$$A_P = \int_0^{z_i/(1+C_1)} \left[1 - \left(1 + C_1\right) \frac{z}{z_i}\right] dz = \frac{z_i}{2\left(1 + C_1\right)} . \tag{5.2}$$

The negative area is

$$A_N = -\int_{z_i/(1+C_1)}^{z_i} \left[1 - \left(1 + C_1\right) \frac{z}{z_i}\right] dz = \frac{C_1^2 z_i}{2\left(1 + C_1\right)} . \tag{5.3}$$

Taking the ratio and solving for C_1 yields:

$$C_1 = \sqrt{\frac{A_N}{A_P}} \tag{5.4}$$

The same can be done with the LES profiles. If the integral heat flux is the same in the LES profile as it is in the ZOM, one can then retrieve the ZOM entrainment flux ratio $\left(\Delta b dz_i / dt\right) / B_s$ from a single, horizontally averaged, LES heat flux profile. Using this ratio follows the Eulerian partitioning ideas of Van Zanten et al. (1999).

Tests show that C_1 is about 10 percent higher using this method than when using the direct estimate $\left(\Delta b dz_i / dt\right) / B_s$ from LES. Nevertheless, C_1 evaluated from (5.4) is essentially constant with time when the equilibrium entrainment regime is reached in the shear-free CBL, and it is independent of *N*. Thinking about this further, there really is no physical reason for the actual negative and positive areas in the heat flux profile to be exactly the same as they are the ZOM profile, but if the ideas presented in Lilly (2002a) are exactly true, then they should be.

The alternative method of estimating C_1 is the heat flux extrapolation technique mentioned above. This may seem like a less quantitative method, but it provides a closer match to $\left(\Delta bdz_i / dt\right) / B_s$. This C_1 estimate is also constant with time and independent of N in entraining CBLs, suggesting it may be the best estimate of $\left(\Delta bdz_i / dt\right) / B_s$ that one can obtain from an individual profile. Figure 5-1 shows the results of using these two methods of estimating C_1 from the individual profile and compares them to the direct estimate of $C_1 = \left(\Delta bdz_i / dt\right) / B_s$. As can be seen in this figure, the heat flux extrapolation matches $\left(\Delta bdz_i / dt\right) / B_s$ more closely. However, given the relative noise in both these estimates, they are, for most practical purposes, essentially the same.

5.2 Bulk Model Experiments

These results still do not explain whether the difference between the ZOM and LES entrainment flux ratios is due to the variability of the upper interface height as in Lilly (2002a) or if the ZOM entrainment flux ratio simply does not apply to the real CBL, making the LES ratio the best to use. This matter might be settled by performing some experiments with higher order analytic profiles of heat flux and buoyancy and relating them to the ZOM profiles. After performing these experiments, one might be able to understand why the extrapolation method works as well as it does (compared to a more quantitative method such as the Eulerian partitioning method), and why the LES entrainment flux ratio is different from the ZOM ratio, despite the fact that the latter predicts $z_i(t)$ in LES so well.

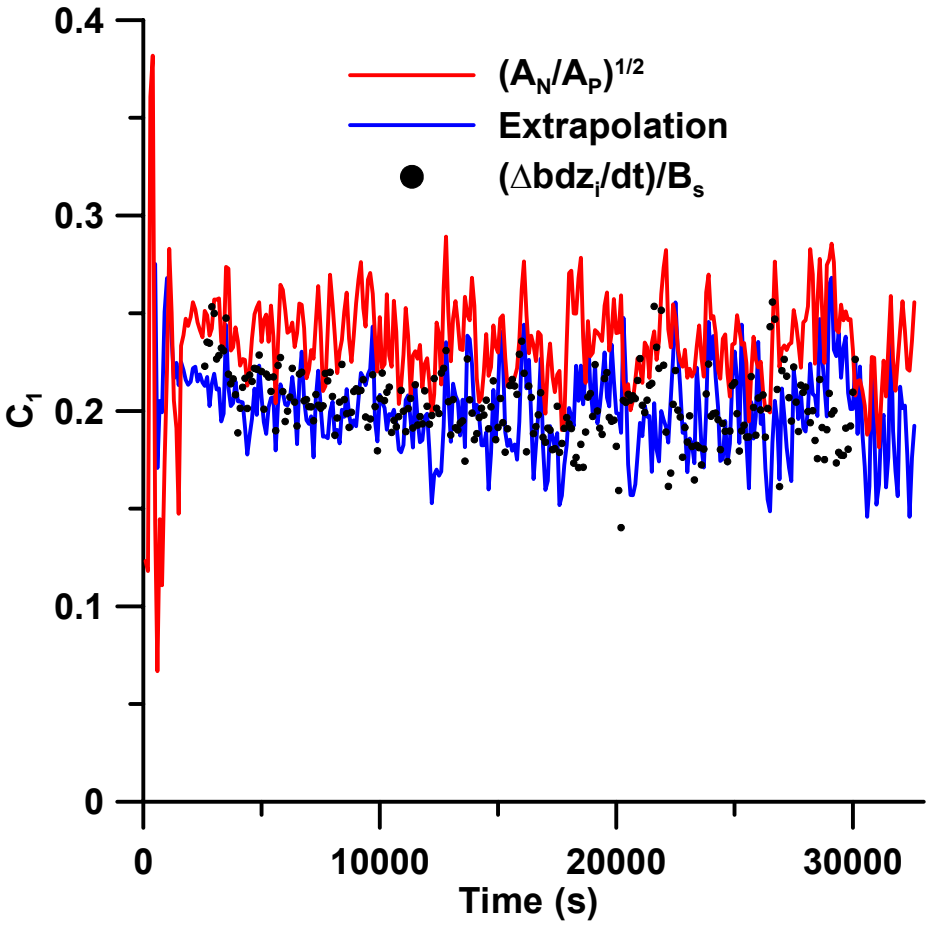

Figure 5.1: Comparison of the methods to determine the ZOM entrainment flux ratio from LES. The red line shows the area integral method, the blue line refers to the heat flux extrapolation method, and the black dots show the direct estimate.

The experiment is designed to quantify the differences among the profiles of buoyancy and buoyancy flux in the ZOM, higher order analytic models, and LES, requiring the equality of integral heat content between the ZOM profile and any higher order profile. The underlying base CBL growth rate is assumed to be the ZOM growth rate for all cases, with the CBL depth defined by the minimum of heat flux. For the basic case, we use an entrainment regime with a surface potential temperature flux of 0.3 Km/s, a potential temperature stratification of 0.010 K/m, and a ZOM entrainment flux ratio of 0.2. The actual values of N and B_s are not important in the models because the equations

are scaled, but they are important for direct comparisons with the simulations. We will start with the simplest models and proceed upward in complexity until a model is found that has a smaller entrainment flux ratio than the ZOM, but dz_i/dt is the same.

The unscaled ZOM equations for z_i versus t and Δb versus t in the equilibrium regime are:

$$z_i = B_s^{1/2} N^{-1} \left[2\left(1+2C_1\right)t \right]^{1/2} \tag{5.5}$$

$$\Delta b = B_s^{1/2} N \left[2t/\left(1+2C_1\right) \right]^{1/2} \tag{5.6}$$

These serve as the basic equations for z_i and Δb, against which the higher order models will be compared.

5.2.1 First Order Model

For the higher order models, we begin with the FOM. For the comparison to be quantitative, we require the integral heat content to be the same between the ZOM and FOM. In the FOM, the entrainment zone is a layer of finite depth with a linear buoyancy profile. The heat flux divergence in this layer is positive, which removes buoyancy from the base state profile. This loss must be compensated by a buoyancy gain in the mixed layer in order for the integral of buoyancy to be conserved. This condition can be stated mathematically:

$$-\int_{z_i}^{z_i+\Delta z} \left(b_{FOM} - b_{ZOM}\right) dz = \int_{0}^{z_i} \left(b_{FOM} - b_{ZOM}\right) dz \tag{5.7}$$

Integrating these expressions using the linear buoyancy profile of the FOM provides the following expression relating the FOM buoyancy change across the entrainment zone to the ZOM buoyancy jump:

$$\Delta b_1 = \Delta b_0 \left(1 + \frac{\Delta z}{2z_i}\right)^{-1} + N^2 \Delta z \,, \tag{5.8}$$

where the first term on the right hand side represents a decrease in Δb_1 (relative to Δb_0) due to the warmer mixed layer, and the second term represents the increase due to a deeper entrainment zone. The expression for FOM mixed layer buoyancy, which, as in the ZOM, is constant with height, is:

$$b_{m1} = b_s + N^2 \left(z_i + \Delta z\right) - \Delta b_1 = b_s + N^2 z_i - \Delta b_0 \left(1 + \frac{\Delta z}{2z_i}\right)^{-1}, \tag{5.9}$$

where Δb_0 and Δb_1 are the ZOM and FOM values for buoyancy jump across the entrainment zone, Δz is the finite entrainment zone depth, and b_s is a constant surface base state buoyancy that would result from the extrapolation of the free atmospheric profile to the surface. Equation (5.9) is similar to the ZOM condition for mixed layer buoyancy, but because the last term on the right hand side is smaller than Δb_0, the mixed layer buoyancy is greater than it is in the ZOM. In the entrainment zone, the buoyancy as a function of height is:

$$b_1 = b_s + N^2 z + \Delta b_0 X^{-1} \left[\frac{z - z_i}{\Delta z} - 1\right], \tag{5.10}$$

where $X^{-1} = \left(1 + \frac{\Delta z}{2z_i}\right)^{-1}$.

The buoyancy flux profiles can be calculated by taking the time derivative of (5.10) and integrating the buoyancy balance equation, $\partial b / \partial t = -\partial B / \partial z$, upward from the surface to the top of the mixed layer, keeping in mind that the quantities z_i, Δb_0, and Δz are time-dependent. The profile is linear in the mixed layer and extends to its minimum, which is located at z_i and has the value

$$B(z_i) = B_s - z_i \left[N^2 \frac{dz_i}{dt} - \frac{d}{dt}\left(\Delta b_0 X^{-1}\right) \right]. \tag{5.11}$$

The buoyancy flux profile in the entrainment zone is:

$$B(z > z_i) = B(z_i) + \left[\frac{d}{dt}\left(\Delta b_0 X^{-1}\right) + \frac{\Delta b_0 X^{-1}}{\Delta z} \frac{dz_i}{dt} \right]\left(z - z_i\right) - \frac{d}{dt}\left(\frac{\Delta b_0 X^{-1}}{\Delta z} \right) \frac{\left(z - z_i\right)^2}{2}. \tag{5.12}$$

These FOM equations for buoyancy and buoyancy flux are now written in terms of their ZOM counterparts and the finite entrainment zone thickness Δz. The only remaining item is to make some assumption about the finite entrainment zone depth as a function of time. To avoid making the analysis more complicated than is absolutely necessary, we assume $\Delta z = 0.2 z_i$, giving the following expression for the heat flux minimum:

$$B(z_i) = B_s - z_i \left[N^2 \frac{dz_i}{dt} - \left(1 + \frac{\Delta z}{2 z_i} \right)^{-1} \frac{d \Delta b_0}{dt} \right] \tag{5.13}$$

This produces an entrainment flux ratio, $-B_i / B_s$, of 0.22, which is constant in time but 10% greater than the ZOM ratio. Because the mixed layer temperature is warmer in the FOM than in the ZOM, more heat must be mixed downward to achieve the higher temperature. Therefore, the FOM cannot explain the smaller entrainment flux ratio in the LES profiles.

5.2.2 Second Order Model

We next shift to a second order model (SOM) in the entrainment zone and relate the SOM equations to the ZOM equations. Where the SOM parameters of entrainment differ from their counterparts in the ZOM or FOM, they are denoted by the subscript "2" to show they are specific to the SOM. The following conditions exist for buoyancy:

$$\begin{aligned} b &= b_s + N^2\left(z+\Delta z_2\right) - \Delta b_2 \quad && z = z_i \\ b &= b_s + N^2\left(z+\Delta z_2\right) && z = z_i + \Delta z_2 \\ \frac{\partial b}{\partial z} &= N^2 && z = z_i \end{aligned} \tag{5.14}$$

The third condition prevents the heat flux minimum from occurring at a level above z_i. The buoyancy profile in the entrainment zone is

$$b_2 = b_s - \Delta b_2 + N^2\left(z+\Delta z_2\right) + \frac{\Delta b_2 - N^2\Delta z_2}{\Delta z_2^2}\left(z-z_i\right)^2, \tag{5.15}$$

and the buoyancy in the mixed layer (below z_i) is

$$b_{m2} = b_s + N^2\left(z_i+\Delta z_2\right) - \Delta b_2 . \tag{5.16}$$

Using the constraint on the integral heat content (5.7), the profile in the entrainment zone can be written in terms of ZOM quantities:

$$b = b_s + N^2 z + \Delta b_0 Y^{-1}\left[\frac{\left(z-z_i\right)^2}{\Delta z_2^2} - 1\right], \tag{5.17}$$

where

$$Y^{-1} = \left(1 + \frac{2\Delta z_2}{3z_i}\right)^{-1}, \tag{5.18}$$

and

$$\Delta b_2 = \Delta b_0 Y^{-1} + N^2\Delta z_2 . \tag{5.19}$$

The buoyancy balance equation is again integrated up to z_i:

$$B(z_i) = B_s - z_i\left[N^2\frac{dz_i}{dt} - \frac{d}{dt}\left(\Delta b_0 Y^{-1}\right)\right], \tag{5.20}$$

and the buoyancy flux profile in the entrainment zone is

$$B = B(z_i) - \frac{S}{3}\left(z - z_i\right)^3 - \frac{U}{2}\left(z - z_i\right)^2 + V\left(z - z_i\right), \tag{5.21}$$

where *S*, *U*, and *V* are defined as follows:

$$S = \frac{d}{dt}\left(\frac{\Delta b_0 Y^{-1}}{\Delta z_2^2}\right),\ U = -2\frac{\Delta b_0 Y^{-1}}{\Delta z_2^2}\frac{dz_i}{dt}, \text{ and } V = \frac{d}{dt}\left(\Delta b_0 Y^{-1}\right). \tag{5.22}$$

The only way to reduce the integral heat content below z_i is to allow the curved part of the buoyancy profile to extend below z_i. We therefore allow the buoyancy profile to curve slowly back to $\partial b/\partial z = 0$ *below* z_i while still holding to $\partial b/\partial z = N^2$ at z_i. In order to conserve heat, it is necessary to shift the entrainment zone profile rightward (to higher temperatures) by a constant amount b_{sh}. This slightly reduces the thickness of the entrainment zone above z_i, and the actual difference between the upper limit of the entrainment zone and z_i is:

$$\Delta z_{rev} = \Delta z_2\sqrt{1 - \frac{b_{sh}}{\Delta b_0 Y^{-1}}}\,. \tag{5.23}$$

The thickness of the layer between z_i, where $\partial b/\partial z = N^2$, and the mixed layer, where $\partial b/\partial z = 0$, is:

$$\Delta z_l = \frac{N^2\Delta z_2^2}{2\left(\Delta b_2 - N^2\Delta z_2\right)} = \frac{N^2\Delta z_2^2}{2\Delta b_0 Y^{-1}}\,. \tag{5.24}$$

The expression for b_{sh} is derived by requiring the conservation of heat and reads

$$b_{sh} = \left(z_i + \Delta z_{rev}\right)^{-1} \left\{ \begin{array}{l} +\frac{1}{3}\frac{\Delta b_0 Y^{-1}}{\Delta z_2^2}\left[2\Delta z_l^3 - \Delta z_{rev}^3\right] - \left(\frac{N^2}{2} + \frac{\Delta b_0 z_i}{\Delta z_2^2}\right)\Delta z_l^2 \\ +N^2 z_i \Delta z_l + \Delta b_0 Y^{-1}\Delta z_{rev} - \Delta b_0\left(1 - Y^{-1}\right) z_i \end{array} \right\}. \tag{5.25}$$

The expressions for Δz_l and b_{sh} must be solved iteratively. Then, the buoyancy flux at the top of the mixed layer can be calculated by integrating the buoyancy balance equation, resulting in

$$B(z_i - \Delta z_l) = B_s - \left(z_i - \Delta z_l\right)\frac{d}{dt}\left(N^2 z_i - \Delta b_0 Y^{-1} - \frac{N^2 \Delta z_l}{2} + b_{sh}\right), \tag{5.26}$$

where

$$\frac{d\Delta z_l}{dt} = \frac{N^4 \Delta z_2}{2\Delta b_0 Y^{-1}}\frac{d\Delta z_2}{dt} - \frac{N^4 \Delta z_2^2}{4\Delta b_0^2 Y^{-1}}\frac{d\Delta b_0}{dt}. \tag{5.27}$$

The integration can be continued into the entrainment zone, where the general buoyancy flux expression becomes

$$\begin{aligned} B(z) = B\left(z_i - \Delta z_l\right) &- \frac{S}{3}\left[\left(z - z_i\right)^3 + \Delta z_l^3\right] - \frac{U}{2}\left[\left(z - z_i\right)^2 - \Delta z_l^2\right] \\ &+ \left(V - \frac{db_{sh}}{dt}\right)\left(z - z_i + \Delta z_l\right). \end{aligned} \tag{5.28}$$

Evaluating this at $z = z_i$ simplifies the expression somewhat:

$$B(z_i) = B_s + S\left(\frac{2}{3}\Delta z_l^3 - z_i \Delta z_l^2\right) + U\left(\Delta z_l^2 - z_i \Delta z_l\right) + z_i\left(V - \frac{db_{sh}}{dt}\right). \tag{5.29}$$

Making the same assumption $\Delta z = 0.2 z_i$ yields a constant entrainment flux ratio of 0.10, which is half what it is in the ZOM (the assumption of $\Delta z_2 \sim z_i$ causes $db_{sh}/dt \sim \Delta b_0/dt$, avoiding the evaluation of a very complicated expression for db_{sh}/dt). The last term in the above expression for $B(z)$ causes the heat flux minimum to occur at a level about 1%

below z_i. In hindsight, the condition $\partial b/\partial t = -\partial B/\partial z = 0$ should have been used, but the equations would have been more complex to derive.

We can understand these results by analyzing them graphically. The buoyancy profiles from this exercise using $\Delta z = \Delta z_2 = 0.18 z_i$ are compared with LES data in Figure 5-2. The LES data, taken at *t*=10,000s, have smooth profiles and fit the SOM model more closely than the others. In the mixed layer, the buoyancy profiles of LES, ZOM, and SOM agree rather closely. The ZOM and FOM both have a sharp interface at z_i. The ZOM interface is between the CBL and the free atmosphere, and the FOM interfaces are between the mixed layer and the entrainment zone, but the basic point is that the buoyancy flux profile at z_i is sharp.

In order for the buoyancy balance equation $\partial b/\partial t = -\partial B/\partial z$ to hold, the buoyancy flux profile must also be sharp. The buoyancy flux profiles for *t*=10,000s are plotted in Figure 5-3. Again, the LES data most closely resemble the SOM profiles. The ZOM and FOM profiles are both sharp.

We find that the differences between the ZOM and SOM entrainment flux ratios $-B(z_i)/B_s$ are mainly due to the lack of sharpness of the interface in the SOM profiles. Only when the interface was made diffuse analytically did the entrainment flux ratio become less than its ZOM counterpart. Considering these results in terms of the horizontally averaged CBLs in LES, it is difficult to say whether the result is due to the variability of the upper interface height as in Lilly (2002a) or if the interface becomes truly diffuse locally. The CBL turbulence structure, which will be discussed in Chapter 8, shows the interface definitely becomes diffuse, but both mechanisms appear to play a role. If the departure of $\delta B_i / B_s$ in LES from the ZOM $-B_i / B_s$ (see Fig. 3.1) is due to either

of these mechanisms, then the integrals of buoyancy and buoyancy flux should be conserved. By the way we defined the FOM and SOM models here, the buoyancy is definitely conserved. Analysis of LES results (see Section 5.1) shows that the buoyancy flux integral is definitely conserved. Calculating (5.4) from the SOM profiles shows that the buoyancy flux integral matches the ZOM integral very closely.

The final portion of the experiment was to vary the entrainment zone thickness, to the extent possible, to test the sensitivity of the heat flux profile to the entrainment zone thickness to try to reproduce the results of Chapter 4 (Fedorovich et al. 2004). The results of this test for the range of entrainment zone thickness over which a solution exists are shown in Table 5.1. The entrainment flux ratio $-B(z_i)/B_s$ approaches its ZOM shear-free counterpart C_1 as the entrainment zone thickness goes to zero, and it approaches zero as the entrainment zone thickness becomes larger. The results are consistent with the differences between the LES entrainment flux ratios in strongly versus weakly stratified environments as seen in Chapter 4. Weaker background buoyancy stratification means a deeper entrainment zone, and, according to the results here and in Chapter 4, that means the LES entrainment flux ratio will be much smaller than it is in the ZOM. Also, Table 5.1 shows the ratio $\sqrt{A_N / A_P}$ departs from 0.2 much less than $-B(z_i)/B_s$ does, suggesting the integral buoyancy flux should remain approximately the same (actually this can be expected anyway for a square root funtion like $\sqrt{A_N / A_P}$), and the diffuse interface does not necessarily change the overall meaning behind $C_1 = 0.2$. That is, the integral production and destruction of TKE by buoyancy flux remains about the same if the flux profile is made more diffuse. Using the ZOM simply allows the

differing heat flux profiles to be placed within a simplified framework in which their entrainment heat fluxes can be directly compared. These results are more robust for the LES profiles than they are here. $\sqrt{A_N / A_P}$ retrieved from LES varies much less than it does in the SOM experiments, and it is essentially constant for shear-free CBLs.

Since we are interested in learning the overall fate of shear- or buoyancy flux-produced TKE, the most direct way to discover this fate is to calculate the integral production and destruction of TKE. The results of Section 5.1 show that the extrapolation method or the integral method (Eqn. 5.4) produce very similar results.

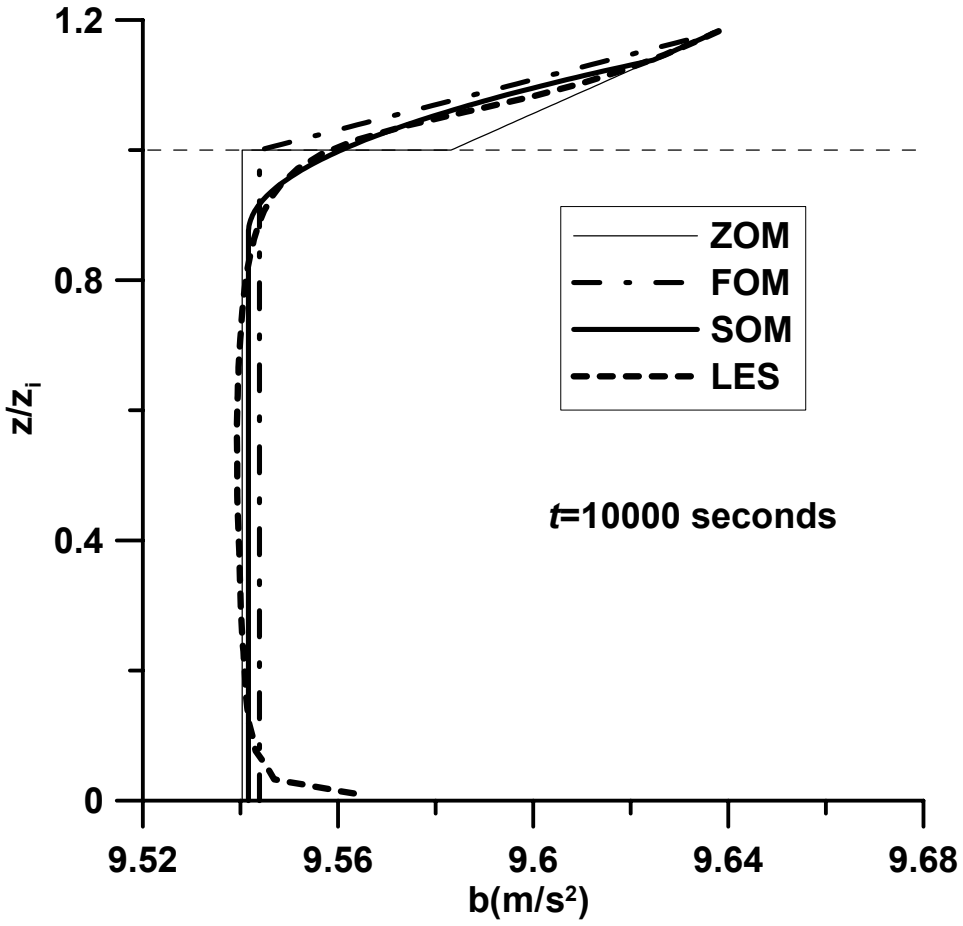

Figure 5-2: Buoyancy profiles in the respective model integrations for $\Delta z = \Delta z_2 = 0.18 z_i$.

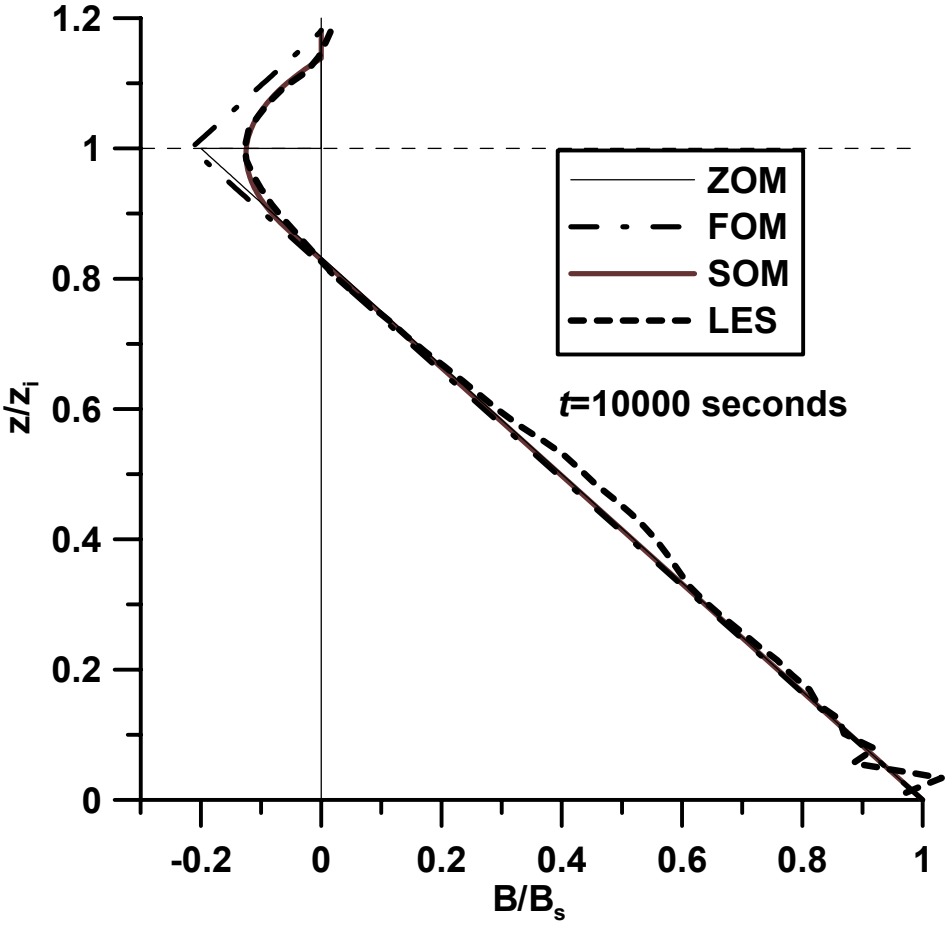

Figure 5-3: Buoyancy flux profiles in the respective model integrations for $\Delta z = \Delta z_2 = 0.18 z_i$.

Table 1. Entrainment Flux Ratio of SOM for Given Δz_2 Values

$\Delta z_2 / z_i$	$\delta z_i / z_i$	$-B_i / B_s$	$\sqrt{A_N / A_P}$	Extrapolated Linear
0.05	0.06	0.200	0.219	0.206
0.10	0.13	0.185	0.232	0.210
0.15	0.21	0.153	0.231	0.209
0.18	0.26	0.125	0.221	0.206
0.20	0.30	0.103	0.211	0.202
0.21	0.32	0.092	0.204	0.200
0.25	0.37	0.039	0.168	0.187

5.3 Comparison of Methods of Defining CBL Depth

With the previous analyses in mind, we attempt to answer the fourth question listed at the beginning of this chapter. Since the *height of maximum potential temperature gradient* produces a much less variable CBL depth than does the *minimum heat flux level*, we want to make sure it is fully evaluated before ruling it out as the method of choice for determining z_i. To answer this question, we can perform tests to distinguish which method of determining z_i might be the best and most consistent with the ZOM-based entrainment equations. We will determine the constant C_1 using both the maximum potential temperature gradient and minimum heat flux methods and compare their respective equilibrium entrainment solutions (3.47) with LES data.

For these tests, we take the actual LES profiles and work with them in a way to retrieve ZOM-based parameters in a manner most consistent with their definitions in the ZOM. We do this in a slightly different manner than Chapter 4. We identify z_i using either the heat flux minimum or the maximum buoyancy gradient (note that these are at *exactly* the same height in the ZOM but not in LES). Then, all levels below z_i are defined to be part of the mixed layer, and the buoyancy is averaged over this depth. The free atmospheric buoyancy profile is extrapolated down to z_i to find the value of buoyancy at the upper edge of the interface. Finally, the net cooling between z_i and the top of the entrainment zone is integrated, and this integrated heat deficit is subtracted from the CBL heat integral to find the mixed layer buoyancy. The ZOM buoyancy jump Δb is then defined as the difference between the buoyancy at the upper edge of the interface and the mean mixed layer buoyancy after the heat removal. This entire process

is done in parallel, using the heat flux minimum and buoyancy gradient maximum methods to define z_i and Δb.

From these two separate estimates of z_i and Δb, estimates of the constant C_1 are made using (3.44). Then, the respective C_1 estimates are used in (5.5), and the resulting ZOM equilibrium entrainment solutions are plotted against the LES data. Whichever method produces the closest match with LES data will be deemed the better of the two.

Figure 5-4 shows the results. The LES C_1 was determined using the definition of the entrainment flux ratio $\left(\Delta b dz_i / dt\right) / B_s$ with z_i and Δb determined in a manner consistent with the respective method and dz_i / dt determined using local least squares fits. The black lines show the result of deriving C_1 from the minimum of buoyancy flux. For all times, the analytic solution is very comparable with the LES z_i. Indeed, there is a bit of scatter in the z_i estimates using this method, but the analytic solution stays generally within this scatter from very early to very late in the LES run.

If the maximum of the potential temperature gradient is used (see the red lines in Fig. 5-4), the scatter in z_i estimates is very small. However, the analytic solution drifts from the LES-determined z_i during the simulation, and overall, it does not match the LES z_i versus t plot as well as in the case using the minimum heat flux method.

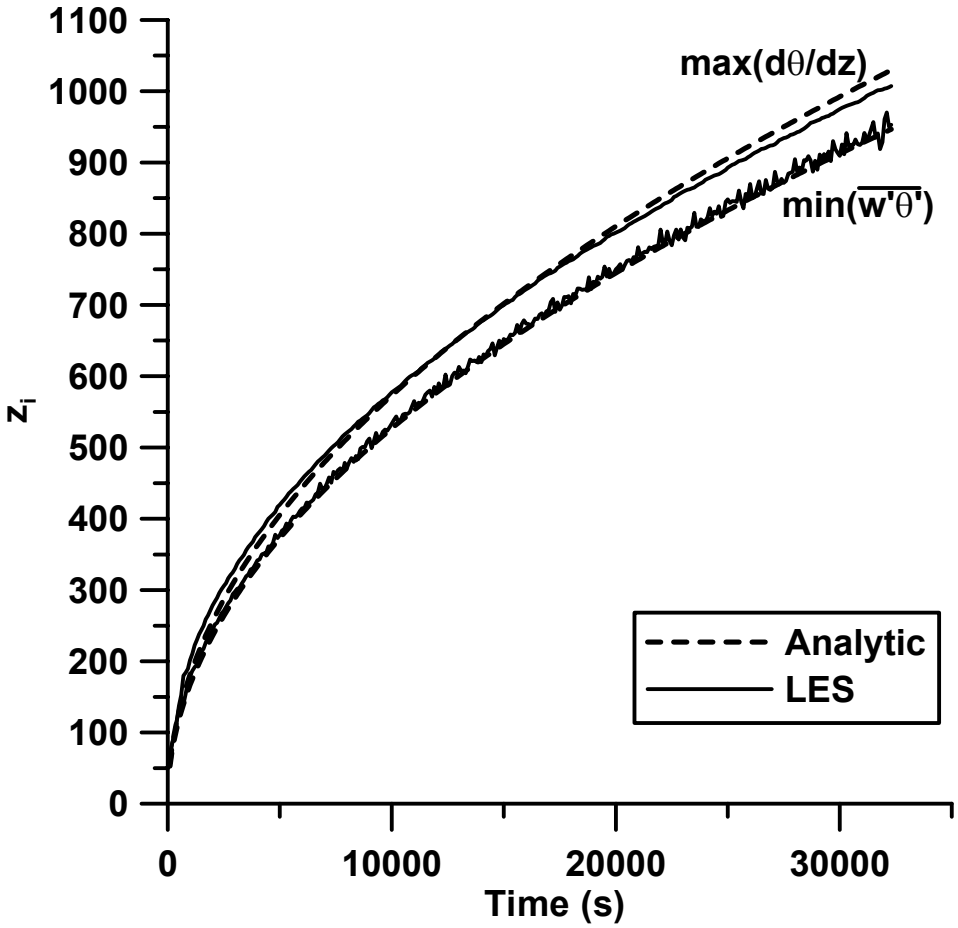

Figure 5.4: Comparisons between CBL depth estimates using the maximum potential temperature gradient and heat flux minimum methods. Red lines refer to the maximum potential temperature gradient method, and the black lines refer to the heat flux minimum method. Dashed lines show the analytic solution using these respective methods.

In the maximum temperature gradient case, the analytic solution for z_i (see Eqn. 5.5) seems to grow faster than the LES z_i during most of the run. The estimate of C_1 using the maximum temperature gradient method is approximately 0.3, whereas it is 0.2 using the buoyancy flux minimum. The high estimate using the maximum gradient seems to affect the performance of the analytic solution relative to the LES z_i. This overestimate occurs because both z_i and Δb are estimated larger using the maximum temperature gradient method (compared to the minimum heat flux method), and the

inconsistency between the analytic and LES plots indicates the maximum temperature gradient is not the most dynamically relevant method to use, at least within the ZOM. The inconsistency is really not all that bad, but the data show that the minimum of heat flux works better than the maximum temperature gradient.

Regardless of the results of this exercise, the maximum potential temperature gradient is still the only way to determine z_i from balloon-borne soundings of the atmosphere, so it is necessary to calculate CBL depths using both methods before comparing them to atmospheric data.

5.4 Summary

Two main conclusions are reached in this chapter. The first is that the height of the minimum heat flux in the entrainment zone is the most dynamically meaningful definition of the CBL depth. Secondly, the LES heat flux minimum does not have to be the same as the ZOM heat flux minimum in order for the framework of the ZOM to apply to LES data. The LES-derived entrainment flux ratio *can* be less than that predicted by the ZOM-based entrainment equations, but the integral production and destruction of TKE by buoyancy flux remains essentially the same as it is in the ZOM, as was seen in Section 5.1. The model experiments of Section 5.2 have shown that the differences between the ZOM entrainment flux ratio $-B_i / B_s$ and the LES entrainment flux ratio $-\delta B_i / B_s$ can be reproduced when the interface is made less sharp in the analytic model. This result can apply to LES, regardless of whether the reduced sharpness is due to the variability in the height of the interface or if it is due to the interface becoming more

diffuse locally. Either way, the integral production and destruction of TKE by buoyancy flux is the same. The main advantage of analyzing LES data within the ZOM framework remains: the entrainment flux ratio of the shear-free CBL is brought to a common value of 0.2 regardless of stratification and buoyancy flux at the surface, and this provides the most convenient framework for comparing sheared CBLs to shear-free CBLs.

Chapter 6

Methodology

6.1 Large Eddy Simulation Setup

The LES code used in this study has already been described in Chapter 4, so this section will concentrate on the selection of the LES domain and the parameters of shear, surface buoyancy flux, and free atmospheric stratification that will be used for the sheared CBL experiments.

6.1.1 LES Domain

Within the context of the horizontal averaging of the CBL turbulence, as has been described in Chapter 3, it is important to take into account the sampling of the CBL structure in order to construct a representative estimate of turbulence statistics, as well as the computer processor speed and memory limitations. For sufficient statistical sampling, the width of the LES domain must be significantly wider than the depth of the CBL in order to sample the largest number of possible turbulence structures to construct turbulence statistics. On the other hand, the domain must also be sufficiently deep to resolve the vertical structure of turbulence within the CBL. Because of the isotropy

assumptions of the subgrid turbulence closure, horizontal grid cell dimensions should be approximately equal to the vertical dimensions.

It is important also to resolve structures in the interfacial layer that are the most important contributors to entrainment. General consensus in the boundary layer community to date is that 20 meters is the maximum grid spacing that should be used in this layer for dry CBLs. The grid spacing is most critical for CBLs growing through strong stratification, in which case the entrainment zone is shallower.

With these considerations in mind—grid cell size, CBL aspect ratio, vertical resolution, for a computer with 2 Gigabytes of memory and a 2.8GHz processor, a grid of 256×256×80 is the optimal to use. With 20-meter grid cells, this makes the LES domain $X \times Y \times Z = 5.12 \times 5.12 \times 1.6$ km^3.

6.1.2 Selection of the Parameter Space for Sheared CBLs

The study of Fedorovich et al. (2004a), described in Chapter 4, provides groundwork for much of this study. It used a LES parameter space of free atmospheric stratification of 0.001 K/m to 0.010 K/m, which is roughly representative of its range in the atmosphere. That same range is adopted here, but in order to allow more computer time for investigation of the shear parameter space, only three gradations of stratification are used: $\partial\theta/\partial z$ =0.001 K/m, 0.003 K/m, and 0.010 K/m (N=0.006, 0.010, and 0.018 s^{-1}). Fedorovich et al. (2004a) and Sorbjan (1996a) performed a more thorough investigation of the effects of stratification on entrainment, so it is not necessary to investigate a large number of different free atmospheric stratifications in this study.

If we want to study the effects of shear on CBL entrainment, the best way to choose the parameter space to be investigated by LES is to perform a scale analysis on the entrainment equations themselves. In reality, the method of selecting the particular combinations of shear and buoyancy forcing in this study had to do a bit with trial and error. Preliminary simulations showed little noticeable enhancement of CBL growth (Conzemius and Fedorovich 2002), so the shear in the runs was increased and the surface buoyancy flux decreased until significant effects on CBL growth could be seen. Nevertheless, a scale analysis can be used to more fully elucidate the conditions under which the buoyancy and shear forcings for entrainment might be expected to be of nearly equal magnitude.

The easiest way to do this is with the ZOM entrainment equations developed in Chapter 3. We focus on the TKE equation (3.38), which is repeated below, and estimate the values of each of the terms with various forcings of surface buoyancy flux, stratification, and shear.

$$\int_0^{z_i} \frac{\partial e}{\partial t} dz = -u_m \overline{w'u'}_s - v_m \overline{w'v'}_s + \frac{1}{2}\left(\Delta u^2 + \Delta v^2\right)\frac{dz_i}{dt} + \frac{1}{2}\left(\overline{w'b'}_s - \Delta b \frac{dz_i}{dt}\right) z_i - \Phi_i - \int_0^{z_i} \varepsilon dz \tag{6.1}$$

Because we are currently interested in the relative differences between shear-forced turbulence and buoyancy-forced turbulence, we concentrate on the terms that describe shear and buoyancy forcings.

For a typical value of free atmospheric stratification, we adopt the $\partial\theta/\partial z$=0.003 K/m for this scale analysis. For the surface shear terms, we can assume a typical mixed layer momentum of 10 m/s, and a surface friction velocity of 0.5 m/s. This provides an

estimate of the surface shear contribution to the integral TKE of 2.5 m^3/s^3. For the entrainment zone shear term, we can assume a typical thermal wind component associated with a horizontal temperature gradient of 10 K per 1000 km. This provides a shear magnitude of 0.003 s^{-1}. If the CBL is 1000 meters deep, and assuming the shear across this layer accumulates at the top of the CBL, the velocity jump would be 3 m/s. Squaring this would yield approximately 10 m^2/s^2. For the CBL growth rates, we use the values from the Fedorovich et al. (2004a) study, which occurred with a surface heat flux of 0.3 Km/s, which is typical for a day with relatively strong sensible heating. dz_i / dt would be 0.15 m/s with this heating rate. This yields an entrainment zone shear term of approximately 0.8 m^3/s^3.

Next, the buoyancy flux term can be split into two parts—the surface flux and the entrainment flux. The former is 0.01 m^2/s^3 times the boundary layer depth, z_i, yielding 5 m^3/s^3 for the surface buoyancy flux term. Since the entrainment flux ratio is 0.2 in the ZOM for the shear-free CBL, we can say that $\Delta b dz_i / dt$ is 0.2 times $\overline{w'b'}$ and therefore, the entrainment zone heat flux term would be -1 m^3/s^3. Combined, these two terms amount to 4 m^3/s^3.

From this scale analysis, the buoyancy flux terms are nearly an order of magnitude greater than the entrainment zone shear term. Additionally, the surface shear term may or may not be an important contributor to the generation of TKE that might enhance entrainment, since previous analyses of TKE budgets near the surface shows that dissipation largely balances the surface shear generation (Deardorff and Willis 1982; Moeng and Sullivan 1994).

Since the CBL runs in the domain are terminated when z_i is approximately 1000 meters deep, a more typical z_i for the LES run might be closer to 500 meters. Considering this shallower CBL depth in the scale analysis results in no change in the surface shear term, and the entrainment zone shear term and buoyancy terms are 0.4 m^3/s^3 and 2 m^3/s^3 respectively. Thus the surface shear may be relatively more important for a shallower CBL, but the effects of entrainment zone shear and buoyancy are still the same relative to one another.

Based on this analysis, one of two things is necessary for the effects of shear to be nearly equal to the effects of buoyancy in the LES runs. The first is for the shear to be stronger. An initial momentum of 20 m/s in the flow provides a strong surface shear that is not unrealistic for atmospheric cases, so that value is adopted here. For the entrainment zone shear term to become comparable in magnitude to the buoyancy flux term, the geostrophic shear would need to be increased to a value several times its typical value. One must keep in mind that such levels of shear in the geostrophic wind would also require horizontal temperature gradients that are more than three times the typical value of 10 K per 1000 km and that these temperature gradients cannot be represented using the periodic boundary conditions of LES. The setup therefore does not represent the atmospheric thermal wind—neither in terms of its magnitude nor in terms of its temperature gradients. If the temperature gradients were represented, they would not be as large as the local temperature gradients associated with thermals, and they would also not generate thermally direct circulations whose vertical velocity scales would compete with the velocity scales of convective elements within the CBL. It must also be noted that where such a strong thermal wind exists, the conditions are possibly favorable for

baroclinic instability, and in the real atmosphere, the relatively pristine conditions of LES (with zero mean upward vertical motion over a horizontal domain of 5 km width) are unlikely to be seen.

However, despite all these apparent problems, the strong values of shear mentioned above *can* be found in the atmosphere—they are just not geostrophic. Assuming geostrophic balance in the initial simulation wind profiles provides an easy method for keeping the forcing constant with time as the CBL grows in the simulations. Also, the idealized setup allows for a more detailed analysis of the dependence of CBL growth on shear, as the shear values should change slowly and smoothly during the simulations. LES is therefore being used in a manner to isolate the effects of shear on entrainment. The use of actual atmospheric profiles in LES will be addressed in Chapter 9.

The other way to allow the relative effects of shear to be seen is to decrease the surface buoyancy flux. If the surface buoyancy flux is decreased by a factor of ten from what it is in the scale analysis above, the entrainment shear term and the buoyancy terms become nearly equal in magnitude. Since Fedorovich et al. (2004a) used Q_s=0.3 Km/s, we adopt this value as the upper limit of the range of Q_s used in this study. The lower limit will be one tenth this value, and a value of Q_s=0.1 Km/s will also be added to explore the middle portion of this parameter space.

6.1.3 LES Parameters

The setup of the shear cases is also designed to elucidate the effects of surface shear versus shear across the CBL top. With this in mind, the shear cases were divided

into a set that has a constant geostrophic wind, in which all the initial shear is concentrated at the surface, and other cases in which the surface geostrophic wind is zero, but the shear in the geostrophic wind is strong, so the growing boundary layer encounters changing wind with height, focusing most of the shear at the CBL top. The runs with height-constant geostrophic wind are denoted as GC cases, and the runs with shear in the geostrophic wind are called GS. They will be compared against a shear-free case, designated NS.

The wind is initialized in geostrophic balance throughout the model domain, and the initial CBL depth is zero. The initial profiles of momentum and buoyancy for the GS and GC cases are shown in Figure 6.1. The surface heat flux is kept constant at its prescribed value during the run, and the model run is allowed to proceed until the CBL depth reaches approximately 60 percent of the model domain depth. At this point, to avoid spurious effects associated with the entrainment zone impinging upon the sponge layer, the simulation is stopped.

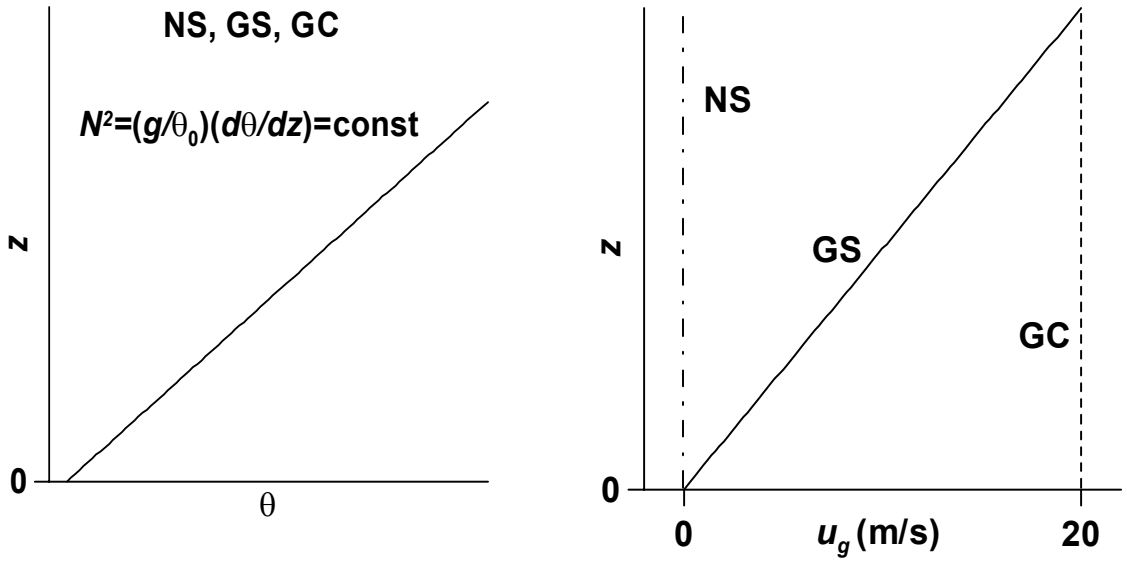

Figure 6.1: Initial profiles of the virtual potential temperature θ and the x-component of the geostrophic wind velocity, u_g, for the simulated CBL cases.

The general settings used in the LES for this study are found in Table 6.1. The combination of LES cases is shown in Table 6.2. There are a total of 27 possible runs covering all values of surface buoyancy flux, atmospheric stratification, and shear proposed. The three simulations (NS, GS, GC) with the strongest stratification and weakest surface buoyancy flux were not run because of the excessive time necessary to bring the simulations to completion (approximately three weeks per simulation) and because the entrainment zone in these three cases might not be too shallow for the grid to resolve the energy-containing motions of turbulence there. Therefore, the total number of simulations was 24.

Table 6.1 Parameters of Conducted LES

Parameter	**Setting**
Domain size	$5.12\times5.12\times1.6\text{km}^3$
Grid	256×256×80
Surface kinematic temperature flux	0.03, 0.1, and 0.3 Km/s
Temperature stratification above CBL	0.001, 0.003, and 0.010 K/m
Geostrophic wind	0 m/s throughout domain (NS) 20 m/s throughout domain (GC) 0 m/s at lower boundary, 20 m/s at top (GS)
Time step	0.5 s (to synchronize NS, GS, and GC cases)
Lateral boundary conditions	Periodic for all prognostic variables and pressure
Upper boundary conditions	Neumann with zero gradient; a sponge layer imposed in the upper 20% of simulation domain
Lower boundary conditions	No-slip for velocity, Neumann for temperature, pressure and subgrid TKE, Monin-Obukhov similarity functions as in Fedorovich et al. (2001a)
Subgrid turbulence closure	Subgrid TKE-based after Deardorff (1980)

Table 6.2 List of LES Runs

		Surface kinematic temperature flux (Km/s)		
		0.03	0.10	0.30
Potential temperature gradient (K/m)	0.010		NS,GS,GC	NS,GS,GC
	0.003	NS,GS,GC	NS,GS,GC	NS,GS,GC
	0.001	NS,GS,GC	NS,GS,GC	NS,GS,GC

6.1.4 LES Output Evaluation

Model output statistics are formed by averaging across horizontal planes in LES. The statistics are calculated every 100 seconds in the simulation, which, in most cases, is much less than the convective time scale (defined by z_i / w_*) in the simulations. The statistics calculated are listed in Table 6.3. Because a staggered grid is used, all variables were interpolated to the center of the grid cell, if necessary, before calculating their statistics. The spectra and cospectra were calculated across horizontal planes at all model levels. TKE transport and the dissipation rate calculations were added to the LES code after most of the simulations were completed. For this reason, some of the cases were re-simulated: $d\theta/dz$=0.010 K/m with Q_s=0.30 Km/s and $d\theta/dz$=0.003 with Q_s=0.03 K/m.

Table 6.3 Statistics Calculated in LES

Statistics	Quantities calculated
First order	$\overline{u}, \overline{v}, \overline{\theta}, \overline{E}$ (subgrid energy), ε**
Second order*	$\overline{u'^2}, \overline{v'^2}, \overline{w'^2}, \overline{\theta'^2}, \overline{E'^2}, \overline{w'\theta'}, \overline{w'u'}, \overline{w'v'}, \overline{w'e'}$**, $\overline{w'p'}$**
Third order	$\overline{w'w'w'}, \overline{\theta'\theta'\theta'}$
Spectra	$\overline{u'^2}, \overline{v'^2}, \overline{w'^2}, \overline{\theta'^2}$
Cospectra	$\overline{w'\theta'}, \overline{w'u'}, \overline{w'v'}$

* For the statistics $\overline{u'^2}, \overline{v'^2}, \overline{w'^2}, \overline{w'\theta'}, \overline{w'u'}$, and $\overline{w'v'}$, both resolved and total (resolved plus subgrid) components were calculated. Overbars represent horizontal averages in LES, which are intended to be representative of ensemble averages.
** Not available for all cases.

6.1.5 Methods for Finding z_i and Parameters of Entrainment

There are numerous definitions of the CBL depth based on LES [e.g. Moeng and Sullivan (1994); Lewellen and Lewellen (1998)]. Based on the analyses presented in Chapters 4 and 5, the level of the heat flux minimum in the entrainment zone will be used to define the CBL depth, z_i.

Compared to Chapter 4, some refinements were made in the determination of the CBL depth and the upper and lower limits of the entrainment zone. Because LES statistics are located at discrete model levels, the time series of z_i sometimes shows a stair-step appearance, and this structure can affect the calculations of other parameters of entrainment. To avoid this, an interpolation procedure was used to refine z_i estimates. The grid level with the minimum heat flux was identified, and a perfect quadratic fit was calculated using the heat flux from that grid level and the surrounding two grid levels. The heat flux minimum on the quadratic curve was then used to define z_i. The z_i determined using the quadratic fit was never more than a half grid point above or below the grid point with the discrete heat flux minimum.

The lower boundary of the entrainment zone z_{il} was defined as the level at which the heat flux profile crossed zero. In order to refine this estimate as much as possible, a linear interpolation was used between the last grid level (in the mixed layer) with a positive heat flux and the first grid level with a negative heat flux. The upper boundary of the entrainment zone z_{iu} was defined in exactly the same manner as Chapter 4.

The potential temperature and momentum at the lower limit of the entrainment zone were determined by taking their value exactly at z_{il}. This required a linear

interpolation between surrounding grid values. The potential temperature and momentum at z_{iu} were simply taken to be their grid point values.

The ZOM parameters of entrainment must be taken from LES in a manner that is consistent with their definition. Following Chapter 5, we define $\Delta b = b(z_i) - b_m$, where b_m is the mixed layer value of buoyancy, but unlike Chapter 4, the approximation $b_m \approx b(z_{il})$ is not used here. Rather, the mixed layer buoyancy b_m is calculated from averaging the buoyancy between z_i and the surface. The buoyancy at the ZOM CBL top, $b(z_i)$, is defined as the buoyancy of the free atmospheric profile extrapolated down to z_i. To further restore the ZOM profile, the integrated buoyancy deficit between z_i and z_{iu} (due to the accumulated buoyancy flux divergence there) is subtracted from the integrated mixed layer buoyancy when calculating b_m. The same procedure is used to retrieve Δu and Δv.

Early in the LES run, when the CBL is not yet entraining heat, z_i is defined as the level at which the heat flux approaches zero. Because there is no significantly negative heat flux with which to define an entrainment zone, the entrainment zone depth is set equal to zero. In this manner, the corresponding values of buoyancy and momentum at the upper and lower limits of the entrainment zone become their values at z_i. The mixed layer averaging (below z_i) is still performed to determine the ZOM parameters Δb, Δu, Δv, which are always defined to be $\Delta\phi = \phi(z_i) - \phi_m$. Early in the run, this can result in negative values of Δb before the CBL has reached an entraining regime. Physically, the negative Δb has sense because when the convection is initiating in the CBL, the plumes are just beginning to rise from the surface layer and have not yet reached their point of

neutral buoyancy. Thus the buoyancy in the convectively mixing portion of the domain is greater than the buoyancy just above the tops of the plumes.

The FOM jumps of buoyancy and momentum are defined as $\Delta\phi_1 = \phi(z_{iu}) - \phi_m$, where the mixed layer quantities are calculated in the same manner as with the ZOM, except that the entrainment zone deficits are *not* subtracted from the mixed layer values as they are in the ZOM.

The ZOM-based constant C_1 was determined by linearly extrapolating the buoyancy flux profile through its zero crossing height to z_i and dividing by B_s. The analysis in Chapter 5 has shown that using the extrapolated heat flux as a proxy for $\left(\Delta b dz_i / dt\right) / B_s$ is the easiest way to estimate C_1, which may become time-dependent with shear.

6.2 Tests of RANS-based Turbulence Closures in NWP

The TKE-based turbulence closures of Xue et al. (2001) (ARPS) and Fiedler and Kong (F&K) were tested against LES data for the same 24 combinations of surface buoyancy flux, free atmosphere stratification, and shear in Table 6.2. The ARPS and F&K closures were described in Chapter 3.

The evaluation of the RANS-based NWP turbulence closures was carried out in a similar manner as in Moeng and Wyngaard (1989) and Ayotte et al. (1996). The LES code was reduced to a one-dimensional form, and the turbulence closure scheme was modified according to the corresponding RANS-based descriptions in Chapter 3. Vertical profiles of turbulence statistics were calculated in the same manner as in LES,

and the parameters of entrainment were determined from the vertical profiles of turbulence statistics in the same manner as in LES.

6.3 Tests of Integral Budget Methods

6.3.1 Tests of ZOM and FOM Parameterizations

The evaluation of the various schemes within the integral budget approach was done by retrieving the parameters B_s, z_i, Δb, Δu, Δv, Δb_1, Δu_1, and Δv_1 from LES data and using them in the respective formulations for the entrainment flux ratio, with the constants indicated in Table 3.1. Unfortunately, the evaluation of the above parameters was not very straightforward. The definitions of parameters of entrainment were dependent on the author evaluating them, regardless of whether the evaluation was made based on atmospheric or LES data. For example, in the ZOM, the buoyancy jump across the entrainment zone can be evaluated in the strict sense of the ZOM, in which case the linear free atmospheric profile of buoyancy is extrapolated downward from the upper edge of the entrainment zone to the defined CBL depth z_i, but many authors [e.g. Boers et al. (1984)] used the full change across the entire depth of the entrainment zone.

In most cases, the actual value of the parameterized heat flux at the inversion is highly sensitive to the size of the jumps used, suggesting an inherent weakness in the parameterizations. Additionally, there is usually a difference between the actual entrainment heat flux, δB_i (the minimum of heat flux in the entrainment zone), and the ZOM-parameterized heat flux, $\Delta b dz_i / dt$. To the extent possible, this study tries to use

the parameterizations in a manner consistent with the way they were originally evaluated by their respective authors.

6.3.2 Numerical Integration of the ZOM and FOM Entrainment Equations

The Newton-Ralphson method was used to numerically integrate the ZOM and FOM equations for entrainment [(3.31)-(3.33), (3.38), (3.63)-(3.65), and (3.74)-(3.77)] derived in Chapter 3. Before this can be done, estimates of the integrals of turbulence kinetic energy and dissipation were made. For the shear-free case, the constants C_e and C_ε were accepted to be 0.5 and 0.4 respectively (see Chapter 3).

When shear contributes to the TKE, the appropriate parameters for scaling will be different. The assumption will be made that the TKE and dissipation are a linear combination of the mechanisms that contribute to them: buoyancy-generated (the shear-free case), surface shear-generated, and entrainment zone shear-generated. The actual determination of scaling parameters must be made on a trial and error basis from LES data, and the resulting values of the constants representing the scaled integrals of TKE and dissipation will be addressed in Chapter 10. For now, the initial hypotheses are that the integrals of surface shear-generated TKE and its dissipation can be scaled by the friction velocity u_* and z_i, and the integrals of entrainment zone shear-generated TKE and its dissipation can be scaled by Δu and z_i. In the FOM, Δu_1 will be used as the scaling parameter for entrainment zone shear, and Δz is also available as a scaling parameter.

Chapter 7

Simulated Convective Boundary Layer Cases

7.1 CBL Depth and Velocity Profiles

Figure 7.1 shows the plots of the CBL depth versus time for the 24 conducted simulations, and Figure 7.2 shows the profiles of the *x*-component of momentum at late stages in the simulations. The figures are organized according to the surface buoyancy flux and the free atmospheric stratification. Cases with weaker stratification are shown on the bottom of the figures (g,h,i), and the strongest stratification cases appear on top (b,c). The cases with the weakest surface buoyancy flux (d,g) appear on the left, and those with the strongest flux (c,f,i) are on the right. This same orientation will be used for all remaining figures in which all LES results are presented together.

The effects of shear on the CBL growth rate are heavily dependent on the combination of stratification and surface buoyancy flux. In general, the effects of shear stand out the most when the surface buoyancy flux is weakest, but they also stand out a bit more when the free atmospheric stratification is weak. The strongest enhancements of CBL growth in the sheared CBLs versus the NS case are seen in Figs. 7.1d and g. Fig. 7.1c shows no enhancement, and Fig. 7.1i shows decreased CBL growth with shear. Some discussion is needed to elucidate the effects that are seen in each individual case and to understand why they are different.

The first cases studied were those with the strongest buoyancy flux, and these cases provided the motivation to perform simulations with weaker surface buoyancy flux and stronger stratification. As seen in the scale analysis presented in Chapter 6, the integral buoyancy production of turbulence is much stronger than the integral shear production of turbulence for these cases. In Fig. 7.1c, the NS, GS, and GC cases experience very similar rates of CBL growth, although the CBL growth in the GS and GC cases is slightly faster. If the maximum temperature gradient is used as the definition of the CBL top, the sheared cases stand out more clearly from the shear-free case. An LES comparison study (Fedorovich et al. 2004c) shows differences in z_i between sheared and shear-free CBLs increase when using the maximum potential temperature gradient to define z_i.

Figure 7.1f shows no consistently meaningful differences among the three cases except that the CBL in the GC case grows more slowly than in the other cases early in the simulation and the GS case CBL appears to grow slightly faster at the end. The difference among these three cases is the least among all the stratification and heat flux combinations simulated. In Fig. 7.1i, we find that the sheared CBLs have smaller growth rates than shear-free CBLs; the NS CBL grows the fastest initially, but once the convection initiates in the GC case, the GC CBL growth rate is fastest. The GS CBL seems to grow relatively slowly throughout the simulation. If there is any evidence in the simulations that supports the theory of the shear sheltering of turbulence (Hunt and Durbin 1999), it is found here. Animations of this particular case show that the shear deforms the thermals rising from the surface, and this appears to weaken their ability to

organize into vertically coherent structures that would efficiently transport heat upward from the surface.

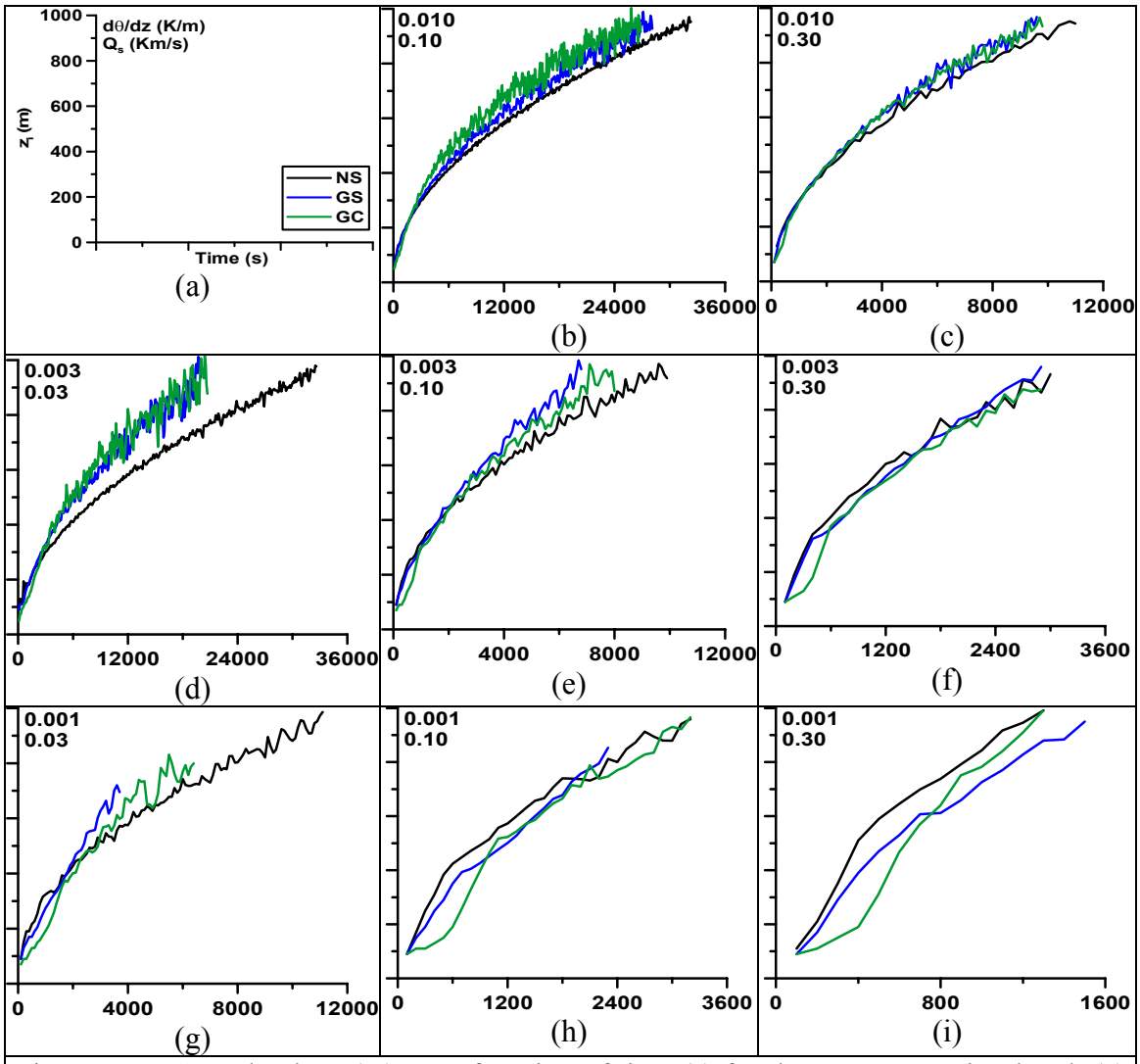

Figure 7.1: CBL depth, z_i (m), as a function of time (s) for the LES cases simulated: (a) legend; (b) $\partial\theta/\partial z = 0.010$ K/m, $Q_s = 0.10$ Km/s; (c) $\partial\theta/\partial z = 0.010$ K/m, $Q_s = 0.30$ Km/s; (d) $\partial\theta/\partial z = 0.003$ K/m, $Q_s = 0.03$ Km/s; (e) $\partial\theta/\partial z = 0.003$ K/m, $Q_s = 0.10$ Km/s; (f) $\partial\theta/\partial z = 0.003$ K/m, $Q_s = 0.30$ Km/s; (g) $\partial\theta/\partial z = 0.001$ K/m, $Q_s = 0.03$ Km/s; (h) $\partial\theta/\partial z = 0.001$ K/m, $Q_s = 0.10$ Km/s; (i) $\partial\theta/\partial z = 0.001$ K/m, $Q_s = 0.30$ Km/s.

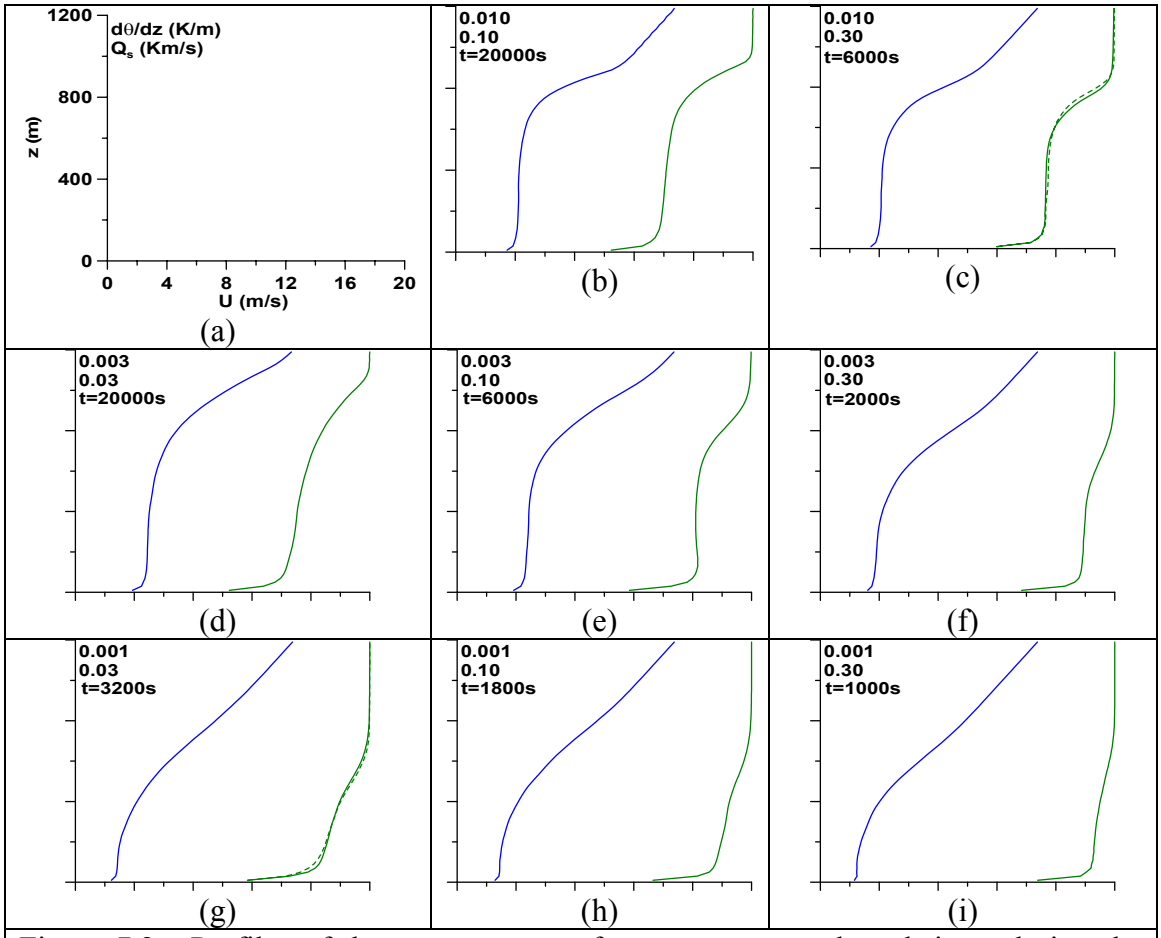

Figure 7.2: Profiles of the *x*-component of momentum at selected times during the simulation for the LES cases: (a) legend; (b) $\partial\theta/\partial z = 0.010$ K/m, $Q_s = 0.10$ Km/s; (c) $\partial\theta/\partial z = 0.010$ K/m, $Q_s = 0.30$ Km/s; (d) $\partial\theta/\partial z = 0.003$ K/m, $Q_s = 0.03$ Km/s; (e) $\partial\theta/\partial z = 0.003$ K/m, $Q_s = 0.10$ Km/s; (f) $\partial\theta/\partial z = 0.003$ K/m, $Q_s = 0.30$ Km/s; (g) $\partial\theta/\partial z = 0.001$ K/m, $Q_s = 0.03$ Km/s; (h) $\partial\theta/\partial z = 0.001$ K/m, $Q_s = 0.10$ Km/s; (i) $\partial\theta/\partial z = 0.001$ K/m, $Q_s = 0.30$ Km/s.

However, the entire simulation in Fig 7.1i is too short to draw any conclusions about this effect. In fact, the simulation is so short that the turbulence structure is still dependent on the characteristics of the onset of turbulence, which, in the simulations, is dependent on the manner in which the initializing disturbances are supplied to the flow at t=0.

Fig 7.2i shows that the momentum in these simulations is not well-mixed, and there is no layer of accumulated shear except at the surface. The turbulent vertical motions associated with buoyantly forced convection have not had sufficient time to mix the momentum in this case.

With increasing stratification, the CBL grows more slowly, allowing more time for turbulence to mix the momentum within the interior of the CBL and for shear to accumulate at the CBL top. The CBL depth in the cases with the moderate stratification (Figs. 7.1f and 7.2f) still grows quickly enough that momentum is not well-mixed, but with the strongest stratification (Figs. 7.1c and 7.2c), the momentum in the CBL is much better mixed, and the shear is concentrated at the CBL top. In the GC case, the momentum throughout the depth of the CBL has decreased from its geostrophic value, resulting in the development of shear at the CBL top, despite the fact that the case was designed to investigate the effects of shear in the surface layer. The stronger shear at the CBL top in both the GS and GC cases has a better chance to generate TKE there and to enhance entrainment. In general, the most well-mixed momentum profiles appear when the CBL growth rate is small, decreasing the entrainment of momentum, and the turbulence is intense enough to mix the momentum in the interior of the CBL. This tends to occur under conditions of strong stratification and moderate to strong surface buoyancy flux (Figs. 7.1b,c and Figs. 7.2b,c).

The simulations in the center column of Figure 7.1 were motivated by the relative insensitivity of the CBL growth to wind shear in the simulations with the strongest heat flux. With a more moderate heat flux, CBL growth under the conditions with weakest potential temperature gradient (Fig 7.1h) still appears to be unaffected by shear. The

CBL growth is rapid in these cases, and the momentum fields (Fig 7.2h) are about as well-mixed as they are in Figs. 7.2i and 7.2f. Strong surface shear exists in the GC case, but this does not seem to enhance the CBL growth relative to the NS and GS cases. In neither the GS nor the GC case is there a layer of intense shear at the CBL top. This changes, however, as the free atmospheric vertical buoyancy gradient increases.

In Fig. 7.1e, the GS case exhibits the fastest CBL growth of all three shear configurations, and the GC case is in-between. Despite the stronger surface shear in the GC case (see Fig 7.2e), the CBL growth is slower than in the GS case. Comparing the GC cases of Figs. 7.1c and 7.1e, the entrainment zone shear appears a little weaker in Fig. 7.2e than in Fig. 7.2c, but the stratification is also weaker, and faster growth is seen. In Fig 7.1e, the GS case has stronger shear across the entrainment layer (Fig 7.2e) and also has the fastest CBL growth.

Although Figure 7.1e shows that the GS CBL grows more quickly than the GC CBL, this relationship is essentially reversed in conditions of stronger stratification (Fig. 7.1b), although the overall enhancement of CBL growth in the sheared cases is not as strong. The stability in the free atmosphere appears to prevent it. Some interesting features of the CBL momentum profiles for these cases are seen in Fig. 7.2b. Both the GS and GC cases have similar momentum profiles in the entrainment zone (near z = 800m), which suggests the entrainment zone shear may be similarly strong between the two cases. The GC interior CBL momentum (below 800m) is well-mixed and is weaker than any of the other GC cases. Since the runs are initialized in geostrophic balance, this slowing of the x-component of momentum can only be accomplished by surface friction and the resultant transport of weaker momentum upward through the mixed layer. The

decrease of momentum throughout the CBL interior causes shear to develop at the CBL top. Because of the accumulated effects of surface friction, slowing of mixed layer flow, and resulting accumulation of shear at the CBL top, the entrainment zone shear in Fig 7.2b is the strongest of all the GC cases. This GC case also has the fastest CBL growth relative to that of the corresponding GS case. In fact, it is much faster early in the run and then slower during the latter stages, when the GS case catches up. As will be seen later in this chapter, GC case CBLs such as these (with slower growth) develop entrainment zone shear much more rapidly than the GS CBLs do, but GS entrainment zone shear grows and eventually becomes larger, and the GS CBLs grow faster in the middle of the simulation, catching up to the GC CBL by the end. The evidence therefore suggests the entrainment zone shear plays a more dominant role than surface shear in enhancing CBL growth. Additionally, the mixed layer momentum is weaker, so the surface layer shear in this case, although it is still pretty strong, is the weakest among all the GC simulations, but only by a small amount. Despite the fact that the GC surface shear is stronger than GS surface shear in the latter part of the simulation, the CBL growth is slower.

Finally, we come to the leftmost column. In the bottom row, we find the case in which shear provides the largest enhancement of entrainment. It is also the case in which the buoyancy forcing is smallest, both in terms of the surface buoyancy flux and the stratification in the free atmosphere. With this particular combination of buoyancy forcing, the GS case exhibits the fastest CBL growth, but the GC CBL growth is also significantly faster than it is in the NS case. One note of caution must be made when analyzing these particular GS cases: the gradient Richardson number of the free

atmosphere is only 0.21, a value less than the critical Richardson number for the onset of Kelvin-Helmholtz (K-H) instability in a continuously stratified laminar flow (Kundu 1990). The critical value of Ri=0.25 is a *necessary* but not *sufficient* condition for the onset of K-H instability, so even though Ri<0.25 in this case, the presence of a solid underlying surface or the sponge layer probably prevents the development of K-H instabilities for the Ri values and CBL depths in this case. Regardless, in many laboratory flows, the Richardson number at the onset of K-H instability is much less than 0.25 (Kundu 1990). Additionally, the K-H instability analysis is technically only valid for non-turbulent flow, which is roughly applicable to the atmosphere above the CBL in these simulations.

To see if the sponge layer affected the development of K-H instabilities, a test simulation was performed with the sponge layer removed from the top of the domain. In these conditions, the CBL initially grew at the same rate as in the original simulation, but by the end, the growth was faster than in the original simulation, and it was increasing, suggesting that the background profile in the weakly stratified GS cases may, in fact, be unstable at some distance above the underlying surface.

The momentum in these weakly stratified GS cases is not well-mixed, and there are no layers with shear much greater than in the free atmosphere. The inherent background instability of these cases, in the K-H sense, probably prevents any additional shear from accumulating before turbulence generation occurs. In Fig. 7.1g, the surface shear in the GC case is very large, but the CBL growth slower than in the GS case, which has more of its shear across the entrainment zone (the depth of the entrainment zone will be seen in Figure 7.3).

Finally, we come to the case with weak buoyancy flux and moderate free atmospheric stratification (Fig. 7.1d). The GS and GC cases exhibit essentially the same rate of CBL growth in this situation, and in both cases, CBL growth is quite a bit faster than in the NS case. Looking at the momentum profiles, one sees, perhaps, slightly larger shear in the entrainment zone of the GS case than in that of the GC case, but the exact location and depth of the entrainment zone cannot be defined until looking at the heat flux profiles. We have come to this set of cases last, but it may be the most representative of conditions that might occur in the atmosphere, particularly for the GC case. The strong geostrophic wind and moderate stratification provide conditions most typical of situations when shear enhancement of entrainment might become significant in the atmosphere. This set of cases, therefore, will be the ones most often chosen for more detailed analyses presented later in this chapter, as well as in other chapters. It is the single set of cases where shear effects on entrainment are strongest for CBLs growing against a background profile guaranteed to be stable in the K-H sense.

Overall, a couple of *general comments* can be made about the enhancement of CBL growth in the GS and GC cases. First, the entrainment zone shear definitely appears to be more important than surface shear in determining the CBL growth rate. This point is exhibited by the fact that the GS cases, overall, have the fastest CBL growth and the strongest shear at the CBL top, but when GC cases have relatively rapid CBL growth, they also have strong shear at the CBL top—qualitatively similar to that of the GS cases. Second, the GC case CBLs also accumulate entrainment zone shear in more slowly growing CBL cases (weaker heat flux or stronger stratification), when the surface friction has the longest time to slow the momentum in the mixed layer. The CBLs in the GC

cases, which consistently have strong surface layer shear, never exhibit more rapid growth than in the GS cases, except when the entrainment zone shear is stronger. This suggests that surface layer shear does not play a direct role in increasing the CBL growth rate, but *indirectly*, the slower CBL flow, in general, causes shear to develop at the CBL top.

Finally, it must be emphasized that all the NS cases follow the ZOM equilibrium entrainment CBL growth rate (see Equations 3.47 and 5.5) very closely, supporting the results of Chapter 4.

Another couple of general comments can be made regarding the momentum profiles in Figure 7.2. Rapid CBL growth does not allow sufficient time for turbulence to thoroughly mix momentum in the CBL. This is not a surprising result, since the turbulent diffusivities for heat are often three times greater than the turbulent diffusivities of momentum in the CBL. For the cases with the fastest CBL growth, which are in the lower right portion of Fig. 7.2, the concept of a mixed layer, at least as far as momentum is concerned, does not seem to apply, and this may be evidence that the mixed layer models such as the ZOM and FOM may not describe the momentum profiles (and therefore shear-enhanced entrainment) particularly well. The momentum profiles definitely do not look ZOM-like or FOM-like. Nevertheless, integral shear production may still be similar. The ability of the ZOM and FOM to model sheared CBL entrainment will be assessed in Chapter 10.

The momentum-mixing effects of turbulence seem to be stronger in more stably stratified environments, where the CBL growth rate is slower, but it's not just the CBL growth rate that influences the mixing of momentum. Fedorovich and Conzemius (2004)

have shown that the turbulence in the upper portion of the CBL is greater when the stratification is stronger, and the mixing effects of this turbulence may explain the more well-mixed momentum profiles in the more stably stratified media.

7.2 Entrainment of Heat in Relation to Entrainment Zone Depth

The entrainment zone depths and dynamics of entrainment can be revealed by looking at the heat flux profiles in Figure 7.3. We define the entrainment zone depth δz_i, as $\delta z_i = z_{iu} - z_{il}$, with z_{iu} and z_{il} defined in Chapter 6 (see also Chapter 4 and Fig. 3.1) Basically, this is the layer where the heat flux is negative and the boundary layer is entraining heat from the free atmosphere.

In Fig. 7.3i, there is no layer of significantly negative heat flux. These simulated CBLs cannot be considered entraining CBLs, and in most respects, they can probably be considered encroaching CBLs. The convective plumes in this case have not passed their equilibrium level—that is—the level where their potential temperature is equal to the temperature of the surrounding air. Had the simulation continued further in time, the CBLs in this set of cases likely would have become *entraining* CBLs. All other CBLs in Fig. 7.3 are entraining.

The heat flux profiles typically show the same behavior as described in Fedorovich et al. (2004a) and also described to some extent in Sorbjan (1996b). The heat flux profiles in the cases with strongest stratification (0.010 K/m) are the most ZOM-like of any of the profiles, and with the weakest stratification (0.001 K/m), the profiles do not

look very ZOM-like at all. Rather, the heat flux reaches a minimum in the lower portion of the entrainment zone then decreases very slowly back to zero. In addition to this dependence on free atmosphere stratification, there also appears to be some dependence on the surface heat flux. For example, looking at all cases with a stratification of 0.003 K/m, the profiles with $Q_s = 0.03$ Km/s (Fig. 7.3d) look the most ZOM-like, and the profiles with stronger heat flux (Fig. 7.3f) deviate most significantly from the ZOM profile, with the heat flux returning more slowly to zero from its minimum. Weaker heat flux evidently causes the profiles to bear stronger resemblance to the ZOM, much like stronger stratification does. This effect can be noted for the NS cases, and the GS and GC cases seem to be subject to this effect as well.

In the cases with shear, the entrainment zone depth increases, and the heat flux minimum becomes stronger, meaning the sheared CBLs are entraining more heat than the shear-free CBLs are. The heat flux profile is significantly more variable in time than mean profiles of temperature or momentum, so the details of the heat flux profiles within the entrainment zone are more related to the time variability of the profile than they are to the dynamics of entrainment. However, the general features are still relevant to the entrainment dynamics. The deepening of the entrainment zone is associated with both the lowering of z_{il} (the lower limit of the entrainment zone) and the increase of z_{iu} (the upper limit). The most dramatic deepening of the entrainment zone is seen in Fig. 7.3g. In this GS case, the mixed-layer and entrainment zone are almost of the same depth—about 660 meters, and the heat flux minimum is more than five times its value in the NS case.

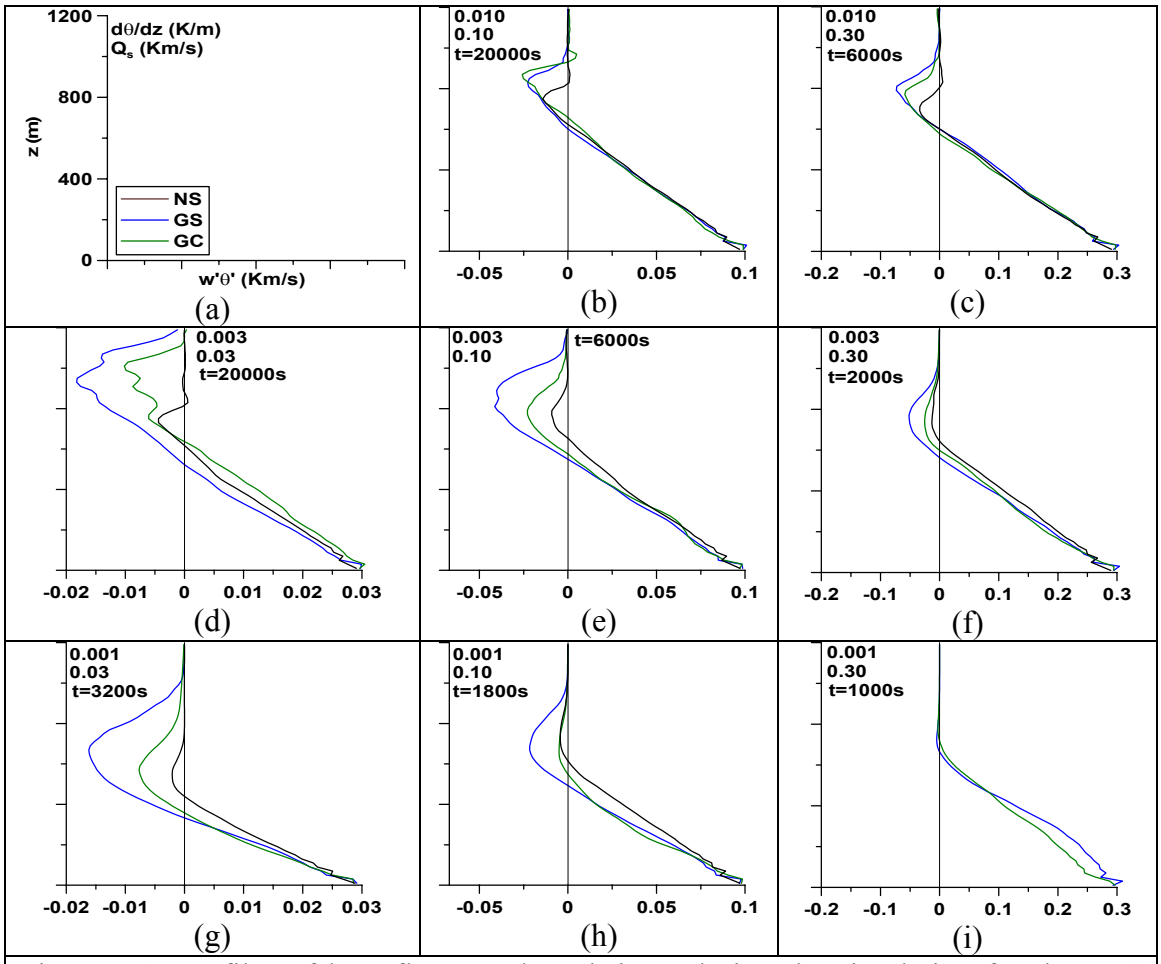

Figure 7.3: Profiles of heat flux at selected times during the simulation for the LES cases: (a) legend; (b) $\partial\theta/\partial z = 0.010$ K/m, $Q_s = 0.10$ Km/s; (c) $\partial\theta/\partial z = 0.010$ K/m, $Q_s = 0.30$ Km/s; (d) $\partial\theta/\partial z = 0.003$ K/m, $Q_s = 0.03$ Km/s; (e) $\partial\theta/\partial z = 0.003$ K/m, $Q_s = 0.10$ Km/s; (f) $\partial\theta/\partial z = 0.003$ K/m, $Q_s = 0.30$ Km/s; (g) $\partial\theta/\partial z = 0.001$ K/m, $Q_s = 0.03$ Km/s; (h) $\partial\theta/\partial z = 0.001$ K/m, $Q_s = 0.10$ Km/s; (i) $\partial\theta/\partial z = 0.001$ K/m, $Q_s = 0.30$ Km/s.

Fig 7.3d shows a similarly strong enhancement of entrainment heat flux in the sheared cases. Because the stratification is stronger, the minimum of heat flux is a little sharper, and the heat flux returns more quickly to zero in the upper portion of the entrainment zone. In the cases with strongest stratification (Figs. 7.3b and c), the shear does not enhance the negative heat flux as strongly, nor does it deepen the entrainment zone as much as in Figs. 7.3d and g. Figs. 7.3f and h show weaker heat flux, but the

weaker heat flux in these cases is a symptom of the short duration of these simulations. They do not cover a time period long enough for the CBL to become strongly entraining.

7.3 Potential Temperature Profiles

Figure 7.4 shows the potential temperature profiles for all the simulated cases. Within each panel, the NS, GS, and GC profiles are all taken at the same time during the simulation to highlight the accumulated effects of the entrainment of heat. The heat (temperature) is better mixed than the momentum, but some of the same differences among the cases are seen in the interior of the CBL: some temperature fields are better mixed than others, but the differences among the cases are not as large as they are with the momentum fields. The fields in (b), (c), (d), and (e) are all well-mixed. Those in (i) are not.

When looking at the differences between sheared and shear-free CBLs, the profiles in (d) stand out, by far, the most clearly. In both the GS and GC cases, considerable heat has been transported from the z=800-900m layer into the CBL interior. The effects are felt all the way to the surface, but the net temperature change is only about 0.25 K. This particular CBL case will be studied in detail later in this chapter as well as in Chapter 8.

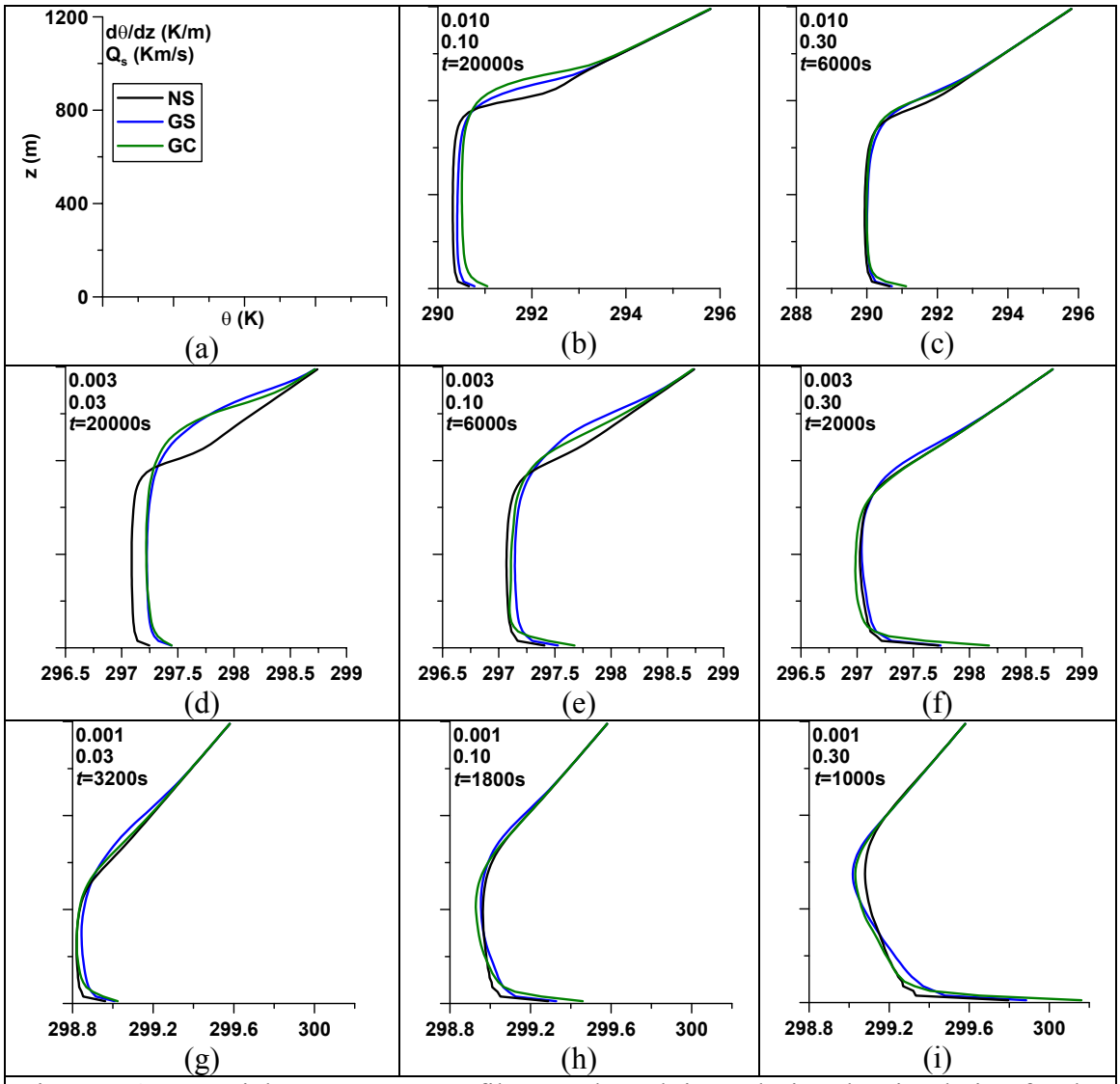

Figure 7.4: Potential temperature profiles at selected times during the simulation for the LES cases: (a) legend; (b) $\partial\theta/\partial z = 0.010$ K/m, $Q_s = 0.10$ Km/s; (c) $\partial\theta/\partial z = 0.010$ K/m, $Q_s = 0.30$ Km/s; (d) $\partial\theta/\partial z = 0.003$ K/m, $Q_s = 0.03$ Km/s; (e) $\partial\theta/\partial z = 0.003$ K/m, $Q_s = 0.10$ Km/s; (f) $\partial\theta/\partial z = 0.003$ K/m, $Q_s = 0.30$ Km/s; (g) $\partial\theta/\partial z = 0.001$ K/m, $Q_s = 0.03$ Km/s; (h) $\partial\theta/\partial z = 0.001$ K/m, $Q_s = 0.10$ Km/s; (i) $\partial\theta/\partial z = 0.001$ K/m, $Q_s = 0.30$ Km/s.

7.4 Entrainment of Momentum

The entrainment of momentum is not directly proportional to the entrainment of heat. Figure 7.5 illustrates the vertical turbulent flux of the *x*-component of momentum.

Since the x-component of momentum per unit volume contains density, these profiles of $\overline{w'u'}$ are formally momentum flux profiles normalized by density. The same applies to the other momentum fluxes and the mean profiles of momentum.

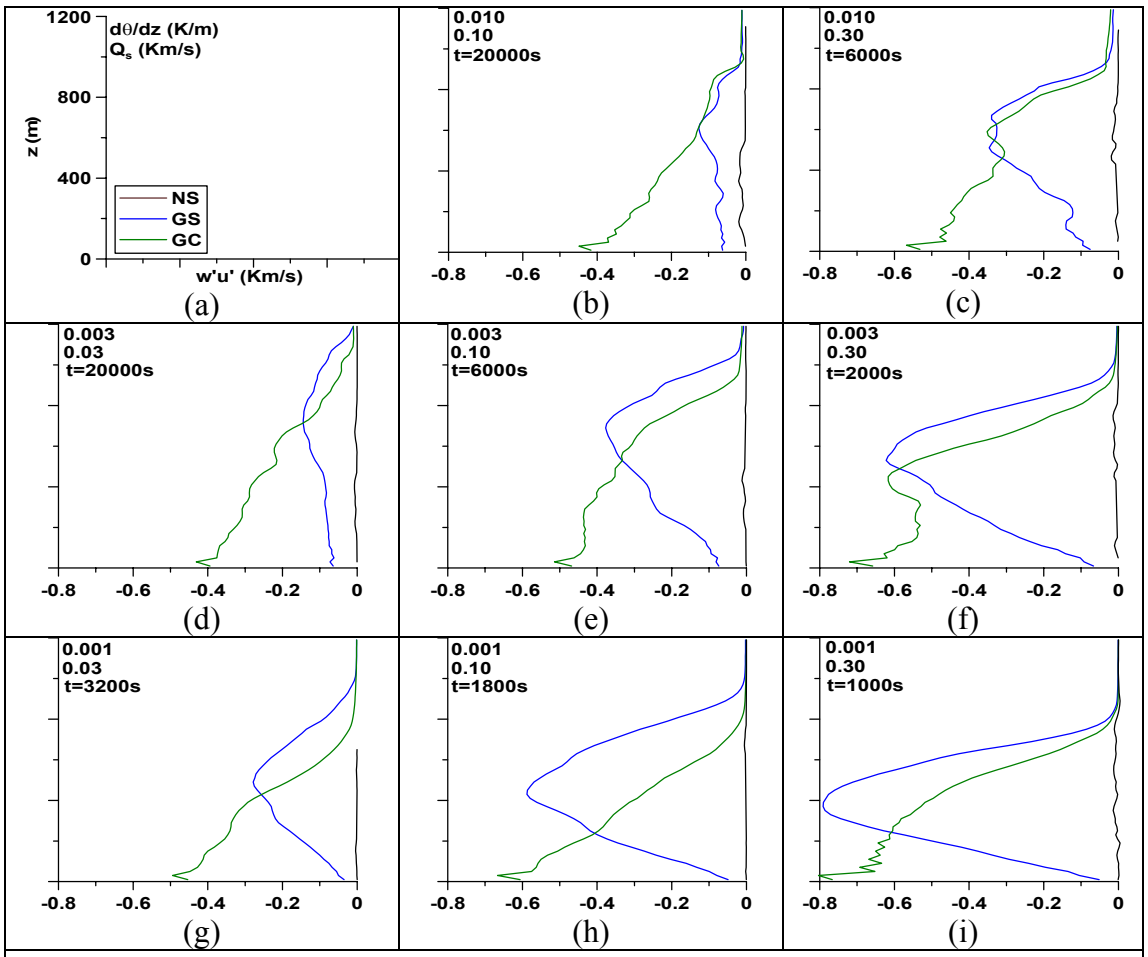

Figure 7.5: Profiles of the x-component of momentum flux at selected times during the simulation for the LES cases: (a) legend; (b) $\partial\theta/\partial z = 0.010$ K/m, $Q_s = 0.10$ Km/s; (c) $\partial\theta/\partial z = 0.010$ K/m, $Q_s = 0.30$ Km/s; (d) $\partial\theta/\partial z = 0.003$ K/m, $Q_s = 0.03$ Km/s; (e) $\partial\theta/\partial z = 0.003$ K/m, $Q_s = 0.10$ Km/s; (f) $\partial\theta/\partial z = 0.003$ K/m, $Q_s = 0.30$ Km/s; (g) $\partial\theta/\partial z = 0.001$ K/m, $Q_s = 0.03$ Km/s; (h) $\partial\theta/\partial z = 0.001$ K/m, $Q_s = 0.10$ Km/s; (i) $\partial\theta/\partial z = 0.001$ K/m, $Q_s = 0.30$ Km/s.

Unlike the lack of heat entrainment in Fig. 7.3i, Fig 7.5i shows the momentum entrainment to be strongest in these most rapidly growing CBLs. The shape of the

momentum flux profiles is significantly different between the GC and the GS cases. In the former, the profile has a fairly typical shape observed in the atmosphere. Momentum in the surface layer is decreased by contact with the ground, and turbulence carries this weaker momentum upward. The momentum flux is therefore is of opposite sign to the momentum throughout the whole depth of the CBL. The GC case momentum flux profile is typically characterized by a minimum near the surface, with the flux slowly increasing throughout much of the CBL interior, and then increasing more rapidly to zero in the upper portion of the CBL. The vertical flux divergence ($\partial \overline{w'u'} / \partial z$) is positive, indicating the loss of momentum in the CBL. $\partial \overline{w'u'} / \partial z$ is more strongly positive in the upper portion of the CBL, indicating the strong entrainment of momentum at the CBL top.

The momentum flux is significantly stronger in the most rapidly growing CBLs, but the stronger flux is insufficient to counter the effects of more rapid CBL growth, so the momentum fields are decidedly less well-mixed in Fig 7.2i compared to Figs. 7.2b and d. If the sheared CBL growth rate is about the same order of magnitude as the shear-free CBL growth rate, which appears to be the case in Fig. 7.1i, then one can derive some conclusions about the relationships among the CBL growth rate, momentum, and momentum flux profiles, using the ZOM entrainment equation (5.5). We see that $z_i(t) \sim B_s^{1/2}$ and also, $z_i(t) \sim N^{-1} \sim \left(\partial\theta / dz\right)^{-1/2}$, where N and $\partial\theta / dz$ are their free atmospheric values. If the temperature gradient increases by a factor of ten, we would expect the CBL growth rate to be about one third as fast. Looking at Equation 3.35, we expect the entrainment of momentum at the CBL top to be proportional to dz_i / dt. We would therefore expect, for momentum profiles to remain well-mixed, that the momentum flux should triple if the potential temperature gradient in the free atmosphere

decreases by a factor of ten. Comparing Fig 7.5i with Fig 7.5c, we see that the momentum flux for the GC case increases only about 50 percent. This is far short of what would be required for the momentum in Fig. 7.2i to be as well mixed as in Fig. 7.2c. For the GS case, there is at least a doubling of the momentum flux (see Fig. 7.5i versus Fig. 7.5c), but this is also insufficient for the momentum fields to remain well-mixed. So, in general, although the momentum flux is weaker in situations with more slowly growing CBLs (Figs. 7.5b,d), its magnitude, relative to the CBL growth rate, makes it more capable of mixing momentum in the interior of those CBLs than in more quickly growing CBLs.

The momentum flux profiles in the GS cases show some fairly interesting characteristics. The flux starts close to zero at the ground, decreases to a minimum value in the middle or upper portion of the CBL, then increases again, returning to zero. The flux divergence is negative in the lower portion of the CBL, indicating the turbulent flux is increasing the momentum in the lower portion of the CBL. In the upper portion of the CBL, the momentum flux is strongly divergent, and there is momentum loss, which is similar to the GC case. Thus, the CBL turbulence is removing momentum from the CBL top and transporting it downward into the lower portion of the CBL. This feature of momentum flux profiles is consistent with the GS momentum profiles shown in Figure 7.2. The momentum in the lower portion of the CBL is greater than its initial geostrophic value, and the momentum in the upper portion of the CBL has become less than its initial value. The momentum flux profile is not exactly ZOM-like. Looking at Equation 3.31, we expect a roughly linear profile of momentum flux in this CBL (if the Coriolis terms

are small). This seems to be the case; however the flux does not jump back to zero very quickly at the CBL top.

The time series of momentum and momentum flux in the GC cases can be fictitiously visualized by considering a fixed level that is initially in the free atmosphere above the CBL. When the CBL reaches this level, the momentum flux divergence increases rapidly, and the momentum experiences a rather sudden drop to its value in the interior of the CBL. After this initial rapid drop, the rate of change is smaller, as stronger momentum continues mixing downward from above, but weaker momentum, due to the effects of surface friction, continues to be mixed upward. The latter effect seems to be slightly stronger.

In the GS case, as the CBL reaches the selected level, the momentum experiences the same initially rapid decrease as in the GC case. However, since the initial near-surface momentum is very small, the effects of surface friction are weaker, and the upward flux of weaker momentum is smaller than what it would be in the GC case. As the CBL continues to grow, it entrains ever stronger momentum from aloft and the effects of momentum entrainment exceed the effects of surface friction. The momentum flux becomes convergent, and momentum slowly increases again.

7.5 Ageostrophic Momentum

As the CBL grows, the vertical turbulent flux of momentum causes the momentum to deviate from its geostrophic value, resulting in the increase of the *y*-component of momentum due to the combined effects of the large scale pressure gradient and Coriolis forces. Figure 7.6 shows the profiles of the mean *y*-component of

momentum. The mean y-component of momentum $\bar{v}$ becomes significant only if the simulation time is long and the Coriolis force has time to act. In the most rapidly growing CBLs (Figs. 7.6f,h,i), the simulations are not long enough for this to happen. For the more slowly growing CBLs (Figs 7.6b,c), $\bar{u} < u_g$ in the GC cases, resulting in an increase in $\bar{v}$ (see Equation 3.11).

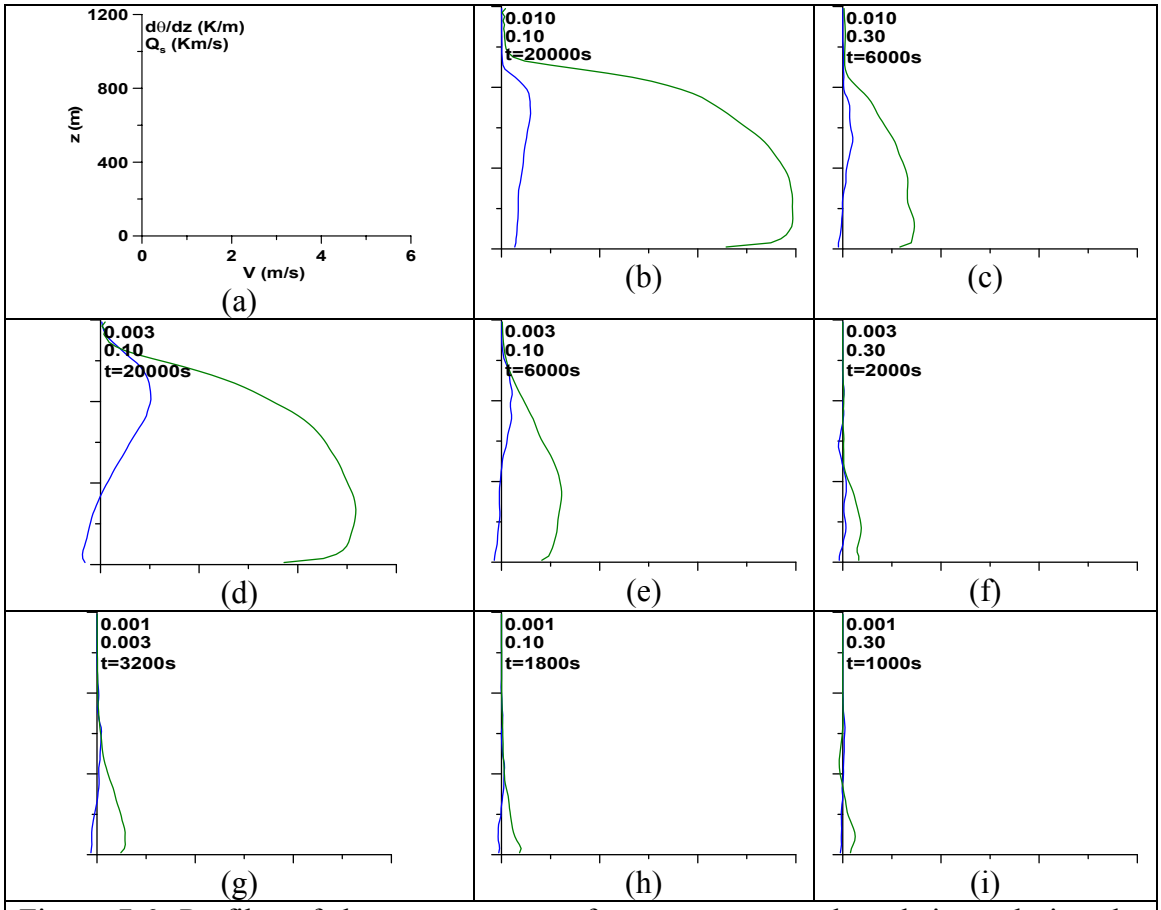

Figure 7.6: Profiles of the *y*-component of momentum at selected times during the simulation for the LES cases: (a) legend; (b) $\partial\theta/\partial z = 0.010$ K/m, $Q_s = 0.10$ Km/s; (c) $\partial\theta/\partial z = 0.010$ K/m, $Q_s = 0.30$ Km/s; (d) $\partial\theta/\partial z = 0.003$ K/m, $Q_s = 0.03$ Km/s; (e) $\partial\theta/\partial z = 0.003$ K/m, $Q_s = 0.10$ Km/s; (f) $\partial\theta/\partial z = 0.003$ K/m, $Q_s = 0.30$ Km/s; (g) $\partial\theta/\partial z = 0.001$ K/m, $Q_s = 0.03$ Km/s; (h) $\partial\theta/\partial z = 0.001$ K/m, $Q_s = 0.10$ Km/s; (i) $\partial\theta/\partial z = 0.001$ K/m, $Q_s = 0.30$ Km/s.

The same does not hold for the GS cases. In the upper portion of the CBL, $\bar{u} < u_g$, so $\bar{v}$ increases, but in the lower portion of the CBL, $\bar{u} > u_g$, so $\bar{v}$ is negative there. These changes in $\bar{v}$ are not symmetric. There is more of an increase in $\bar{v}$ in the upper portion of the CBL than a decrease in the lower portion. In Fig. 7.6b, $\bar{v}$ is positive throughout the depth of the CBL for the GS case, whereas the remaining GS cases have some layer of $\bar{v} < 0$. The momentum flux in the interior of the CBL may be large enough to overcome the effects of the pressure gradient and Coriolis forces in this case.

One might gain a better understanding of this difference by performing a quick scale analysis of the Coriolis force versus the momentum flux divergence. Fig. 7.7 shows the turbulent vertical flux of the lateral component of momentum for the two cases with the strongest $\bar{v}$. In Figure 7.7b, the flux changes 0.1 m^2/s^2 over a depth of approximately 500 meters, making for a flux convergence of 2×10^{-4} m/s^2 over this layer. With a Coriolis parameter of 1×10^{-4} s^{-1} and a departure in $\bar{u}$ from its geostrophic value ranging from 3 m/s to about -1 m/s over this layer, the combined Coriolis and pressure gradient forces, $-f(\bar{u}-u_g)$, are -3×10^{-4} m/s^2 to 1×10^{-4} m/s^2 over this layer, which is similarly strong to the turbulent flux convergence, so either term can become dominant. In Fig. 7.7b, the flux convergence is just a little stronger than the Coriolis or pressure gradient terms, and in Fig. 7.7c, it is a little weaker. In summary, as the simulation proceeds, the Coriolis force increases Δv because of its actions on the ageostrophic component of momentum (Figs. 7.6b,d) in the CBL interior (subgeostrophic $\bar{u}$), enhancing the shear at the CBL top.

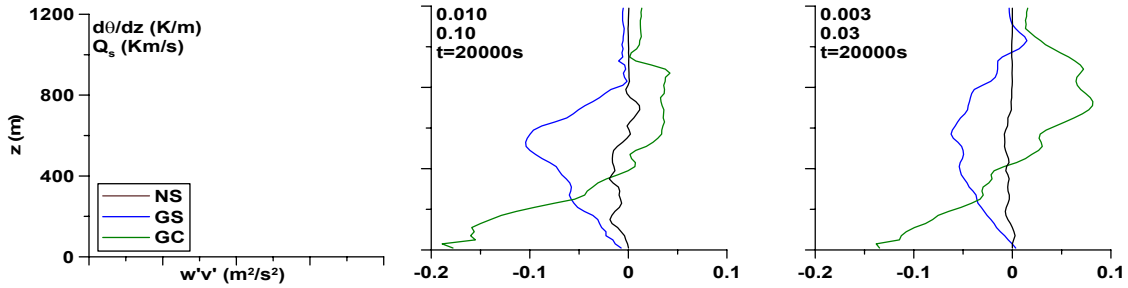

(a) (b) (c)

Figure 7.7: Profiles of the turbulent vertical flux of the *y*-component of momentum at selected times during the simulation for the LES cases: (a) legend; (b) $\partial\theta/\partial z = 0.010$ K/m, $Q_s = 0.10$ Km/s; (c) $\partial\theta/\partial z = 0.010$ K/m.

7.6 Velocity Variance Profiles

Figure 7.8 shows the *u* variance profiles at the selected times during the simulations. The profiles reflect the effects of surface buoyancy flux, free atmosphere stratification, and shear. For the NS cases (except for Fig. 7.8i, which is not an entrainment regime), if the scaling considerations of Deardorff (1980) and Zilitinkevitch (1991) are to apply, the profiles should generally be self-similar and retain the same shape in all the cases. However, there is some dependence on stratification. In Chapter 3, it was stated that, according the Deardorff (1980) and Zilitinkevitch (1991), the profiles of TKE were expected to be self-similar and integrate to a constant when appropriately scaled. However, it is well known (Sorbjan 1996b) that the TKE profiles are dependent on *N*. The dependence of the TKE profiles on the free atmospheric stratification is also discussed in Fedorovich et al. (2004b). This dependence does not greatly affect the equilibrium shear-free entrainment regime, since z_i vs. t in the NS simulations matches the theoretical curve (3.47) very closely for all values of stratification and buoyancy flux tested (see Chapters 4 and 5).

In Figs. 7.8g and h, the NS case u variance starts out large at the surface, decreases gradually through the interior of the CBL, then decreases a little more quickly in the entrainment zone. Where the stratification is stronger (Figs. 7.8b,c), the profiles have a maximum at the surface, followed by a decrease through most of the CBL, then a secondary maximum at the CBL top, owing to the thermals impinging on the strong inversion there.

The variance in the GC cases has a very pronounced maximum in the surface layer, and it decreases in the CBL interior. In Fig. 7.8i, it decreases gradually to zero without encountering a secondary maximum—a characteristic that is most likely due to the non-entraining regime. All other profiles have a secondary maximum near the CBL top. The secondary maximum is generally sharper in cases with stronger stratification, except for Fig. 7.8d, where there is no sharp maximum. The reason behind the lack of a sharp maximum in this GC profile may be associated with the time variability of the second order statistic. Another peculiar characteristic of the GC u-variance profiles is the apparent stratification-dependence of the surface layer maximum. The maximum is largest for cases with the weakest stratification and decreases with stronger stratification. A buoyancy flux-dependence is less obvious in the profiles. The variance is weaker when the mixed layer velocity ($\overline{u}$) is weaker, as occurs in more slowly growing CBLs in stronger N and weaker B_s.

For the GS cases, the maximum variance is located in the entrainment zone. In general, the maxima are sharper when stratification is stronger and larger when the surface buoyancy flux is stronger, but this is not true in all cases. The u-variance does not drop off so fast with more slowly growing CBLs, particularly those in strong

stratification, because the effects of plumes impinging up the strongly stratified entrainment zone are seen. The stronger stratification causes a narrower entrainment zone and suppresses the vertical velocity there. The horizontal velocity variance then increases due to the sideward transport of air from squashed thermals as they crash against the strong inversion. In essence, the vertical velocity variance is converted to horizontal velocity variance by the effects of pressure.

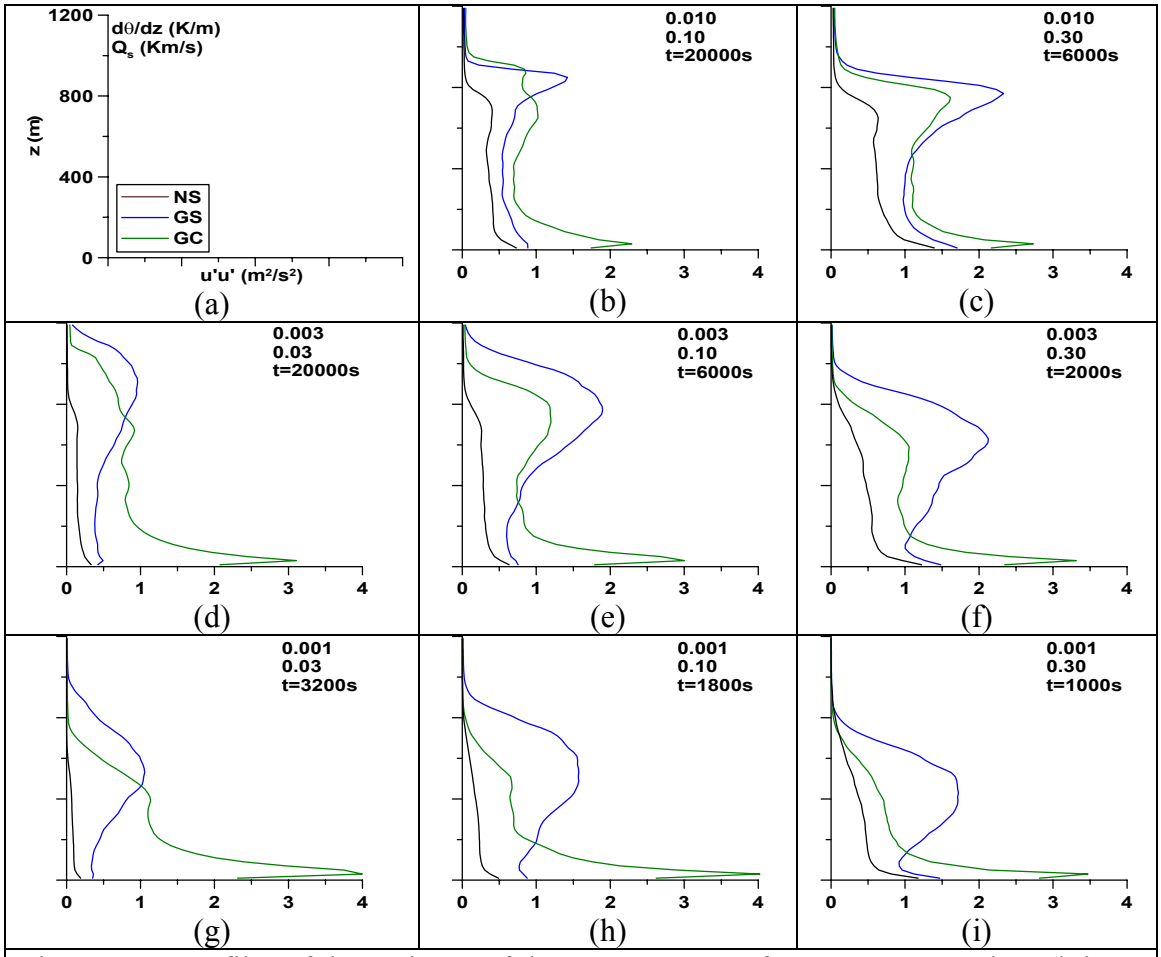

Figure 7.8: Profiles of the variance of the x-component of momentum at selected times during the simulation for the LES cases: (a) legend; (b) $\partial\theta/\partial z = 0.010$ K/m, $Q_s = 0.10$ Km/s; (c) $\partial\theta/\partial z = 0.010$ K/m, $Q_s = 0.30$ Km/s; (d) $\partial\theta/\partial z = 0.003$ K/m, $Q_s = 0.03$ Km/s; (e) $\partial\theta/\partial z = 0.003$ K/m, $Q_s = 0.10$ Km/s; (f) $\partial\theta/\partial z = 0.003$ K/m, $Q_s = 0.30$ Km/s; (g) $\partial\theta/\partial z = 0.001$ K/m, $Q_s = 0.03$ Km/s; (h) $\partial\theta/\partial z = 0.001$ K/m, $Q_s = 0.10$ Km/s; (i) $\partial\theta/\partial z = 0.001$ K/m, $Q_s = 0.30$ Km/s.

Figure 7.9 shows the profiles of *v*-variance. For the NS cases, the profiles are essentially the same as those for the *u*-variance and are caused by the same effects.

For the GC cases, some rather interesting behavior is seen. The two GC cases with the largest vertical gradients of $\bar{v}$ (Figs. 7.6b,d) do not have the largest *v*-variance (Figs. 7.9b,d). This can be explained by the fact that these CBLs are slowly growing and have weaker entrainment of momentum. The surface variance is still large and appears to be largest when the surface buoyancy flux is strongest. This can be explained by the stronger downward transport of *u* in these cases, accompanied by pressure forces working at the surface and converting it to lateral velocity variance. Essentially, this is the transverse circulation of the CBL horizontal convective rolls. In the GS cases, the entrainment zone *v*-variance is largest when the CBL grows the fastest, which seems consistent with the higher *x*-component momentum flux in those cases. Again, pressure forces would have to work to convert some of this *x*-component velocity variance into the variance of the *y*-component.

Finally, the *w*-variance is shown in Figure 7.10. The profiles are generally consistent with what might be expected if shear is enhancing entrainment. In the GS and GC simulations with faster CBL growth, the vertical velocity variance is larger at the CBL top. In Fig. 7.10i, the GC case shows a bit of a sharper maximum in the lower-middle portion of the CBL, and in fact, a majority of the GC cases show this enhanced maximum. Otherwise, the GS, NS, and GC profiles in Fig. 7.10i have qualitatively the same shape. All three profiles diminish smoothly to zero at the CBL top in much the same manner.

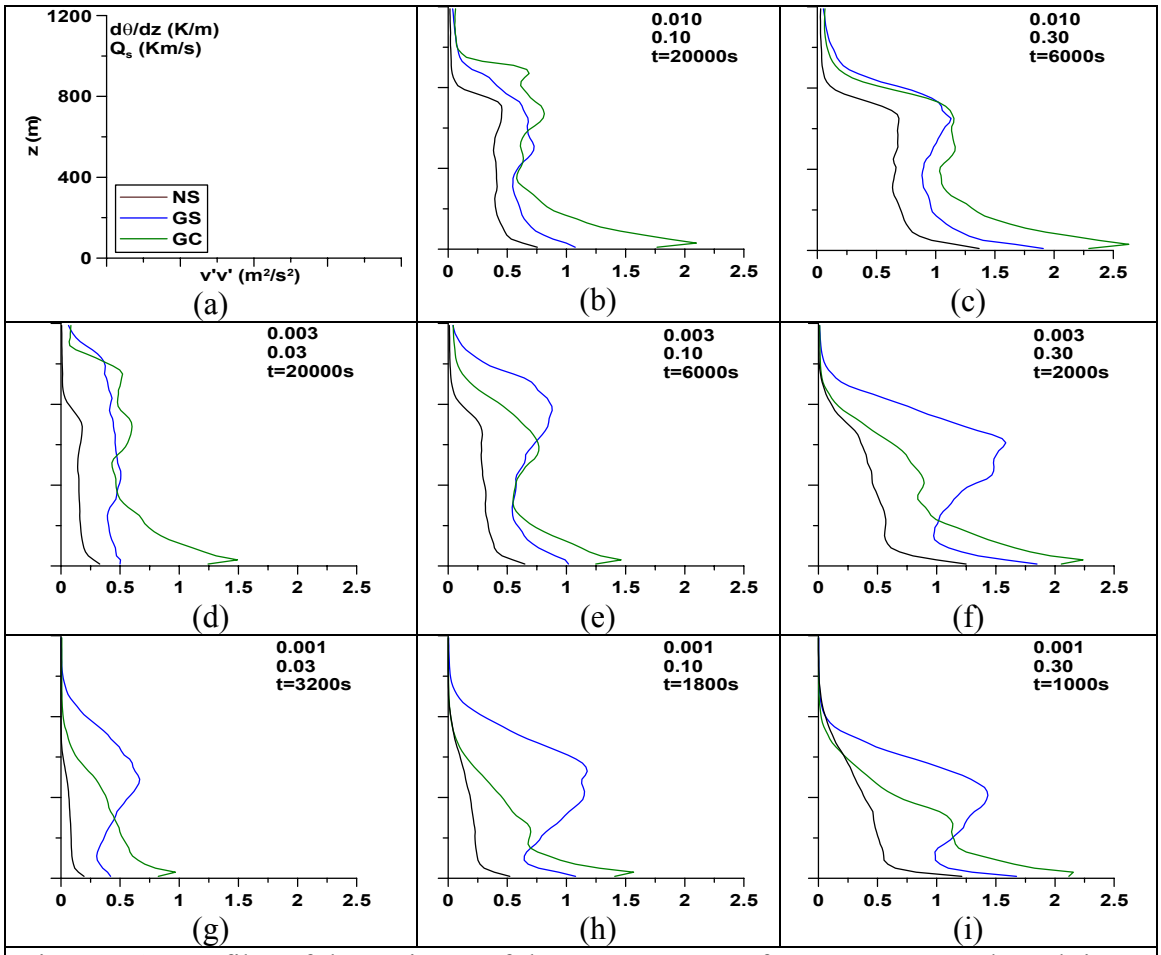

Figure 7.9: Profiles of the variance of the *y*-component of momentum at selected times during the simulation for the LES cases: (a) legend; (b) $\partial\theta/\partial z = 0.010$ K/m, $Q_s = 0.10$ Km/s; (c) $\partial\theta/\partial z = 0.010$ K/m, $Q_s = 0.30$ Km/s; (d) $\partial\theta/\partial z = 0.003$ K/m, $Q_s = 0.03$ Km/s; (e) $\partial\theta/\partial z = 0.003$ K/m, $Q_s = 0.10$ Km/s; (f) $\partial\theta/\partial z = 0.003$ K/m, $Q_s = 0.30$ Km/s; (g) $\partial\theta/\partial z = 0.001$ K/m, $Q_s = 0.03$ Km/s; (h) $\partial\theta/\partial z = 0.001$ K/m, $Q_s = 0.10$ Km/s; (i) $\partial\theta/\partial z = 0.001$ K/m, $Q_s = 0.30$ Km/s.

Outside Fig. 7.10i, however, the similarity among the NS, GS, and GC *w*-variance profiles disappears. In Figs. 7.10f and h, the GS cases show greater *w*-variance than the others in the upper CBL, but the shape of the profile remains much the same as in the NS and GC cases.

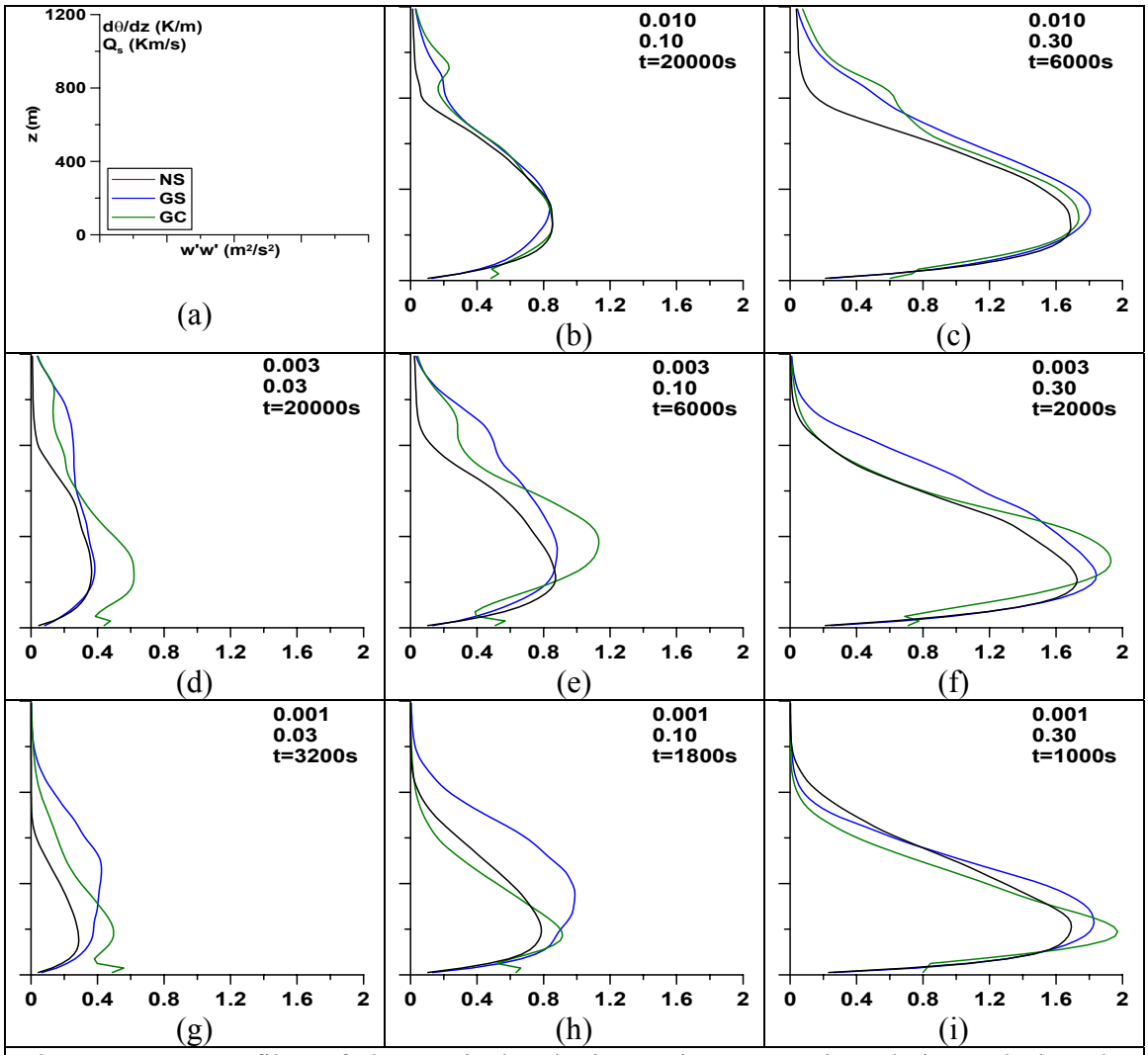

Figure 7.10: Profiles of the vertical velocity variance at selected times during the simulation for the LES cases: (a) legend; (b) $\partial\theta/\partial z = 0.010$ K/m, $Q_s = 0.10$ Km/s; (c) $\partial\theta/\partial z = 0.010$ K/m, $Q_s = 0.30$ Km/s; (d) $\partial\theta/\partial z = 0.003$ K/m, $Q_s = 0.03$ Km/s; (e) $\partial\theta/\partial z = 0.003$ K/m, $Q_s = 0.10$ Km/s; (f) $\partial\theta/\partial z = 0.003$ K/m, $Q_s = 0.30$ Km/s; (g) $\partial\theta/\partial z = 0.001$ K/m, $Q_s = 0.03$ Km/s; (h) $\partial\theta/\partial z = 0.001$ K/m, $Q_s = 0.10$ Km/s; (i) $\partial\theta/\partial z = 0.001$ K/m, $Q_s = 0.30$ Km/s.

It is in Fig. 7.10(g) where the shapes of the profiles really start to differ. The NS profile has a lower-CBL maximum and returns slowly to zero above that maximum, but the GS profile has its maximum much higher in the CBL. The GC profile has its maximum in about the same spot as in the NS case, but the variance returns much more

slowly to zero above that point. In the remaining cases, sheared CBLs have larger variance in the upper CBL, and the GS and GC profiles have an additional bulge in variance at the CBL top, where there is, in some cases, a secondary maximum. So far, no explanation has been found for this secondary maximum, but it is seen in these results as well as in simulations using other LES codes (Fedorovich et al. 2004b). One would expect larger variance but not necessarily a maximum. It could be that some turbulence generation occurs in a stable layer there, or it could be due to some particular feature of convective roll geometry. Regardless of the reasons for these maxima, the variance at the top of the sheared CBLs exceeds that at the top of the shear-free CBL. This supports the idea of shear-generation of TKE at the CBL top and generally refutes the theory of shear sheltering (Hunt and Durbin 1999).

7.7 Entrainment Flux Ratios

An understanding of the dynamics of entrainment in sheared CBLs can be seen by plotting the entrainment flux ratio as a function of time. Also, plotting the time series of the entrainment flux ratio might reveal whether or not the sheared CBLs reach some sort of an equilibrium entrainment regime. If they do, deriving analytic relationships among the parameters of entrainment might become much easier.

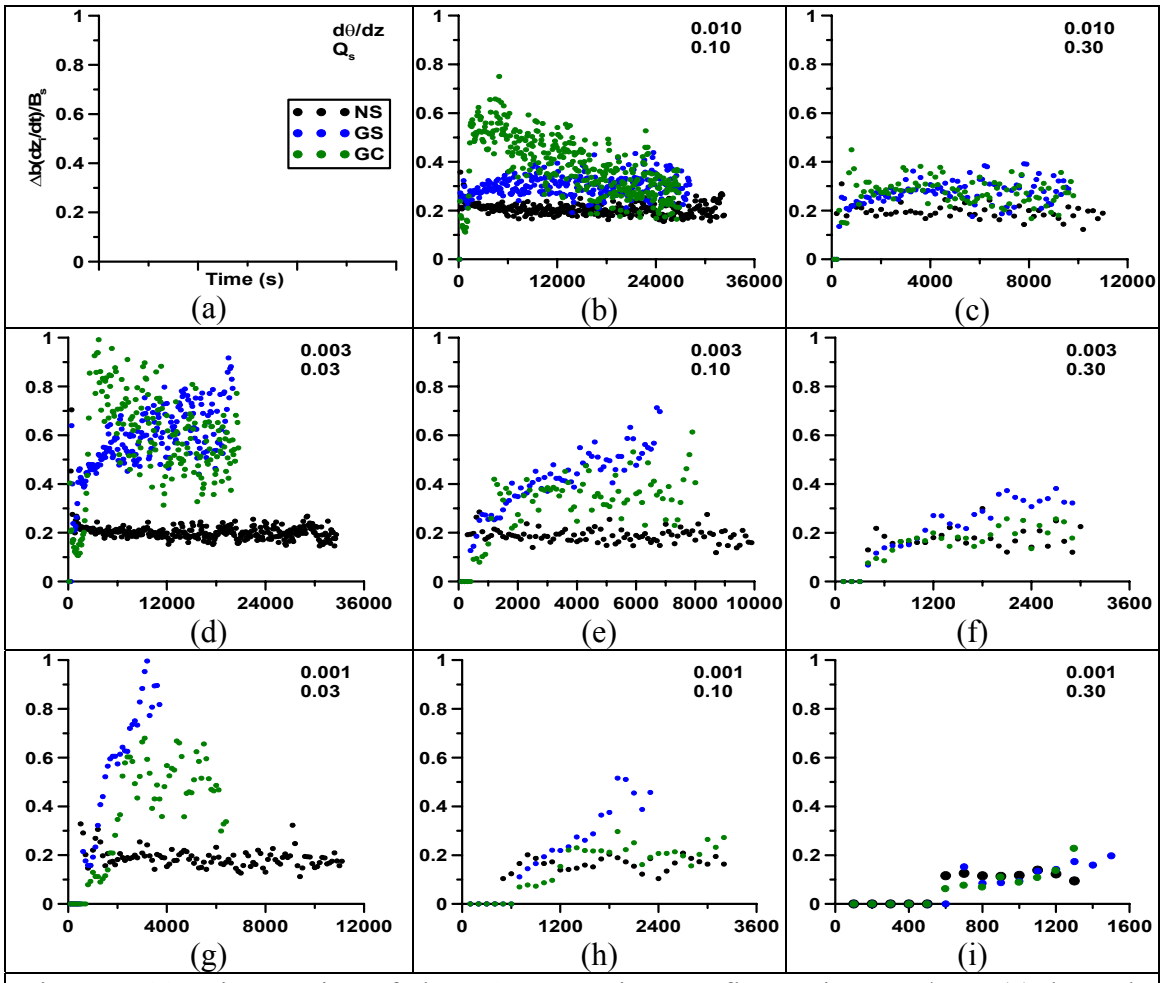

Figure 7.11: Time series of the ZOM entrainment flux ratio $-B_{i0}/B_s$: (a) legend; (b) $\partial\theta/\partial z = 0.010$ K/m, $Q_s = 0.10$ Km/s; (c) $\partial\theta/\partial z = 0.010$ K/m, $Q_s = 0.30$ Km/s; (d) $\partial\theta/\partial z = 0.003$ K/m, $Q_s = 0.03$ Km/s; (e) $\partial\theta/\partial z = 0.003$ K/m, $Q_s = 0.10$ Km/s; (f) $\partial\theta/\partial z = 0.003$ K/m, $Q_s = 0.30$ Km/s; (g) $\partial\theta/\partial z = 0.001$ K/m, $Q_s = 0.03$ Km/s; (h) $\partial\theta/\partial z = 0.001$ K/m, $Q_s = 0.10$ Km/s; (i) $\partial\theta/\partial z = 0.001$ K/m, $Q_s = 0.30$ Km/s.

The time series of the ZOM entrainment flux ratio $-B_{i0}/B_s$ is shown in Figure 7.11. As expected, the sheared CBLs show greater entrainment flux ratios (provided entrainment of heat is occurring). Conceptually, the shear-generated TKE at the CBL top is immediately available to drive the entrainment process, and indeed, enhanced entrainment zone heat flux is observed when there is entrainment zone shear (see Fig. 7.2). Also, the ratio increases as the surface heat flux decreases. This result is intuitively

obvious from a mathematical standpoint, but it is also an affirmation that the shear-generation of TKE does not require the buoyancy generation of TKE. That is, shear-generated turbulence at the CBL top is not necessarily stronger when the surface heat flux is stronger. In fact, the rapid CBL growth when the heat flux is stronger prevents the accumulation of shear at the CBL top, as was discussed in Section 7.1.

In the GS cases, the entrainment flux ratio starts out rather small because shear is initially weak. However, once the CBL becomes more developed, the entrainment flux ratio increases and continues to increase throughout the duration of the simulation. This is true whether the ratio is viewed in terms of its direct LES value or the ZOM value.

The GS case entrainment flux ratio also appears to be dependent on the free-atmosphere stratification. When the stratification is stronger, the entrainment flux ratio grows relatively slowly, and it approaches a nearly constant value that only slightly exceeds its NS value (Fig. 7.11e). With weaker outer stratification, the ratio climbs rapidly and continues to increase throughout the duration of the simulation (Fig. 7.11g). With moderate outer stratification, the ratio climbs somewhat rapidly at first and begins to level off but still is slowly increasing at the end of the simulation. In most of the shear cases, an equilibrium entrainment regime does not become established; the entrainment flux ratio, whether taken directly from LES ($-\delta B_i / B_s$) or interpreted within the ZOM context (see Fig. 3.1; $\delta B_i / B_s$), never reaches a constant, except, perhaps, for the cases with the strongest stratification. An equilibrium regime was not necessarily expected, and it does not occur in the sheared CBLs.

Some surface buoyancy flux dependence of the GS entrainment flux ratio is seen as well. Comparing Figs. 7.11d-f and b-c, one sees that the ratio increases the most when

the surface buoyancy flux is weakest. When all GS simulations are viewed on the same time axis (not shown), the differences among their entrainment flux ratios mostly disappear. The CBLs with the stronger surface buoyancy flux grow more quickly, and for any given real time in the simulation, they are deeper and experience stronger shear, despite the fact that these faster-growing CBLs are not as effective at concentrating shear at their tops.

In the GC cases, the entrainment flux ratio behaves quite differently from the GS ratios. The GC ratios increase much more rapidly near the beginning of the simulation then decrease slowly or remain fairly constant thereafter. The initial jump is associated with the onset of turbulence in the simulated CBL. In this initial stage of its development, the CBL is so shallow that the surface shear is essentially indistinguishable from the entrainment zone shear, and the shear-generated TKE causes very strong entrainment at the onset of resolved turbulence. Also, the proximity of the entrainment zone to the surface layer during these early stages may make it easier for the surface shear-generated TKE to be transported to the entrainment zone where it can be used available for entrainment. This may explain some of the behavior seen in Figs. 7.11b and d in which case the entrainment flux ratio slowly decreases with time.

The decrease with time is not observed in many of the other cases, such as in Figs. 7.11e, but in some situations (e.g. Fig 7.11d), the entrainment flux ratio experiences rather explosive growth during the onset of turbulence. However, characteristics of the immediate onset should be regarded to be dependent on the method of initialization and the numerical scheme in the simulations and not necessarily reflective of the true nature of the transition to turbulence in the atmosphere. Regardless of the onset characteristics,

the gradual decrease of entrainment flux ratio with time during the simulations (Figs. 7.11b,d) is smooth and long enough that the CBL has probably forgotten about these initial conditions. Stronger stratification may act to damp the explosive onset of entrainment in the GC cases of Fig. 7.11b, and weaker stratification might make it easier for the initial random temperature perturbations to initiate convection (Fig. 7.11g).

A look at the TKE budgets might help explain the behavior of the time series of entrainment flux ratio seen above. In particular, the budgets might reveal whether or not the proximity of the entrainment zone to the surface layer during these early stages allows the surface shear-generated TKE to be transported to the entrainment zone.

7.8 Turbulence Kinetic Energy Budgets

7.8.1 Profiles of Terms in the Turbulence Kinetic Energy Equation

The TKE budgets for the simulations with $\partial\theta/\partial z = 0.003$ K/m and Q_s=0.03 Km/s are compared in Figure 7.12. These profiles were chosen at moments when the CBL depth in all cases was nearly 800 m, so that the resolution was the same. The NS case is shown in the center so that the sheared CBLs can most easily be compared to the shear-free CBL.

The effects of shear stand out quite vividly. As is shown in Figs. 7.4 and 7.12, the heat flux minimum is larger in both the sheared cases than in the shear-free case, and the entrainment zone is considerably deeper. The shear production terms in the entrainment zone are of comparable magnitude in the GS and GC cases, although at this late time in the simulation, the GS case shear production has become a little larger. Consistent with the work of Price et al. (1978), it is evident that a significant portion of the shear-

generated TKE in the entrainment zone is dissipated, but the dissipated fraction appears to be more than suggested by Price (1978), who indicated that roughly 30 percent of the shear-generated TKE was dissipated. The entrainment zone TKE dissipation is a bit larger in the GS case than in the GC case, but so is the shear generation of TKE. In the upper portion of the entrainment zone, the buoyancy flux and dissipation become roughly equal.

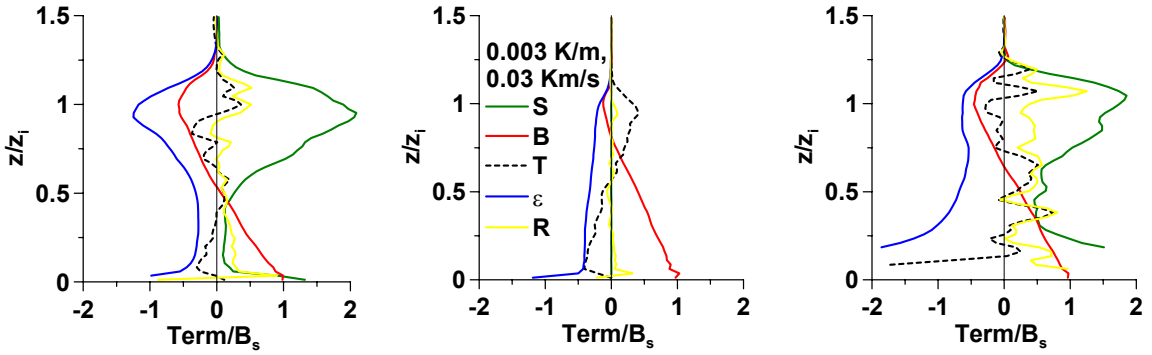

Figure 7.12: TKE budgets, in the RANS sense, for the simulations with a stratification of $d\theta/dz$=0.010 K/m and a surface heat flux of Q_s=0.3 Km/s for (a) GS, (b) NS, and (c) GC cases. The green lines denote the shear production term, solid black lines the buoyancy term, dashed black line the vertical transport term, blue line the dissipation, and yellow the residual.

The transport in the NS case is strongly related to the buoyancy production of turbulence. The transport move moves TKE from the lower portion to the upper portion of the CBL, and it has roughly a linear profile (see also Moeng and Sullivan 1994), much like the buoyancy flux profile, but opposite in sign. In the GS and GC cases, the transport term is smaller in the vicinity of the entrainment zone and becomes slightly negative where the shear term is largest. This does not necessarily mean there is less upward transport of the buoyancy-produced TKE. Rather, there is probably some

compensating downward transport of shear-generated TKE from the entrainment zone into the interior of the CBL.

Essentially, wherever there is shear, the dissipation of TKE is enhanced. This is seen particularly well in the GC case, where the shear production of TKE and dissipation in the surface layer are both particularly strong. The GC transport of TKE is enhanced right at the surface, but the profile does not differ much from the NS transport above that, suggesting that nearly all the shear-generated TKE near the surface is dissipated locally or transported into the middle of the CBL, where it is dissipated. In the GS surface layer, where the shear is weak, the transport profile more closely matches the NS transport profile.

7.8.2 Evolution of the TKE Budgets

We now examine the evolution of some of the mean wind profiles, turbulent moments, and TKE budgets in order to understand the evolution of the entrainment flux ratios in the GC and GS cases. In the GC case, the rapid onset of very high entrainment flux ratios, especially in Fig. 7.11b, d, and g, followed by a gradual decrease, needs to be analyzed to understand if it is a result of the upward transport of surface shear-generated TKE or if it is related to some other phenomenon. The cases with $\partial\theta/\partial z$=0.003 K/m and Q_s=0.03 Km/s will be examined. Because the entrainment rate in this particular GC case is strongest relative to that in the GS case.

We start by looking at the evolution of the GC momentum profiles, which are displayed in Fig 7.13. The evolution of the *x*- and *y*-components of the mean wind proceeds in quite a different manner. The value of $\overline{u}$ in the interior of the CBL decreases

very quickly early in the simulation, due to the effects of surface friction, but decreases rather slowly thereafter. The overall jump in $\bar{u}$ across the entrainment zone changes very little between t=2500s and t=20,000s, maintaining a value of about 4 m/s. In terms of $\bar{u}$ alone, the shear across the entrainment zone, relative to the CBL depth, is very large early in the simulation and smaller later on, suggesting the entrainment zone shear drives the CBL evolution early in the simulation (generating TKE) but does not have as large an influence when the CBL becomes deeper. This alone may explain the decrease in the entrainment flux ratio with time.

Meanwhile, the $\bar{v}$ profiles show a substantial increase in the $\bar{v}$ jump across the entrainment zone as the simulation proceeds, increasing to over 4 m/s late in the simulation. Shear in $\bar{v}$ seems to become more important with time, suggesting the importance of entrainment zone shear in the CBL evolution may not decrease so much. The magnitude of the velocity jump vector increases from roughly 4 m/s at t=2500s to just over 6 m/s at t=20,000s, which is about a 50 percent increase. Since the ZOM-parameterized shear production takes the square of this velocity jump, the shear production can be considered doubled based on the velocity jump alone, yet dz_i/dt decreases, so it really does not become that large. Meanwhile, the CBL depth nearly triples over this same time interval.

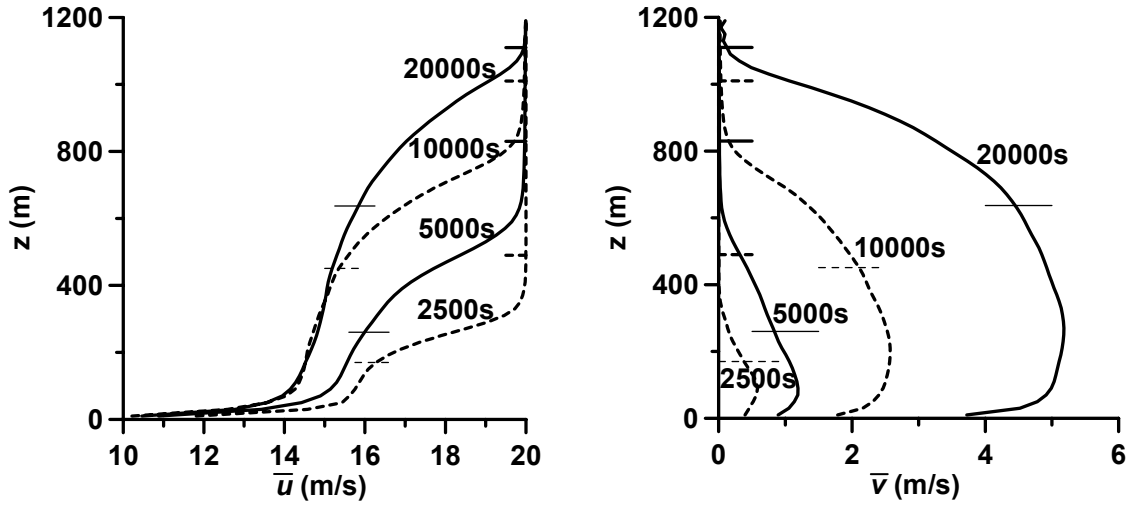

Figure 7.13: Evolution of the mean wind profiles for the GC case with $d\theta/dz$=0.003 K/m and Q_s=0.03 Km/s: (a) x-component, and (b) y-component. The profiles are labeled according to the elapsed times into the simulation, and the upper and lower limits of the entrainment zone (defined as the region of negative heat flux) are marked by horizontal lines.

Figure 7.14 shows the evolution of the vertical momentum flux profiles. First of all, the flux of u is a fair bit stronger than the flux of v (the profiles are plotted with different x-axes to illustrate the evolution of the profiles). The fluxes exhibit a substantial change across the entrainment zone, approaching zero near the top of the entrainment zone, as turbulence diminishes. For u, the largest fluxes are between the surface and the lower limit of the entrainment zone. In general, the magnitude of the flux in the entrainment zone shows a gradual decrease with time. At t=2500s, the flux is -0.37 m^2/s^2 at the bottom of the entrainment zone, and at t=20,000s, it is about -0.21 m^2/s^2. The v fluxes in the entrainment zone increase a bit over the same time interval, but not enough to compensate for the decrease in the magnitude of $\overline{w'u'}$. As time proceeds in the simulation, the CBL growth rate, dz_i/dt becomes smaller, and this decreases the entrainment of momentum.

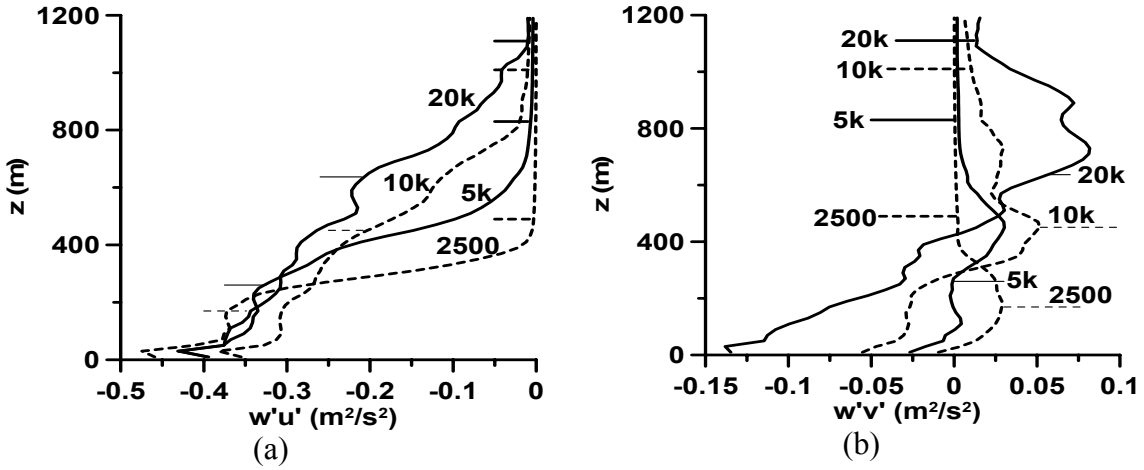

Figure 7.14: Evolution of the vertical momentum flux profiles for the GC case with $d\theta/dz$=0.003 K/m and Q_s=0.03 Km/s: (a) x-component, and (b) y-component. The profiles are labeled according to the elapsed times into the simulation, and the upper and lower limits of the entrainment zone (defined as the region of negative heat flux) are marked by horizontal lines.

The decreasing momentum entrainment also leads to a weaker shear production of turbulence as is shown in Figure 7.15. The profiles are plotted in z_i-normalized vertical coordinates in order to show the location of the production relative to z_i, and the surface shear generation of TKE is truncated in order to highlight the TKE production by entrainment zone shear (surface shear production does not change much during the simulation). The decrease in shear production with time in the entrainment zone is very obvious. Consequently, the buoyancy consumption of TKE in the entrainment zone also decreases with time, but not in as dramatic a fashion as the shear term decreases. One can also see that the largest shear production of TKE occurs in the lower portion of the entrainment zone, with the maximum *below* z_i, where the shear is a little weaker but the momentum flux is much stronger.

The evolution of the transport of TKE (not shown) during the simulation is rather unrevealing. One might have expected the upward transport of surface shear-generated TKE into the entrainment zone to be more efficient in the shallower CBL at the

beginning of the simulation, but the profiles of the transport of TKE all look similar to Fig. 7.12c, shortly after the onset of turbulence.

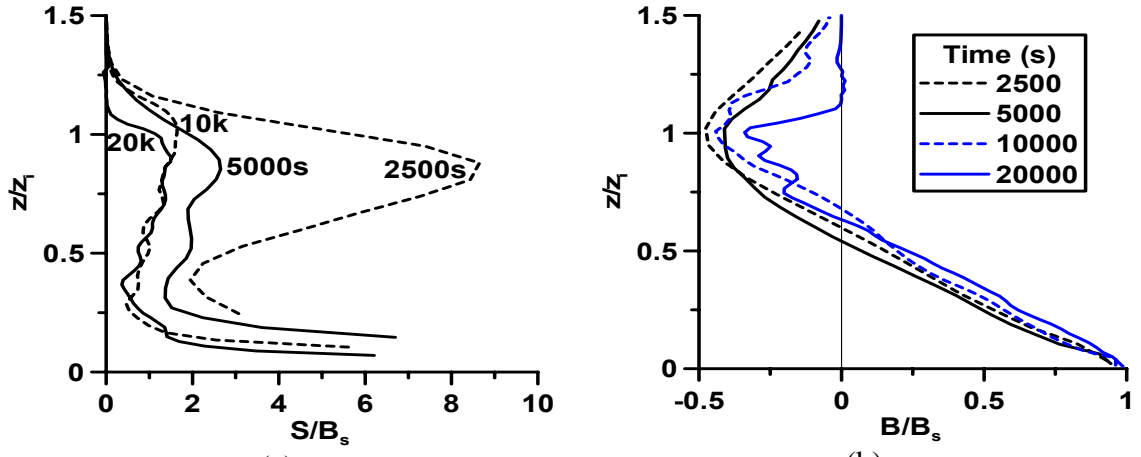

Figure 7.15: Evolution of the TKE budget profiles for the GC case with $d\theta/dz$=0.003 K/m and Q_s=0.03 Km/s: (a) shear term, and (b) buoyancy term. The profiles are labeled according to the elapsed times into the simulation.

Based on this analysis, one can conclude that the evolution of the entrainment flux ratio in the GC case is directly tied to the entrainment zone shear—not to the upward transport of surface shear-generated TKE as originally believed.

The simulations do have some differences from real atmospheric boundary layers in that the initial simulated momentum profiles are in geostrophic balance right down to the surface. In the atmosphere, the effects of surface shear would slow the flow there below 20 m/s, so the LES initial profile is not in balance with the combined surface friction, pressure gradient, and Coriolis forces, forcing the simulated CBL to adjust to these a bit more rapidly early in the simulation than might be the case for an early morning boundary layer undergoing transition from a nocturnal (stable) boundary layer to a CBL. On the other hand, the depth of the layer in which friction plays a role in

decreasing the momentum in the nocturnal boundary layer is pretty small, and it would not be well-resolved anyway. Such a shallow layer may be relatively unimportant after the initial onset of CBL buoyancy-produced turbulence. Simulations based on data from field experiments can be conducted to see if onset is any different when the ageostrophic component of the wind is used in the initial profile. This will be a focus of Chapter 9.

Meanwhile, we continue the analysis for the GS cases. Figure 7.16 shows the profiles of $\bar{u}$ and $\bar{v}$. The net change of $\bar{u}$ across the entrainment zone increases dramatically during the simulation, climbing from 3.5 m/s at t=2500s to 9 m/s at t=20,000s. The $\bar{v}$ profile also shows shear across the entrainment zone, but it is not nearly as large (the x-axis in Fig. 7.16b covers a much smaller range).

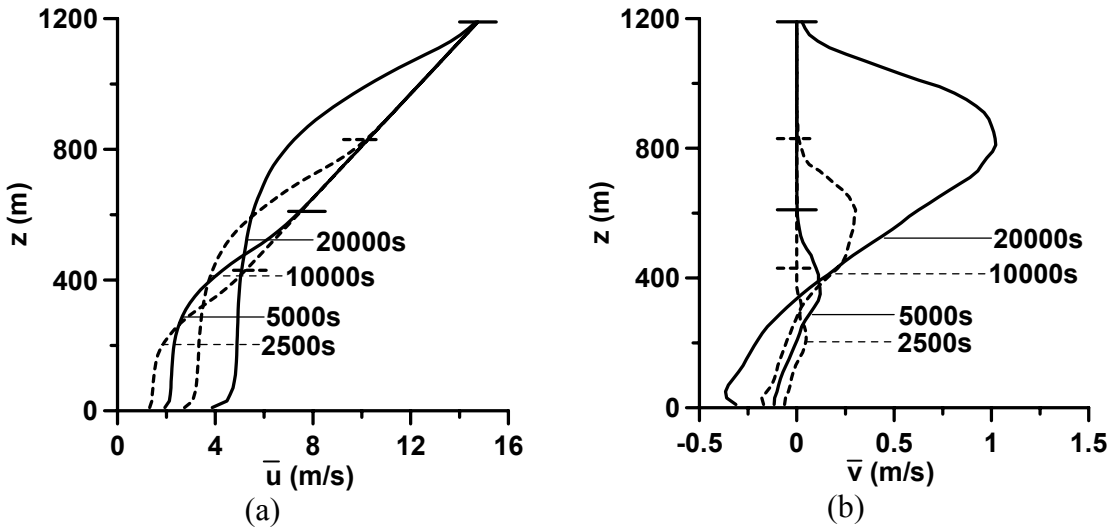

Figure 7.16: Evolution of the mean wind profiles for the GS case with $d\theta/dz$=0.003 K/m and Q_s=0.03 Km/s: (a) x-component, and (b) y-component. The profiles are labeled according to the elapsed times into the simulation, and the upper and lower limits of the entrainment zone (defined as the region of negative heat flux) are marked by horizontal lines. The labels point to the lower limit of the entrainment zone.

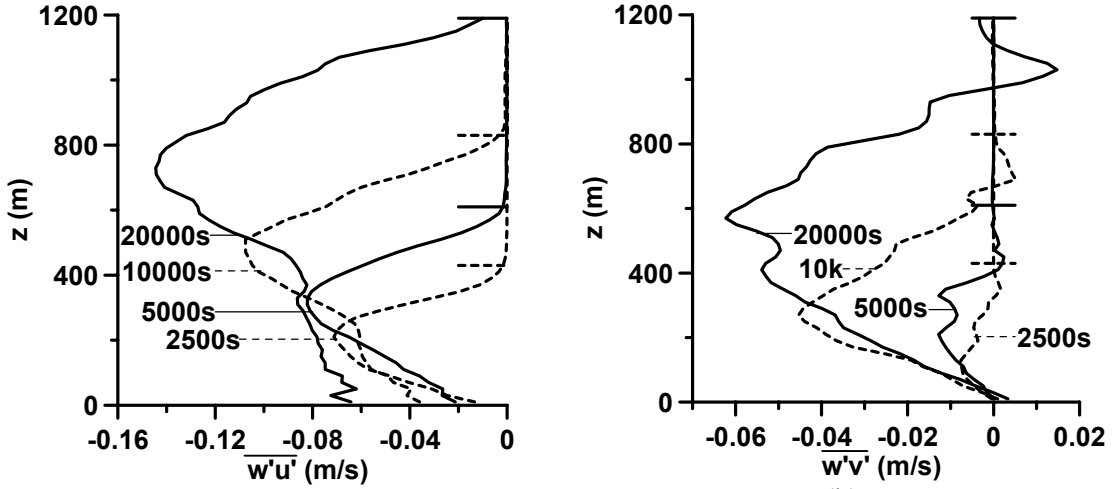

Figure 7.17: Evolution of the momentum flux profiles for the GS case with $d\theta/dz$=0.003 K/m and Q_s=0.03 Km/s: (a) x-component, and (b) y-component. The profiles are labeled according to the elapsed times into the simulation, and the upper and lower limits of the entrainment zone (defined as the region of negative heat flux) are marked by horizontal lines. The labels point to the lower limit of the entrainment zone.

Figure 7.17 shows the momentum flux profiles. The x-component flux dominates, and its magnitude increases throughout the simulation as the growing CBL encounters ever greater momentum at its top.

With both the magnitude of the momentum flux and the momentum change across the entrainment zone increasing during the simulation, it would be rather intuitive to expect the shear generation of TKE to increase as well. Figure 7.18 shows exactly that. Both the shear generation and buoyancy consumption of TKE increase during the GS simulation. With due regard to the variability of the statistics, the location of the maximum shear production appears to be a little closer to z_i, and a bit more symmetric about z_i, compared to the GC case.

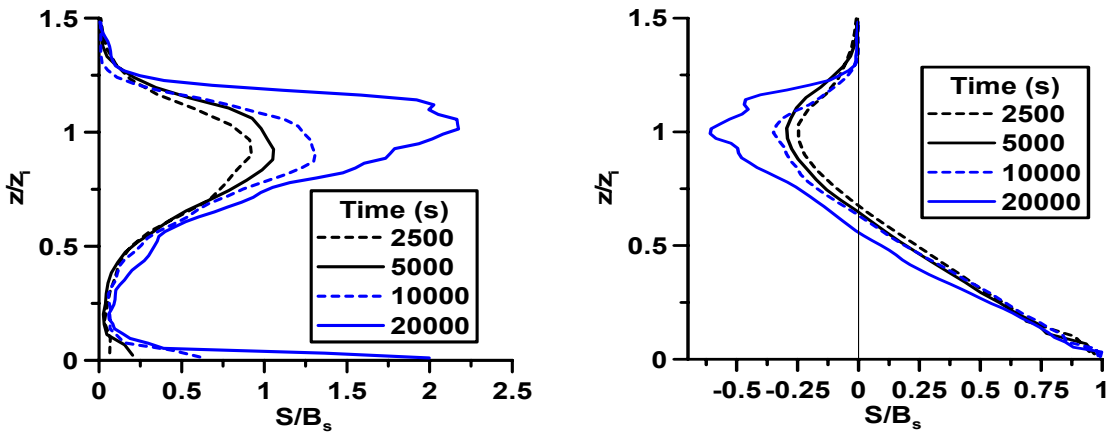

Figure 7.18: Evolution of the TKE budget profiles for the GC case with $d\theta/dz$=0.003 K/m and Q_s=0.03 Km/s: (a) shear term, and (b) buoyancy term.

Certainly, the increasing entrainment flux ratio in the GS cases appears to be driven by the shear production of turbulence, which is a result of the increasing shear across the entrainment zone as the CBL grows. In contrast, the GC case's entrainment zone shear (as seen earlier) increases only very slowly during the course of the simulation, while the momentum flux decreases due to the slowing CBL growth, and the shear production of turbulence decreases, leaving relatively less TKE to be consumed by entrainment. Furthermore, the analysis shows that in the GC case, it is the shear production of TKE resulting from *entrainment* zone shear, *not* the upward transport of surface shear-generated TKE, which drives the enhanced entrainment. The entrainment zone shear appears in the GC case as soon as the CBL becomes established because the surface friction rapidly slows the CBL momentum. In the GS case, entrainment zone shear is initially zero, and it grows with time, increasing the entrainment flux ratio gradually over the course of the simulation. In typical atmospheric CBLs, one would probably not expect this large increase because the GS case has abnormally strong

geostrophic shear, but whenever there is any shear, whether geostrophic or not, one would expect that entrainment zone shear exerts the primary influence on entrainment.

7.9 Bulk Richardson Numbers

The shear generation of TKE in the entrainment zone occurs simultaneously with K-H type instabilities at the CBL top. Kim et al. (2003) performed a detailed analysis of the K-H billow structures at the top of the CBL and presented the gradient Richardson number profiles in the entrainment zone. The gradient Richardson number used here is defined in the following manner:

$$Ri = \frac{N^2}{\left(\frac{\partial \bar{u}}{\partial z}\right)^2 + \left(\frac{\partial \bar{v}}{\partial z}\right)^2}, \tag{7.1}$$

where N, $\partial \bar{u} / \partial z$, and $\partial \bar{v} / \partial z$ are evaluated locally. If the entrainment zone shear is driven by K-H instabilities, one might expect Ri to fall between 0 and 0.25, with 0.25 being the necessary but not sufficient condition for the onset of K-H instability in laminar flow. Since the entrainment zone is at least weakly turbulent, one would not necessarily expect the flow to behave as it would if it were laminar. Nevertheless, we expect $Ri<1$ in any layer with $d\theta/dz>0$ where shear-driven turbulence is being generated.

An analysis of Ri can be done by at least two different methods. Ri can be evaluated separately at each grid point in order to understand the local generation of K-H type instabilities. Since turbulence is largely episodic and intermittent in the stable nocturnal boundary layer, and making an analogy between the stable nocturnal boundary layer and the entrainment zone at the top of a sheared CBL, a local analysis of Ri might

provide particularly useful information. Such an analysis can easily become quite cumbersome, because there are over five million grid points in the LES domain.

A much easier analysis would be to evaluate *Ri* from the horizontally averaged profiles. The horizontal averaging in this analysis would mask areas where *Ri* is locally small, but it would reveal layers where K-H instabilities might exist in a bulk sense. We apply this analysis to the sheared CBL simulations with $d\theta/dz$=0.003 K/m and Q_s=0.03 Km/s. Figure 7.19 shows the profiles of $\overline{u}$, $\overline{\theta}$, $\overline{w'\theta'}$, and *Ri* at *t*=15,000s in the GS case. Figure 7.20 shows the same for the GC case. All profiles are plotted together in order to show some of the basic relationships among *Ri*, $\overline{u}$, and $\overline{\theta}$. The heat flux profile is plotted to illustrate the locations of features relative to z_i (the heat flux minimum) and the upper and lower limits of the entrainment zone.

The most striking feature in these plots is the layer of nearly constant *Ri* over much of the entrainment zone [see Kim et al. (2003) for comparison]. In fact, $Ri \cong 0.25$ over this layer even though the potential temperature and momentum profiles are changing with height. The layer of constant *Ri* extends from around *z*=600 m to a point just above z_i. Above that level, it returns to its background value of 0.63 over the top quarter of the entrainment zone. The depth of the $Ri \cong 0.25$ layer is approximately 300 m, which means that it should be reasonably well-resolved on the LES grid.

The GC simulation also features a layer with $Ri \cong 0.25$. The layer covers most of the lower two thirds of the entrainment zone, and *Ri* climbs rapidly above that point (*Ri* is infinitely large in the initial background profile). Likewise, the relationships among the momentum, heat flux, and momentum profiles appear qualitatively similar to their relationships in the GS case.

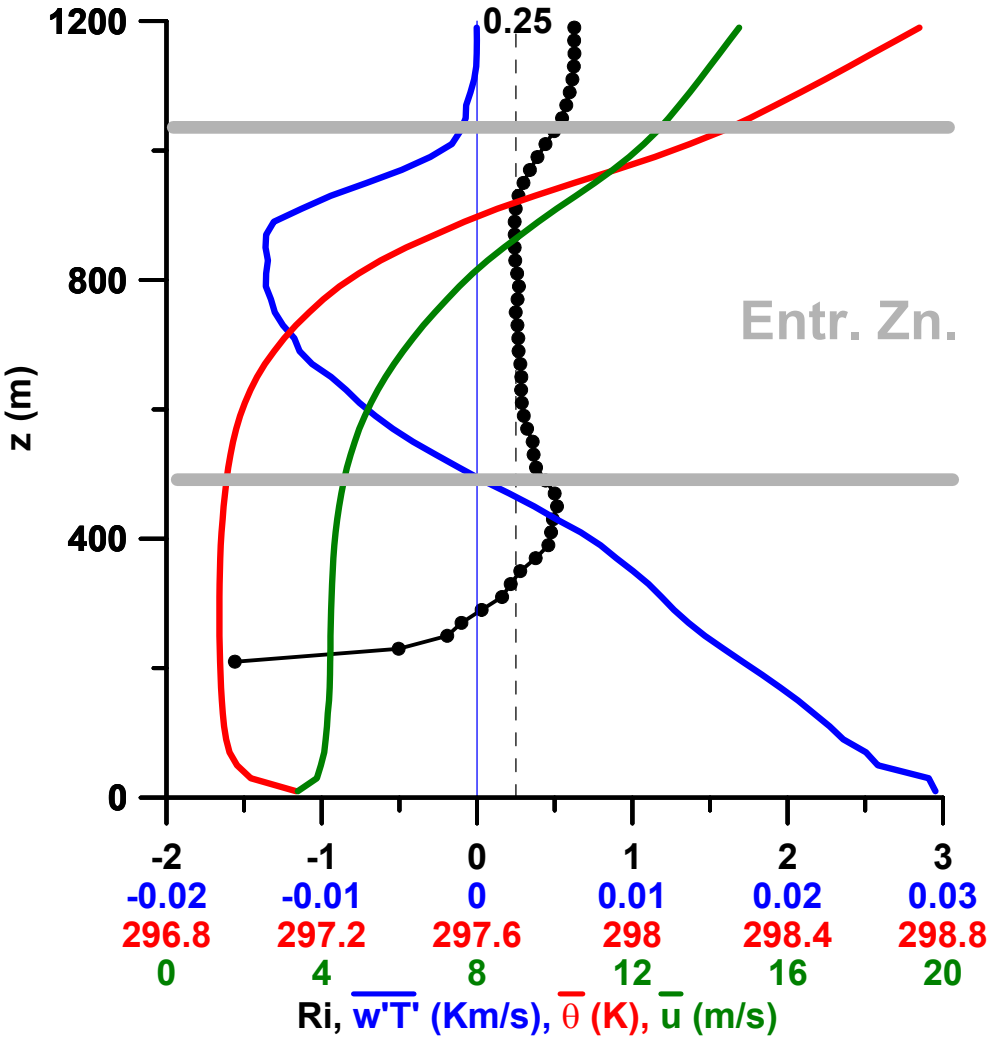

Figure 7.19: Profiles of Richardson number, heat flux, potential temperature, and the x-component of momentum at t=15,000s in the GS simulation with $d\theta/dz$=0.003 K/m and Q_s=0.03 Km/s. The colors of the x-axis labels correspond to the colors of the profiles, and the black dots on the Ri profile mark the locations of grid points in order to indicate grid resolution.

Given the existence of a $Ri \cong 0.25$ layer in these two cases, I looked through the other cases in search of similar layers. Not all simulations contain such layers with constant Ri. In many of these cases, the entrainment zone may be too narrow for the grid to resolve such a layer. In other cases, the CBL growth is too fast to allow the development of a layer in which the shear at the CBL top achieves a balance with the

potential temperature and turbulence structure there. The penetration of thermals and resulting contortion of the interface when buoyancy flux is strong may also obscure the *Ri* in the horizontally averaged profiles.

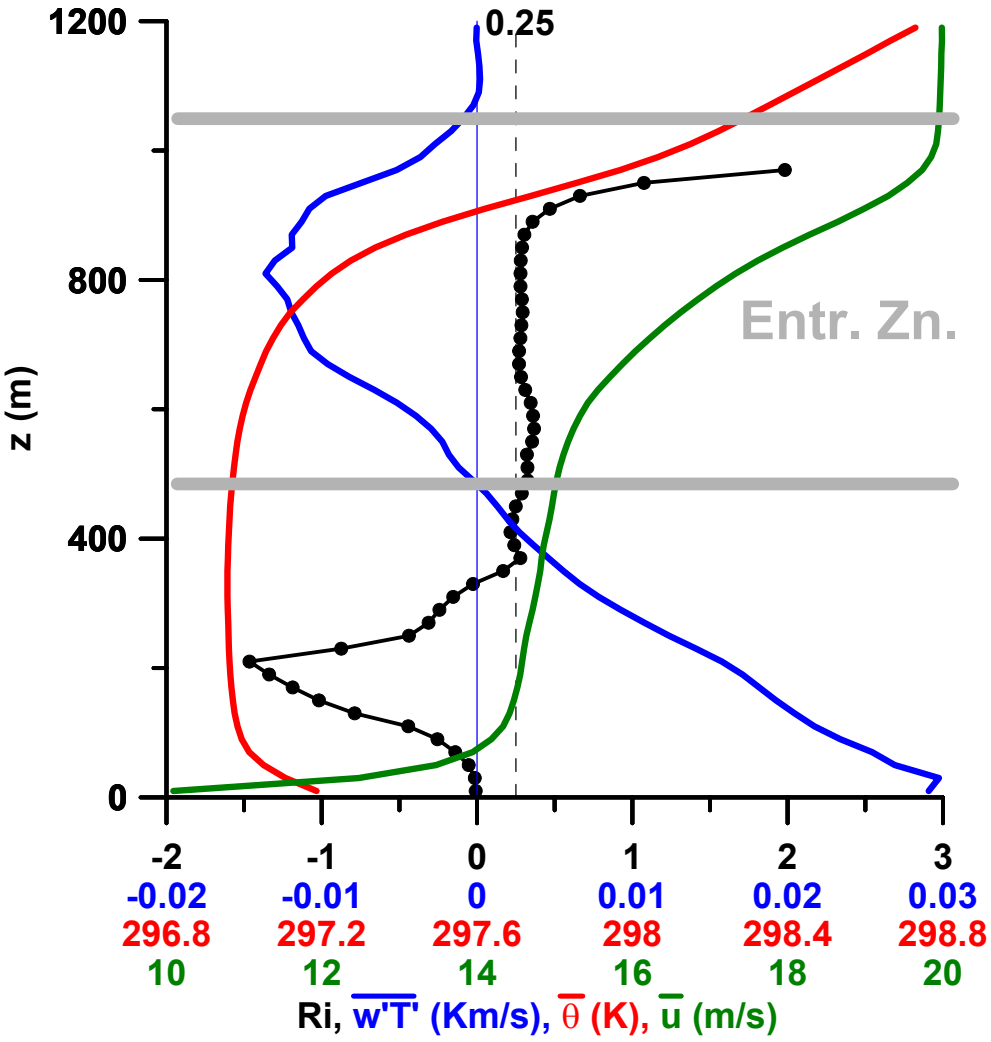

Figure 7.20: Profiles of Richardson number, heat flux, potential temperature, and the *x*-component of momentum at t=15,000s in the GC simulation with $d\theta/dz$=0.003 K/m and Q_s=0.03 Km/s.

Figure 7.21 shows the time series of *Ri* at z_i for all of the GS simulations, and Figure 7.22 shows the same for the GC simulations. Within the set of GS simulations,

the results are dependent on the free atmosphere stratification. For the cases with moderate stratification ($d\theta/dz$=0.003 K/m), the values approach Ri=0.25 rather quickly and then stay there. For the cases with weakest stratification, the free atmospheric profile has Ri=0.22, so the time series cannot be expected to approach Ri=0.25. Rather, it decreases rather quickly from Ri=0.22 and then climbs slowly back in that direction. For the strongest stratification, Ri starts out large and asymptotically approaches Ri=0.25 over the course of the simulation. For the Q_s=0.3 Km/s case, the simulation finishes long before this value is approached.

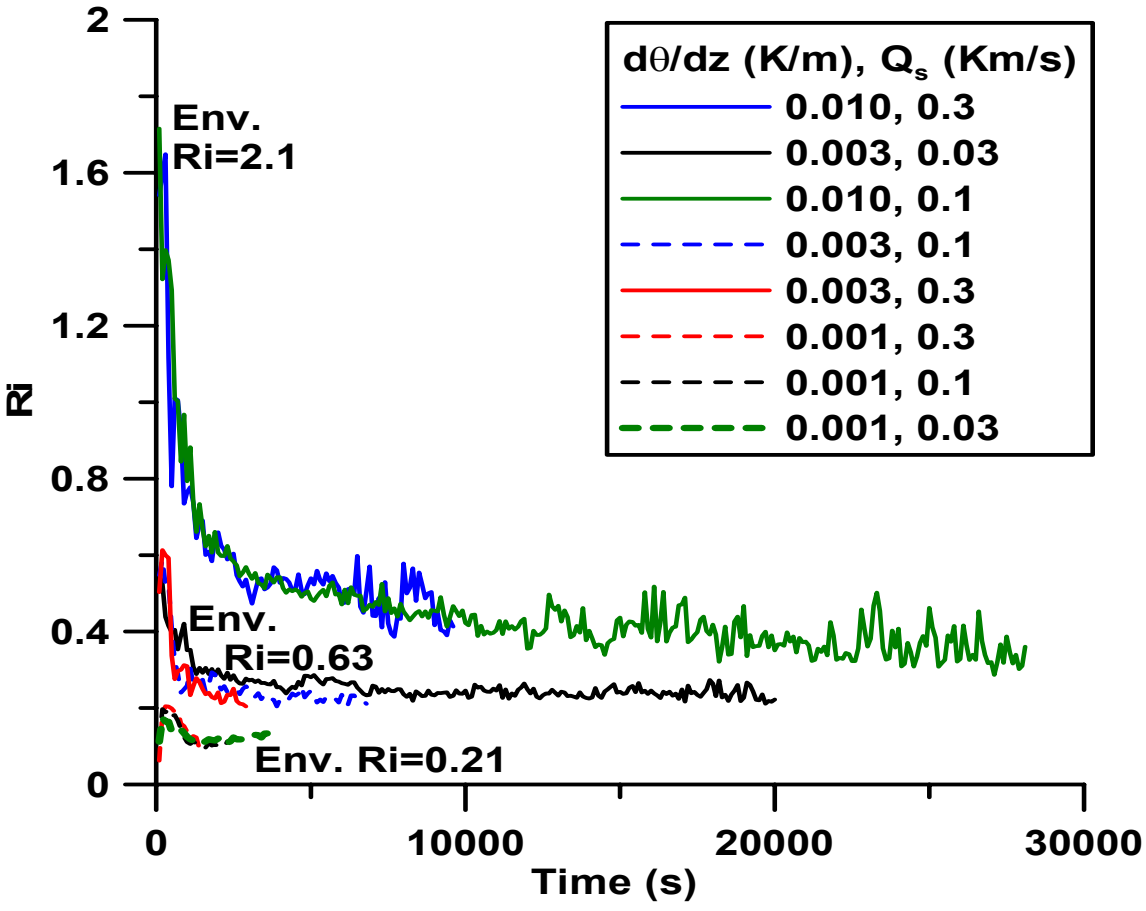

Figure 7.21: Bulk Richardson number Ri at z_i as a function of time for all the GS cases. "Env. Ri" on the plots refers to Ri of the free atmospheric profile.

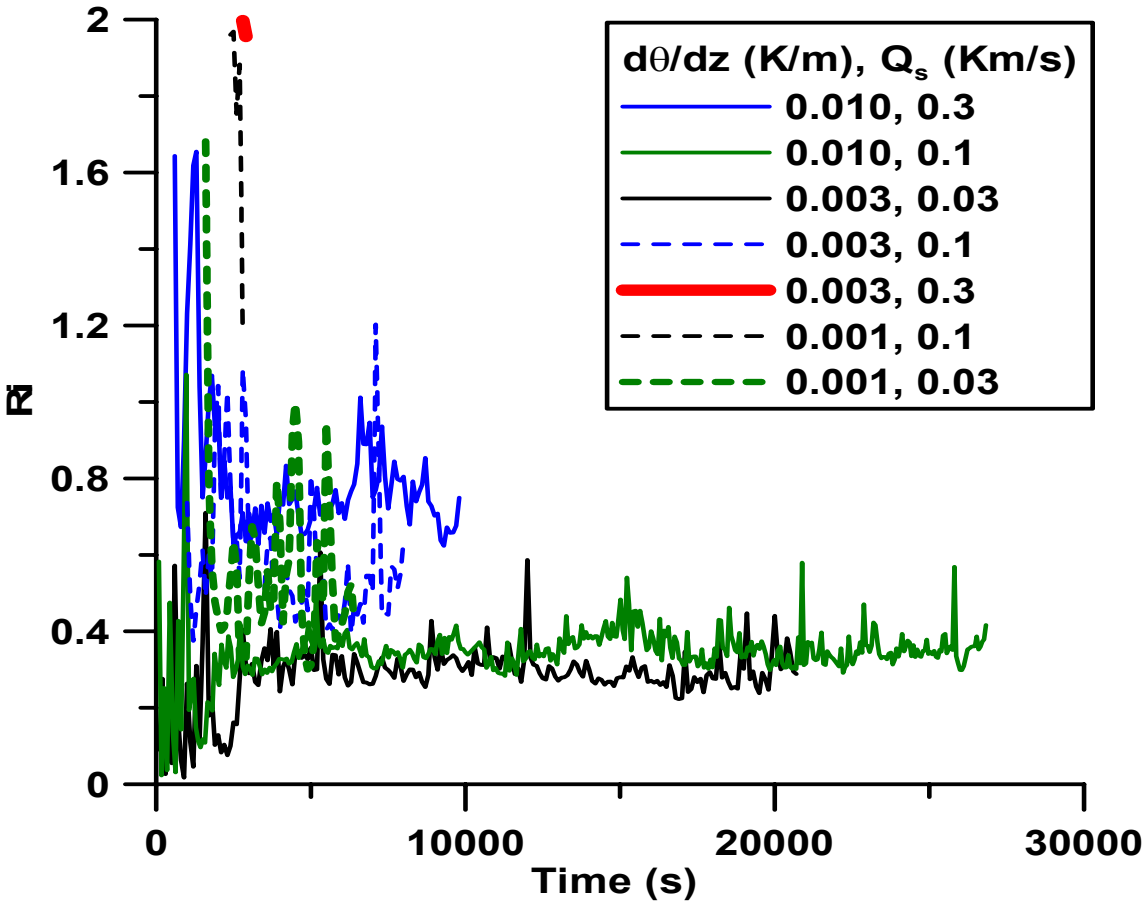

Figure 7.22: Bulk Richardson number *Ri* at z_i as a function of time for all the GC cases.

For the GC cases, the results do not group according to stratification. Rather, there appears to be a weak grouping based on the rate of CBL growth. The two most slowly growing cases have *Ri*<0.4, and these are the same cases in which the shear accumulates at the top, and enhancement of CBL growth is greatest compared to the GS and NS cases. In fact, in all cases in which shear has a substantial impact on entrainment, these low *Ri* layers are seen in the simulations. The absence of such a layer does not necessarily mean shear does not have an impact on the CBL structure or entrainment. For example, the 0.010 K/m, 0.1 Km/s GS case has a larger *Ri* initially, but its CBL still entrains faster than its NS case counterpart. In these cases with strong stratification, the

entrainment zone may be too shallow for the grid to resolve a layer with Ri=0.25. It may also be that local patches with $Ri \leq 0.25$ may exist in the entrainment zone, but the horizontal averaging in the mean profiles does not allow them to be seen. In either case, when the shear contribution to entrainment becomes large enough, such patches may become more ubiquitous and spread to the point where they are seen everywhere on the horizontal plane and thereby appear in the mean profiles. Also, Ri<1 in most GC cases, which means it is generally in a range of values that supports turbulence.

Since the thickest of these layers is still only about 20 grid cells deep, the subgrid model may still have some impact on the simulations. When shear is strong there is also greater potential for artifacts of the numerical scheme to impact turbulence structures in the entrainment zone. These impacts can be assessed by looking directly at the simulated turbulence structures and spectra, which is the focus of the next chapter. Additionally, some comparison with atmospheric data would be particularly beneficial, but temporal and spatial resolution in the atmospheric data may be too coarse, especially in data on thermodynamic properties of the mean flow.

7.10 Summarizing Remarks

The LES results clearly show shear has an impact on entraining CBLs. For all cases in which the simulated CBLs spent a significant amount of time in some sort of an entrainment regime, the results of the simulations indicated that shear enhanced the entrainment in these CBLs.

Some arguments have been made that the sheared CBLs really can be considered as two separate layers (Lewellen 2000), which consist of a stable boundary layer above a

more classic CBL. Such structure should be borne out in the turbulence statistics in the simulations, and if this is the case, the structure of the CBL interior should be essentially unaffected by the shear at the CBL top. The shear may cause the interface at the top of the CBL to become a bit more diffuse, but since the entrainment zone has significant density stratification and limited TKE, the effects of shear in the entrainment zone should only be able to mix downward into the CBL to a limited extent, and the structure of the lower CBL should be unaffected.

The results of these simulations suggest that the entrainment zone shear affects the whole structure of the CBL. Figure 7.4 in particular shows that when shear leads to a deeper CBL, the temperature of the entire CBL is affected; it is warmer than in shear-free CBLs, indicating the shear-enhanced entrainment of heat is felt throughout the entire CBL and not just at the top. Additionally, the entrainment of momentum affects the structure of the turbulent momentum transport throughout the depth of the CBL and not just at the top. Based on these results, the sheared CBL would best be considered as a single entity rather than as two separate, overlying CBLs.

The results of the simulation also have implications regarding the applicability of mixed layer models such as the ZOM and FOM to sheared CBLs. In some sense, the self-similarity of temperature structure observed in the simulations is not dramatically affected by shear. The vertical potential temperature gradient is negative in the lower CBL, changes sign somewhere in the middle CBL, and becomes increasingly positive towards the CBL top. This is the case whether shear is present or not. Use of a mixed layer with this type of structure has worked well in the past, and there is no reason to

believe that it would not work for the temperature structure observed in sheared CBLs as well.

The case may be different for the momentum profiles. The vertical gradient of $\overline{u}$ is always positive in these simulations, and in many of the simulations, the momentum fields in the interior of the CBL do not look well-mixed. Additionally, it is rather well established that the eddy diffusivities of momentum and heat are different, as heat is vertically transported more efficiently than momentum, the latter being subject to dynamics pressure effects that impart some of the "environmental" momentum on any rising air parcel (Stull 1988). In this case, the use of a mixed layer model assuming a constant momentum with height in the interior of the CBL may concentrate too much shear at the CBL top and thereby overestimate the shear generation of turbulence there. Perhaps the assumption of a linearly varying profile of $\overline{u}$ in the CBL interior would work better. However, in a bulk model, the shear production of TKE may be insensitive to the distribution of shear. Chapter 10 will evaluate the performance of mixed layer models for the simulated CBLs in this study.

Finally, the analysis presented in this chapter has provided strong evidence that surface shear has relatively little effect on entrainment. In all strongly entraining GC cases examined, the *entrainment zone shear* was seen as the primary driver of enhanced entrainment. Analysis of *Ri* in the entrainment zone and within individual profiles of velocity and potential temperature shows that if the shear becomes strong enough in a background that is stable in the *K-H* sense, a well-resolved layer of constant *Ri* develops in the simulations. This may have implications for application of the FOM to sheared CBLs.

Chapter 8

Turbulence Structure in Sheared Convective Boundary Layers

8.1 Motivation

This chapter is focused on the analysis of turbulence structure in sheared and shear-free CBLs. The purpose of the analysis is twofold: 1) to see what differences exist in turbulence structure between sheared CBLs and shear-free CBLs, and 2) to evaluate the length scales of the turbulence structures that are important for entrainment in both the sheared and shear-free CBL simulations to assess whether a change in l might improve the predicted entrainment rate in e-l models and to assess the resolution of entraining turbulence structures on the LES grid. Greater confidence can be placed in the LES results with regard to entrainment if the entraining structures are well-resolved, but if it appears that poorly resolved structures are the main contributors to the entrainment of heat and momentum, the results might be much more sensitive to the subgrid model and to artifacts of the numerical scheme.

8.2 Cross Sections of Temperature and Velocity

We begin by showing flow fields over several cross-sections throughout the CBL, oriented horizontally and vertically, normal and parallel to the mean wind direction. Figure 8.1 shows potential temperature and velocity patterns in an *x*-*z* cross section of the shear-free CBL with $d\theta/dz$=0.003 K/m and Q_s=0.1 Km/s. The coloring in the figure corresponds to the potential temperature, and the arrows show the projection of the velocity vectors onto the *x*-*z* plane. The cross section shows some well-known features of the CBL that have been discussed in a number of references such as Deardorff (1974a), Moeng and Sullivan (1994), and Stull (1988). In the shear-free CBL (Fig. 8.1a), the warm updrafts are rather narrow and intense and are surrounded by larger areas of weakly subsiding motion. At the top of the CBL are areas of rather sharp gradients, mostly at the tops of plumes that penetrate into the free atmospheric layer. In these areas, the interface between the CBL air and overlying free-atmospheric air is rather well-defined. Surrounding these plume tops are areas with much weaker gradients where it is much harder to find the interface. Qualitatively, the picture is similar to CBL structure shown by the lidar measurements of Kiemle et al. (1995) and Davis et al. (2000) in the dry atmospheric CBL. This structure of the dry CBL has implications for the application of the coordinate transformations suggested in Lilly (2002a). A sharp interface can be identified at the tops of plumes, but not everywhere. The sharpness of the upper interface is also pretty variable in Figs. 8.1b and 8.1c.

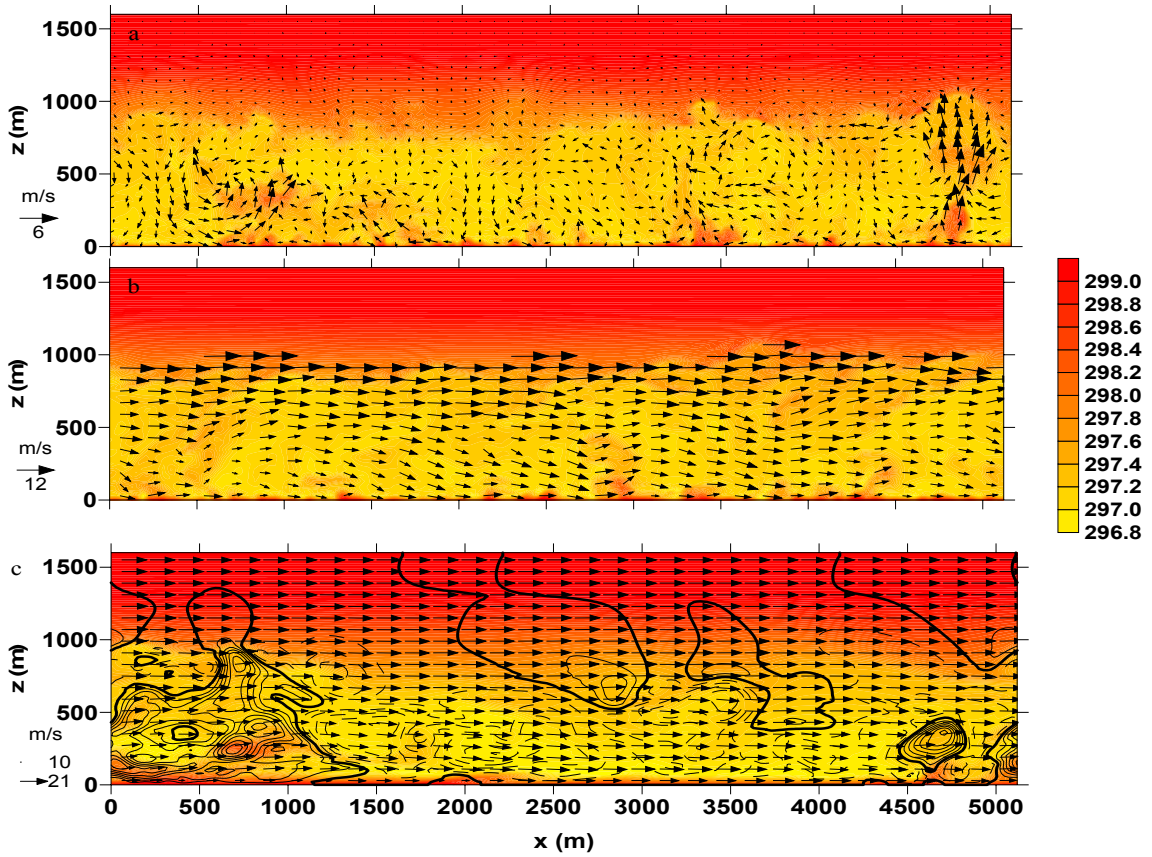

Figure 8.1: *x-z* cross section showing temperature and velocity structure in the simulations with $d\theta/dz$=0.003 K/m and Q_s=0.3 Km/s: (a) NS, (b) GS, and (c) GC. In (c), because the momentum is dominated by the *x*-component, vertical velocity contours (contour interval 0.4 m/s) are added to identify areas of upward and downward motion. The negative countours are denoted by dashed lines, and the bold contour represents 0 m/s.

In the GS case (Fig. 8.1b), it can be seen that the shear has a large impact on the structure of the CBL. Fig. 8.1b is marked by the absence of the narrow, columnar type updrafts that are found in Fig. 8.1a. While the updrafts may still be narrower than the downdrafts, they are no longer vertically upright. One example of such updraft structure is located between *x*=500m and *x*=1000m. The base of this area of upward vertical motion is located near *x*=500m, but its top is located closer to *x*=1000m. Also, this updraft carries much weaker horizontal momentum than the surrounding downdrafts.

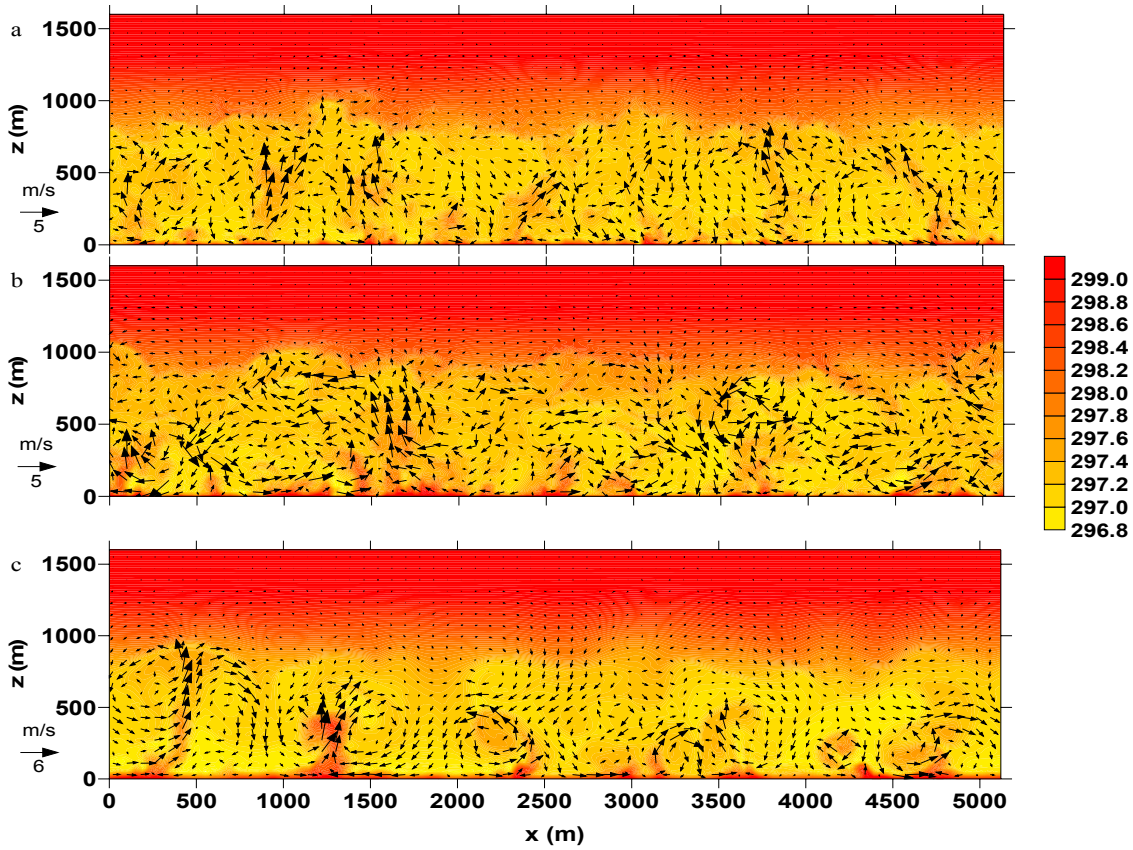

Figure 8.2: *y-z* cross section showing temperature and velocity structure in the simulations with $d\theta/dz$=0.003 K/m and Q_s=0.3 Km/s: (a) NS, (b) GS, and (c) GC.

In the GC case (Fig. 8.1c), the updrafts and downdrafts are obscured by the fact that the vector components are dominated by the horizontal flow $\bar{u}$. However, it is immediately obvious that the CBL turbulence structure looks very horizontally elongated on this cross section compared to the others. The vertical velocity contours show that, for this cross section, downward vertical motion occupies a much larger area than upward vertical motion. This is due to the placement of the cross section. The CBL structure in the GC case is dominated by horizontal convective rolls, and the cross section in Fig. 8.1c is oriented nearly parallel to the rolls and samples a region mostly within the downdraft of a roll.

Figure 8.2 shows the *y*-*z* cross sections, and Fig 8.2c shows them for the GC case. The GC *y*-*z* cross section is oriented perpendicular to the rolls. In this plane, the updrafts and downdrafts look a bit more similar to those in the NS case, with more isolated regions of warm updrafts surrounded by broader regions of downward vertical motion. As discussed in Chapter 5, the interface between the CBL air and the free atmospheric air looks sharper at the tops of the areas of ascent and is much less defined in between, where the motion is downward. It is quite evident that the stretching deformation, at least as seen within this particular cross-section, acts to intensify gradients at the tops of updrafts and to weaken them at the tops of downdrafts. The structure in the NS case (Fig. 8.2a) looks qualitatively the same as it does in Fig. 8.1a, which should be expected in the shear-free case, and in the *y*-*z* plane, there is relatively little visual information to distinguish between the NS case and the GS case (Fig. 8.2b). The GS updrafts may look a little less vertically coherent than the NS ones, as they are tilted through the *y*-*z* plane.

Figure 8.3 shows a horizontal (*x*-*y*) cross section near the surface for the NS case. As is discussed in Moeng and Sullivan (1994) and Kanna and Brasseur (1998), the CBL structure forms into quasi-hexagonal cells in the absence of mean shear. The horizontal motions push air outward from the downdrafts at the centers of the cells. Along its motion near the surface, the air acquires heat due to the surface heat flux, and this heated air then accumulates at the vertices of the cells, where it then begins its ascending motion at the base of the plume. The upward vertical motion (not shown) is most intense at the corners of the cells. In Figure 8.3, the warmest temperatures are found at these locations.

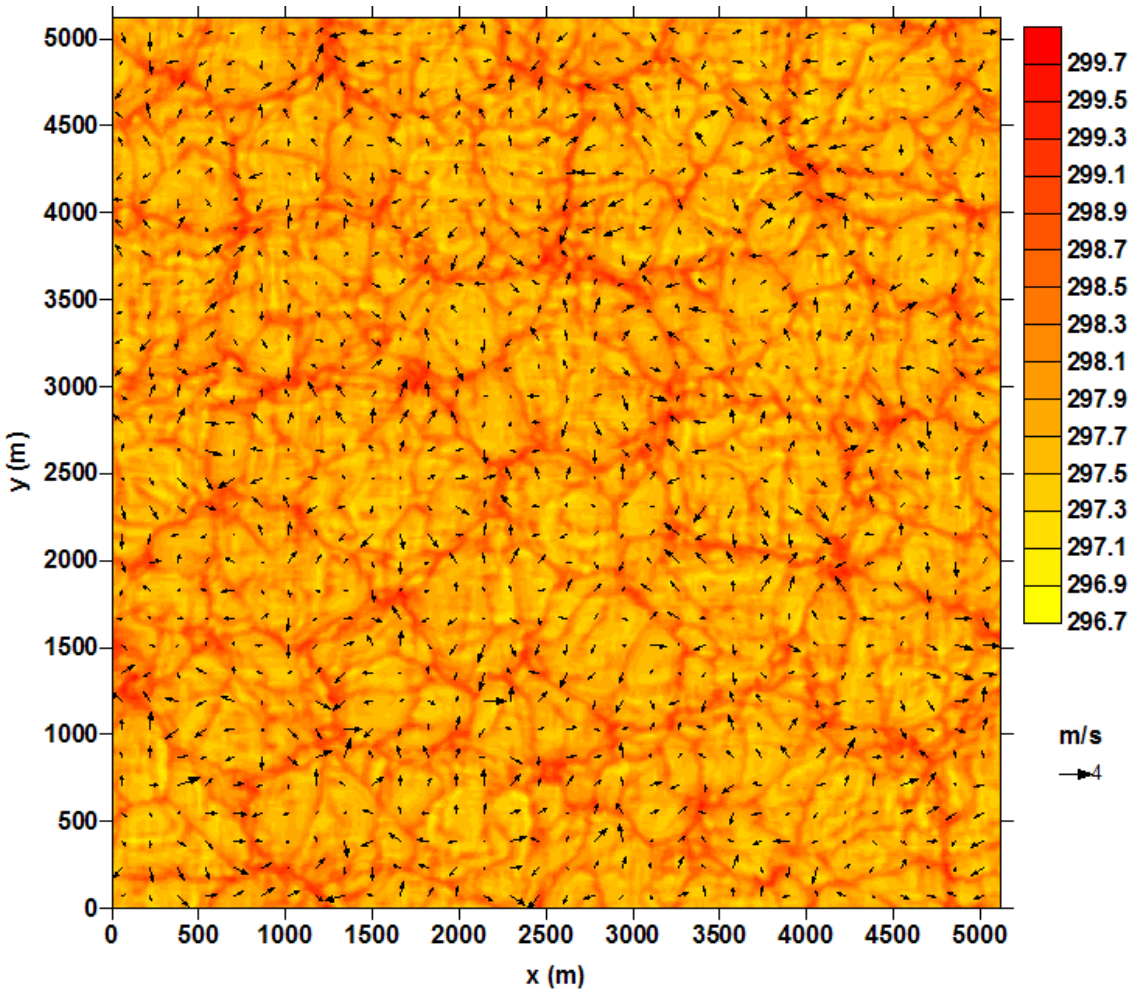

Figure 8.3: *x*-*y* cross section near the surface showing temperature and velocity structure for the NS simulation with $d\theta/dz$=0.003 K/m and Q_s=0.3 Km/s.

Figure 8.4 shows the corresponding horizontal cross section for the GS case. There is not a very large difference in the shape of the thermal structures, but there does appear to be somewhat of a loss of hexagonal structure. The areas of cooler air appear more in bowing type structures, with the narrower hot zones located at the leading edge of these structures as they are pushed rightward by the momentum. Horizontal motion has a positive *x*-component everywhere in the picture, being faster in some areas and having a *y*-component of either sign, depending on location.

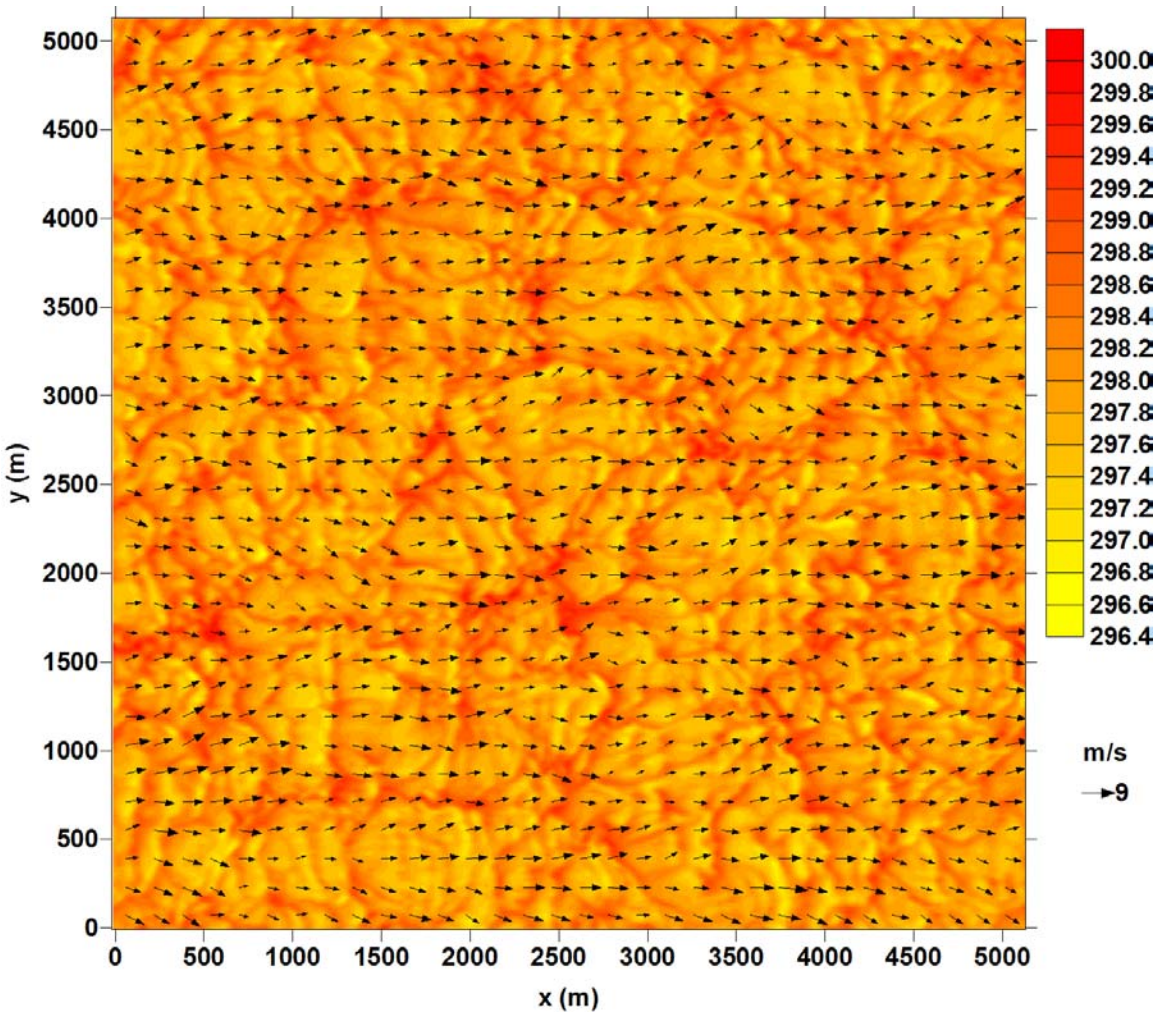

Figure 8.4: *x-y* cross section near the surface showing temperature and velocity structure for the GS simulation with $d\theta/dz$=0.003 K/m and Q_s=0.3 Km/s.

The biggest difference in structure is seen in the GC case, shown in Figure 8.5. The alignment of the turbulent structures into horizontal roll shapes is very obvious in this picture. This is a feature common to CBLs with strong surface wind and has been discussed by Lilly (1966), Lemone (1973), Moeng and Sullivan (1994), Kanna and Brasseur (1998) and others. The surface shear definitely plays a larger role in organizing the CBL turbulence into horizontal convective rolls.

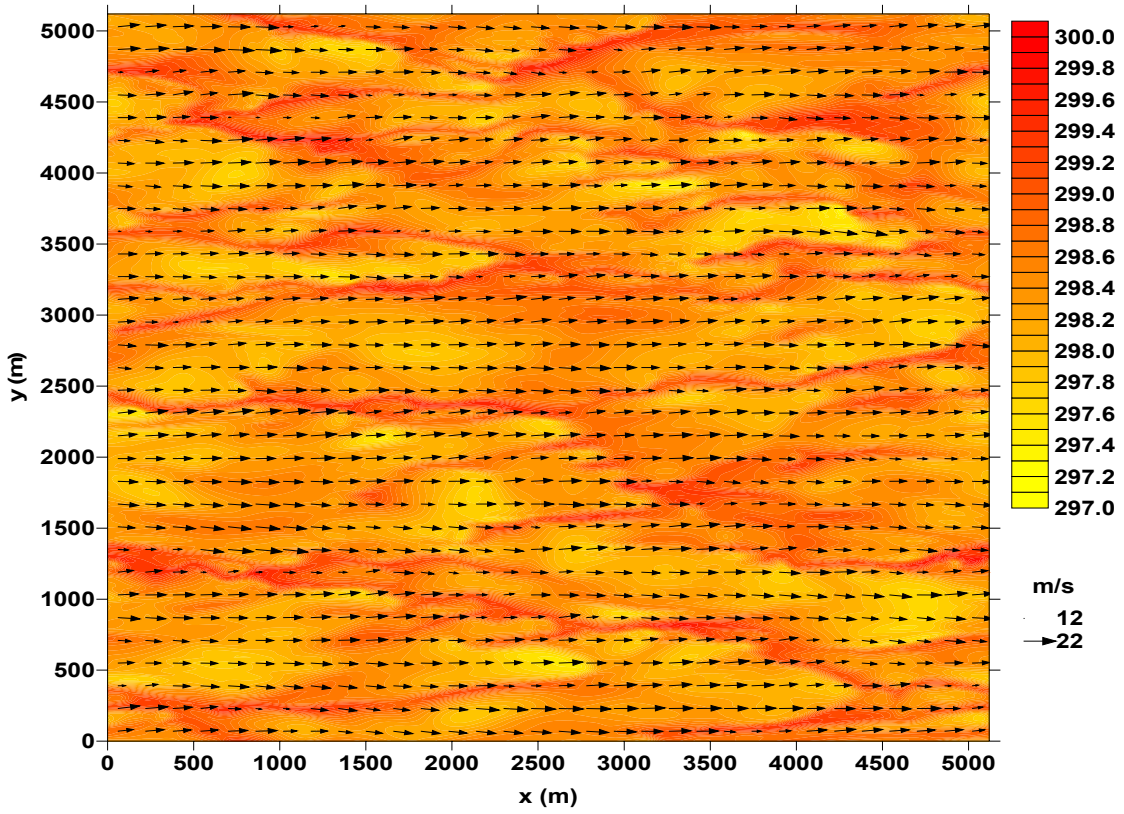

Figure 8.5: *x-y* cross section near the surface showing temperature and velocity structure for the GC simulation with $d\theta/dz$=0.003 K/m and Q_s=0.3 Km/s.

One additional feature that is seen in the sheared CBLs, especially in the GC case, is that the structures appear to be a bit smoother than in the NS case, particularly in Fig. 8.5. It will be necessary to see if the smoothness is reflected in the LES turbulence spectra and to see if it is consistent with observed atmospheric spectra. It will also be interesting to see how the structural differences between the hexagonal cells in the NS case and the rolls in the GC case affect the spectra.

8.3 Spectra of Turbulence

The one-dimensional vertical velocity spectra for these cases are shown in Figure 8.6. These spectra were calculated across horizontal planes. Figure 8.6a shows the spectra halfway between the surface and the CBL top (z/z_i=0.5), and Figure 8.6b shows the spectra at the CBL top. For the middle CBL, in all cases, the peak in the spectrum is near z/z_i=2π, and this fact is consistent with the dominant length scale (and turbulence production scale) of CBL turbulence being approximately equal to the CBL depth (Stull 1988).

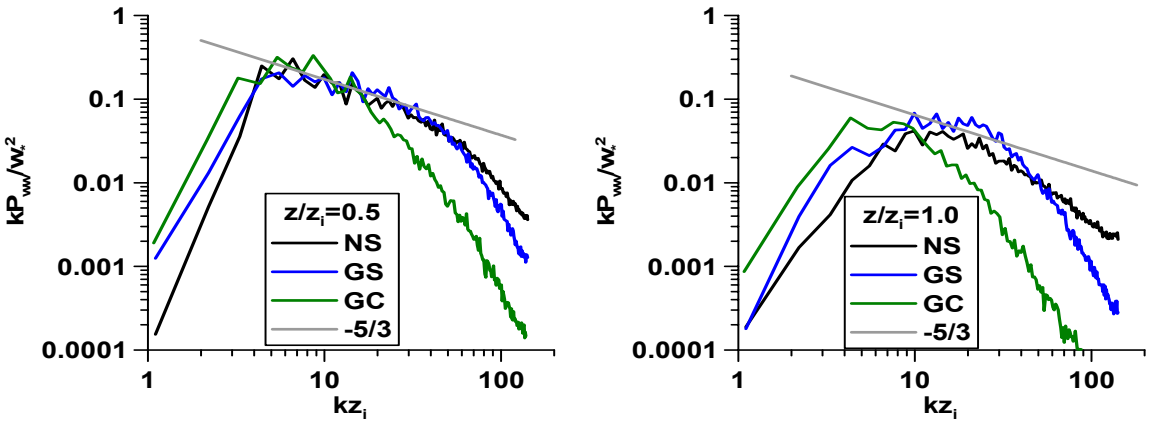

Figure 8.6: Vertical velocity spectra for the simulations with $d\theta/dz$=0.003 K/m and Q_s=0.3 Km/s. The spectra are calculated across horizontal planes at the following levels with respect to zi: (a) z/z_i=0.5, and (b) z/z_i=1.0.

The spectra for the NS and GS cases also suggest the presence of a Kolmogorov inertial subrange, with the simulation resolving approximately one decade of this range. The $k^{-5/3}$ line is shown as a reference. If the simulation resolved all turbulence, the $k^{-5/3}$ range would extend at least another six decades, but at kz_i=40, the combined damping

effects of the subgrid eddy viscosity and the numerical scheme become rather pronounced, and the energy drops off more rapidly than $k^{-5/3}$.

For the sheared CBLs, there are two notable differences in the spectra. First is the larger energy density at the lowest wavenumbers, which is most noticeable for the GC case. Second is the decrease in the energy density in the highest wavenumbers, and this is most dramatic in the GC case, both in the middle CBL (Fig. 8.6a) and at the CBL top (Fig. 8.6b). For the GC case, there appears to be no $k^{-5/3}$ range, and the energy density falls off rapidly immediately beyond the production range. The rapid drop-off is consistent with the smoother structure shown in Fig. 8.5, but there are no atmospheric data suggesting the dropoff in energy should be so rapid. Atmospheric data characteristically have a $k^{-5/3}$ range (e.g. Kaimal 1978).

We look further at the integral length scales of turbulence, defined as:

$$l_{ww} = \frac{2\pi}{K_{ww}}; \quad K_{ww} = \frac{1}{\sigma_w^2} \int_{2\pi/L}^{\pi/\Delta} k P_{ww} dk$$

These are shown in Figure 8.7. The integral length scale in the GC case is more than 50% larger than it is in the NS and GS cases.

Figure 8.8 shows the heat flux cospectra in the entrainment zone for the same simulations at the same times shown in Figs. 8.1 through 8.7. These spectra indicate that the smallest wavenumber (largest length scale) structures are the primary contributors to the heat flux of entrainment into the growing CBL. For the GC case, there is no appreciable flux at wavenumbers larger than about kz_i=20, which is consistent with the lack of energy in the higher wavenumbers of the vertical velocity spectrum and the longer integral length scales. These characteristics are qualitatively consistent with the cospectra displayed in Schmidt and Schumann (1989) and Kaiser and Fedorovich (1998).

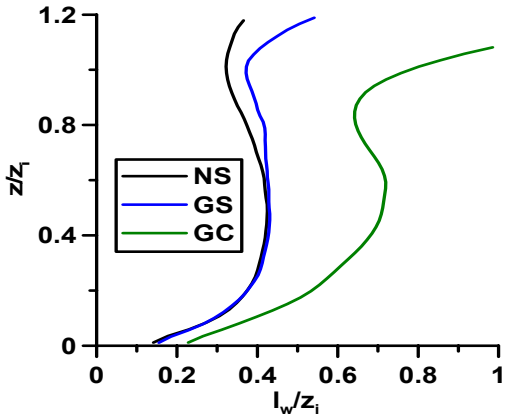

Figure 8.7: Integral length scales for the vertical velocity spectra for the simulations with $d\theta/dz$=0.003 K/m and Q_s=0.3 Km/s.

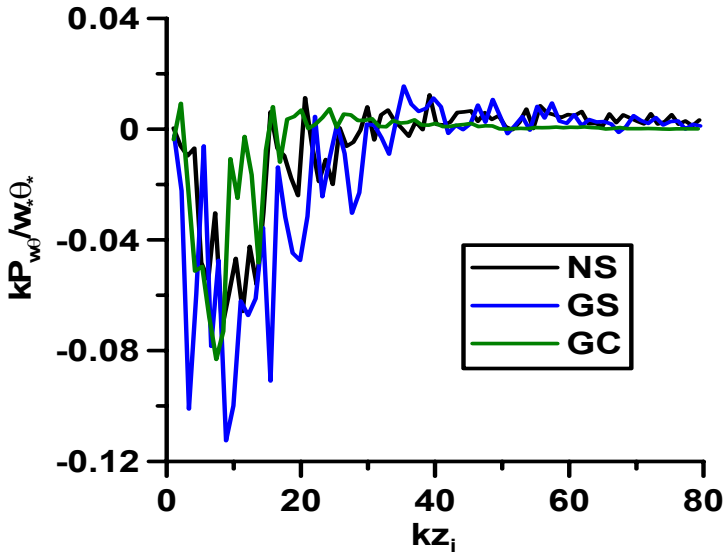

Figure 8.8: Heat flux cospectra at z/z_i=1.0 for the simulations with $d\theta/dz$=0.003 K/m and Q_s=0.3 Km/s.

Specially conducted numerical experiments have shown that the primary cause of the smooth structures and the rapid dropoff in the higher wavenumber energy density in the GC case is the Asselin (1972) filter, which is used with the leapfrog time-stepping scheme to prevent splitting of the numerical solution and to damp numerical modes. Unfortunately, it also damps high wavenumber features. Formally, the leapfrog scheme

is a centered, second order accurate scheme in time, but the Asselin filter, which must be used to prevent time-splitting of the solution and to damp artificial numerical modes, reduces the scheme to first order accuracy, meaning that it is highly dissipative. Since this filter acts in time and not in space, it can only act on structures that change rapidly or move rapidly through the grid, and this occurs when advection is strong. If the turbulence structure remains relatively stationary, the filter does not affect it so dramatically.

One can derive an equation describing the damping as a function of wavenumber, and this is done in Appendix B. The damping is most severe at $k = \pi / 2\Delta$, which is the $4\Delta x$ wave. At infinitely small wavenumbers and at $k = \pi / \Delta$, there is no damping. The lack of damping at $k = \pi / \Delta$ occurs because $2\Delta x$ waves have zero phase velocity on the grid (due to numerical phase speed errors), and because they do not move, they are immune to the effects of the filter. The subgrid turbulent viscosity dissipates the $2\Delta x$ features.

To minimize the damping, the simulations are now run in a frame of references that moves with the turbulent flow, which minimizes the grid-relative advection. Several of the GS and GC simulations were rerun to test the effects of the frame of reference on the spectra and to see if the numerical damping had an effect on the entrainment. For the GC cases, the grid is typically set in a frame of reference that moves at a ground-relative speed approximately 80 percent of the geostrophic wind speed. The Monin-Obukhov similarity condition at the surface has been revised to comply. Since the lower boundary condition is $u=v=w=0$ at the surface, this might imply that the moving grid would damp turbulence features at the surface more than the stationary grid would. However, the flow

at the lowest grid level (10 meters above the surface) is approximately 12 m/s with respect to the surface at rest, so the grid-relative flow is only 4 m/s with the moving grid.

Figure 8.9 shows the results of the simulations performed in the flow-relative frame of reference. One can immediately see that the GC spectra in the flow-relative simulations match the NS spectra much more closely. An inertial subrange is seen, and the energy at the lower wavenumbers, including the peak of the spectrum, is reduced and matches the NS spectrum more closely. At the CBL top, the change in the frame of reference does not affect the energy at the lowest wavenumber in the spectrum, but the GC spectrum is brought much closer to the NS spectrum elsewhere.

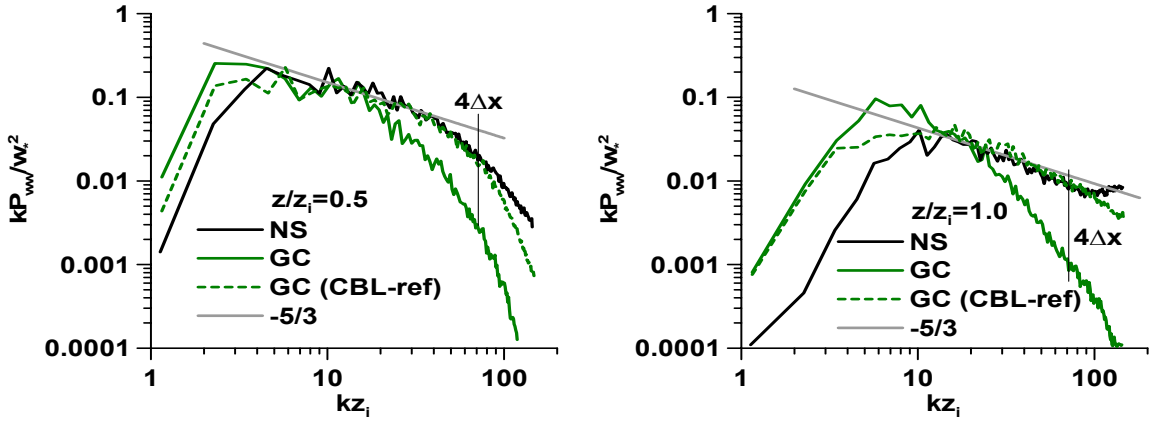

(a) (b)

Figure 8.9: Vertical velocity spectra for the simulations with $d\theta/dz$=0.010 K/m and Q_s=0.3 Km/s. The spectra are calculated across horizontal planes at the following levels with respect to zi: (a) z/z_i=0.5, and (b) z/z_i=1.0. The dashed green lines are spectra from a simulation performed with the grid frame of reference moving with the mean flow in the CBL, which was approximately 16 m/s.

As a further test of the numerical damping, the NS spectrum can be modified using the equation from Appendix B that describes the damping as a function of wavenumber. When the equation is iterated 20 times with the NS spectrum, the output spectrum matches the original GC spectrum almost identically between the energy

production range and k=4Δx, as illustrated in Figure 8.10. Again, the major difference between the NS and GC cases (without the moving grid) is the advection term, which is much stronger in the GC case, so if the affects of the filter damping of advected turbulence, quantified in Appendix B, are applied to the NS spectra, the NS spectra are brought to match the GC spectra.

For the simulations that were repeated, there were no noticeable differences in the CBL growth rate between the simulations performed in the ground-relative and CBL-relative frames of reference. Because the heat flux cospectra show the entraining structures are at the lowest wavenumbers, it is reasonable to expect that the grid frame of reference should not have a large overall effect on simulated entrainment. Additionally, LES comparison exercises among codes using different numerical schemes (Fedorovich et al. 2004c), some of which have considerably less damping, show that the simulated CBL growth rates compare favorably between the code used in this study and codes using higher order schemes (Moeng 1984; Sullivan et al. 1994). In the comparison exercises, three cases (NS, GS, and GC) with a surface heat flux of Q_s=0.2 Km/s and stratification of $\partial\theta/\partial z$=0.003 K/m were simulated using six different LES codes. The horizontally averaged vertical profiles of first and second order turbulence statistics were very similar among most of the codes participating in the comparison.

Additional simulations were performed, as described at the end of Chapter 7, to investigate whether the $Ri \cong 0.25$ layer seen in the GS and GC simulations in Figs. 7-22 and 7-23 could be duplicated under slightly different conditions of shear and buoyancy. These most recent simulations were carefully designed to minimize the effects of

numerical damping in the entrainment zone and to see what effects the primarily shear-generated turbulence in the $Ri \cong 0.25$ layer had on the integral length scale of turbulence.

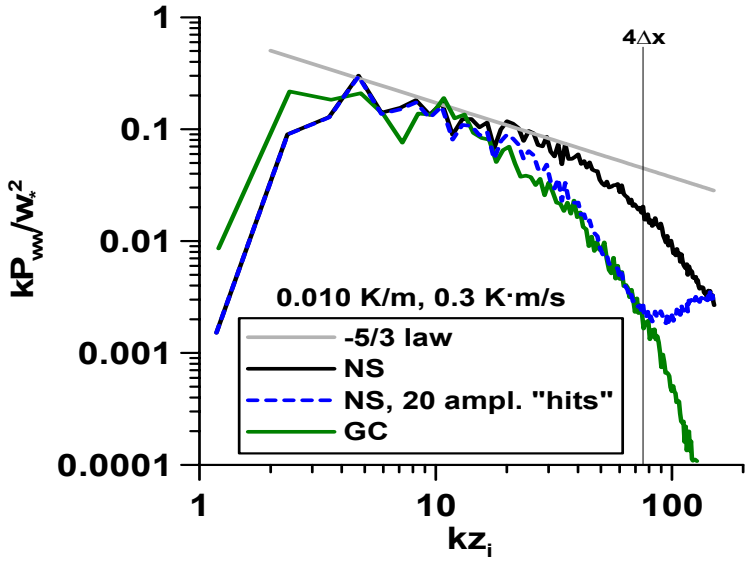

Figure 8.10: Vertical velocity spectra for the NS and GC simulations with $d\theta/dz$=0.010 K/m and Q_s=0.3 Km/s along with the NS spectra, damped according to the amplitude error, as a function of wavenumber, of the leapfrog scheme with the Asselin filter.

Figure 8.11 shows the vertical velocity spectra from these simulations at z/z_i=0.9, 1.0 and 1.1. These locations fall within the entrainment zone, which covers $0.82<z/z_i<1.11$ for the NS case, $0.71< z/z_i<1.21$ for the GS case, and $0.67<z/z_i<1.14$ for the GC case. Fig. 8.11a shows the comparison between the NS and GS spectra, and Fig. 8.11b is a comparison between the NS and GC cases. Far and away the most striking feature separating the sheared CBL spectra from the shear-free spectra is the greater energy density in the upper portions of the entrainment zone of the sheared CBLs. In the spectrum from the shear-free CBL, energy decreases with height, and in the sheared CBLs there is no substantial decrease. These differences can be compared with the profiles of vertical velocity variance that were shown in Figure 7.10.

In the lower portion of the entrainment zone (z/z_i=0.9), where the flow should be mostly turbulent, there is almost no difference among the NS, GS, and GC spectra, and they fall almost on top of one another. At $z=z_i$, some differences begin to appear. The GC case spectral energy density in the lower wavenumber portion of the energy production range is somewhat larger than in the NS case. At higher wavenumbers, though, the spectra are nearly identical. For the GC case (Fig. 8.11b), the spectral energy density is larger over most of the energy production range and into the inertial subrange. The tails of the spectra in the NS case show the effect of insufficient damping of high wavenumber energy by the Deardorff (1980) subgrid model, which reduces subgrid energy in stably stratified layers (Otte and Wyngaard 2001). At z/z_i=1.1, the NS energy is significantly reduced from what it was in the middle and lower portions of the entrainment zone, but the effects of shear keep the GS and GC energy density rather high.

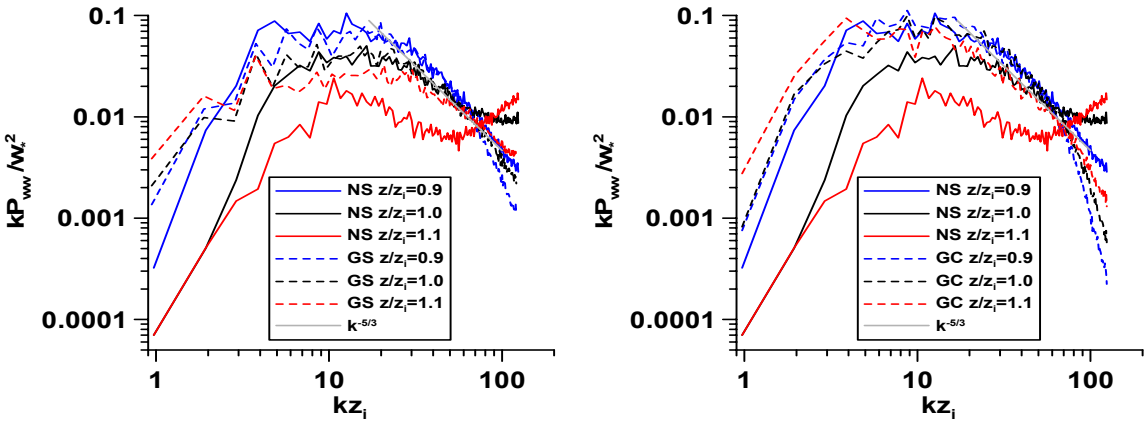

Figure 8.11: Vertical velocity spectra for simulations with $d\theta/dz$=0.003 K/m and Q_s=0.03 Km/s at times in the simulation when the CBL depth was 800m. The comparisons are made between the NS case and: (a) a GS case with geostrophic wind changing linearly with height at a rate of 14 m/s per 1600 meters, (b) GC case with a geostrophic wind of 14 m/s.

The peak of the NS spectrum shifts toward lower wavenumbers as one moves upward through the entrainment zone, whereas in the GS and GC cases, the peak remains in about the same spot. All the spectra roughly follow the $k^{-5/3}$ line in the resolved portion of the inertial subrange, except for the NS spectra in the middle and upper portions of the entrainment zone, where the motions may not be truly turbulent, and the turbulent viscosity is too small to remove these motions.

Figure 8.12 shows the integral length scales of the fluctuating motions as a function of height. The most remarkable feature of this figure is that when the simulations are run in a CBL or entrainment zone flow-relative framework, the integral length scales in the interior portion of the CBL are nearly identical among all three cases. The main differences appear in the entrainment zone, where the NS case integral length scale decreases rapidly, but the GC and GS length scales, affected by the shear-generated turbulence, do not, but above the CBL top, these results cannot be easily interpreted because the analysis technique cannot distinguish between fully turbulent and wavy, non-turbulent motions. It is possible that the K-H type instabilities associated with the shear generation of turbulence are of a relatively large length scale, and according to the analysis done by Kim et al. (2003), this seems to be the case. However, Fig. 8.12 does show a small decrease in the GS length scale for $0.5 < z / z_i < 0.9$.

Figure 8.13 shows the heat flux cospectra at z/z_i=1.0 for the new simulations. In all cases, most of the negative area is at kz_i<20. Compared to Figure 8.8, there is little qualitative difference in the shape of the cospectra. Essentially all the entrainment of heat is occurring on spatial scales that are well-resolved on the LES grid. This is a very important requirement for the validity of the simulation results.

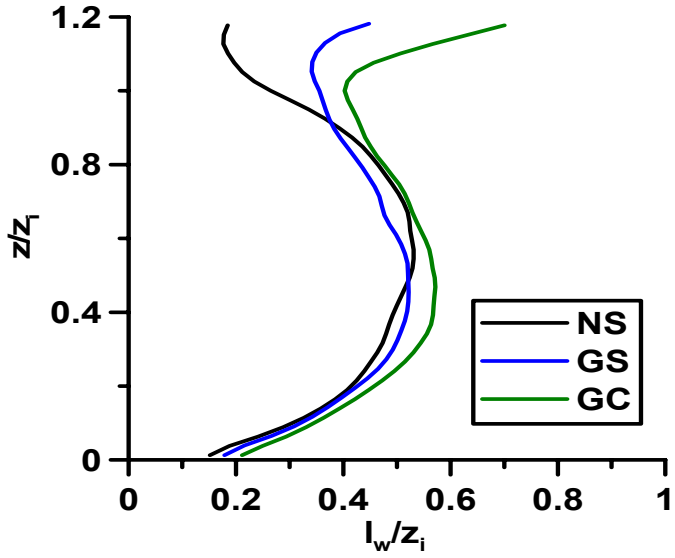

Figure 8.12: Integral length scales as a function of height for the vertical velocity spectra shown in Fig. 8.10.

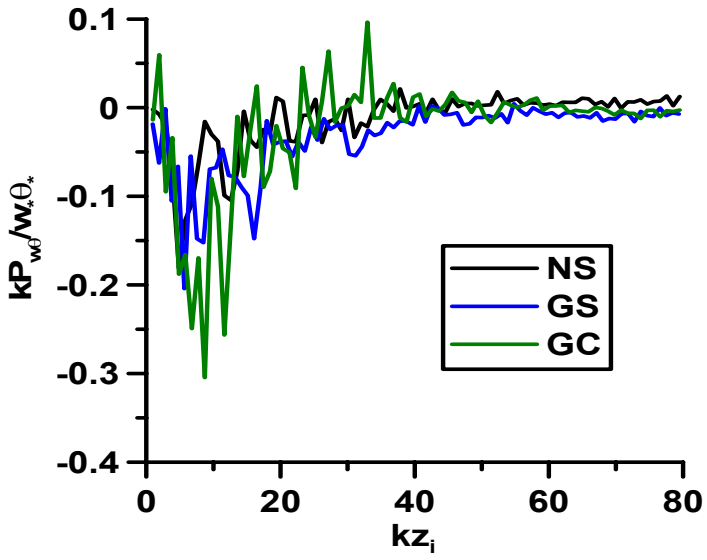

Figure 8.13: Heat flux cospectra for the simulations described in Figs. 8.11 and 8.12.

8.4 Vertical Velocity Skewness

Finally, we present a feature of the simulated CBLs for which some quantitative comparison with atmospheric data can be made. According to the results of the

simulations in this study, the presence of shear changes the skewness of the vertical velocity in the CBL. Plotted in Fig. 8.14 are the vertical velocity skewness profiles for the cases with $d\theta/dz$=0.003 K/m and Q_s=0.03 Km/s. As discussed in Moeng and Rotunno (1990), the vertical velocity skewness profile in LES of shear-free CBLs does not match atmospheric data very closely. Indeed, our NS LES data show much the same thing, with large positive skewness peaking in the upper portion of the CBL. However, in the GS and GC cases, the vertical velocity skewness is much lower, with values of about 0.5 in the middle of the CBL, matching the atmospheric data quite closely. The geostrophic shear in the GS case is much stronger than would typically occur in the atmosphere, but the conditions of the GC case are a bit more representative, although the winds speeds are still rather strong. For simulations with a stronger heat flux, the differences between the vertical velocity skewness profiles of the sheared and shear-free CBLs are not as distinct, and the skewness in the sheared CBLs becomes larger. This behavior is generally expected when considering the simulated CBLs within a range of CBL types. Skewness is large and positive in purely buoyancy-driven CBLs (upward vertical velocity is concentrated in tall, narrow plumes) and small when surface buoyancy flux is weak and shear is a significant factor in CBL growth.

The relationship between the structures in Figs. 8.1 through 8.3 and the skewness profile (Fig. 8.14) can be understood with some qualitative reasoning. In the NS case, the updrafts are fed primarily at the intersections of hexagonal cells (see Fig. 8.3), which are essentially isolated structures. The updrafts are therefore rather narrow, as seen in Fig. 8.1. In the GC case, the intense surface shear deforms the temperature perturbations near the surface and causes them to elongate. As a result, the updrafts in the GC case form

along lines, and when combined with the mass-compensating downdrafts, form the horizontal convective rolls in the GC case (Kanna and Brasseur 1998). Since the updrafts are not as isolated and intense as in the NS case, the skewness drops. Even in the GS case, the plumes of warmer air are tilted by the shear relative to the more vertically erect structures seen in the NS case. Also, the shear-generated turbulence would not be expected to have a directional preference for transport, unlike the NS case, where warm air rises.

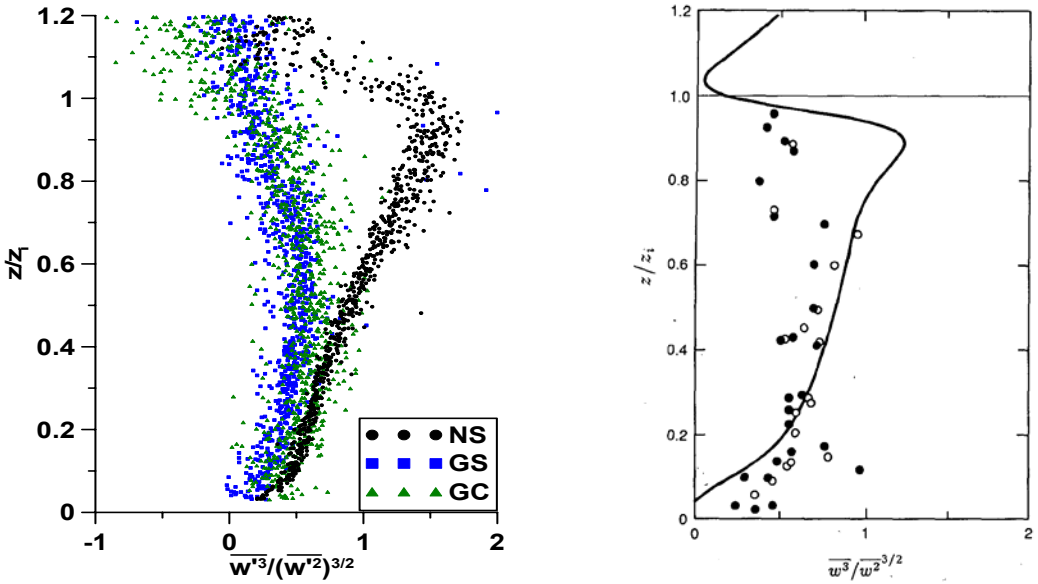

Figure 8.14: Vertical velocity skewness for (a) the simulations with $d\theta/dz$=0.003 K/m and Q_s=0.03 Km/s, (b) Moeng and Rotunno (1990)

These overall results are consistent with the effects of shear on the TKE budgets presented in Chapter 7. Since one component of the TKE transport is $\overline{w'w'w'}$, smaller skewness implies that the upward transport of energy is reduced in sheared CBLs or that it is compensated by the downward transport of shear-produced TKE from the entrainment zone.

8.5 Chapter Summary

The results of this chapter can be summarized within the framework of the goals that were stated at the beginning of the chapter. The shear has rather significant effects on the turbulence structure within the CBL. In the GC case, it aligns turbulent motions into horizontal convective rolls (as has been simulated by others and observed in the atmosphere), and in the GS case, the shear tilts the thermals out of the vertically upright orientation they have in the NS case. Relative to the NS case, the resulting updrafts are not as narrow, and the upward transport of TKE that is seen in the NS case is reduced in the GS and GC cases, particularly in the middle and upper portions of the CBL. This is reflected in both the TKE budgets and skewness profiles. There could also be some compensating downward transport of energy from the entrainment zone.

Aside from differences in total variance, the vertical velocity spectra in the interior of the CBL and in the lower portion of the entrainment zone are not greatly changed in the presence of shear. Although there is some greater energy in the lower wavenumber portion of the production range when shear is present, the rest of the energy production range and inertial subrange look similar to the shear-free spectra. The differences among the GS, GC, and NS spectra in the initial simulations (Fig. 8.6) are mostly due to the damping effects of the numerical scheme, which are more severe at higher wavenumbers (except for $\pi/2\Delta \le k \le \pi/\Delta$), and when the simulations are conducted in a frame of reference moving with the CBL mean flow, most of these differences disappear.

The integral length scales of turbulence are largest in the middle of the CBL, and they do not depend much on shear there; the integral length scales of the NS, GS, and GC

cases are nearly identical. At the CBL top, the GS and GC integral length scales are larger than they are in the NS case, which indicates the structures associated with the K-H type instabilities that have been documented in other studies (Kim et al. 2003), are probably well-resolved on the LES grid. However, it is difficult to distinguish between turbulent and wavy motions there, so the results must be interpreted with some caution.

The heat flux cospectra in the entrainment zone (z/z_i=1.0) show that the turbulent motions responsible for entrainment are well-resolved on the LES grid. This result lends greater confidence to the results of Chapter 7. It remains to be seen, however, what the evolution of the CBL would be like in the simulations, given the input of atmospheric data as an initial condition. This is the focus of the next chapter.

Chapter 9

Comparison of LES with Atmospheric Data

9.1 Introduction

This chapter considers measurement techniques to estimate the entrainment rate of sheared CBLs. After considering the variety of methods and data available, a case study of CBL development, simulated by LES and observed in the atmosphere, will be examined and the LES and atmospheric data compared.

As mentioned in Chapters 1 and 2, the effects of horizontal heterogeneity, mesoscale and synoptic scale forcing for vertical motion, and advection are at least as large as the effects of shear on the convective boundary layer depth. Therefore, it would seem more feasible to measure not the CBL depth as a function of time (although lidar CBL depth measurements do seem fairly robust), but to directly measure entrainment velocity in terms of the heat flux in the entrainment zone δB_i (see Fig. 3.1 and Chapter 5). Entrainment zone heat flux measurements in the atmosphere are difficult and expensive to make so they are not conducted on a routine basis.

9.2 Atmospheric Boundary Layer Measurement Methods

9.2.1 Discussion of Selected Previous Studies

Direct measurements of heat flux in the entrainment zone are limited to a few select field experiments, from which there is a limited quantity of data. A number of studies such as Lenschow (1970), Davis et al. (1997), Flamant et al. (1997), and Young et al. (2000) have measured entrainment zone heat flux using aircraft, but it is very difficult to identify and fly exactly at the level where the horizontally averaged heat flux is at its minimum. Flamant et al. (1997) therefore relied on the extrapolation of the heat flux profile from three measurement levels within the CBL, using a linear best fit, up to the CBL top z_i, which was determined by lidar. LES data certainly support the idea that the heat flux profile is linear, at least below the level where the heat flux crosses zero. The lidar-determined z_i, is likely to be higher than that from the heat flux minimum because it relies on maximum gradients, which place z_i higher than the height of the heat flux minimum, but the same methods can be applied to LES data, so a direct comparison is possible. Flamant et al. (1997) have relatively modest values of entrainment zone shear, with generally 3 m/s or less velocity change across the entrainment zone. At these values, LES results do not show significant effects of shear, and their data, plotted as $-B_{i0}$ versus Δu, do not show a significant trend either.

Another study involving aircraft measurements is the Dynamics and Chemistry of Marine Stratocumulus (DYCOMS-II) experiment (Stevens et al. 2003). Aircraft were flown in circular patterns over marine stratocumulus layer off the California coast, and a

divergence technique was used to accurately estimate the entrainment rate in the stratocumulus-topped CBL:

$$w_e = \frac{dz_i}{dt} + \int_0^{z_i} \left(\frac{\partial u}{\partial x} + \frac{\partial v}{\partial y} \right) dz \,, \tag{9.1}$$

where w_e is the entrainment velocity, which is distinct from the CBL growth rate, dz_i/dt, when divergence is nonzero. In the DYCOMS-II flights, it was thought that the divergence could be accurately estimated by integrating the track-normal component of the horizontal velocity around a closed flight track (Lenschow 1996; Lenschow et al. 1999), however, analysis of the data showed that the divergence estimates were not as good as expected (Douglas Lilly and Bjorn Stevens, personal communication).

Entrainment estimates were also constrained by the use of a tracer method, which employs the ZOM parameterization of fluxes at the CBL top:

$$w_e = \frac{\overline{w'c'}_i}{\Delta c} \tag{9.2}$$

The tracer method worked well for the stratocumulus-topped marine CBL, which has a sharply defined top, but it might not do well over land, where the CBL top is not so sharp. Dimethyl sulfide works as a good tracer over the ocean, but a different tracer would have to be chosen over land.

Angevine et al. (2001) infer the entrainment heat flux from sequential profiles of temperature measured at the 200-meter tall Cabauw tower in the Netherlands during the morning transition from a nocturnal boundary layer to a convective boundary layer. The sequential profiles of temperature during the transition were used as a proxy for heat flux and showed that the entrainment flux ratio in such transitioning CBLs is large. During the transition, surface heat flux is relatively modest, and winds at the top of the nocturnal

boundary layer are relatively strong, allowing the effects of shear to stand out. The tower is only tall enough to observe the transition itself and not the evolution of the CBL once it is established.

The Boulder Atmospheric Observatory (BAO) in Colorado is another tall (300m) tower that has been designed for atmospheric experiments. Television transmission towers can be even taller (up to 500 meters), but access to them is limited, and the proximity of high-powered transmitters may increase the likelihood of electromagnetic interference. Even the tallest towers are still shorter than the typical CBL depth, so in most CBLs, *in-situ* measurements of the entrainment zone are only possible with aircraft. Nevertheless, shear tends to be most important during the morning transition when the CBLs are shallower, and towers are able to measure the transition relatively effectively.

LES and atmospheric data indicate the heat flux profiles are generally linear between the surface layer and the zero crossing height, so if measurements are made over a sufficient depth of the CBL to establish a linear profile, then this profile could be extrapolated to a lidar-determined z_i, and the ZOM-equivalent heat flux of entrainment could be established (Flamant et al. 1997, Angevine et al. 2001). The biggest limitation of retrieval of second order statistics from a stationary platform is that a long sampling time is necessary for the average profiles to converge to an ensemble mean, which itself is difficult to define. When the winds are very light, the use of the Taylor frozen turbulence hypothesis becomes problematic, making it difficult to relate time averages to spatial averages. Despite these problems, Angevine et al. (2001) shows that it is possible to use tower measurements during the morning transition period, when shear is expected to be the most important in the CBL development.

Pino et al. (2003) compared LES with radiosonde measurements taken at an Atmospheric Radiation Measurement (ARM) Program site. ARM is funded by the United States Department of Energy and is aimed at improving the understanding of the effects of clouds and their radiative feedback on global climate change. The ARM Southern Great Plains Facility (SGP) consists of a central facility near Lamont, Oklahoma and several surrounding facilities in other parts of Oklahoma and southern Kansas. The data collected at the sites include balloon-borne atmospheric soundings, Atmospheric Emitted Radiance Interferometer (AERI) measurements, measurements of surface energy balance and fluxes, 915 MHz profiler winds, and Raman lidar aerosol backscatter and water vapor data (Goldsmith et al. 1998; Whiteman et al. 1992; Turner and Goldsmith 1999; and Turner et al. 2000). When balloon-borne atmospheric soundings cannot be collected, AERI data (Feltz et al. 1998, 2003; Smith et al. 1999) can substitute. Comparison studies indicate the difference between the AERI and radiosonde measurements is typically about 1 K.

9.2.2 Additional Platforms

Additional platforms are available for measuring CBL turbulence. Tethered balloon-borne systems (Frehlich et al. 2003) can measure wind and temperature continuously at several levels along the tether that ties the system to the ground. Such systems can operate in the nocturnal boundary layer or in the CBL under light wind conditions (generally 10 m/s or less). During stronger wind conditions, when shear plays a larger role in entrainment, it becomes much more difficult to operate these systems. Garcia et al.

(2002) have done a case study of the morning evolution of the CBL depth using a tethered measurement system.

Lidar measurements have been used in LES-atmospheric dataset comparisons (Mayor et al. 2003). High resolution Doppler lidar (HRDL—Grund et al. 2001) can be used to measure turbulence structures in the CBL using range gates as low as 30m. HRDL was used in the Cooperative Atmosphere Surface Exchange Study in 1999 (CASES-99), which took place in the Walnut Creek watershed in southeastern Kansas to study the structure of intermittent turbulence in the nocturnal boundary layer. During the 2002 International H_2O Project (IHOP), HRDL was to be operated from aircraft flying above the CBL, but a number of technical difficulties prevented the collection of a large amount of data. With its range resolution of only 30 meters, it has the capability of resolving turbulence structure in the entrainment zone, particularly if it can be used in a downward-pointing position in aircraft flying just above the CBL. Ground-based Doppler lidar measurements of the entrainment zone are also possible, but this requires the beam to penetrate the entire depth of the CBL, worsening the attenuation of the signal from the entrainment zone. Nevertheless, it has been used to retrieve vertical velocity in the CBL using an adjoint technique (Chai et al. 2004) in a domain about a quarter of the area of the LES domain in Chapters 6 and 7. This may allow some further comparison between LES and atmospheric measurements.

Profiler measurements of the vertical structure of the mean horizontal wind have improved remarkably over the past several years. 915-MHz profilers can be operated to retrieve data with 60-meter vertical resolution (Grimsdell and Angevine 1998; Mead et al. 1998; White and Senff 1999; Pollard et al. 2000). A multiple antenna profiler (MAPR—

Cohn et al. 1997, 2001) was operated during the IHOP experiment and provided data on mean winds and vertical velocity at the Homestead site in the Oklahoma panhandle. Additionally, the use of interferometry shows potential to further increase the resolution of wind profilers. Sound detection and ranging (SODAR) can also provide some wind and temperature data closer to the ground or in particularly shallow CBLs, where profilers may be less effective (Seibert and Langer 1996; Beyrich and Gryning 1998).

Some attempts have been made to estimate the CBL depth from 915 MHz profilers (Grimsdell and Angevine 1998; White and Senff 1999; Bianco and Wilczak 2002). With a wavelength of approximately 30 cm, the radiation is scattered by large gradients in density, which are relatively common in the turbulent CBL and especially at the CBL top. Therefore, looking for regions of high signal to noise ratio can help identify the CBL top. Because the ratio reaches a maximum at the CBL top as opposed to lidar backscatter, which decreases rapidly at the CBL top, the same Haar wavelet techniques (Davis et al. 2000; Brooks 2003) that are used on lidar data may not be easily used on profiler data. Additionally (Guiliano, personal communication), some efforts have been made to retrieve profiles of vertical velocity variances from the 915-MHz profiler data, but there have been problems with these retrievals. Lambert et al. (2003) have recently discussed the performance and quality control of 915-MHz profilers.

Finally, the use of mobile radar systems needs to be mentioned. Gal-Chen and Kropfli (1984) developed a technique to retrieve buoyancy fields from dual-Doppler observations of the atmospheric CBL. During the IHOP experiment, mobile Doppler radars were deployed to observe the CBL structure on days when boundary layer-based deep convection was expected to develop or when observing the evolution of the CBL

from its initial development in the morning to its mid-afternoon state. For these experiments, four mobile Doppler radars were deployed at the corners of a box usually about 20 km on a side. Using range gates on the order of 100 meters, these deployments were capable of resolving temporally and spatially coherent CBL structures when the CBL was well-developed from late morning into the evening (Markowski, personal communication). During the early morning transition from a nocturnal to convective boundary layer, radar returns were weaker, and it was much more difficult to detect these CBL structures.

The mobile radars deployed in these boxes were C-band (5-cm wavelength) and X-band (3-cm wavelength) radars. More extensive radar datasets are available from the operational network of S-band Doppler radars across the United States. These radar systems have 250-meter range gates for velocity data and 1 km range gates for reflectivity. This resolution may be a bit too coarse to provide details about the boundary layer structure, but horizontal convective rolls and other z_i-scale structures can be routinely identified in the afternoon and evening in reflectivity and velocity images from these radars during the warm season. The velocity azimuth display (VAD) technique can also be used to retrieve the vertical structure of the mean winds. When an optimal scanning strategy is used, this technique can provide vertical resolution well less than 100m (Martin, 2003) at a height 250 meters above the surface for just about any radar configuration. Plans exist to evaluate the usefulness of this data, but how useful it will be remains to be seen. Already, Schneider and Lilly (1999) have analyzed dual-Doppler radar data for the CBL. One clear advantage of using radar data is that the scanning techniques cover a fairly extensive horizontal area (greater than the LES domain), so

undersampling is much less of an issue when calculating turbulence statistics. Although methods are being developed to automate the process of data retrieval from radar, it usually requires considerable effort to process the data and retrieve full three-dimensional velocity vectors and temperature from them.

9.2.3 Data Comparability Issues

The differences between the time-averaging used in many stationary atmospheric observation platforms and horizontal averaging used in LES need to be considered when making comparisons between the two. Mayor et al. (2003) made a comparison between LES and atmospheric data for a horizontally evolving atmospheric boundary layer and consider these differences.

Perhaps the bigger issue for intercomparison between atmospheric data and LES is the heterogeneity of the atmospheric CBL. The heterogeneity presents problems when performing horizontal averages, because the land surface elevation and vegetative cover vary, and so do the sensible and latent heat fluxes. The concept of a horizontally homogeneous CBL, easily simulated in LES, may be not directly applicable to atmospheric CBLs, which are affected by spatial variability in the underlying buoyancy forcing, and it cannot be expected that boundary layer scale motions would be well separated from mesoscale motions (Schneider and Lilly 1999). The current LES setup simulates only horizontally homogeneous CBLs because of its periodic boundary conditions. Atmospheric measurements (Caughy and Palmer 1979; Caughy et al. 1979) show that the principal energy-containing length scales of turbulence in the CBL are approximately equal to the CBL depth, meaning larger length scales are not large

contributors to the TKE. This does not mean that the CBL depth won't still be highly variable on the mesoscale. The IHOP experiment was designed to measure the heterogeneity of the CBL over land, and it found exactly that, even under atmospheric conditions that might be considered favorable for a more homogeneous CBL, such as extensive areas of clear skies and light winds that occur under an anticyclone. This inherent heterogeneity remains a primary concern for the comparison of LES results with atmospheric observations for shear-driven CBLs.

9.3 Proposed Comparison

9.3.1 Methods

If a suitable tracer can be found to provide a constraint on the aircraft-measured entrainment rate over land, then the DYCOMS-II techniques (Stevens et al. 2003) would be the most preferable for estimating the entrainment velocity. For the time being, it appears best to make use of boundary layer measurements that are made on a more or less routine basis. The study of Pino et al. (2003) is limited to a single case, but it demonstrates the feasibility of making comparisons between LES and atmospheric data and takes advantage of routine measurements made at the ARM SGP site. Repeating such LES/data comparisons for a larger number of cases would make these comparisons more complete and defendable. On some days, the effects of surface heat flux heterogeneity and larger scale atmospheric vertical motion may be the dominant effects on the CBL depth. On other days, when the fetch of mean flow covers areas with relatively little variation in land surface, and large scale forcing for vertical motion is

weak, the effects of wind shear may be detectable. However, it may require several detailed case studies to show this.

The study of Pino et al. (2003) provides a basis for the proposed comparison between atmospheric and LES data. The measurements at the ARM SGP site in northern Oklahoma provide enough data to make a fairly detailed comparison between the atmospheric data and LES. The initial temperature and wind data for LES can be taken from a variety of measurements. Soundings are launched at somewhat regular intervals from the site, sometimes as often as every three hours during intensive operations periods such as IHOP. AERI profiles of temperature and moisture are taken every eight minutes and the profiles are available at least once per hour. They can be compared with radiosonde data or used as the sole temperature data source when radiosonde data are not available. The AERI resolution ranges from 100 meters near the surface to 250 meters at z=3km.

In addition to radiosonde data, wind data can be taken from the 50 MHz and 915 MHz profilers at the SGP site. The 50 MHz profiler (Nastrom and Eaton 1995; Angevine and MacPherson 1995) has range gates varying from 0.3 km to 1 km, and profiles cover a range of z=2 km to z=12 km. The profiler also has a radio acoustic sounding system (RASS), which can take virtual temperature measurements between 2 and 4 km. The 915 MHz profiler samples from 0.1 km up to 5 km and has range gates as small as 60 m. It also has a RASS and can take virtual temperature measurements between 0.1 and 1.5 km.

The CBL depth measurements can be made with the Raman lidar, which measures water vapor, aerosol backscatter, and backscatter depolarization ratio (Goldsmith et al. 1998; Whiteman et al. 1992; Turner and Goldsmith 1999; and Turner et

al. 2000). The wavelet techniques of Davis et al. (2000) or Brooks (2003) can be applied on the backscatter and water vapor profiles to identify the CBL top and perhaps the entrainment zone thickness (Boers and Eloranta 1986; Cohn and Angevine 2000). The CBL depth estimates can also be made from the AERI soundings if necessary.

The surface flux data can come from systems that use the eddy correlation method (these use a sonic anemometer) (Hart et al. 1998) or the energy balance Bowen ratio (EBBR) method (Field et al. 1992). The EBBR method relies on in-situ sensors and radiation measurements to make estimates of the surface energy balance. The eddy correlation technique measures the correlation between temperature and vertical velocity measured by a sonic anemometer. These measurements can be checked against each other, as well as against data from other ARM SGP facilities. During IHOP, there were also several integrated surface flux facilities located within about 100 km.

During the IHOP experiment, intensive measurements were also taken at a site about 30 km southwest of Beaver, Oklahoma. This measurement facility, designated the Homestead site, had the same quantity of flux and profiler measurements but a greater variety of lidar measurements. Because of the greater variety of available lidar data, atmospheric measurements from the Homestead site became slightly preferable to those from the ARM SGP site during IHOP.

The main effort involved in the comparisons would be to run the LES with surface heat flux measurements and initial temperature and wind profiles from the atmospheric data. The simulation would then be carried out and compared with subsequent atmospheric profiles of wind and temperature and lidar estimates of CBL

depth. If desired, separate, shear-free simulations can also be performed using the same surface heat flux data and initial temperature profiles.

9.3.2 Selected days for analysis

Data from May 22, June 3, June 9, and June 14, 2002 have preliminarily been selected for comparison between LES and atmospheric data. The first three of these days had a strong wind, and the third was a boundary layer evolution mission that had relatively light winds and clear skies. The IHOP project ran from the middle of May until late June and was an intensive operation period for the ARM SGP site. Radiosonde launches were made every three hours, and a 404 MHz profiler was also deployed at the site. However, more intensive measurements were made at a site in the Oklahoma Panhandle (designated the Homestead site) during IHOP. Data from the Homestead site were also used.

9.4 Simulation of May 22, 2002 Case

9.4.1 Motivation

This section summarizes the efforts to simulate the CBL development for a particular atmospheric case in which the wind shear was strong. For this case, some atmospheric data are available, which allows comparison between LES predictions and atmospheric observations of CBL evolution. The immediate motivation for studying this case was to simulate turbulence structures comparable to observed structures to assist in the testing of the radar data assimilation of scheme (Weiss 2004). Unfortunately, the comparison is

conceptually not completely adequate, since the radar was performing transects of the dryline, which can be considered a boundary between two different CBL types. The LES code is designed to study horizontally homogeneous CBLs and, in its current configuration (which has periodic boundary conditions), is unable to simulate heterogeneous CBLs. Considerable modification of the code and much greater computer power (i.e. much larger grid) would be required to simulate heterogeneous CBLs associated with dryline type circulation patterns.

The goals of the study in this chapter became threefold. First, simulate the structure of the shallower CBL east of the dryline. The simulation should then be able to provide some turbulence patterns that are qualitatively comparable with the patterns that are observed in the atmosphere next to the dryline. Second, the simulated CBL depth can be compared with the CBL depth determined from lidar data obtained for this particular case. This will additionally allow the ability of the code to simulate atmospheric sheared CBLs to be tested. The third and perhaps most significant goal of this study is to discover where difficulties may be encountered when making comparisons between LES predictions and atmospheric observations of sheared CBLs.

9.4.2 Data and Methods

The case to be studied is the May 22, 2002 convection initiation experiment that formed a part of IHOP. Numerous CBL measurements were taken in the vicinity of a north-south oriented dryline that moved slowly eastward across the Oklahoma and Texas panhandles. The data available for input to the simulation consisted of balloon-borne sounding data from National Weather Service launch sites at Amarillo, Texas (AMA) and Dodge City,

Kansas (DDC), wind profiler and radiometer data from the National Center for Atmospheric Research (NCAR) Integrated Sounding System (ISS), which was located at the Homestead site, and surface flux measurements from the Integrated Surface Flux Facility (ISFF), which included three sites in the Oklahoma panhandle and the northern Texas panhandle. CBL depth determinations were available from several lidars that were collocated with the ISS. The IHOP field campaign is described in greater detail in Weckwerth et al. (2004).

The wind data in the initial profiles were taken from a combination of the AMA and DDC soundings. Since the measurement sites are about midway between AMA and DDC, the wind data were interpolated approximately in a linear fashion between the two soundings. Additionally, the geostrophic wind was estimated by finding the geopotential height gradients by triangulating between the AMA, DDC, and Norman, Oklahoma (OUN) soundings. With the initial geostrophic wind estimate, the surface wind in LES veered with time much more than in the atmospheric data, so the profiles were adjusted to increase V_g a bit near the surface.

The initial mean wind configurations can be considered representative of the actual conditions of May 22, 2002. The initial profiles of actual and geostrophic wind and the AMA and DDC sounding wind data are shown in Figure 9.1. The geostrophic wind was taken to be constant in time during the simulation. The sounding data showed that the geopotential height gradients changed relatively little during the day on May 22, 2002, so this seems to be a reasonable assumption.

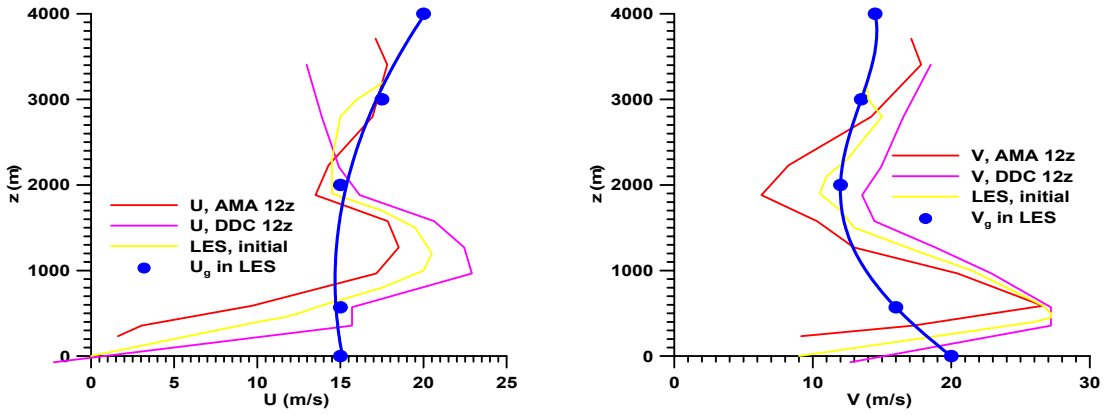

Figure 9.1: Initial wind profiles for the May 22, 2002 case: (a) x-component ($\bar{u}$), and (b) y-component ($\bar{v}$). The yellow profile indicates the initial LES wind, the blue profile is the initial geostrophic wind, the red profile is from the Amarillo, Texas 1200 UTC sounding, and the pink profile is from the Dodge City, Kansas 1200 UTC sounding.

The initial profiles indicate wind speeds up to 30 m/s, and although the geostrophic wind shear was not particularly strong, the shear in the measured wind was even stronger than in the LES cases described in Chapters 6 and 7. The x-component alone changes by 20 m/s over the lowest kilometer, and the overall wind speed changes by 20 m/s in less than 1 km.

A 1200 UTC radiosonde launch directly from the measurement site would have been very helpful in setting the initial LES profiles, but onsite launches were not conducted until midday during this phase of the field campaign. Therefore, the initial LES potential temperature profile was taken from a combination of AMA and DDC sounding data and ISS radiometer data as shown in Figure 9.2. The radiosonde data showed higher temperatures than the radiometer data did, but since the radiosonde data come from *in-situ* measurements of the atmosphere, the LES initial temperature profile was adjusted slightly toward the AMA and DDC data. Above z=2km, the radiosonde data were used. The data indicate the potential temperature stratification is roughly 0.010

K/m in the lowest kilometer, which corresponds to the strongest stratification in the simulations of Chapter 7.

Flux data are presented in Figure 9.3. Half-hourly averages of sensible heat flux from all three ISFF measurement stations were averaged to produce the LES input flux data. The flux data are indicative of the strong insolation and absence of cloud cover that occurred during this particular case. The variability of fluxes among stations was relatively small.

The LES settings were mostly the same as those listed in Table 6.1. Those parameters that differed are listed in Table 9.1. The domain size and grid cell dimensions were chosen to best meet the data requirements of the data assimilation algorithm tests. The grid cells had to be 30 m in order to match the range gates of the radar (Weiss 2004). The domain needed to be deep enough to simulate the 2.5-km deep CBL that was present during this particular case, and it needed to be as wide as possible to most closely match the radar scanning range. The domain width was limited to 7.68 km because of computational memory constraints. In order to minimize numerical damping of large wavenumber turbulence and to maximize the time step, the grid frame of reference was chosen to be u=10 m/s and v=14 m/s.

Table 9.1 Parameters of LES Conducted for May 22, 2002 IHOP Case

Parameter	**Setting**
Domain size	$7.68\times7.68\times3.99\text{km}^3$
Grid	256×256×133 (30-meter cells)
Initiation	Random temperature perturbation with standard deviation of 2K.
Grid frame of reference	Moved at u=10 m/s and v=14 m/s relative to the ground.
Time step size	Dynamically determined at each time step

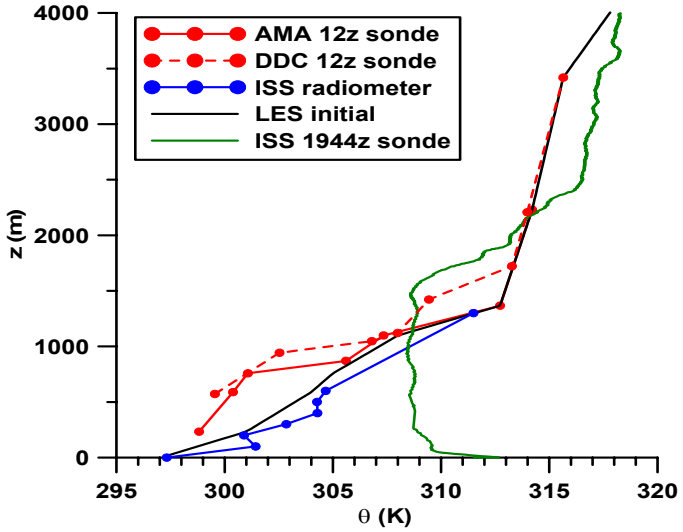

Figure 9.2: Initial potential temperature profiles for the May 22, 2002 case. The black profile indicates the initial LES wind, the blue profile is from the ISS radiometer data, the solid red profile is from the Amarillo, Texas 1200 UTC sounding, and the dashed red profile is from the Dodge City, Kansas 1200 UTC sounding. The green profile is from the ISS 1944 UTC sounding and is plotted to illustrate the change in the measured temperature profile over the course of the simulation.

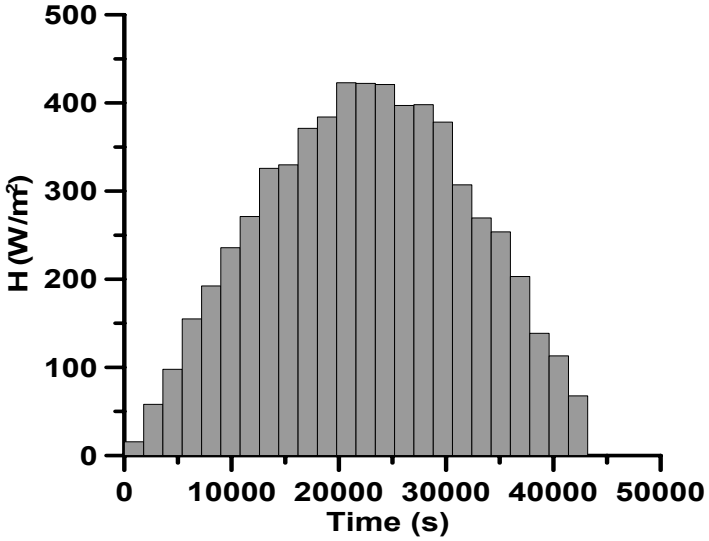

Figure 9.3: Surface sensible heat flux (W/m^2) as a function of time in the simulation of the May 22, 2002 case obtained from ISFF data.

The atmospheric CBL depths were determined from the Holographic Airborne Rotating Lidar Instrument Experiment (HARLIE) data. HARLIE is a 1-micron wavelength aerosol backscatter lidar that was deployed during the IHOP experiment at the Homestead measurement site south-southwest of Beaver, OK. It scans at a constant elevation angle of 45 degrees and rotates continuously in azimuth at a rate of 30 degrees per second. This provides five scans per minute. A more detailed description of HARLIE can be found in Guerra et al. (1999). There are some sampling issues when comparing HARLIE data to LES data. The HARLIE scanning lidar only samples a cone-shaped surface, the interior of which is not sampled. Nevertheless, the scanning strategy covers a circle whose diameter is at least 2 km for the CBL considered here, making its CBL estimates comparable to those from LES.

The CBL depth was determined using a wavelet technique described in Davis et al. (2000). A wavelet dilation of 10 was used, and the transform was applied to the one-minute averaged vertical profiles of lidar backscatter (five scans). The same wavelet technique was also applied to the LES potential temperature profiles in order to compare CBL depth estimates from the buoyancy flux minimum with those from the wavelet technique. Although the wavelet analysis is applied to *aerosol backscatter* data from HARLIE versus *potential temperature* data from LES, the Haar wavelet transform used in this technique reaches its maximum in areas of large gradients, both of which should be located at roughly the same height, as long as the interface is sharp. The wavelet technique provides CBL depth estimates that are consistent with those from the maximum temperature gradient technique that was discussed in Chapter 5.

9.4.3 Results

9.4.3.1 Evolution of the Entrainment Flux Ratio

Although the free atmospheric stratification and surface heat flux in the described LES runs are comparable to those from the GS and GC simulations of Fig 7-1c (shear had little effect on entrainment in those simulations), the shear in this case appears to have a rather substantial effect on entrainment. About one hour into the simulation, when resolved turbulence develops, the entrainment flux ratio becomes extremely large, reaching a peak much larger than was seen in any of the GS or GC simulations discussed in Chapter 7. After this initial burst of entrainment, the entrainment flux ratio rapidly decreases to around 1, where it fluctuates for about 30 minutes. Then, between t=7000s and t=15,000s, it gradually diminishes to values typical of the NS simulations (see Chapter 7). Towards the end of the simulation, it increases again.

The strong variation in entrainment flux ratio shows that the CBL is far from the *equilibrium* regime of entrainment discussed in Chapters 3 and 4. This is no surprise given the variability of all the parameters that were held constant in Chapter 4. The free atmospheric stratification is heterogeneous, requiring the CBL to adjust to the changing stratification, and the surface buoyancy flux also changes, requiring additional adjustment. As the CBL grows, it also encounters layers of different shears. All these factors strongly suppress the establishment of an equilibrium regime during much of the simulation.

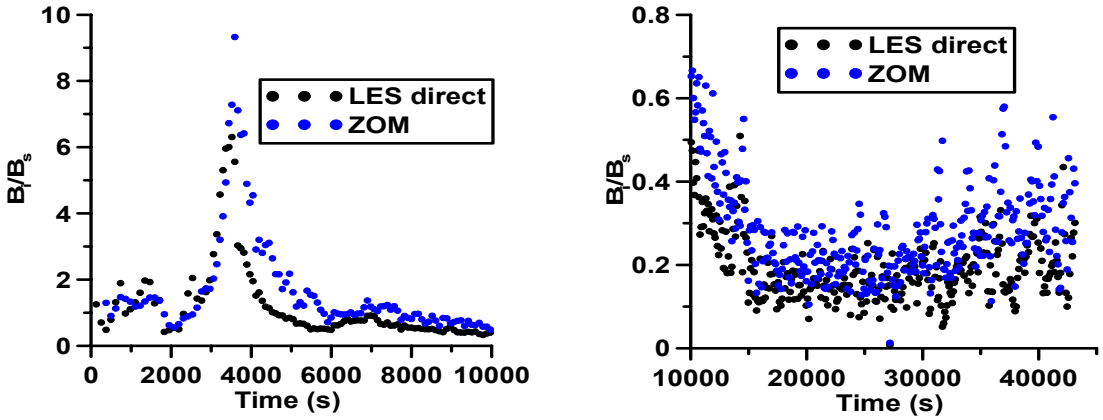

Figure 9.4: Entrainment flux ratio as a function of time for the simulation of the May 22, 2002 case with the entrainment zone heat flux taken directly from LES (black dots) and linearly extrapolated through the zero crossing height to find the ZOM heat flux of entrainment (blue dots). The *y*-axes are scaled differently in order to highlight the evolution of the entrainment flux ratio.

The transition and onset of resolved turbulence in LES is highly dependent on the numerical setup, and the extremely strong entrainment around t=3600s may be an artifact of the LES resolved turbulence onset. The characteristics of the CBL are best be analyzed by looking at simulated data *after* the resolved turbulence has become fully established. The entrainment flux ratio is still rather large at t=7000s, so a look at momentum profiles at this time may elucidate what is happening during the early portion of the simulation. Other interesting time-dependent features of entrainment are observed at t=25,000s, when the entrainment flux is at its minimum, and also around t=40,000s, when it increases again.

9.4.3.2 Evolution of Mean Profiles

The potential temperature profiles at these selected times are plotted in Figure 9.5, and the momentum profiles are shown in Figure 9.6. Also plotted on these profiles are the upper and lower limits of the entrainment zone and the CBL top z_i. At the early time

period, despite the CBL growing against a very stably stratified potential temperature profile, the entrainment zone is rather deep because of the strong shear production of turbulence in this layer. There is more than 12 m/s velocity change across the entrainment zone at this time.

At about t=25,000s, the CBL is still growing through a rather strong inversion, but the shear has diminished substantially. The layer of very strong momentum seen below z=1500m at about t=7000s has largely disappeared due a combination of the entrainment of this momentum into the growing CBL and the effects of the Coriolis and large scale pressure gradient forces (accelerations due to the deviation of the wind from geostrophic balance). The entrainment zone, rather than growing as it typically would in conditions of uniform stratification and shear, has not deepened during this time interval. By about t=40,000s, both the CBL and the entrainment zone become much deeper, influenced by a combination of the weaker stratification aloft and the increasing shear at the CBL top.

Unlike the LES cases examined in Chapter 7, a substantial component of the shear in the entrainment zone is forced by the ageostrophic component of the initial wind in the simulation. If the momentum is not in geostrophic balance, the wind field undergoes an inertial oscillation, and the amplitude and phase of this oscillation is heavily dependent on the initial conditions of the simulation. Therefore, the simulation results, at least with regard to the influence of shear on entrainment, appear highly sensitive to the initialized values of the actual and geostrophic wind. Perhaps the initial profiles of wind would be better taken from NWP model grids, since these models have data assimilation

algorithms considerably more sophisticated than the interpolation techniques used here. Future studies might use NWP model wind profiles if they prove to be beneficial.

9.4.3.3 Turbulence Kinetic Energy Budgets

The TKE budgets at the selected times are displayed in Figure 9.7. The shear production of turbulence in the early portion of the simulation dominates all the other terms in the TKE budget. The shear production and dissipation in the surface layer are very large, but the profiles have been truncated near the surface in order to highlight their features in the entrainment zone. The entrainment zone shear production of TKE is nearly four times the buoyancy production of TKE at the surface. The dominance of the entrainment zone shear production is so strong that the transport term becomes negative in the lower portion of the entrainment zone and positive near z/z_i=0.3, indicating some of the shear-generated turbulence may be transported downward. The positive transport at z/z_i=0.3 could also be due to the upward transport of shear- or buoyancy-produced turbulence from the surface.

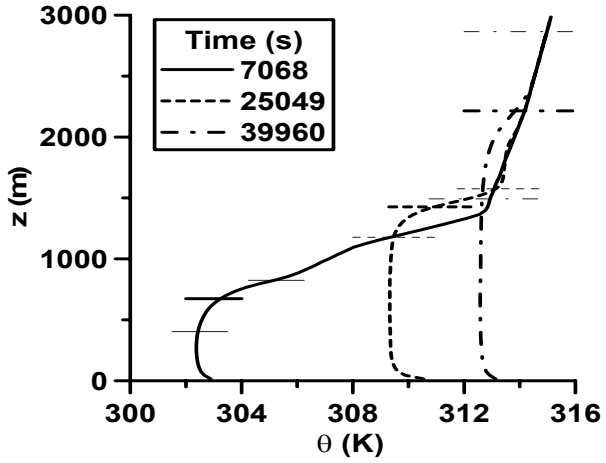

Figure 9.5: Potential temperature profiles (K) at selected times during the simulation of the May 22, 2002 case.

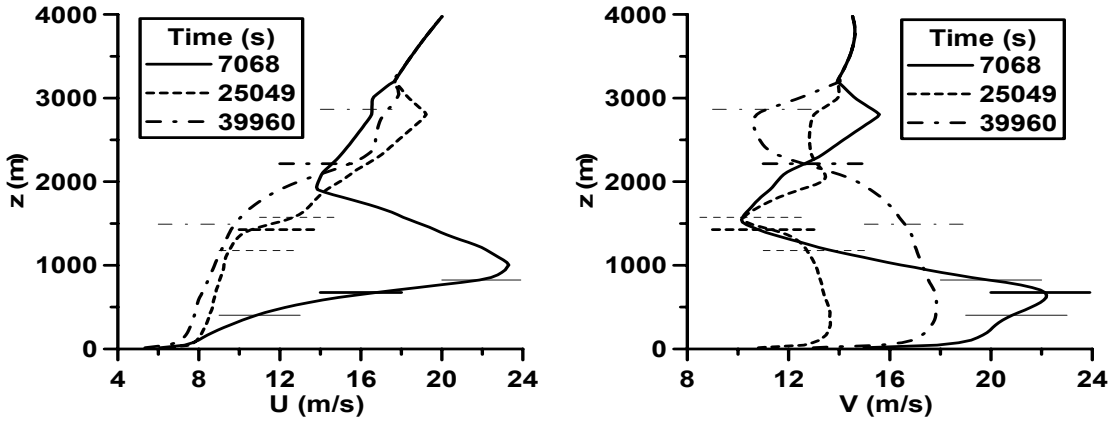

Figure 9.6: Momentum profiles at selected times during the simulation of the May 22, 2002 case. Thick horizontal lines crossing the profiles indicate the CBL depth (z_i), and the thin horizontal lines mark the lower and upper limits of the entrainment zone.

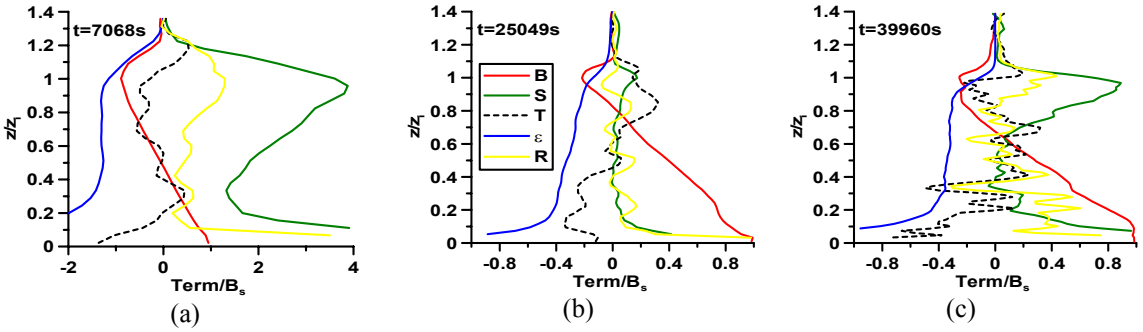

Figure 9.7: TKE budgets from simulation data at selected times during the simulation: (a) t=7068s, (b) t=25,049s, (c) t=39,960s. The line coloring corresponds to the individual terms in the TKE budget: buoyancy (red), shear (green), transport (black dashed), dissipation (blue), and residual (yellow).

Also of particular note in Fig. 9.7a is the residual term, which is rather large in the entrainment zone. A significant portion of the shear-produced TKE is, in essence, entering the reservoir of turbulence in the growing CBL (Zilitinkevitch 1975) rather than being dissipated or spent for the entrainment of heat. It should be noted that the surface buoyancy flux at this time in the simulation is not terribly strong (see Fig. 9.3), so the relative effects of shear are very significant. Despite the strong stratification, the entrainment zone is nearly as deep as the so-called mixed-layer.

By t=25,049s (see Fig. 9.7b), the shear production of turbulence has become almost negligible in the entrainment zone. This is due to both the weakening of the entrainment zone shear and the strengthening of the surface buoyancy flux, both of which act to diminish the relative importance of shear on entrainment. In fact, the surface buoyancy flux is stronger than in any of the simulations in Chapter 7. Despite the strong flux, the strong inversion keeps the CBL growth very slow, and this decreases the momentum entrainment contribution to the shear production of TKE. Because of these changes, the CBL appears to enter more of an equilibrium regime in which the buoyancy production of turbulence in the CBL is balanced by dissipation and the negative buoyancy flux of entrainment. Also, the transport profile bears a stronger resemblance to that of the NS case in Fig 7-13b. Despite this, the shear production and dissipation in the surface layer are very strong, but they appear to balance each other and do not seem to affect entrainment (it is unclear why the residual term is so large at the surface). The entrainment zone is rather shallow, which is characteristic of the other simulations with strong stratification.

By the end of the simulation (t=39,960s, see Fig. 9.7c), the entrainment zone shear production of turbulence has once again become about as strong as the buoyancy production at the surface. The entrainment zone becomes deeper as the growing CBL encounters a layer of much weaker buoyancy stratification, and its depth may be influenced by shear as well. Once again, it should be noted that the relative effects of shear appear large because the surface buoyancy flux has weakened considerably from its maximum value that occured in the middle of the simulation. There may be an artifact of this in the buoyancy flux profile, which departs from its typically linear shape near the

surface. The surface buoyancy flux in the simulation undergoes a series of step changes as shown in Fig. 9.3, and the profiles shown in Fig. 9.7c occur only 360 seconds after one of these step changes.

9.4.3.4 Convective Boundary Layer Depth Compared to Observations

The CBL depths determined from HARLIE data are compared with the simulated CBL depths in Figure 9.8. Unfortunately, the lidar data are missing during the portion of the simulation that might be considered the most interesting—that is, when shear dominates the production of turbulence. In the simulation, the CBL initially undergoes very rapid growth until about t=10,000s, after which the shear at the CBL top diminishes and the entrainment flux ratio settles down a bit. The surface buoyancy flux compensates for this a bit, and the CBL continues to undergo steady but slow growth (very roughly according to the $t^{1/2}$ dependence discussed in Chapter 4) between t=10,000s and t=25,000s. After that point, the growth is a bit more rapid as the weaker stratification is encountered aloft [see Fedorovich et al. (2004b) for a discussion on the effects of heterogeneous stratification on entrainment].

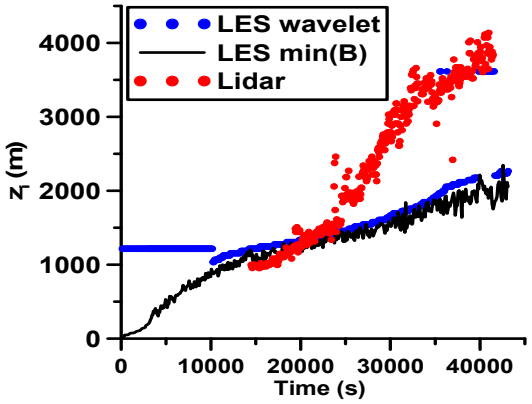

Figure 9.8: CBL depth z_i (m) as a function of time (s) for the May 22, 2002 simulation and concurrent lidar (HARLIE) data.

As expected, the wavelet-determined CBL depths in the simulation are a bit higher than those determined from the minimum of buoyancy flux. Before t=10,000s, the technique identifies the inversion at z=1200m as the CBL top because the temperature gradient is sharpest there during the early part of the simulation. Atmospheric lidar data often have the same problems when the wavelet technique is applied to them. Once the CBL depth comes close to this level and the entrainment zone inversion strengthens, the wavelet technique performs a bit more reliably.

The HARLIE CBL depths overlap the simulated CBL depths between t=15,000s and t=25,000s. This overlap could be taken as evidence that the simulations accurately predicted the effects of shear and buoyancy forcing on the CBL growth. However, the inversion at the CBL top is very strong at this point, and it constrains the CBL to a depth of 1000-1200m until the surface heating has allowed the potential temperature profile to fill the area under the inversion (see Fig. 9.5). During that time, the CBL experiences relatively little growth until it finds the weaker stratification aloft. Also, the CBL growth rates in the atmospheric data are much greater than in the simulation. Clearly, there are processes occurring in the atmosphere that are not accounted for in the simulation. The differences could also be due to differences between the LES initial temperature profile and the true state of the atmosphere at t=0. These differences are not precisely known. The initial temperature profile must be determined with very high resolution compared to the resolution typical of available atmospheric measurements. For example, radiosonde data (such as the DDC and AMA data used in this exercise) are typically taken every six seconds during a balloon flight, but these are vertically averaged to a considerable degree, smoothing out sharp gradients that may exist in the nocturnal boundary layer at sunrise.

Radiosonde data were not available at the measurement site at 1200 UTC, and even if the initial temperature profile were known exactly at the measurement site, temperature advection might also be an important effect.

Between t=25,000s and t=35,000s, the lidar CBL depth undergoes a very dramatic jump as a dryline passage occurs. The initial CBL is shallow, moist, and capped by a strong inversion. After the dryline passage, the CBL is very deep and dry and lies underneath a layer of somewhat weaker stratification. The LES code is not structured to deal with the types of CBL heterogeneity occurring in this case. It also does not account for the mechanisms responsible for this heterogeneity, such as variations in the land surface elevation, surface sensible heat flux, moisture flux, and potential temperature advection. Although the dryline is a rather extreme example of CBL heterogeneity, there are really no land areas where the CBL can be considered to be completely free of from the effects of land surface heterogeneity. Kimmel et al. (2002) estimated that up to 25% of the observed temperature variance in the mid-CBL may be due to mesoscale variations. Schneider and Lilly (1999) also address issues of heterogeneity in their analysis of radar data and tower measurements in the CBL at the Boulder Atmospheric Observatory. Larger scale atmospheric phenomena, such as baroclinic processes or deep, moist convection, impart additional heterogeneity on the CBL.

Another factor not accounted for in these simulations is the interaction between the two CBL types. If there is a significant westerly wind component (wind blowing from the west and wind vectors pointing east), as is usually true in the vicinity of the dryline, some turbulence from the deeper CBL on the west side of the dryline may be advected above the CBL to the east of the dryline, and although this turbulence probably

decays quite rapidly, they layer above the eastern CBL can no longer be assumed to be free of turbulence, especially for locations close to the dryline. Fochesatto et al. (2001) have found evidence of dynamical coupling between the residual layer and the developing CBL, analogous to the "overrunning" interactions between the two CBLs east of the dryline.

9.4.3.5 Turbulence Structure in Simulations Compared to Observations

To wrap up this chapter, we look at two cross sections showing the turbulence structure from the simulations and compare them to a time-height cross section from FM-CW S-band radar, which was located next to HARLIE in the IHOP experiment. Figure 9.9 shows the *y*-*z* cross section at t=43,000s, when the CBL was experiencing more rapid growth as it developed through a layer of relatively weak stratification and encountered increasing shear. The temperature structure at the CBL top does show some evidence of the effects of shear. It most strongly resembles temperature patterns from the GS cases in Chapter 8. There are no large, well-resolved K-H type billows at the CBL top, however, unlike some of the GC cases in Chapters 7 and 8.

The time-height cross section of signal-to-noise ratio from the FM-CW radar is displayed and compared to the simulated potential temperature field in Figure 9.10. Assuming a mean motion of 17 m/s in the CBL (from LES data) and using the Taylor frozen turbulence hypothesis (Stull 1988), the time span of one hour in Fig. 9.10b would correspond to a horizontal domain width of 61 km in Fig. 9.9. Likewise the CBL domain in Fig. 9.9 corresponds to roughly the first seven minutes of Fig. 9.10b.

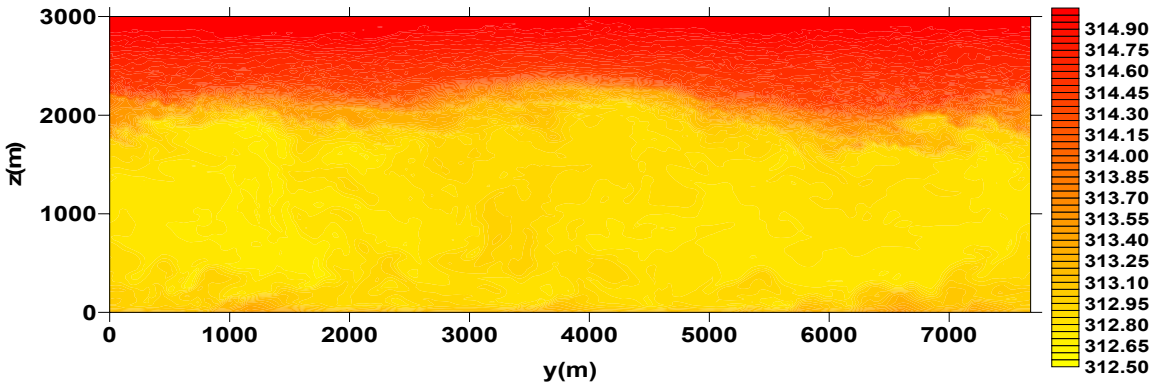

Figure 9.9: The *y*-*z* cross section showing potential temperature (K) at *t*=43,131s into the simulation, when the data were output for the radar data assimilation algorithm test.

The FM-CW cross section refers to the moment of time when the observed CBL had the same depth as the simulated CBL. At this point, the transition was occurring from the rather shallow CBL found east of the dryline to a deeper CBL as the dryline moved through (the dryline moved from west to east). Likewise, in LES, the CBL was making a transition from a strongly stratified environment to a more weakly stratified one. The UTC times listed in the FM-CW data correspond to *t*=27,000 through *t*=30,600 in the simulation, but the CBL cross section was not taken at these same times because the simulated CBL did not reach the measured depths of 2200 to 3000m (seen in Figure 9.10b), until the end of the simulation.

In the FM-CW data, the CBL top is marked by the large gradient in signal-to-noise ratio where the interface between the CBL air and the free atmospheric air is most sharp. The variability of the upper interface height in FM-CW is a bit larger than it is in LES. The increased variability in the FM-CW data may also be due to the earlier occurrence of transition, when the surface heat flux was still strong, forcing the apparently more vigorous plume-like structures.

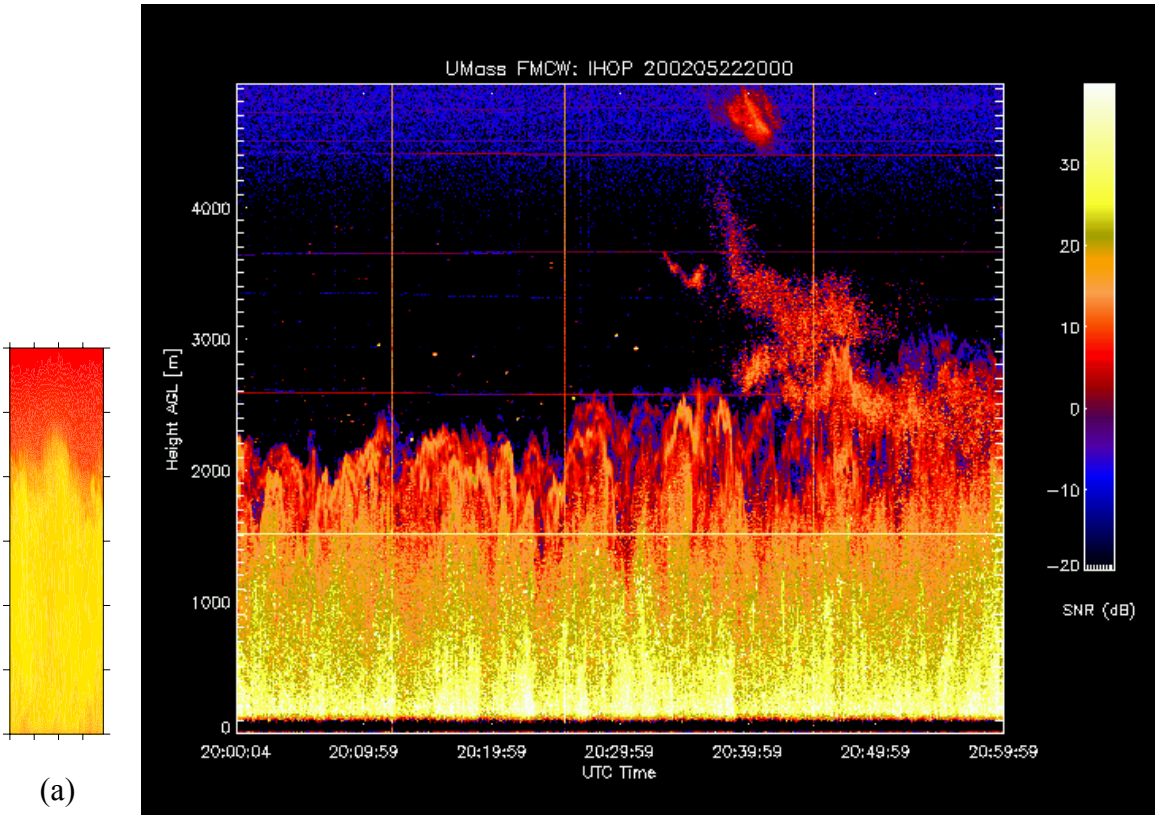

(a) (b)

Figure 9.10: Cross sections of the CBL at times when the CBL was approximately 2 km deep: (a) the simulated potential temperature cross section at t=43,000s with its aspect ratio changed to match that of (b), the time-height cross section of signal to noise ratio (dB) from the University of Massachusetts FM-CW S-band radar. The times (UTC) in (b) correspond to t=27,000 to t=30,600 in the simulation.

One particular feature to note is the variation of the sharpness of the interface height. When the tops of tall plumes penetrate into the free atmosphere, the interface is sharper. In between, during times of what is most likely downward motion, the interface is much less sharp and harder to define, resembling the LES cross sections that were discussed in Chapter 8. The FM-CW signal can come either from scatterers such as insects or aerosols or from strong density gradients, the latter of which are more intense at the CBL top where potential temperature gradients are also large.

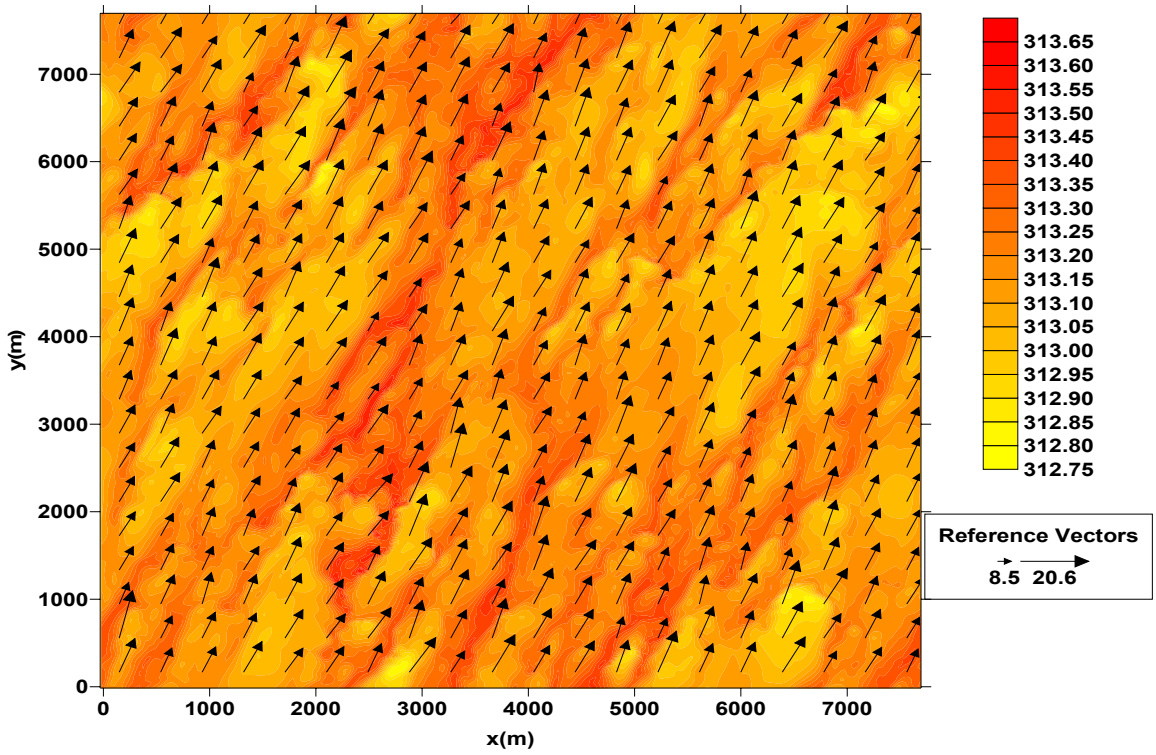

Figure 9.11: The *x*-*y* cross section showing potential temperature (K) and horizontal wind vectors (m/s) at *t*=43,000s in the simulation, when the data were output for use in the radar data assimilation algorithm test.

Finally, Figure 9.11 shows the *x*-*y* cross section of potential temperature and horizontal wind from LES. The figure shows that roll-type structures are present. Moeng and Sullivan (1994) indicate that roll structures are present when the negative of the ratio of the CBL depth to the Obukhov length is $-z_i / L < 2$ and that quasi-hexagonal cells dominate when $-z_i / L \gg 2$. The Obukhov length is defined as:

$$L = -\frac{u_*^3}{\kappa B_s} \tag{9.1}$$

where κ is the von-Karman constant. For the simulation at *t*=43,000s, $-z_i / L = w_*^3 / u_*^3 = 2.1$, which is close to the transition range. The ratio $-z_i / L$ varies from 0.5 at the beginning of the simulation, when heat flux is weak and the CBL depth is

small, to 3.6 in the middle, when the heat flux is strong and the CBL depth is large. The estimated friction velocity, taken from the point closest to the ground in the momentum flux profiles, changes relatively little during the simulation.

Given the range in $-z_i / L$ during the simulation, one should expect the turbulence structures to change. Indeed, at the beginning, the structures appear more like the streaks that were simulated by Kanna and Brasseur (1998) for shear-dominated boundary layers. The streaks evolve into horizontal convective roll structures and become much less streaky in appearance. However, a complete transition to cellular structures never occurs. Apparently, $-z_i / L$ is not far enough away from 2 for this to happen.

Figure 9.11 shows the wind vectors are roughly parallel to the convective rolls. The strongest wind speeds are found in the cooler air that has descended from the middle of the CBL (yellow colors in Fig. 9.11), and the weakest winds are generally found in the narrower rows of warmer temperatures, which are rising from the surface and carrying near-surface heat and momentum with them.

The wind direction in Fig. 9.11 is not characteristic of the near surface winds at the measurement site at the same time on May 22, 2002, where the winds had begun to acquire a negative *x*-component after having had a positive *x*-component for much of that afternoon. The simulated near-surface wind velocity has a much larger *x*-component and smaller *y*-component than the measured near-surface wind vectors did. The velocity vectors have a similar direction at locations west of the dryline, but there, the CBL is at least 1 km deeper than it is in the simulations, as indicated in the AMA sounding at about the same time (not shown). The lack of agreement may be due to the poor initialization of the large scale pressure gradients in the simulation. However, the simulated CBL

depth is not representative of locations well east of the dryline or well west of the dryline. The initial data in LES are representative of locations very close to the later afternoon dryline location, so the CBL depth at the end of the simulation is representative of what it might have been had there been no dryline (i.e. if there were no heterogeneity in land elevation or surface fluxes). However, a periodic LES on a 7-km domain is unable to simulate the dryline. It cannot take into account the effect of its solenoidal circulation on the CBL wind structure, and it cannot simulated the heterogeneity of the CBL. Unfortunately, the IHOP experiment was designed to study CBL heterogeneity, so its measurement sites were concentrated in areas where heterogeneous features like the dryline might be more likely located. Because of the shortcomings of horizontally homogeneous LES in its utility in studying atmospheric cases, and because the dryline represents an example of a larger scale atmospheric flow that is strongly associated with CBL heterogeneity, we are motivated to study the dryline in greater detail. Plans are to modify the LES code so that it can be used to simulate heterogeneous CBLs using larger LES domains. If the two interacting CBL types can be simulated simultaneously, it may elucidate the dynamics that drive dryline processes. It is an interesting topic for further study.

9.5 Summary and Conclusions

The results of this chapter can be summarized in terms of the stated goals at the beginning of the chapter. The results of the study show that, using initial conditions from atmospheric data, CBL entrainment can be influenced by shear to at least as large a degree as seen in the simulations of Chapter 7. Simulations based on May 22, 2002 data

have shown the shear-enhanced entrainment can be greater than in the simulations starting with the idealized, linear profiles. Grid-resolvable turbulence that might have been present at t=0 was not taken into account in the simulation and consequently, the transition from a nocturnal to a convective boundary layer in the simulation is probably not representative of the actual transition in the atmosphere. Once the resolved turbulence is fully developed, the simulated data can be trusted a bit more.

Additional care must be taken to ensure that the large scale pressure gradients are initialized accurately. In the nocturnal boundary layer, the assumption of geostrophic balance does not hold like it does in the idealized initial profiles in Chapters 6 and 7, so it is necessary to appropriately initialize the strength and direction of the ageostrophic wind so that the LES wind mean profiles remain consistent with those of the atmosphere.

Despite these problems, the evolution of the entrainment process during the simulation was rather indicative of how it might occur in the atmosphere. During the early stages of the simulation, shear enhancement of entrainment was fairly large. During the middle stages, shear had little influence on entrainment, but by the end, the effects of shear were seen again. This partially mirrors the change in surface buoyancy flux, which allows the relative effect of shear to be more protuberant early and late in the simulation. The entrainment zone shear was also changing accordingly. It was strong early in the simulation, weak in the middle, then a little stronger at the end. When the shear was strong, its effects were seen in the entrainment zone depth, the entrainment flux ratio, and the TKE budgets.

From a qualitative perspective, the resolved turbulence structures appear similar to the measured turbulence structures, as was seen in Fig. 9.10. As long as differences in

the measurement methods are accounted for, some useful qualitative comparisons can be made between observed and simulated features of the CBL turbulence structure.

Some useful CBL depth comparisons have been made between lidar and simulation data. Depth determinations from the HARLIE lidar data show approximately the same scatter as the LES CBL depth. The scanning strategies used by such instruments seem to measure a large enough area of the CBL to avoid problems with z_i estimates that are associated with undersampling.

As a result of the CBL depth comparisons between LES and atmospheric data, it is obvious that other factors not accounted for in LES have a significant influence on the CBL depth, making it difficult to isolate the effects of shear. The most significant effect on CBL depth for the May 22, 2002 case was the dryline passage, which could not be simulated in the present version of LES. Large scale advection was also taken into account, and variability in land surface conditions was also not simulated. Given these problems, it cannot be expected that a perfectly horizontally homogeneous CBL would develop anywhere and that the influences on heterogeneity would not exceed those of shear on the CBL depth. In many cases, however, there are conditions that are more horizontally quasi-homogeneous than those that existed during this case study. The fact that the IHOP field experiment was focused on finding heterogeneity makes it difficult to compare its data with the horizontally homogeneous CBLs reproduced by LES. This provides motivation for studying data from the ARM SGP site.

Chapter 10

Evaluations of Numerical Models of Entrainment

10.1 RANS-Based Closures in NWP

The RANS-based turbulence models, which form the middle of the hierarchy of numerical methods described in Chapter 3, are commonly used in NWP. One commonly used RANS-based model is the *e-l* model, which contains a prognostic equation for TKE (*e*)and a master length scale (*l*). One example of an *e-l* model is used in the Advanced Regional Prediction System (ARPS), a regional NWP model described by Xue et al. (2001). The ARPS e-l scheme will be referred to as ARPS for the remainder of this chapter. Another example is the model used by Fiedler and Kong (2003). It will be denoted F&K. Details of both these models have already been described in Chapter 3, and the methods for evaluating them against LES have been outlined in Chapter 6. This section presents the results of the comparisons between LES and the ARPS and F&K *e-l* models. The cases with a heat flux of 0.03 Km/s and a free atmospheric stratification of 0.003 K/m were used to study the differences between the various numerical models of entrainment and LES. With this particular combination of surface heat flux and free atmospheric stratification, the shear promotes a significant deepening of the CBL in the GS and GC cases, relative to the shear-free (NS) case. These results have also been presented in Conzemius and Fedorovich (2004).

10.1.1 ARPS

The CBL depth versus time for the ARPS *e-l* closure is compared with LES in Fig. 10.1. The CBL depth for the NS case grows more slowly with the ARPS *e-l* model than with LES. For the GC case, and particularly in the GS case, the relationship is reversed, and the *e-l* model predicts faster CBL growth than is seen in LES.

Figure 10.2 compares the heat flux profiles in LES against those from the ARPS *e-l* closure. In the LES, the heat flux profiles are generally smoother than in the ARPS closure, and it is obvious that, in the cases with shear, the RANS-based entrainment heat flux is much larger than in LES. Figure 10.3 shows the overall effect on the potential temperature profiles. If a different definition of the CBL depth, such as the height of the maximum temperature gradient, were used, the results would qualitatively be the same.

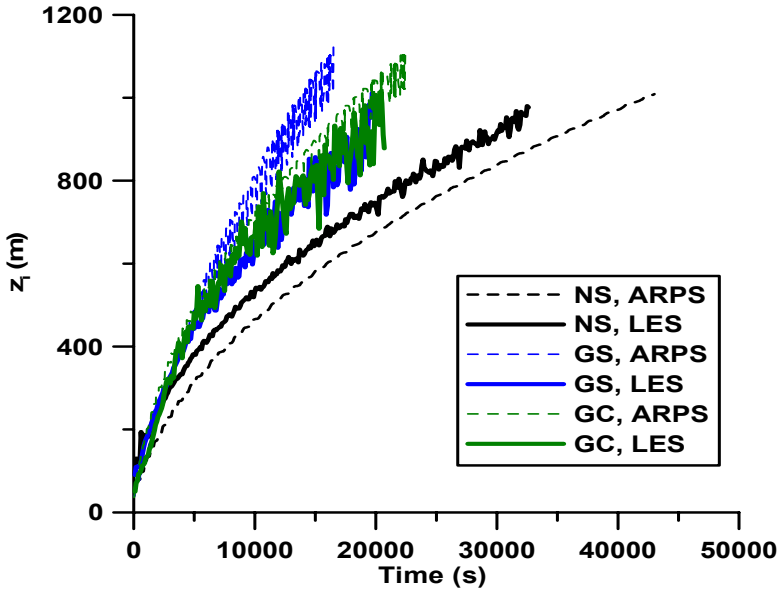

Figure 10.1: Comparison of the CBL depth evolution predicted by the ARPS *e-l* closure versus LES.

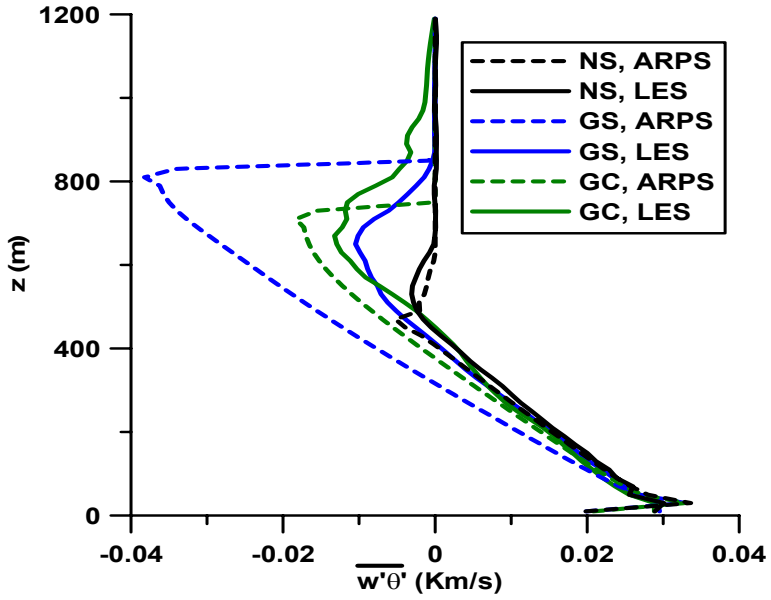

Figure 10.2: Comparison of the heat flux profiles predicted by ARPS *e-l* closure versus LES at *t*=10000s.

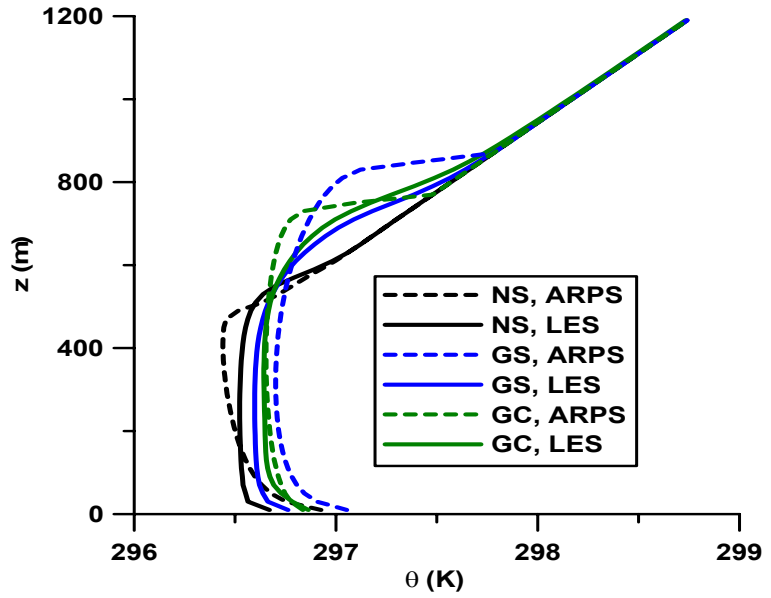

Figure 10.3: Comparison of the potential temperature profiles predicted by ARPS *e-l* closure versus LES at *t*=10000s.

The considered RANS-based closures predict much faster CBL growth compared to LES when shear is present. Figure 10.4 shows the TKE profiles. Surprisingly, the TKE in the ARPS *e-l* closure is less than in LES, despite the greater entrainment of heat. Looking at the profile for the GS case more carefully, it can be seen that the TKE at the top of the CBL is greater in the ARPS *e-l* closure than in LES. For the GC case, the energy from LES is greater. However, one should keep in mind that the energy calculations in LES do not distinguish between truly turbulent motions associated with entrainment and wave-like motions that do not mix heat. The calculation of heat flux can still be too large if the length scales (l) and constants (α_K) are too large in (3.17) or if the turbulent Prandtl number (3.21) is too small.

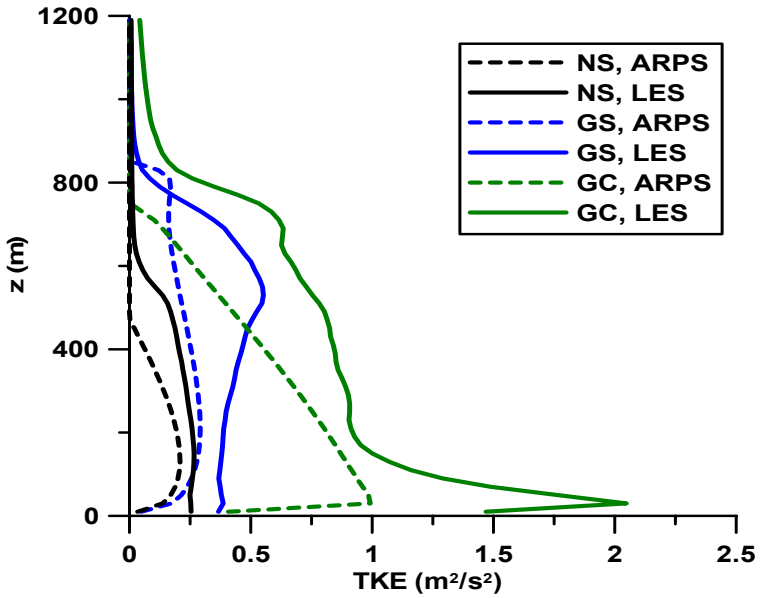

Figure 10.4: Comparison of the TKE profiles of ARPS *e-l* closure versus LES at t=10000s.

10.1.2 F&K

The F&K closure predictions of the CBL depth are compared with LES data in Fig. 10.5. Basically, the results, in a relative sense, are similar to those in the ARPS case. The CBL depths agree very closely with LES for the NS case, but in the GS and GC cases, the entrainment is remarkably faster than in LES.

The heat flux profiles calculated according to the F&K closure are shown in Fig. 10.6. If the maximum temperature gradient height is used for the definition of the CBL depth, the results are very similar, as can be seen in Fig. 10.7. In Fig. 10.8, the TKE is shown. Unlike the ARPS closure (Fig. 10.4), the F&K closure leads to greater TKE in the cases with shear when compared to LES data, and the TKE in the NS case is very comparable to the LES TKE. In sheared CBLs, the TKE values in the interior of the CBL are actually rather similar to the LES predictions, but at the top of the CBL (where shear is fairly large), there is much more TKE predicted by F&K than by LES.

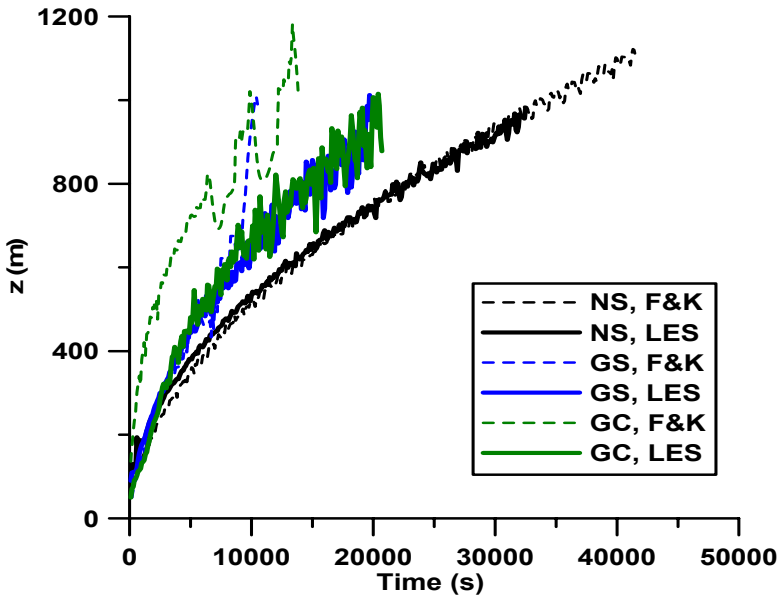

Figure 10.5: Comparison of the CBL depth evolution predicted by F&K *e-l* closure and LES.

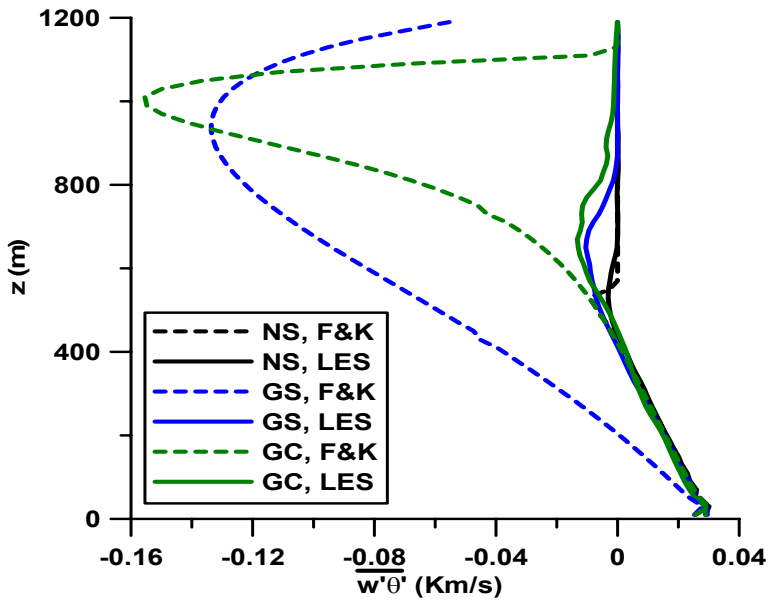

Figure 10.6: Comparison of the heat flux profiles obtained with F&K *e-l* closure and LES at t=10000s.

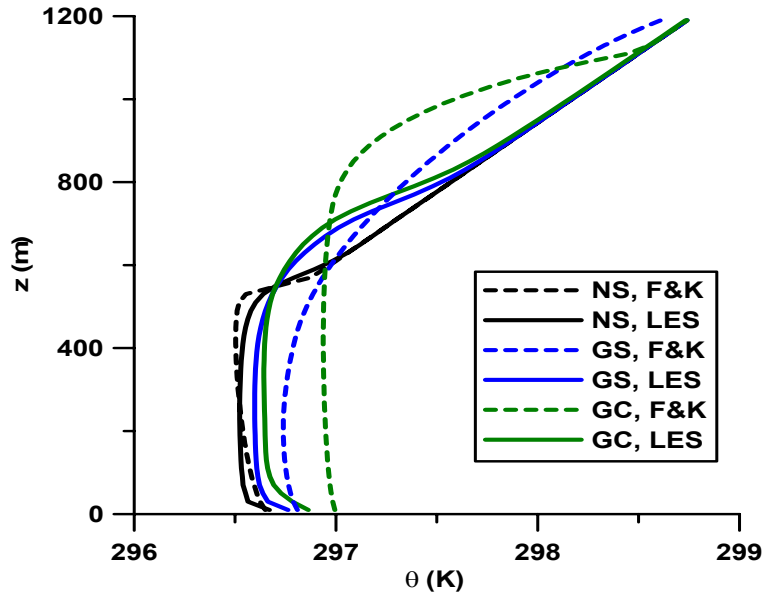

Figure 10.7: The potential temperature profiles from F&K *e-l* closure and LES at t=10000s.

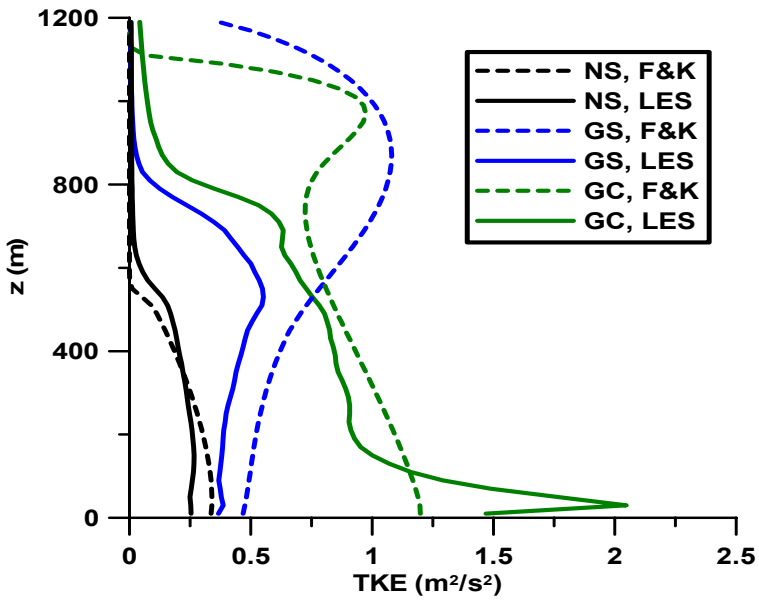

Figure 10.8: The TKE profiles from F&K *e-l* closure and LES at *t*=10000s.

Finally, the momentum profiles from the ARPS F&K models and LES are compared in Figure 10.9. Between the two *e-l* models, the momentum gradients from F&K more closely match the LES momentum gradients than do those from ARPS, but the values of momentum are greater in the F&K data for the GS case because of the enhanced entrainment of momentum. The GC momentum from F&K is less than predicted by LES in the CBL interior, perhaps due to the enhanced upward mixing of weaker momentum from the surface. Note that because the dissipation is not enhanced at the surface in F&K, the TKE is larger there, and frictional effects are thereby enhanced. In ARPS, the TKE is much smaller in the lowest model grid level because of the greater dissipation there. This causes less frictional slowing of the flow, and momentum throughout most of the CBL in ARPS is greater than the LES momentum for the GC case.

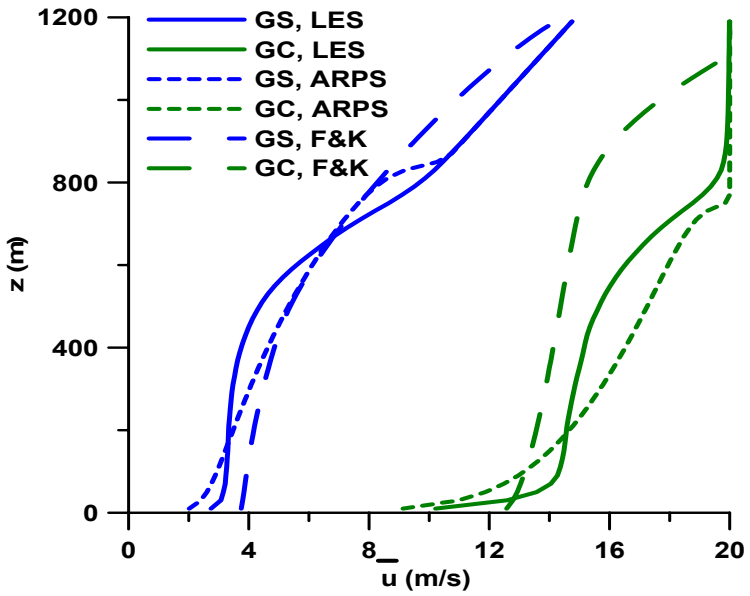

Figure 10.9: The profiles of the *x*-component of wind velocity from the F&K and ARPS *e-l* models and LES at *t*=10000s.

The primary conclusion regarding the performance of the two considered *e-l* closures is that for CBL cases with shear, they predict faster entrainment than LES does. This overestimation is not as large with ARPS as it is with F&K, but the ARPS-predicted CBL growth for the NS case is also slower than in LES. Another common feature of the two closures is the larger relative difference in CBL entrainment between shear-free and sheared CBL cases than is predicted by LES. One more disadvantage of *e-l* closures, earlier noted in Moeng and Wyngaard (1989), is their inability to directly account for counter-gradient turbulent flux in the upper portion of the CBL. However, adding a counter-gradient term in the *e-l* closures here does not reduce the exaggerated differences between sheared and shear-free CBLs relative to LES. The closures still have problems with entrainment. The problems seem mostly related to the development of TKE as the CBL grows into nonturbulent air at the CBL top.

10.2 Integral Budget Parameterizations

Prognostic entrainment equations are formulated by integrating the buoyancy, momentum, and TKE balance equations over the depth of the CBL and making some assumptions about the scaling of the TKE and dissipation integrals. The integration is performed over a simplified representation of the CBL vertical structure, and the integral budget-based models are classified roughly according to the degree of polynomial that is used to represent the CBL profiles of momentum and buoyancy. The derivation of these closures is provided in Chapter 3, an evaluation of these methods for shear-free CBLs has been made in Chapters 4 and 5, and the methods for evaluating them from LES data for sheared CBLs are described in Chapter 6. We present here the results of the evaluations of the ZOM and hybrid parameterizations for the entrainment flux ratio in sheared CBLs. They are listed below according to their authors.

10.2.1 ZOM and Hybrid Parameterizations

The results of the integral budget methods are grouped according to the type of method. The parameterizations of Tennekes (1973), Driedonks (1982), and Batchvarova and Gryning (1990, 1994) take into account only the surface shear through their friction velocity terms and are presented together as Group I. The parameterizations of Zeman and Tennekes (1977), Tennekes and Driedonks (1981), Boers et al. (1984), and Pino et al. (2003) include the friction velocity and also take into account either the spin-up term, velocity jump across the entrainment zone (although some may use the full jumps rather than the ZOM jumps), or both and are thus assigned to Group II. Finally, the

parameterizations of Stull (1976a,b) and Sorbjan (2004) deviate from the typical ZOM methodology and constitute Group III.

10.2.1.1 GS Cases

Figure 10.10 shows results obtained with the parameterizations of Group I for the GS case. The parameters of entrainment were retrieved from LES data and input to the respective expressions for $-B_i / B_s$ as they are defined in Chapter 3. The black dots denote the ZOM entrainment flux ratio $-B_{i0} / B_s$ retrieved from LES using the method described in Chapters 5 and 6. The blue dots denote the entrainment flux ratio defined from the actual minimum of buoyancy flux in the LES entrainment zone (i.e. $\delta B_i / B_s$).

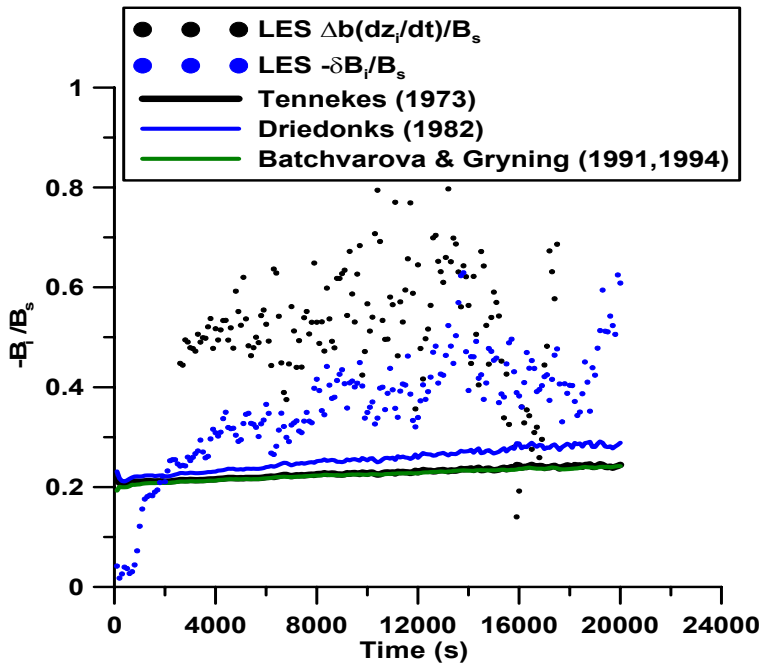

Figure 10.10: Entrainment flux ratio predictions of Group I closures (surface shear only) compared with LES for the GS case with free atmospheric stratification of $\partial\theta / \partial z = 0.003$ K/m and $Q_s = 0.03$ K m/s.

Since the parameterizations in Fig. 10.10 take into account only the surface shear, which is initially zero, they underestimate the entrainment flux ratio in the GS case and predict values consistent with commonly accepted shear-free value of about 0.2.

Figure 10.11 shows results for parameterizations from Group II (see Equations 3.57 and 3.62). The entrainment parameterization of Zeman and Tennekes (1977) does not take entrainment zone shear into account and fortuitously performs better than the others when compared to LES data. Among those that do take the entrainment zone shear into account, the parameterization of Pino et al. (2003) performs the best. However, all parameterizations of Group II suffer from problems with the denominator going to zero (see Equation 3.54) and the entrainment rate becoming unbounded.

Figure 10.12 shows the comparisons with the Group III parameterizations. Since these parameterizations do not include negative-sign shear terms in the denominator, the parameterized entrainment flux ratio does not become unbounded. The Stull (1976a,b) parameterization (3.59) predicts an entrainment flux ratio that climbs steadily with time, while LES data show a fairly constant value. The Sorbjan (2004) entrainment flux ratio (3.86) also increases with time.

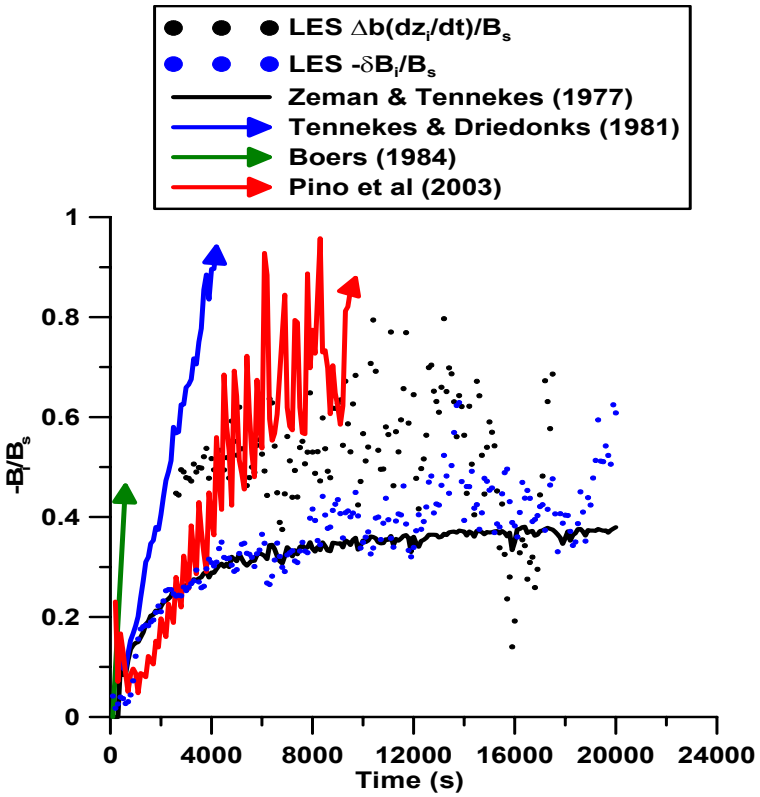

Figure 10.11: Entrainment flux ratio predictions by Group II closures (surface and entrainment zone shear and/or TKE spin-up) compared to LES for the GS case with free atmospheric stratification of $\partial\theta/\partial z = 0.003$ K/m and $Q_s = 0.03$ K m/s.

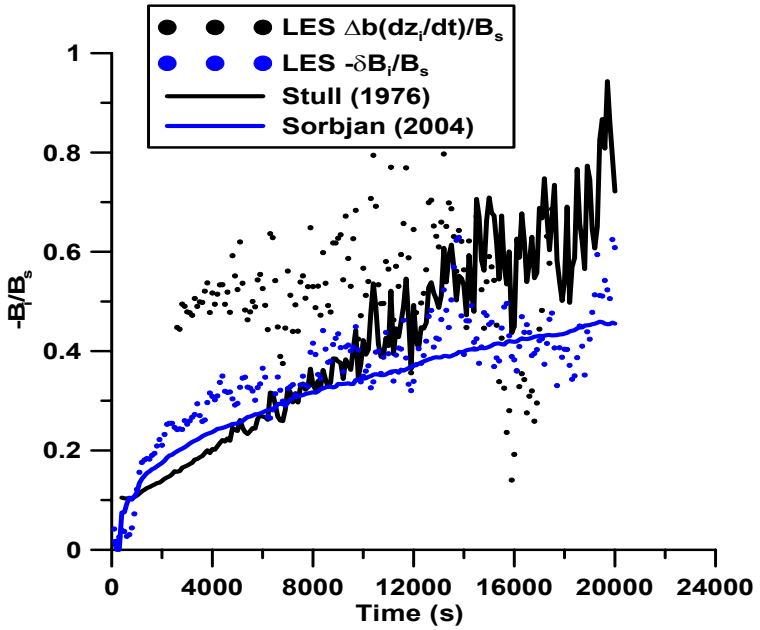

Figure 10.12: Entrainment flux ratio predictions by Group III closures compared to LES for the GS case with free atmospheric stratification of $\partial\theta/\partial z = 0.003$ K/m and $Q_s = 0.03$ K m/s.

10.2.1.2 GC Cases

Figure 10.13 shows the entrainment flux ratios by the Group I parameterizations for the GC case. All methods predict higher entrainment flux ratios than LES. The predicted ratios decrease with time, and the LES data show this decrease to some extent as well.

The initial value of surface shear is very large, and so the shear-generated TKE at the surface should be very large as well. As friction decreases the momentum in the CBL, the surface shear-generated TKE also decreases, resulting in a decrease in the predicted entrainment flux ratio.

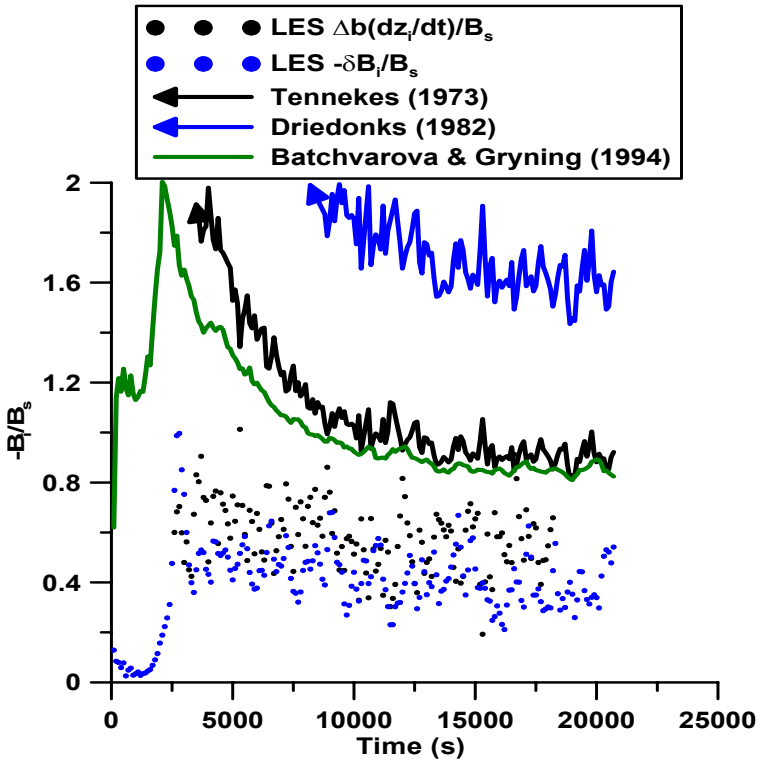

Figure 10.13: Entrainment flux ratio predictions of Group I closures (surface shear only) compared to LES for the GC case with free atmospheric stratification of $\partial\theta/\partial z = 0.003$ K/m and $Q_s = 0.03$ K m/s.

Figure 10.14 shows entrainment predictions for the GC case by the Group II parameterizations. Again, all of them overpredict the entrainment flux ratio, but the Pino (2003) parameterization performs the best. The denominator goes to zero in these expressions for the GC case just like it does for the GS case.

Figure 10.15 shows performance of the Group III parameterizations for the GC case. These perform the best of all the groups of parameterizations. The parameterization of Stull (1976a,b), which takes both surface and elevated shears into account, performs better than the Sorbjan (2004) parameterization, which only uses entrainment zone shear. This does not necessarily mean that the surface shear is equally important to the entrainment zone shear. It merely means that the Stull parameterization is better tuned for this particular case. Certainly, LES results (see Chapter 7) indicate that it is primarily the entrainment zone shear that drives the enhancement of entrainment relative to the shear-free cases. Even the GC cases, which start without entrainment zone shear, eventually develop strong shear at the CBL top that is comparable to the entrainment zone shear of the GS cases.

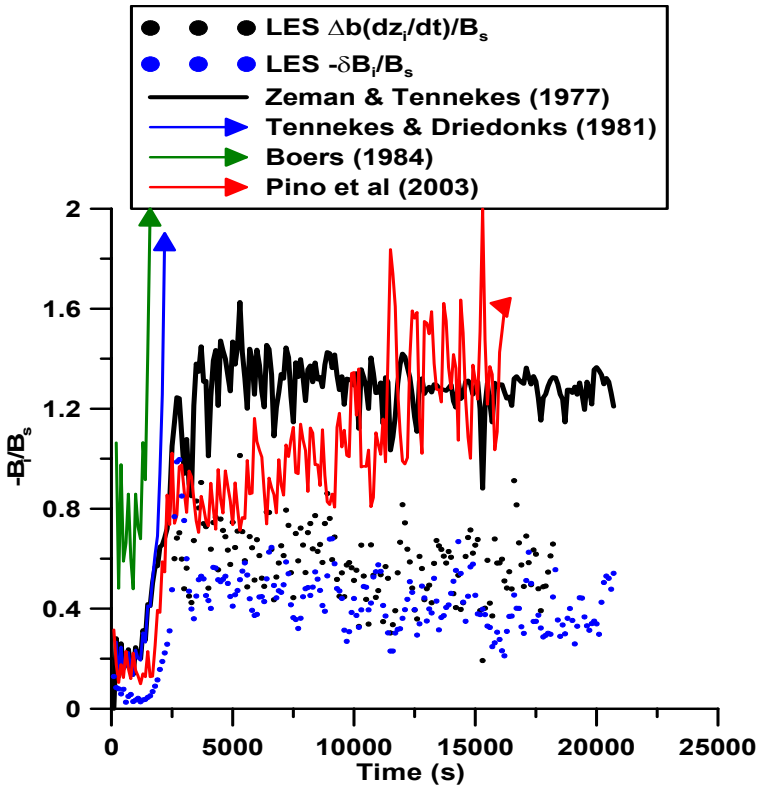

Figure 10.14: Entrainment flux ratio predictions of Group II closures (surface and entrainment zone shear and/or TKE spin-up) compared to LES for the GC case with free atmospheric stratification of $\partial\theta / \partial z = 0.003$ K/m and surface heat flux of 0.03 K m/s.

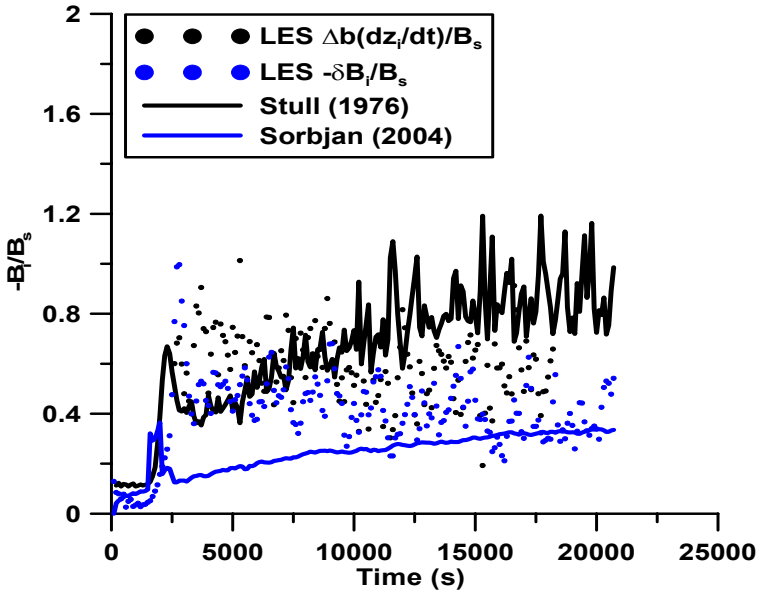

Figure 10.15: Entrainment flux ratio predictions of Group III closures compared to LES for the GC case with $d\theta/dz$=0.003 K/m and surface heat flux of 0.03 K m/s.

In order to illustrate a situation in which the parameterizations perform reasonably well, we show in Fig. 10.16 the Group II parameterizations for the GS case with a surface kinematic heat flux of 0.10 K m/s and a free atmospheric stratification of 0.010 K/m.

All parameterizations perform reasonably well, but the entrainment flux ratio is close to the shear-free value of 0.2 anyway. Of those methods that take entrainment zone shear into account, the Pino et al. (2003) parameterization is closest to the LES entrainment flux ratio. Overall, the Zeman and Tennekes (1977) parameterization is the closest to the LES results, but it does not specifically take the entrainment zone shear into account.

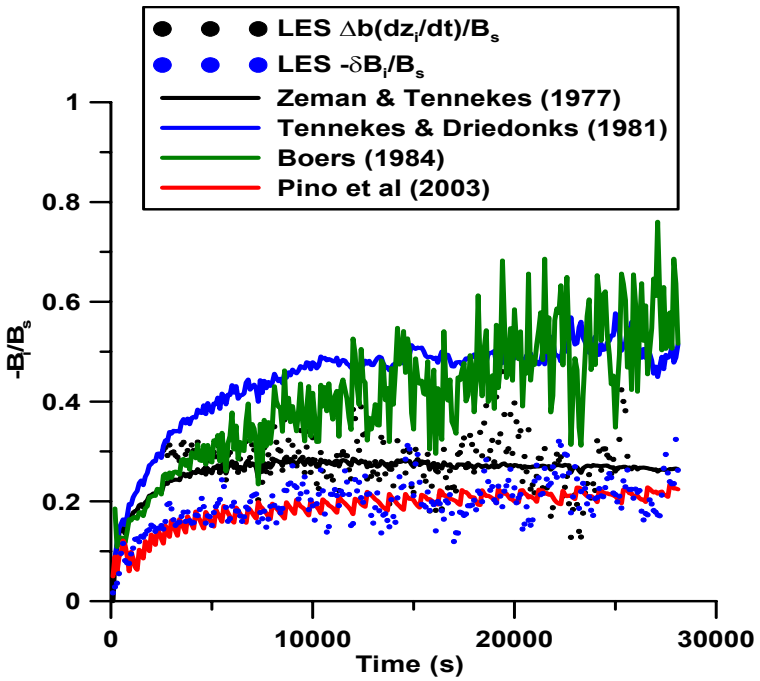

Figure 10.16: Entrainment flux ratio predictions by the Group II parameterizations compared to LES for the GS case with $d\theta/dz$=0.010 K/m and surface heat flux of 0.10 K m/s.

10.2.2 FOM-Based Parameterizations

The first order parameterizations based on Mahrt and Lenschow (1976) and Kim (2001) were tested, retrieving the parameters of entrainment from LES in a manner consistent with their definition in the FOM (see Chapter 6). Since these parameterizations take a finite entrainment zone thickness into account, which seems to be necessary in the presence of shear, they might be expected to perform better than the ZOM entrainment parameterizations. The results indicated just the opposite. The drawbacks of the parameterizations are the same, in that a critical value of shear is reached at which the denominator in the parameterizations goes to zero, and the entrainment flux ratio becomes unbounded. This should not happen when the surface heat flux is positive.

Since these FOM-based parameterizations make some simplifying assumptions, it might be a good idea to test the validity of these assumptions. Mahrt and Lenschow (1976) assume $\Delta z \ll z_i$, and that Δz can be neglected in all equations except for the TKE budget equation. A quick look at Figure 7.4 shows that Δz, even when retrieved in a manner consistent with the FOM (i.e., Δz was take as the thickness between the heat flux minimum and the level where the heat flux approaches zero), is not small relative to z_i, particularly in cases where shear plays a significant role in entrainment. Thus, the $\Delta z \ll z_i$ assumption fails.

Kim (2001) assumes that $d\Delta z/dt$ can be neglected and that the equation for Δz is merely a diagnostic one. If Δz and z_i both start at zero and reach similar magnitudes at the end of the run, then there are two possibilities: 1) $d\Delta z/dt$ cannot be neglected, and

2) dz_i / dt can be neglected along with $d\Delta z / dt$. Since the whole basis of the integral budget methods is to derive prognostic equations for z_i, the latter certainly cannot be true.

Based on these results, the full FOM-based TKE equation (3.74-3.77) was then subjected to a scale analysis to see which terms could be neglected for *all* simulations performed in this study. The FOM parameters of entrainment were retrieved from the LES cases, and the range of values seen in the LES cases were tested in (3.74-3.77). In some situations, a small group of terms could be neglected, but in other situations, the negligible terms were an entirely different group. The outcome of the scale analysis was that none of the terms could be neglected in all situations studied in LES, and the major reason was that Δz, $d\Delta z / dt$, or both were significant in many situations.

10.3 Numerical Integration of Full ZOM and FOM Equations

As a last attempt to apply the integral budget equations to the sheared CBL, one can start from scratch, without any assumptions about the values of A, C_F, C_T, or C_P in the ZOM parameterizations or the values of C_e or C_ε in the equations developed by Zilitinkevitch (1991) (see Equation 3.41).

For the ZOM equations, the vertical structure of the simulated CBL (see Chapter 7) can be compared with the simplified CBL vertical structure assumed in the ZOM (Figure 3.1). One thing stands out immediately: the simulated entrainment zone thickness can become rather large, whereas there is no real entrainment zone depth defined in the ZOM [except for the geometric relation of Stull (1976a), which is not representative of the entrainment zone depth (Fedorovich et al. 2004a)]. For the shear-free CBL, the

entrainment zone thickness does not cause any problems when applying the ZOM-derived entrainment equations to the simulated CBL, as long as the parameters of entrainment are retrieved from the simulations in a manner consistent with their definition in the ZOM. Lilly (2002a) made one attempt to resolve the discrepancy between the finite entrainment zone thickness analyzed in CBL simulations and the ZOM sharp-edged CBL top, and Chapter 5 examines this issue further.

However, for the shear-driven CBL, some rather significant assumptions leading to the ZOM entrainment equations are violated. In particular, the left hand side of (3.39) can be expanded, using Leibniz' rule:

$$\frac{d}{dt}\int_0^{z_i+} \bar{e}\,dz = \int_0^{z_i+} \frac{\partial \bar{e}}{\partial t}\,dz + \bar{e}(z_i+)\frac{dz_i}{dt}, \tag{10.1}$$

where z_i+ indicates that the integration is take an infinitesimally small distance past z_i. The second term on the right is neglected in the ZOM because turbulence is assumed to vanish at the top of the interface. Figure 10.17 indicates that, under realistic conditions, the second term cannot be neglected. At that point, in order to remain within the framework of the ZOM, the second term must be parameterized and grouped with the loss term in Equation (3.22). However, exactly how one should go about doing this is unclear. Since TKE is significant at z_i, it becomes pointless to stop the integration there to stay within the simplified framework of the ZOM. It is necessary to look at higher order models.

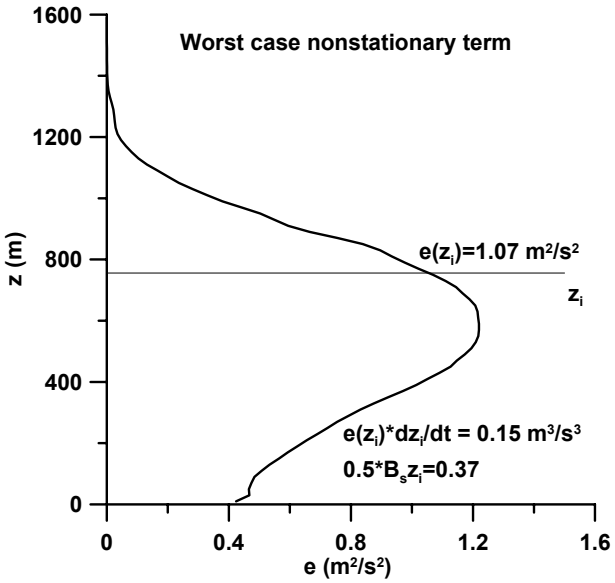

Figure 10.17: Profile of TKE at t=1000s in the simulation with $d\theta$/dz=0.001 K/m and Q_s=0.03 Km/s.

The next step up in bulk model complexity is the FOM. The FOM equations allow the entrainment zone thickness to become large, and the integration is carried to the top of the entrainment zone. The FOM integral budget equations for z_i, Δb_1, Δu_1, and Δv_1 are derived in Chapter 3, but there are only four equations, and Δz is an additional dependent variable. Before the set of equations can be closed, a fifth equation is needed to relate the FOM entrainment zone thickness Δz to the other parameters of entrainment.

In light of the need for such an equation, one can consider the LES results from Chapter 7. Many of the simulations had a finite, reasonably well-resolved layer, in which the Richardson number was nearly constant, with $0.25 < Ri < 0.5$. Other simulations did not have such a layer, but in those cases, it may be possible that the variability of the interface height obscured the layer of low Ri, and if this variability in the interface height were somehow removed or accounted for, as suggested by Lilly (2002a), then the constant Ri layer might be revealed. Exactly how to do this with the simulation data is

not clear, but based on the evidence seen in the simulations in which the entrainment zone was well-resolved, the most reasonable constraint on Δz would be to require it to change in a manner such that the entrainment zone Ri approaches a constant, critical value.

For the FOM, Ri_1 is constant with height in the entrainment zone, and its value is

$$Ri_1 = \frac{\Delta z \Delta b}{\Delta u^2 + \Delta v^2 + w_*^2}. \tag{10.2}$$

There are two possible constraints on Ri_1. The first is to require it to be constant at some critical value, which we define as Ri_{crit}. The entrainment zone thickness Δz is then

$$\Delta z = \frac{Ri_{crit}\left(\Delta u^2 + \Delta v^2 + w_*^2\right)}{\Delta b} \tag{10.3}$$

One can also relax this constraint slightly, and specify that the Richardson number returns to its critical value over some specified time scale Δt:

$$\frac{dRi_1}{dt} = -\frac{Ri_1 - Ri_{crit}}{\Delta t} \tag{10.4}$$

The behavior of the entrainment zone thickness Δz is basically the same.

Before the set of equations can be solved, one must make estimates of the surface friction velocity and the integrals of TKE and dissipation. We handle the surface momentum flux by using a surface drag coefficient parameterization.

$$-\overline{w'u'}_s = C_D u_{m1}^2 \tag{10.5}$$

$$-\overline{w'v'}_s = C_D v_{m1}^2 \tag{10.6}$$

Based on the LES data, a value of $C_D = 0.002$ was estimated. For the GC cases, the value of $C_D = 0.002$ was a good estimate throughout the run. For the GS cases, the value of $C_D = 0.002$ was approached asymptotically during the run.

Next, some assumptions need to be made regarding the integrals of TKE and dissipation and their appropriate scaling. Recall the Deardorff (1980) scaling hypothesis for the integrals of TKE and dissipation in the shear-free CBL:

$$e = w_*^2 \varphi_e(\zeta), \quad \varepsilon = \frac{w_*^3}{z_i} \varphi_\varepsilon(\zeta), \quad \zeta = \frac{z}{z_i} \tag{10.7}$$

The velocity scale used was the convective velocity scale, and the length scale used was the CBL depth. Applying the same logic here and making the assumption that the TKE is a linear combination of several production mechanisms, the TKE integral takes on the form:

$$\begin{aligned} \int_0^{z_i+\Delta z} e dz &= w_*^2 z_i \int_0^{z_i+\Delta z} \varphi_e\left(\frac{z}{z_i}\right) d\frac{z}{z_i} + u_*^2 z_i \int_0^{z_i+\Delta z} \varphi_{eSS}\left(\frac{z}{z_i}\right) d\frac{z}{z_i} + \Delta u^2 \Delta z \int_0^{z_i+\Delta z} \varphi_{eES}\left(\frac{z}{z_i}\right) d\frac{z}{z_i} \\ &= w_*^2 z_i C_e + u_*^2 z_i C_{eSS} + \Delta u^2 \Delta z C_{eES}, \end{aligned} \tag{10.8}$$

where φ_{eSS} and φ_{eES} are the functions, which are assumed to be universal, describing the profiles of surface shear-generated TKE and entrainment zone shear-generated TKE, respectively. C_{eES} is the constant for the entrainment zone shear-generated TKE, and C_{eSS} is the constant for the surface shear-generated TKE.

The method to find the scaling is to rely on the assumption of the self-similarity of the TKE profile. If the profile is self-similar, its shape will remain essentially unchanged with time and the function $\varphi_e(\zeta)$ can be estimated from LES data for the shear-free CBLs. The function is integrated over the depth of the turbulent layer (from

the surface to the point where TKE disappears) to find C_e. For the sheared CBLs, we find the residual between the actual TKE integral and the de-scaled self-similar shear-free integral (from C_e) and rescale the residual by length and velocity scales appropriate for the shear forcing. This is done separately to find C_{eES} and C_{eSS}. It is tough to treat the surface and entrainment zone shears separately, since all LES cases have at least some of both, but some have much more of one than the other.

Because the GS cases have very little surface shear and strong entrainment zone shear, we made the assumption that the residual TKE in the GS case can be fully attributed to entrainment zone shear. The residual integral was scaled by $\Delta z\sqrt{\Delta u_1^2 + \Delta v_1^2}$ to find C_{eES}. For the GC cases, a second residual was calculated (actual TKE minus the *first* residual minus the shear-free TKE), and the scaling $u_*^2 z_i$ was used to find C_{eSS}.

The same basic method can be used to find the dissipation scaling. The assumptions regarding the dissipation integral are essentially the same:

$$\begin{aligned}\int_0^{z_i+\Delta z} \varepsilon dz &= w_*^3 \int_0^{z_i+\Delta z} \varphi_\varepsilon\left(\frac{z}{z_i}\right) d\frac{z}{z_i} + u_*^3 \int_0^{z_i+\Delta z} \varphi_{\varepsilon SS}\left(\frac{z}{z_i}\right) d\frac{z}{z_i} + \Delta u^3 \int_0^{z_i+\Delta z} \varphi_{\varepsilon ES}\left(\frac{z}{z_i}\right) d\frac{z}{z_i} \\ &= w_*^3 C_\varepsilon + u_*^3 C_{\varepsilon SS} + \Delta u^3 C_{\varepsilon ES}\end{aligned} \tag{10.9}$$

As it turns out, this assumption works well for the shear-free CBL, but for the shear-driven CBL, the assumption causes some highly undesirable mathematical consequences in the resulting entrainment equations. The mathematical effects are best understood by looking at the ZOM TKE equation (3.38) and the entrainment parameterizations (3.54) presented in Chapter 3. The FOM equations are structurally similar, so the arguments apply to them as well. Treating the integral shear-production of turbulence separately from the integral dissipation of shear-produced turbulence does not allow these two

opposing effects to balance each other in the equations. Because shear-produced turbulence depends on dz_i/dt, the shear production term ends up in the *denominator* of the entrainment equation, and it has a negative sign. However, the dissipation term, using the above scaling, ends up as a term of negative sign in the *numerator*. Obviously, this is not a configuration that allows these two terms to balance each other. The denominator can easily go to zero if the shear term is large enough, and the solution becomes unbounded. Alternatively, the dissipation integral in the numerator may dominate the other terms there, and the entrainment rate would become negative.

The alternative is to change the scaling of the dissipation integral to $\Delta u_1^2 dz_i / dt$, allowing it to be placed in the numerator as an opposite sign term to the shear-production term. Essentially, this is equivalent to assuming that a constant fraction of the entrainment zone shear-produced TKE is dissipated, as the authors of the entrainment parameterizations have done. The two terms can then be combined into one, and this is exactly what most authors did with their respective ZOM-based entrainment parameterizations, but the assumption was not stated in terms of the scaling of the integral.

Also, the LES results indicate that the integral surface layer shear production and dissipation largely balance each other and do not exert a substantial influence over the entrainment rate. Deriving scalings for surface shear production and dissipation terms from LES data causes additional uncertainties in the entrainment equations that are really unnecessary and, since these terms are large, errors in those terms can dominate the other terms, so it is best to leave them out. Nevertheless, the surface shear strongly influences

the mixed layer momentum, so its effects are retained in the momentum equations using the drag coefficient parameterization.

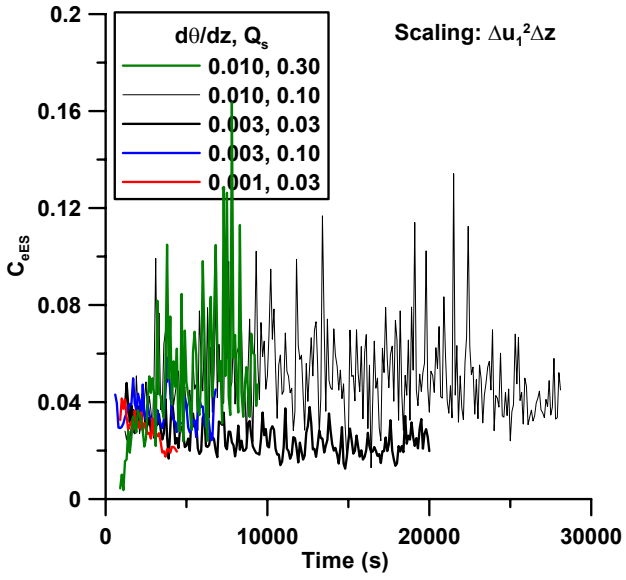

Figure 10.18: Determinations of the constant C_{eES} based on LES data for the GS cases.

The value for the scaled integral of the shear-produced TKE is $C_{eES} = 0.04$. Figure 10.18 shows the values of this C_{eES} for all the GS cases.

The integration of the equations was performed using the Newton-Ralphson method, which is described in Press et al. (1992). The ZOM equations and the FOM equations were integrated for the same CBL cases. Based on the FOM-based analysis of the LES data, a critical value of Ri=0.15 was selected for the constraint on Δz

The final integrated FOM equations are (3.63)-(3.65), (3.74), and (10.4). For the ZOM, the equations are (3.31)-(3.33) and (3.38).

Results of the calculations show that for the shear-free cases, z_i from the FOM and ZOM equations matched the simulated CBL depth as well as can be expected. The most important results can be summarized by looking at the integrations for the $d\theta/dz$=0.003

K/m and 0.001 K/m cases with Q_s=0.03 Km/s. In the shear-free case (not shown), both models predict nearly identical CBL growth but are slightly slower than the CBL growth in the simulations. The differences between the simulations and the models in the NS case can be attributed to the TKE spin-up term in the models. Removing this term allows their predictions of CBL depth to match those from LES much more closely.

Figure 10.19 shows the CBL evolution for the CBL cases with $\partial\theta/\partial z = 0.003$ K/m and $Q_s = 0.03$ Km/s integrations. In the GS case, the ZOM matches the LES CBL growth much more closely than does the FOM, but these differences are not really indicative. In both the FOM and ZOM, the dissipation scaling can be tuned to allow either to match the simulated CBL growth rate more closely. In the GC case, the FOM slightly overestimates the CBL growth rate (especially in its early stages), and the ZOM solution does not exist because the denominator in (3.53) goes to zero. It appears the use of a finite thickness entrainment zone using a critical *Ri* value is important in these cases, but this does not appear to be the answer to all the problems of the integral budget methods.

Figure 10.20 shows the GS and GC CBL growth curves from LES, the FOM, and the ZOM for the $\partial\theta/\partial z = 0.001$ K/m and $Q_s = 0.03$ Km/s cases. In the GS case, the FOM integration fails completely, suggesting the ZOM might be a better model to use, but the ZOM does not provide a very reasonable solution either, at least in terms of comparison with the LES results. $d^2 z_i / dt^2$ in the ZOM solution is definitely positive, and the solution appears to be headed for unboundedness. In the GC cases, the ZOM numerical solution does not exist because it immediately becomes unbounded. The GC cases have very strong shear production of turbulence early in the simulation, and the

ZOM cannot handle this strong shear. The FOM, on the other hand, is able to handle the strong shear in the early portion of the GC cases because it can regulate the balance between shear production and buoyancy destruction of turbulence through the finite entrainment zone thickness it allows. In the GS cases with the weakest stratification, the model fails, but this may be a sign that those GS cases are inherently unstable anyway. Ri<0.25 in the free atmosphere in those cases, and even though the ZOM can be integrated for those cases, neither the ZOM or FOM produces a solution that behaves well. It may simply be that these GS cases are inherently unstable, and expecting bounded growth of turbulence may be unrealistic. Indeed, running this case without a sponge layer in LES shows that the CBL growth rate increases at the end of the run.

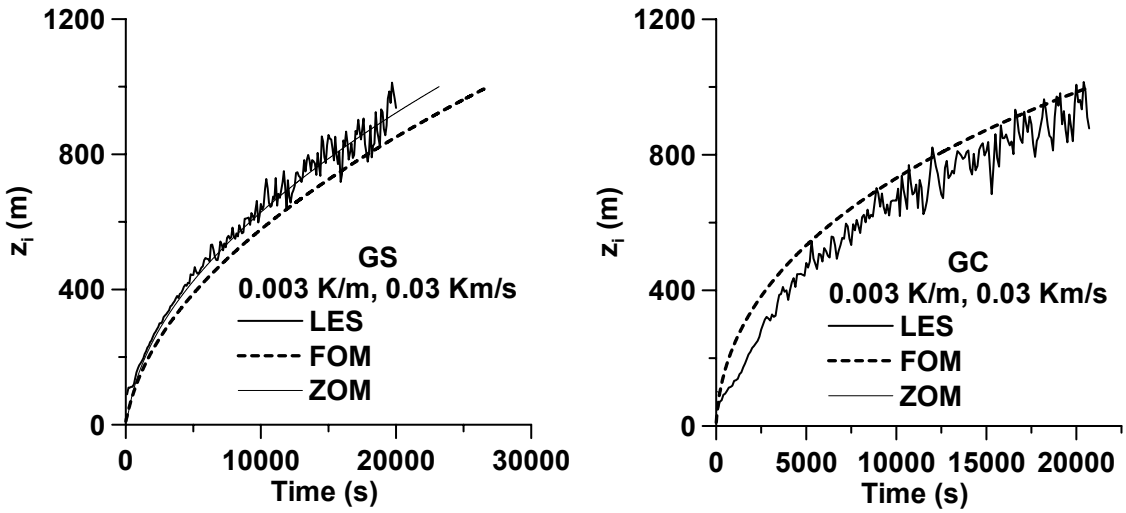

Figure 10.19: Comparison among LES, FOM, and ZOM predictions of CBL depth z_i versus time for simulations with $\partial\theta/\partial z = 0.003$ K/m and $Q_s = 0.03$ Km/s: (a) GS case, and (b) GC case.

Adding the entrainment zone thickness into a bulk model of the CBL adds a considerable amount of complexity to the equations. To see if this provides any benefit,

it is necessary to examine the sensitivity of the solutions to perturbations in Δz to see if, in fact, if Δz acts to regulate the shear-production of turbulence by balancing it with dissipation and buoyancy destruction of TKE.

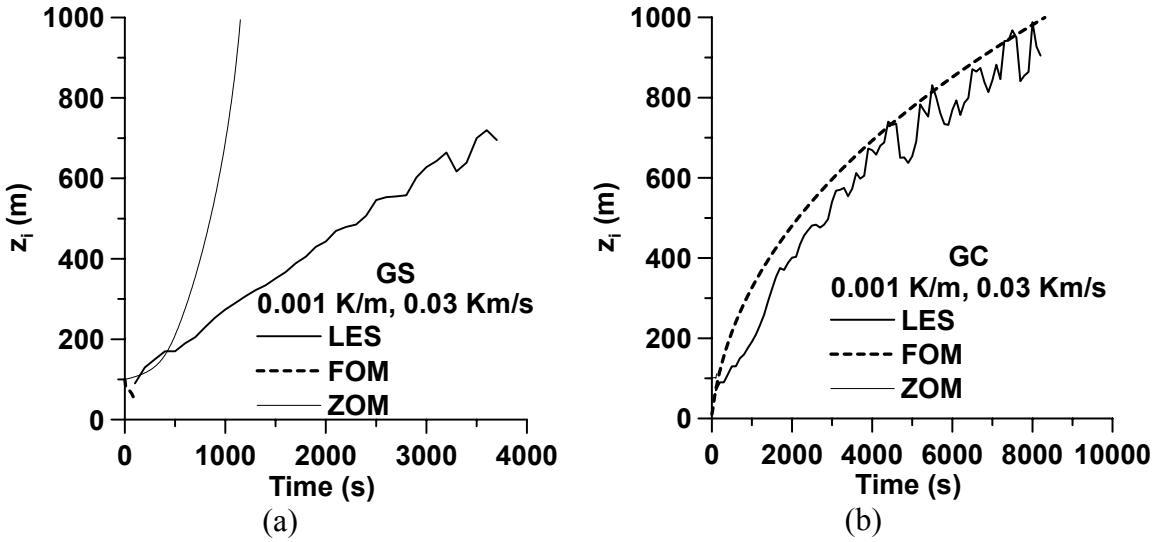

Figure 10.20: Comparison among LES, FOM, and ZOM predictions of CBL depth z_i versus time for simulations with $d\theta/dz$=0.001 K/m and Q_s=0.03 Km/s: (a) GS case, and (b) GC case.

Figure 10.21 shows the behavior of the various terms in the FOM TKE equation (3.74-3.77) given perturbations in Δz. The solution is shown at t=5000s for the $d\theta/dz$=0.003 K/m and Q_s=0.03 K/m GS and GC cases. The entrainment zone thickness was varied from $\Delta z = 0$, as it would be in the ZOM, to five times its value in the FOM integration. The figure clearly shows that Δz has a beneficial effect. In the GS case, the shear term increases as Δz is increased, but the increase in integral shear production is offset by decreases in the integral buoyancy production and integral dissipation terms. The residual shows that an increase in Δz results in a decrease in TKE, so Δz acts to regulate TKE production when shear is present. In the GC case, the increase of Δz is

more beneficial because the shear in the background profile is zero, so an increase in Δz more rapidly favors a decrease in TKE.

The general behavior of the TKE equation with respect to perturbations in Δz in the GS case is seen when comparing the $d\theta/dz$=0.003 K/m case with the 0.001 K/m case. For the $d\theta/dz$=0.001 K/m GS cases, the shear term increases rapidly, and the buoyancy stratification in the background profile is so weak that the buoyancy term cannot compensate for the increase in the shear term, and increasing Δz only makes things worse. In essence, Δz reaches into a background environment, with strong shear, that may be inherently unstable in the K-H sense. In these cases, it is reasonable to expect any CBL growth to become unbounded. Leaving these aside and focusing on the cases in which the background profile can be considered stable (i.e. Ri>0.25), it seems to be important to use Δz. Whether Δz is used in the ZOM sense or in the framework of a higher order model is essentially immaterial. LES data (see Chapter 7) show that Ri is constant in the entrainment zone when the buoyancy and velocity profiles are not linear as they would be in the FOM, but the FOM is the lowest order model that can represent an entrainment zone with constant Ri. Since its equations, although complex, are simpler than those of the higher order models, it can model the effect of the constant Ri layer in the least computationally expensive manner.

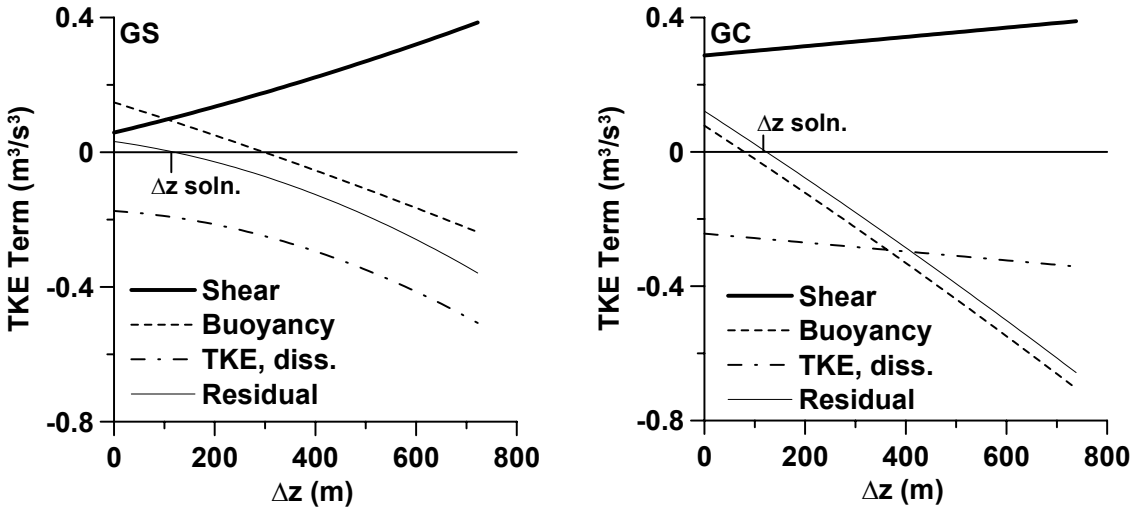

Figure 10.21: Sensitivity of the terms in the integral TKE budget (3.74-3.77) to perturbations in Δz in the FOM for the integrations with $d\theta/dz$=0.003 K/m and Q_s=0.03 Km/s: (a) GS case, and (b) GC case.

10.4 Chapter Summary

This chapter has examined the behavior of the numerical models of entrainment in sheared CBLs by comparing their predictions with LES. The first comparison evaluated the RANS-based *e-l* closures described in Xue et al. (2001) (ARPS) and Fiedler and Kong (2003) (F&K). The parameterizations based on integral budget methods were evaluated. Finally, the full set of ZOM and FOM equations, with the minimum number of parameterizations, were integrated to show how these models behaved in their full form (without neglecting any terms).

The *e-l* closures of Xue et al. (2001) and Fielder and Kong (2003) both predict a greater difference in the CBL growth rate between shear-free CBLs and sheared CBLs than is predicted by LES, with CBL growth for sheared CBLs being too fast. At the same time, the F&K closure predicts CBL growth very close to the LES predictions for the NS case. The more rapid entrainment in *e-l* closures for sheared CBLs seems to occur

regardless of the TKE values in the parameterized CBL. The ARPS scheme produces less TKE than LES but still predicts too rapid CBL growth when shear is present. The F&K scheme generally produces TKE values that are comparable to those of LES, but the TKE in the entrainment zone of sheared CBLS is significantly greater than the LES-predicted TKE. It is possible that the shear production of TKE in such schemes is overestimated, perhaps because the appropriate length scales for shear-generated turbulence in the CBL are different from the length scales for buoyancy-generated turbulence, and it is possible that the formulation of the master length scale l for CBL turbulence needs to be revised to account for the effects of shear. The LES data do not seem to provide much help in this regard, because the integral length scales derived from LES of sheared CBLs are not consistently smaller than they are for shear-free CBLs, and the velocity variance calculations are unable to distinguish turbulent motions from non-turbulent ones. Numerical artifacts of LES may obscure some of the true differences in integral length scales, damping motions with a smaller length scale and shifting the integral length scale towards larger scales. When simulations are performed in a CBL-relative frame of reference, the integral length scales decrease (see Chapter 8).

The analysis here may be somewhat limited by the fact that the initial momentum profiles used in the simulations do not necessarily reflect real atmospheric profiles, as has been discussed in Chapter 7. The surface winds in the GC case would probably have a significant ageostrophic component, so any NWP model initialization would probably differ from the simulations. Likewise, the GS case has very large geostrophic shear, probably three or four times greater than its typical atmospheric value. Nevertheless, similar magnitudes of total shear (between 10 meters above ground level and a kilometer

or so above ground level) are pretty common (see Chapter 9). In this manner, the cases with strong shear serve as a critical test of how an *e-l* scheme in NWP might perform with respect to the development of the CBL. It is particularly important for NWP and air quality model schemes to correctly predict boundary layer depth, because this affects the concentration of moisture in the lower atmosphere as well as the concentration of air pollutants. Additionally, the *e-l* schemes may behave differently in the NWP model where they are implemented, due to either an interaction with other parameterizations or by having a larger amount of TKE above the CBL.

The tests of the integral budget-based entrainment parameterizations here show they also overestimate entrainment in situations when strong shear is present. Again, it must be stated that the shear in the LES cases is rather strong, but the cases were designed in this manner so that the relative effects of shear could be more easily seen. Adhering to the strict mathematical form of the ZOM provides entrainment equations that contain the entrainment zone shear as a negative sign term in the denominator. This results in a denominator that drops to zero, and the entrainment flux ratio becomes unbounded well before the surface heat flux goes to zero. Entrainment equations by Stull (1976a,b) and Sorbjan (2004), which deviate from the traditional ZOM methodology in this respect, avoid this problem and therefore produce more realistic entrainment flux ratios for the strong shear conditions. The success of these two parameterizations suggests the importance of accounting for the finiteness of the entrainment zone thickness in any entrainment equation for the sheared CBL.

Additionally, integration of the complete FOM entrainment equations shows that taking the entrainment zone thickness into account is beneficial, but only if the full FOM

equations, without simplifications, are integrated. The FOM equations are also not fail-proof, and for a majority of simulated cases, the full ZOM equations can be also be integrated without problems. Nevertheless, the FOM works in many GC cases where the ZOM fails, and its success is primarily due to the inclusion of entrainment zone thickness as a dependent variable. If the background stability is too weak, however, Δz does not help, and the equations are subject to the same mathematical problems as the ZOM equations.

Given that Kelvin-Helmholtz instabilities appear to be an inherent feature of convective entrainment in the presence of wind shears, as our and other LES show (see, e.g., Kim et al. 2003), any *Ri*-limited entrainment equation would seem to be most suited to model the growth dynamics of sheared CBL. The FOM is the simplest framework in which to do this.

Chapter 11 Summary and Conclusions

11.1 Summary of Activities

The entrainment rate in convective boundary layers (CBLs) developing in shear-free conditions has been thoroughly studied using laboratory water tanks, wind tunnels, atmospheric measurements, and LES, and the entrainment equations developed for the shear-free CBLs have been well-tested. However, relatively few studies have focused on the influence of shear on CBL entrainment. The goal of the present study was to thoroughly investigate the effects of shear on CBL entrainment and to closely examine the dynamics of entrainment when wind shear is present in the CBL. Given the scarcity of atmospheric observations that can be used for such a purpose, this study has been focused on simulating sheared CBLs and comparing the simulations with models of entrainment. Some comparisons were also made with available atmospheric data.

A series of large eddy simulations (LES) has been conducted to investigate the effects of shear on convective boundary layer (CBL) entrainment. The series of simulations had different combinations of atmospheric stratification, surface buoyancy flux, and shear. Within any given simulation, the atmospheric stratification had values of $\partial\theta/\partial z = 0.001$, 0.003, or 0.010 K/m, and the surface heat flux had values of Q_s=0.03, 0.10, and 0.30 Km/s. The shear had three different configurations. In the no shear (NS) case, the initial mean profile had zero flow throughout the simulation domain. The two

shear cases were a case with a height-constant geostrophic wind (GC) and a case with a shear in the geostrophic wind of 0.0125 s^{-1} (GS), starting with 0 m/s at the surface. The momentum profiles were initialized in geostrophic balance. The LES domain was $5.12\times5.12\times1.6$ km^3 on a $256\times256\times80$ grid. The combination of all possible configurations of shear, stratification, and surface buoyancy flux would result in 27 simulations, but the cases with the combined strongest stratification and weakest buoyancy flux were not run because of the excessive computer time required to bring these simulations to completion, so the total number of simulations was 24.

First and second order turbulence statistics were calculated for all simulations, and turbulence spectra and dissipation were calculated for a subset of runs whose results were considered to be most representative of the simulations as a group and the atmosphere in general. Horizontal and vertical cross sections of potential temperature and momentum were also output in order to study the turbulence structures. The parameters of entrainment were retrieved from the mean profiles of first and second order statistics in a manner consistent with the definitions of those parameters within respective bulk CBL models. These bulk models were the zero order model (ZOM) and first order model (FOM—see below).

Two turbulence closure schemes based on the Reynolds-averaged Navier-Stokes (RANS) approach, typically used in numerical weather prediction (NWP) models, were compared with the simulation results to test their representation of entrainment in sheared CBLs against LES. The tested schemes had the turbulence kinetic energy e (TKE) equation at their core, combined with an integral turbulence length scale l, and are therefore known as *e-l* closures. The two schemes differed in their specification of l.

Since the subgrid TKE equation in the LES code is also a 1.5-order, TKE-based turbulence closure, the LES subgrid model can be easily modified into a RANS-based *e-l* model. The main change to the subgrid model was to replace the length scale with the respective length scale formulations of either Xue et al. (2001) (ARPS) or Fiedler and Kong (2003) (F&K) and to use the proper coefficients in their respective expressions for eddy diffusivities, turbulent Prandtl number, and dissipation. The vertical equation of motion and horizontal gradient calculations were removed from the LES code, and the resulting column model was integrated for the same initial conditions as in LES. To the extent possible, the same first and second order turbulence statistics were output and compared to the statistics from LES to reveal the reasons behind the differences in entrainment rate predictions by LES and *e-l* models.

The RANS-based equations for momentum, buoyancy, and TKE can be integrated over the CBL depth to derive entrainment equations based on the integral budgets of these quantities. To facilitate the integrations, a simplified CBL structure is assumed. For the zero order model (ZOM), the CBL is represented by a mixed layer with height-constant momentum and buoyancy, with zero-order discontinuities at the CBL top, and in the first order model (FOM), a finite entrainment zone depth is included in the CBL structure. The entrainment rates in sheared CBLs, predicted by these two integral budget-based (bulk) models, were compared with LES entrainment rates. Several entrainment parameterizations based on the ZOM or FOM were tested: Tennekes (1973), Mahrt and Lenschow (1976), Stull (1976a), Zeman and Tennekes (1977), Tennekes and Driedonks (1981), Driedonks (1982), Boers et al. (1984), Batchvarova and Gryning (1991,1994), Kim (2001), Pino et al. (2003), and Sorbjan (2004). These

parameterizations were tested using retrieved parameters of entrainment from LES. Then, the full zero order model (ZOM) and first order model (FOM) entrainment equations were integrated for the same initial conditions as in LES, with the intention of revealing whether or not the entrainment zone thickness was an important parameter to include in the integral budget-based models.

Finally, an assessment of the uncertainty of LES results, with respect to atmospheric data, needed to be made. Taking direct entrainment measurements at the top of the CBL is a very difficult and expensive task, so the best way to test the LES results is to compare LES-predicted entrainment rates with the CBL growth observed in atmospheric measurements, accounting for CBL horizontal wind divergence and temperature advection as accurately as possible. A basic method for comparing LES and atmospheric data has been proposed, and a particular case of a developing sheared CBL has been studied. The atmospheric measurements of sensible heat flux and the initial temperature and momentum profiles were input to LES, and the simulation was performed from sunrise to sunset to test the simulated entrainment rates against the observed CBL growth rates.

11.2 Findings of the Study

From the conducted large eddy simulations, there are two fundamental findings. The first is that the entrainment zone shear is much more important than the surface shear in enhancing CBL entrainment. The other is the discovery of a layer of constant *Ri* that forms within the entrainment zone when the relative effects of shear stand out strongly enough.

It cannot be definitively argued that the surface shear has no influence on CBL entrainment, but the level of influence is definitely secondary compared to the effect of the entrainment zone shear. In particular GC simulations with strong surface shear, the entrainment rate was roughly equal, in some cases, to the entrainment rate in the GS cases, but in those GC cases, the entrainment zone shear was comparably large to that of the GS cases.

These results can be analyzed with respect to the regions of generation, direction of transport, and the dissipation of the CBL turbulence. In the shear-free CBL, the buoyancy production occurs throughout most of the mixed layer, and the rising plumes of surface-heated air ascend into the entrainment zone. Most of the TKE is dissipated in this process, but the nature of the process (rising warm air) means that the TKE is transported preferentially upward. In the sheared CBL, the main role of surface shear-generated turbulence is to smooth out surface momentum gradients, and once this turbulence leaves the surface layer and enters the mixed layer, where the mean shear is generally much weaker, the capability of turbulence to sustain itself against dissipation is reduced. The TKE generation region (the surface layer in this case) is well-separated from the entrainment zone, so there is an additional delay in energy transport across the mixed layer, allowing more dissipation to occur.

The TKE generated in the entrainment zone, on the other hand, is immediately in a position to promote entrainment, so despite the fact that roughly half the TKE is dissipated in place, such shear is able to strongly affect entrainment. The mixing process in the interior of the CBL places the shear primarily in the entrainment zone and allows it to accumulate to the point where Kelvin-Helmholtz (K-H) type instabilities ensue. These

instabilities generate additional turbulence that mixes the accumulated shear to the point that it no longer supports the growth of TKE in the entrainment zone.

When the relative effects of shear become strong enough, and the entrainment zone structure is less dominated by wave-like motions along the interface, a well-resolved layer of nearly constant *Ri* forms in the entrainment zone of the simulations. This layer manifests a balance between the turbulence generation mechanism of shear and the destruction mechanisms of negative buoyancy flux and dissipation. If enough shear accumulates in this layer that the balance is disrupted ($Ri<0.25$), the shear-generated TKE works to increases the depth of the layer to the point where the integral negative buoyancy flux (entrainment) and dissipation increase to restore the balance. If the layer deepens to the point that $Ri>0.25$, or the shear decreases, the turbulence intensity fades, and the layer collapses so that the balance is restored. The conducted simulation using an initial setup based on May 22, 2002 data has provided evidence for this. The relative entrainment zone thickness $\delta z / z_i$ (where δz is the entrainment zone thickness and z_i is the CBL depth) is large early in this simulation, but it decreases substantially during the middle of the simulation, when entrainment zone shear decreases.

Any model of entrainment based on the integral budget (bulk) approach does well in sheared CBLs if it takes the entrainment layer into account. Although the ZOM incorporates the basic concept of balance between buoyancy destruction and shear generation of TKE in the entrainment zone, it does not consider how the entrainment zone depth acts to regulate this balance. The FOM and higher order models, with their inclusion of the entrainment zone depth as a dependent variable, are able to model this process and are then able to reproduce shear effects on entrainment in many cases where

the ZOM fails. Analysis of the response of the FOM integral TKE equation to perturbations in Δz (the FOM entrainment zone thickness) shows that Δz acts to restore the balance between these terms whenever the background stability is not too weak.

The usefulness of the FOM comes at a price. The full FOM equations are much more cumbersome than the ZOM equations for sheared CBLs, and the results of the model integrations, scale analysis, and parameterization tests show that it is necessary to include all terms in the TKE equation. Simplifications resulting from assumptions such as $\Delta z \ll z_i$ and $d\Delta z / dt \approx 0$ do not work for the CBL cases considered in this study.

The FOM, despite its superior performance to the ZOM for sheared CBLs, happens to fail in the cases with geostrophic shear (GS) and weak background stratification. This underscores the basic weakness in the mathematical formulation of the FOM, which it shares with the ZOM, and might suggest that the FOM is still not sufficient to model sheared CBLs within their broad variety, but it might also mean that the GS cases in which it fails have background profiles of potential temperature and momentum that are inherently unstable to perturbations. Because the free atmosphere *Ri* value in these simulations is 0.21, this may indeed be the case, but one cannot say so for certain. For uniformly stratified and sheared layers above a solid surface, the value of *Ri* that is sufficient for K-H instability may well be dependent on the distance from the solid surface, which limits vertical motions. The FOM integral budget equations are not designed to model the growth of these instabilities or the propagation of the turbulent layer through an unstable background profile.

The momentum and potential temperature profiles in the entrainment zones of simulated CBLs are still not linear as they are in the FOM, suggesting a higher order

model may be more appropriate for modeling sheared CBLs. However, FOM equations are already quite cumbersome, and going to higher order models will make the equations even more cumbersome. The increasing complexity of the equations will require additional assumptions to be made, based on less well-known relationships. At some point, the utility of increasing the complexity of the bulk model is lost, and it becomes more worthwhile just to integrate the RANS-based *e*-*l* equations. For shear-free CBLs, the ZOM models the CBL growth rate almost perfectly, but for sheared CBLs, any *Ri*-limited entrainment equation seems much better suited to model entrainment. The lowest order model that does this is the FOM. Other ZOM/FOM hybrid parameterizations, such as Stull (1976a,c) and Sorbjan (2004) take entrainment zone *Ri* into account, either implicitly or explicitly, and also model the entrainment flux ratio reasonably well.

Some arguments have been made that the sheared CBL can, in fact, be considered as two separate layers (Lewellen 2000): a stable boundary layer above a more classic CBL, with the effects of entrainment zone shear not penetrating into the interior of the CBL. To some extent, this is a reasonably accurate statement, since the entrainment zone atop a sheared CBL does behave in a similar fashion to the stable nocturnal CBL, and animations of the simulated temperature and velocity cross-sections show an intermittent nature to the turbulence at the CBL top (Otte and Wyngaard 2001). Nevertheless, unlike the nocturnal boundary layer, the entrainment zone has no rigid underlying surface, and the effects of the shear-generated turbulence do extend downward into the CBL. The entrainment zone becomes thicker and encroaches upon the mixed layer while the potential temperature increases throughout the depth of the mixed layer. Additionally,

the entrainment of momentum affects the structure of the velocity profiles. If the shear is strong and entrainment is rapid, the mixed layer does not really appear so well-mixed.

Overall, the features of simulated turbulence structure in the CBL are consistent with those described in other studies (e.g. Kanna and Brasseur 1998). In the GC case, the surface shear aligns the convection into horizontal rolls (as has been simulated by others and observed in the atmosphere), and in the GS case, the thermals are tilted with respect to their vertically upright orientation in the NS case. In sheared CBLs, the upward transport of TKE is reduced, particularly in the middle and upper portions of the CBL, and this is reflected in both the TKE budgets and skewness profiles.

Despite the large qualitative differences between the flow observed in sheared and shear-free CBLs, the vertical velocity spectra in the interior of the CBL and in the lower portion of the entrainment zone are not greatly changed in the presence of shear. Any differences among the GS, GC, and NS spectra in the initial simulations (Fig. 8-6) were mostly due to the damping effects of the numerical scheme. It appears the numerical artifacts have notable effects only on the high wavenumber portions of the spectra, where the energy density is pretty low. It was shown by numerical experiments that the effects of these artifacts can be minimized by conducting the simulations in a frame of reference moving with the CBL mean flow.

The heat flux cospectra in the middle of the entrainment zone (around z/z_i=1) show that the turbulent motions responsible for entrainment are well-resolved on the LES grid. Additionally, the entrainment rate appears insensitive to whether the simulation is run in the ground-relative or CBL-relative frame of reference. These two facts lend greater confidence to the overall simulation results.

The comparisons between LES and the lidar data for the May 22, 2002 sheared CBL case show that CBL depth comparisons can be made relatively easily when the appropriate lidar scanning strategy is used. Because lidar relies on first order statistics (aerosol concentrations) rather than second order statistics (e.g. heat flux), a reasonable mean can be constructed with a relatively small sample. The May 22, 2002 comparison shows that even well before the dryline passage, the simulated CBL growth rate differs from the observed growth rate rather significantly. It is apparent that factors not taken into account in LES have a significant influence on the CBL depth. These could include differences between the real potential temperature profile and the LES-initialized potential temperature profile, but the most significant and worrisome difference may be due to CBL heterogeneity, advection, and mean CBL divergence, which may make suitable comparisons between atmospheric data and simulations very difficult for sheared CBLs.

Tests of RANS-based *e-l* closures against the LES data show that the *e-l* closures exaggerate the differences between the entrainment rates of shear-free CBLs and sheared CBLs. Generally, the entrainment predicted by *e-l* closures for sheared CBLs is too large, regardless of whether the modeled entrainment zone TKE is larger (F&K) or smaller (ARPS) than that in LES. The TKE levels do seem to affect the momentum and potential temperature profiles, however. The fields are less well-mixed in the ARPS output than they are in LES. The degree of mixing with the F&K closure, which predicts larger TKE, seems to match the simulations more closely.

It is possible that the shear production of TKE and resulting entrainment in the considered closure schemes are too large because the length scales for shear-generated

turbulence are overestimated. It is possible that the formulation of the master length scale l for CBL turbulence needs to include a parameterized reduction in scale when shear is the dominant production mechanism. The LES data, in some cases, support the idea of a decrease in l, but the results are inconsistent, and in a majority of simulated sheared CBLs, the integral length scales are not really smaller than they are for shear-free CBLs. Additionally, the integral length scale calculations are unable to distinguish turbulent motions from non-turbulent ones. The non-turbulent, wave-type motions (especially above the entrainment zone) do appear biased toward larger length scales.

The *e*-*l* schemes tested are among many interacting parameterizations in NWP models, so their behavior in this study, which tested them in isolation, may differ to some extent from their behavior in NWP. However, the results do suggest entrainment and associated CBL mixing may become too strong in NWP models using TKE-based closures when strong shear is present.

11.3 Suggestions for Further Research

The analysis presented here by no means constitutes an exhaustive study of sheared CBLs. The conclusions above need to be tested more fully against atmospheric data. The relatively low resolution of routine measurements and the expense of higher-resolution experimental measurements have prevented a large number of atmospheric sheared CBL studies from being conducted to date. One must nevertheless consider the motivation for conducting atmospheric CBL experiments specifically to address the effects of shear on CBL entrainment. Regardless of the strength of the shear, the surface buoyancy flux still dominates the CBL evolution during the middle of the day, and shear

is typically weaker than in the conducted numerical simulations. In the simulations, the differences between dz_i/dt of shear-free and sheared CBLs in all but a few cases may be within the error of estimates due to mesoscale heterogeneity of the CBL and uncertainties in the estimates of divergence.

There are two motivations to make such studies in spite of these problems. First, the technology for remote sensing of temperature and wind in the CBL is rapidly advancing. For instance, the existing 915-MHz profiler technology is allowing vertical resolution down to 60 meters or less, and the use of velocity-azimuth display (VAD) techniques with routinely gathered 10-cm radar data may permit similar resolution of the vertical structure of the mean horizontal winds. Radiometer technology is allowing vertical resolution as low as 100 meters for temperature. In the Dynamics and Chemistry of Marine Stratocumulus (DYCOMS-II) experiment, the dual constraints of the divergence and scalar flux methods on the entrainment velocity estimates allowed those estimates to be made with higher precision than in the past. Although the relatively diffuse nature of the interface makes application of these techniques for dry, sheared CBLs less certain, the utility of these methods probably needs to be examined in greater detail, as they could provide very useful data for testing the simulation results. Because of the uncertainties in entrainment velocity estimates, comparisons between LES and atmospheric data need to utilize a reasonably large set of cases, and the comparisons should rely on first order statistics as much as possible.

Alternatively, the LES code could be modified so that it represents the heterogeneity and consequent mesoscale flows observed in the atmosphere. With the May 22, 2002 case in particular, if the LES code can be modified to simulate two CBL

types within a single domain, the effects of the dryline circulation can be included in the simulated CBLs that are compared with the atmospheric data from that day. Specifically, the domain could be split into three areas—two of them being homogeneous CBLs and the center portion of the domain containing the interacting CBLs. There is a plethora of data available, so modification of LES may open opportunities for more comprehensive comparisons between LES and atmospheric data.

The turbulence closure schemes in NWP need to be further tested to measure their ability to model entrainment in sheared CBLs. Both *e-l* closure schemes tested in the current study overestimate the entrainment rate into sheared CBLs, and their behavior needs to be examined more closely. In particular, the evolution of the shear generation, transport, and dissipation of TKE needs to be compared with LES and atmospheric measurements to see how these terms are affected by the assumptions of RANS-based closures. Doing so may yield clues about where those assumptions fail with respect to entraining, sheared CBLs. For example, the length scales may be shorter in the entrainment zone of sheared CBLs than in shear-free CBLs, and new length scale formulations may need to be developed and tested. Alternatively, constraints on entrainment zone *Ri*, based on LES results, may help to solve the problem, but neither of these questions can be answered without further study of the problem. Also, a larger variety of schemes, such as the Mellor and Yamada (1974, 1982) closure, which also employs a TKE equation, need to be tested as well to see if these effects are characteristic of other turbulence closures commonly employed in NWP models.

Finally, LES has shown some rather interesting vortical structures in the entrainment zone of sheared CBLs in this study as well as others (Kim et al. 2003). Kim

and Park (2003) also found vortical structures in the surface layer. LES served as a very useful tool to explore the parameter space for sheared CBLs, and the interaction between shear and vorticity in the entrainment zone was simulated. Therefore, LES may serve as an equally useful tool for exploring the parameter space for other interactions between vorticity and shear. In particular, the development of vertical vorticity in regions of strong horizontal velocity gradients should be studied numerically to further understand the development of intense vortices in regions of shear and strong vertical velocity.

References

Angevine, W. M. and J. I. MacPherson. 1995. Comparison of Wind Profiler and Aircraft Wind Measurements at Chebogue Point, Nova Scotia. *J. Atmos. and Oceanic Tech.* **12,** 421-426.

Angevine, W. M., 1999: Entrainment results including advection and case studies from the Flatland boundary layer experiments. *J. Geophys. Res.,* **104,** 30947-30963.

Angevine, W. M., H. K. Baltink, and F. C. Bosveld, 2001: Observations of the morning transition of the convective boundary layer. *Bound.-Layer Meteor.*, **101,** 209-227.

Arya, S. P. S., and J. C. Wyngaard, 1975: Effect of baroclinicity on wind profiles and the geostrophic drag law for the convective planetary boundary layer. *J. Atmos. Sci.,* **32,** 767-778.

Asselin, R., 1972: Frequency filter for time integrations. *Mon. Wea. Rev.,* **100,** 487-490.

Ayotte, K. W., P. P. Sullivan, A. Andren, Scott C. Doney, A. A. M. Holtslag, W. G. Large, J. C. McWilliams, C.-H. Moeng, M. J. Otte, J. J. Tribbia, and J. C. Wyngaard, 1996: An evaluation of neutral and convective planetary boundary-layer parameterizations relative to large eddy simulations. *Bound. Layer Meteorol.,* **79,** 131-175.

Ball, F. K., 1960: Control of inversion height by surface heating. *Quart. J. Roy. Meteor. Soc.,* **86,** 483-494.

Barr, A. G., and G. S. Strong, 1996: Estimating regional surface heat and moisture fluxes above prairie cropland from surface and upper air measurements. *J. Atmos. Sci.,* **35,** 1716-1735.

Batchvarova, E., and S.-E. Gryning, 1991: Applied model for the growth of the daytime mixed layer. *Bound.-Layer Meteor.*, **56**, 261-274.

Batchvarova, E., and S.-E. Gryning, 1994: An applied model for the height of the daytime mixed layer and the entrainment zone. *Bound.-Layer Meteor.*, **71**, 311-323.

Betts, A. K., 1973: Non-precipitating cumulus convection and its parameterization. *Quart. J. Roy. Meteorol. Soc.*, **99**, 178-196.

Betts, A. K., 1974: Reply to comment on the paper "Non-precipitating Cumulus Convection and its Parameterization". *Quart. J. Roy. Meteorol. Soc.*, **100**, 469-471.

Betts, A. K. and J. H. Ball, 1994: Budget analysis of FIFE 1987 sonde data. *J. Geophys. Res.,* **99,** 3655-3666.

Betts, A. K., and A. G. Barr, 1996: First International Satellite Land Surface Climatology Field Experiment 1987 sonde budget revisited. *J. Geophys. Res.,* **101,** 23285-23288.

Betts, A. K., R. L. Desjardins, and J. I. MacPherson, 1992: Budget analysis of the boundary layer grid flights during FIFE 1987. *J. Geophys. Res.,* **97,** 18533-18546.

Beyrich, F., and S-E. Gryning, 1998: Estimation of the entrainment zone depth in a shallow convective boundary layer from sodar data. *J. Appl. Meteor.,* **37,** 255-268.

Bianco, L., and J. M. Wilczak, 2002: Convective boundary layer depth: improved measurement by Doppler radar wind profiler using fuzzy logic methods. *J. Atmos. and Oceanic Tech.,* **19,** 1745-1758.

Black, T. L., 1994: The new NMC mesoscale Eta model: description and forecast examples. *Weather and Forecasting,* **9,** 265-278.

Boers, R., 1989: A parameterization of the depth of the entrainment zone. *J. Appl. Meteor*., **28**, 107-111.

Boers, R., and E. W. Eloranta, 1986: Lidar measurements of the atmospheric entrainment zone and the potential temperature jump across the top of the mixed layer. *Bound.-Layer Meteor.*, **34**, 357-375.

Boers, R., E. W. Eloranta, and R. L. Coulter, 1984: Lidar observations of mixed layer dynamics: tests of parameterized entrainment models of mixed layer growth rate. *J. Climate Appl. Meteor.*, **23**, 247-266.

Bougeault, P., and P. Lacarrere, 1989: Parameterization of orography-induced turbulence in a mesobeta-scale model. *Mon. Wea. Rev.,* **117,** 1872-1890.

Brooks, I. M., 2003: Finding boundary layer top: application of a wavelet covariance transform to lidar backscatter profiles. *J. Atmos. Oceanic Technol.,* **20,** 1092-1105.

Brost, R. A., D. H. Lenschow, and J. C. Wyngaard, 1982a: Marine stratocumulus layers. Part I: mean conditions. *J. Atmos. Sci.,* **39,** 800-817.

Brost, R. A., D. H. Lenschow, and J. C. Wyngaard, 1982b: Marine stratocumulus layers. Part II: turbulence budgets. *J. Atmos. Sci.,* **39,** 818-836.

Brown, A. R., 1996: Large-eddy simulation and parametrization of the baroclinic boundary-layer. *Quart. J. Roy. Meteor. Soc.,* **122,** 1779-1798.

Carson, D. J., 1973: The development of dry inversion-capped convectively unstable boundary layer. *Quart. J. Roy. Meteorol. Soc.*, **99**, 450-467.

Caughey, and S. G. Palmer, 1979: Some aspects of turbulence structure through the depth of the convective boundary layer. *Quart. J. Roy. Meteor. Soc.*, **105**, 811-827.

Caughey, S. J., J. C. Wyngaard, and J. C. Kaimal, 1979: Turbulence in the evolving stable boundary layer. *J. Atmos. Sci.,* **36,** 1041-1052.

Chai, T., C.-L. Lin, and R. K. Newsom, 2004: Retrieval of microscale flow structures from high-resolution Doppler lidar data using an adjoint model. *J. Atmos. Sci.* **61,** 1500–1520.

Chou, S.-H., D. Atlas, and E.-N. Yeh, 1986: Turbulence in a convective marine atmospheric boundary layer. *J. Atmos. Sci.,* **43,** 547-564.

Cohn, S. A., and W. M. Angevine, 2000: Boundary layer height and entrainment zone thickness measured by lidars and wind-profiling radars. *J. Appl. Meteor.,* **39,** 1233-1247.

Cohn, S. A., W. O. J. Brown, C. L. Martin, M. E. Susedik, G. Maclean, and D. B. Parsons, 2001: Clear air boundary layer spaced antenna wind measurement with the multiple antenna profiler (MAPR), *Annales Geophysicae,* **19(8)**, 845-854.

Cohn, S. A., C. L. Holloway, S. P. Oncley, R. J. Doviak and R. J. Lataitis, 1997: Validation of a UHF spaced antenna wind profiler for high resolution boundary layer observations, *Radio Sci.,* **32,** 1279-1296.

Conzemius, R. and E. Fedorovich, 2002: Dynamics of convective entrainment in a heterogeneously stratified atmosphere with wind shear. *American Meteorological Society 15th Symposium on Boundary Layers and Turbulence*. Wageningen, the Netherlands.

Conzemius, R. and E. Fedorovich, 2004: Numerical models of entrainment into sheared convective boundary layers evaluated through large eddy simulations. Preprints, *16th Symp. on Boundary Layers and Turbulence*, Amer. Meteor. Soc., 9-13 August, Portland, Maine, USA, CD-ROM, 5.6.

Davis, K. J., N. Gamage, C. R. Hagelberg, C. Kiemle, D. H. Lenschow, and P. P. Sullivan, 2000: An objective method for deriving atmospheric structure from airborne lidar observations. *J. Atmos. Oceanic Technol.,* **17,** 1455-1468.

Davis, K. J., D. H. Lenschow, S. P. Oncley, C. Kiemle, G. Ehret, A. Giez, and J. Mann, 1997: Role of entrainment in surface-atmosphere interactions over the boreal forest. *J. Geophys. Res.,* **102,** 29219-29230.

Deardorff, J. W., 1970a: Preliminary results from numerical integration of the unstable boundary layer. *J. Atmos. Sci.*, **27**, 1209-1211.

Deardorff, J. W., 1970b: Convective velocity and temperature scales for the unstable planetary boundary layer and for Raleigh convection. *J. Atmos. Sci.*, **27**, 1211-1213.

Deardorff, J. W., 1972a: Numerical investigation of neutral and unstable planetary boundary layers. *J. Atmos. Sci.,* **29,** 91-115.

Deardorff, J. W., 1972b: Parameterization of the planetary boundary layer for use in general circulation models. *Mon. Wea. Rev.,* **100,** 93-106.

Deardorff, J. W., 1974a: Three-dimensional numerical study of turbulence in an entraining mixed layer. *Bound.-Layer Meteor.,* **7,** 199-226.

Deardorff, J. W., 1974b: Three-dimensional numerical study of the height and mean structure of a heated planetary boundary layer. *Bound.-Layer Meteor.,* **7,** 81-106.

Deardorff, J. W., 1979: Prediction of convective mixed-layer entrainment for realistic capping inversion structure. *J. Atmos. Sci.*, **36**, 424-436.

Deardorff, J. W., 1980: Stratocumulus-capped mixed layers derived from a three-dimensional model. *Bound.-Layer Meteor.,* **18,** 495-527.

Deardorff, J. W., and G. E. Willis, 1982: Dependence of mixed-layer entrainment on shear stress and velocity jump. *J. Fluid Mech.,* **115,** 123-140.

Deardorff, J. W., and G. E. Willis, 1985: Further results from a laboratory model of the convective planetary boundary layer. *Bound. Layer Meteor.,* **32,** 205-236.

Deardorff, J. W., G. E. Willis, and D. K. Lilly, 1969: Laboratory investigation of nonsteady penetrative convection. *J. Fluid Mech.,* **35,** 7-31.

Deardorff, J. W., G. E. Willis, and B. H. Stockton, 1980: Laboratory studies of the entrainment zone of a convectively mixed layer. *J. Fluid Mech.,* **100,** 41-64.

Doswell, C. A. III, and P. M. Markowski, 2004: Is buoyancy a relative quantity? *Mon. Wea. Rev.,* 132, 853-863.

Doswell, C. A. III, and L. F. Bosart, 2001: Extratropical synoptic-scale processes and severe convection. *Severe Convective Storms.* American Meteorological Society, 561 pp.

Driedonks, A. G. M., 1982: Models and observations of the growth of the atmospheric boundary layer. *Bound.-Layer Meteor* ., **23**, 283-306.

Durran, D. R., 1999: *Numerical methods for wave equations in geophysical fluid dynamics.* Springer-Verlag New York, Inc. 465 pp.

Fairall, C. W., 1984: Wind shear enhancement of entrainment and refractive index structure parameter at the top of a turbulent mixed layer. *J. Atmos. Sci.*, **41,** 3472-3484.

Fedorovich, E., 1995: Modeling the atmospheric convective boundary layer within a zero-order jump approach: an extended theoretical framework. *J. Appl. Meteor.*, **34,** 1916-1928.

Fedorovich, E., 1998: Bulk models of the atmospheric convective boundary layer. *Buoyant Convection in Geophysical Flows*, E. J. Plate et al., Eds., Kluwer, 265-290.

Fedorovich, E., R. Conzemius, and D. Mironov, 2004a: Convective entrainment into a shear-free, linearly stratified atmosphere: bulk models reevaluated through large eddy simulations. *J. Atmos. Sci.,* **61,** 281-295.

Fedorovich, E., R. Conzemius, and A. Shapiro, 2004b: Nonstationarity of convective boundary layer growth in a heterogeneously stratified, shear-free atmosphere. *Proc. 16th Symp. On Boundary Layers and Turbulence,* Portland, Maine, U.S.A.

Fedorovich, E., R. Conzemius, I. Esau, F. Katapodes-Chow, D. Lewellen, C.-H. Moeng, P. Sullivan, D. Pino, and J. V.-G. de Arellano, 2004c: Entrainment into sheared convective boundary layers as predicted by different large eddy simulation codes. *Proc. 16th Symp. On Boundary Layers and Turbulence,* Portland, Maine, U.S.A.

Fedorovich, E., and R. Kaiser, 1998: Wind tunnel model study of turbulence regime in the atmospheric convective boundary layer. *Buoyant Convection in Geophysical Flows*, E. J. Plate et al., Eds., Kluwer, 327-370.

Fedorovich, E., R. Kaiser, M. Rau, and E. Plate, 1996: Wind tunnel study of turbulent flow structure in the convective boundary layer capped by a temperature inversion. *J. Atmos. Sci.*, **53**, 1273-1289.

Fedorovich, E., and D. V. Mironov, 1995: A model for a shear-free convective boundary layer with parameterized capping inversion structure. *J. Atmos. Sci.,* **52,** 83-95.

Fedorovich, E., F. T. M. Nieuwstadt, and R. Kaiser, 2001a: Numerical and laboratory study of horizontally evolving convective boundary layer. Part I: transition regimes and development of the mixed layer. *J. Atmos. Sci.,* **58,** 70-86.

Fedorovich, E., F. T. M. Nieuwstadt, and R. Kaiser, 2001b: Numerical and laboratory study of horizontally evolving convective boundary layer. Part II: effects of elevated wind shear and surface roughness. *J. Atmos. Sci.,* **58,** 546-560.

Fedorovich, E., and J. Thäter, 2001: Vertical transport of heat and momentum across a sheared density interface at the top of a horizontally evolving convective boundary layer. *Journal of Turbulence*, **2**, 007.

Feltz, W. F., H. B. Howell, R. O. Knuteson, H. M. Woolf, and H E. Revercomb, 2003: Near continuous profiling of temperature, moisture, and atmospheric stability using the atmospheric emitted radiance interferometer (AERI). *J. Appl. Meteor.,* **42,** 584-597.

Feltz, W. F., W.L. Smith, R.O. Knuteson, H.E. Revercomb, H.M. Woolf, and H.B. Howell, 1998: Meteorological applications of temperature and water vapor retrievals from the ground-based atmospheric emitted radiance interferometer (AERI). *J. Appl. Meteor.,* **37,** 857-875.

Fernando, H. J. S., 1991: Turbulent mixing in stratified fluids. *Annu. Rev. Fluid Mech.,* **23,** 455-93.

Fernando, H. J. S., and J. C. R. Hunt, 1997: Turbulence, waves and mixing at shear-free density interfaces. Part 1. A theoretical model. *J. Fluid Mech.,* **347,** 197-234.

Fiedler, B. H., 2002: Grid adaptation and its effect on entrainment in an *E-l* model of the atmospheric boundary layer. *Mon. Wea. Rev.,* **130,** 733-740.

Fiedler, B. H., and F. Kong, 2003: The performance of an *E-l* scheme for the atmospheric boundary layer in a mesoscale model with grid spacing as small as 1 km. *Meteorol. Atmos. Phys.,* **84,** 1-10.

Field, R. T., L. Fritschen, E. T. Kanemasu, E. A. Smith, J. Stewart, S. Verma, and W. Kustas, 1992: Calibration, comparison, and correction of net radiation instruments used during FIFE. *J. Geophys. Res.*, **97**, 16681-18695.

Flamant, C., J. Pelon, P. H. Flamant, and P. Durand, 1997: Lidar determination of the entrainment zone thickness at the top of th eunsbale marine atmospheric boundary layer. *Bound.-Layer Meteor.,* **83,** 247-284.

Fochesatto, G. J., P. Drobinski, C. Flamant, D. Guedalia, C. Sarrat, P. H. Flamant, and J. Pelon, 2001: Evidence of dynamical coupling between the residual layer and the developing convective boundary layer. *Bound.-Layer Meteor.,* **99,** 451-464.

Frehlich, R., Y. Meillier, M. L. Jensen, and B. Balsley, 2003: Turbulence measurements with the CIRES tethered lifting system during CASES-99: calibration and spectral analysis of temperature and velocity. *J. Atmos. Sci.,* **60,** 2487–2495.

Gal-Chen, T., and R. A. Kropfli, 1984: Buoyancy and pressure perturbations derived from dual-doppler radar observations of the planetary boundary layer: applications for matching models with observations. *J. Atmos. Sci.,* **41,** 3007-3020.

Garcia, J. A., M. L. Cancillo, and J. L. Cano, 2002: A case study of the morning evolution of the convective boundary layer depth. *J. Appl. Meteor.,* **41,** 1053-1059.

Garratt, J. R., 1992: The atmospheric boundary layer. *Cambridge University Press.* 316 pp.

Garratt, J. R., and J. C. Wyngaard, 1982: Winds in the atmospheric convective boundary layer – prediction and observation. *J. Atmos. Sci.,* **39,** 1307-1316.

Glickman, T. S., et al., 2000: Glossary of Meteorology, 2nd Edition. *American Meteorological Society*. 855 pp.

Goldsmith, J. E. M., F. H. Blair, S. E. Bisson, and D. D. Turner, 1998: Turn-key Raman lidar for profiling atmospheric water vapor, clouds, and aerosols. *Applied Optics*, **37,** 4979-4990.

Grabowski, W. W., and T. L. Clark, 1991: Cloud-environment interface instability: rising thermal calculations in two spatial dimensions. *J. Atmos. Sci.,* **48,** 527-546.

Grabowski, W. W., and T. L. Clark, 1993: Cloud-environment interface instability. Part II: extension to three spatial dimensions. *J. Atmos. Sci.,* **50,** 555-573.

Grabowski, W. W., and T. L. Clark, 1993: Cloud-environment interface instability. Part III: direct influence of environmental shear. *J. Atmos. Sci.,* **50,** 3821-3828.

Grimsdell, A. W., and W. M. Angevine, 1998: Convective boundary layer height measurement with wind profilers and comparison to cloud base. *J. Atmos. and Oceanic Tech.,* **15,** 1331-1338.

Grossman, R. L., 1992: Convective boundary layer budgets of moisture and sensible heat over an unstressed prairie. *J. Geophys. Res.,* **97,** 18425-18438.

Grund, C. J., R. M. Banta, J. L. George, J. N. Howell, M. J. Post, R. A. Richter, and A. M. Weickmann, 2001: High-resolution Doppler lidar for boundary layer and cloud research. *J. Atmos. Oceanic Technol.* **18,** 376–393.

Gryning, S.-E., and E. Batchvarova, 1994: Parameterization of the depth of the entrainment zone above the daytime mixed layer. *Quart. J. Roy. Meteorol. Soc.*, **120**, 47-58.

Guerra, D., G. Schwemmer, A. Wooten, S. Chaudhuri, T. Wilkerson, 1999: Prototype holographic atmospheric scanner for environmental remote sensing. *J. Geophys. Res.*, **104**, (D) 22,287-22,292.

Hageli, P., D. G. Steyn, and K. B. Strawbridge, 2000: Spatial and temporal variability of mixed-layer depth and entrainment zone thickness. *Bound.-Layer Meteor.,* **97,** 47-71.

Hart, R. L., D. R. Cook, and M. L. Wesely, 1998: The ARM eddy correlation system for monitoring surface fluxes. *Proc. 10th Symp. Meteorological Observations and Instrumentation,* Phoenix, AZ, 11-16 January 1998, Amer. Meteorol. Soc., Boston, MA, pp. 335-336 (1998).

Holton, J. R., 1979: *An Introduction to Dynamic Meteorology, Second Edition.* Academic Press, 391 pp.

Hoxit, L. R., 1974: Planetary boundary layer winds in baroclinic conditions. *J. Atmos. Sci.,* **31,** 1003-1020.

Hunt, J. C. R., and P. A. Durbin, 1999: Perturbed vortical layers and shear sheltering. *Fluid Dyn. Res.*, **24**, 375-404.

Janjic, Z. I., 1990: The step-mountain coordinate: physical package. *Mon. Wea. Rev.,* **118,** 1429-1443.

Janjic, Z, 1994: The step-mountain eta coordinate model: further developments of the convection, viscous sublayer, and turbulence closure schemes. *Mon. Wea. Rev.,* **122,** 927-945.

Kaimal, J. C., 1978: Horizontal velocity spectra in the unstable surface layer. *J. Atmos. Sci.,* **35,** 18-24.

Kaimal, J. C., J. C. Wyngaard, D. A. Haugen, O. R. Coté, Y. Izumi, S. J. Caughey, and C. J. Readings, 1976: Turbulence structure in a convective boundary layer. *J. Atmos. Sci.*, **33**, 2152-2169.

Kaiser, R., and E. Fedorovich, 1998: Turbulence spectra and dissipation rates in a wind tunnel model of the atmospheric convective boundary layer. *J. Atmos. Sci.,* **55,** 580-594.

Kato, H., and Phillips, O. M., 1969: On the penetration of a turbulent layer into stratified fluid, *J. Fluid. Mech.*, **37,** 643-655.

Khanna, S., and J. G. Brasseur, 1998: Three-dimensional buoyancy and shear-induced local structure of the atmospheric boundary layer. *J. Atmos. Sci.,* **55,** 710-743.

Kiemle, C., M. Kaestner, and G. Ehret, 1995: The convective boundary layer structure from lidar and radiosonde measurements during the EFEDA '91 campaign. *J. Atmos. Oceanic Tech.,* **12,** 771-782.

Kim, S.-W., 2001: *Entrainment parameterization in sheared convective boundary layers.* Ph.D. Dissertation, Korean National University, Seoul.

Kim, S.-W., and S.-U. Park, 2003: Coherent structures near the surface in a strongly sheared convective boundary layer generalized by large-eddy simulation. *Bound.-Layer Meteor.*, **106**, 35-60.

Kim, S.-W., S.-U. Park, and C.-H. Moeng, 2003: Entrainment processes in the convective boundary layer with varying wind shear, *Bound.-Layer Meteor.*, **108**, 221-245.

Kimmel, S. J., J. C. Wyngaard, and M. J. Otte, 2002: "Log-chipper" turbulence in the convective boundary layer. *J. Atmos. Sci.,* **59,** 1124-1134.

Kundu, P. K., 1990. *Fluid Mechanics.* Academic Press, 638 pp.

Lambert, W. C., F. J. Merceret, G. E. Taylor, and J. G. Ward, 2003: Performance of five 915-MHz wind profilers and an associated automated quality control algorithm in an operational environment. *J. Atmos. Oceanic Technol.,* **20,** 1488–1495.

Lemone, M. A., 1973: The structure and dynamics of horizontal roll vortices in the planetary boundary layer. *J. Atmos. Sci.,* **30,** 1077-1091.

Lemone, M. A., M. Zhou, C.-H. Moeng, D. H. Lenschow, L. J. Miller, and R. L. Grossman, 1999: An observational study of wind profiles in the baroclinic convective mixed layer. *Bound.-Layer Meteor.,* **90,** 47-82.

Lenderink, G. and A. A. M. Holtslag, 2000: Evaluation of kinetic energy approach for modeling turbulent fluxes in stratocumulus. *Mon. Wea. Rev.,* **128,** 244-258.

Lenderink, G., M. C. VanZanten, and P. G. Duynkerke, 1999: Can an E-l turbulence closure simulate entrainment in radiatively driven boundary layers? *J. Atmos. Sci.,* **56,** 3331-3337.

Lenschow, D. H., 1970: Airplane measurements of planetary boundary layer structure. *J. Appl. Meteor.,* **9,** 874-884.

Lenschow, D. H., 1974: Model of the height variation of the turbulence kinetic energy budget in the unstable planetary boundary layer. *J. Atmos. Sci.,* **31,** 465-474.

Lenschow, D. H., Wyngaard, J. C., Pennell, W. T., 1980: Mean-Field and Second-Moment Budgets in a Baroclinic, Convective Boundary Layer. *J. Atmos. Sci.,* **37,** 1313–1326.

Lenschow, D. H., 1996: A proposal for measuring entrainment into the cloud-capped boundary layer. *Proc. ETL/CSU Cloud-Related Process Modeling and Measurement Workshop,* Boulder, CO, NOAA/ETL, 29-55.

Lenschow, D. H., P. B. Krummel, and S. T. Siems, 1999: Measuring entrainment, divergence, and vorticity on the mesoscale from aircraft. *J. Atmos. Oceanic Technol.,* **16,** 1384-1400.

Lewellen, D. C., 2000: Sheared convective boundary layers. *Proc. 14th Symp. Bound. Layers and Turb.*****

Lewellen, D. C., and W. S. Lewellen, 1998: Large-eddy boundary layer entrainment. *J. Atmos. Sci.,* **55,** 2645-2665.

Lilly, D. K., 1966: On the instability of Ekman boundary flow. *J. Atmos. Sci.,* **23,** 481-494.

Lilly, D. K., 1967: In *Proc. IBM Sci. Comp. Symp. On Environmental Sciences,* Yorktown Heights, NY.

Lilly, D. K., 1968: Models of cloud-topped mixed layers under a strong inversion. *Quart. J. Roy. Meteor. Soc.,* **94,** 292-309.

Lilly, D. K., 2002a: Entrainment into mixed layers: Part I. sharp-edged and smooth-edged tops. *J. Atmos. Sci.,* **59,** 3340-3352.

Lilly, D. K., 2002b: Entrainment into mixed layers: II. A new closure. *J. Atmos. Sci.,* **59,** 3353-3361.

Long, R. R., 1975: The influence of shear on mixing across density interfaces. *J. Fluid. Mech.,* **70,** 305-320.

Lyons, T. and B. Scott, 1990: *Air Pollution Meteorology*. CRC Press. 224 pp.

Mahrt, L., and D. H. Lenschow, 1976: Growth dynamics of the convectively mixed layer. *J. Atmos. Sci.,* **33,** 41-51.

Manins, P. C., and J. S. Turner, 1978: The relation between the flux ratio and energy ratio in convectively mixed layers. *Quart. J. Roy. Meteor. Soc.,* **104,** 39-44.

Margulis, S. A., and D. Entekhabi, 2004: Boundary-layer entrainment estimation through assimilation of radiosonde and micrometeorological data into a mixed layer model. *Bound.- Layer Meteor.,* **110,** 405-433.

Martin, W. R., 2003: Measurements and Modeling of the Great Plains Low-Level Jet. Ph.D. dissertation, University of Oklahoma, Norman, Oklahoma.

Mason, P. J., 1989: Large-eddy simulation of the convective atmospheric boundary layer. *J. Atmos. Sci.,* **46,** 1492-1516.

Mayor, S. D., G. J. Tripoli, and E. W. Eloranta, 2003: Evaluating large eddy simulations using volume imaging lidar data. Mon. Wea. Rev., **131,** 1428-1452.

McGrath, J. L., H. J. S. Fernando, and J. C. R. Hunt, 1997: Turbulence, waves and mixing at shear-free density interfaces. Part 2. Laboratory experiments. *J. Fluid Mech.*, **347**, 235-261.

Mead, J. B., G. Hopcraft, S. J. Frasier, B. D. Pollard, C. D. Cherry, D. H. Schaubert, and R. E. McIntosh, 1998: A volume-imaging radar wind profiler for atmospheric boundary layer turbulence studies. *J. Atmos. Oceanic Technol.,* **15,** 849-859.

Mellor, G. L., 1973: Analytic prediction of the properties of stratified planetary surface layers. *J. Atmos. Sci.,* **30,** 1061-1069.

Mellor, G. L., and T. Yamada, 1974: A hierarchy of turbulence closure models for planetary boundary layers. *J. Atmos. Sci.,* **31,** 1791-1806.

Mellor, G. L., and T. Yamada, 1982: Development of a turbulence closure model for geophysical fluid problems. *Rev. Geophys. Space Phys.,* **20,** 851-875.

Moeng, C.-H., 1984: A large-eddy-simulation model for the study of planetary boundary layer turbulence. *J. Atmos. Sci.,* **41,** 2052-2062.

Moeng, C.-H., and J. C. Wyngaard, 1988: Spectral Analysis of Large-Eddy Simulations of the Convective Boundary Layer. *J. Atmos. Sci.,* **45,** 3573–3587.

Moeng, C.-H., and J. C. Wyngaard, 1989: Evaluation of turbulent transport and dissipation closures in second-order modeling. *J. Atmos. Sci.,* **46,** 2311-2330.

Moeng, C.-H., and R. Rotunno, 1990: Vertical-velocity skewness in the buoyancy-driven planetary boundary layer. *J. Atmos. Sci.,* **47,** 1149-1162.

Moeng, C.-H., and P. P. Sullivan, 1994: A comparison of shear- and buoyancy-driven planetary boundary layer flows. *J. Atmos. Sci.,* **51,** 999-1022.

Nastrom, G.D. and F.D. Eaton. 1995. Variations of Winds and Turbulence seen by the 50-MHz Radar at White Sands Missile Range, New Mexico. *J. Appl. Meteorol.* **10,** 2135-2148.

Nelson, E., R. Stull, and E. Eloranta, 1989: A prognostic relationship for entrainment zone thickness. *J. Appl. Meteor.,* **28,** 885-903.

Nieuwstadt, F. T. M., and R. A. Brost, 1986: The decay of convective turbulence. *J. Atmos. Sci.,* **43,** 532-546.

Otte, M. J., and J. C. Wyngaard, 2001: Stably stratified interfacial-layer turbulence from large eddy simulation. *J. Atmos. Sci.,* **58,** 3424-3442.

Pennel, W. T., and M. A. LeMone, 1974: An experimental study of turbulence in the fair-weather trade wind boundary layer. *J. Atmos. Sci.,* **31,** 1308-1323.

Pino, D., J. V.-G. de Arellano, and P. J. Duynkerke, 2003: The contribution of shear to the evolution of a convective boundary layer. *J. Atmos. Sci.,* **60,** 1913-1926.

Piomelli, U., and J. R. Chasnov, 1996: Large-eddy simulations: theory and applications. *Turbulence and Transition Modelling*. Kluwer Academic Publishers.

Pollard, B. D., S. Khanna, S. J. Frasier, J. C. Wyngaard, D. W. Thomson, and R. E. McIntosh, 2000: Local structure of the convective boundary layer from a volume-imaging radar. *J. Atmos. Sci.,* **57,** 2281-2296.

Pope, S. B., 2000: *Turbulent Flows.* Cambridge University Press, 771 pp.

Press, W. H., S. A. Teukolsky, W. T. Vetterling, and B. P. Flannery, 1992: Numerical Recipes in Fortran 77, 2nd Ed. Cambridge University Press, 933 pp.

Price, J. F., Mooers, C. N. K., and van Leer, J. C., 1978: Observation and simulation of storm-induced mixed layer deepening. *J. Phys. Oceanogr.,* **8,** 582-599.

Randall, and Schubert, 2004: Dreams of a stratocumulus sleeper. *Turbulence and Mesoscale Meteorology*, pp. 71-94. Cambridge University Press (*in press*).

Schneider, J. M., and D. K. Lilly, 1999: An observational and numerical study of a sheared, convective boundary layer. Part I: Phoenix II observations, statistical description, and visualization. *J. Atmos. Sci.,* **56,** 3099-3078.

Schmidt, H., and U. Schumann, 1989: Coherent structure of the convective boundary layer derived from large eddy simulations. *J. Fluid Mech.,* **200,** 511-562.

Seibert, P., and M. Langer, 1996: Deriving characteristic parameters of the convective boundary layer from sodar measurements of the vertical velocity variance. *Bound.-Layer Meteor.,* **81,** 11-22.

Smagorinsky, J. 1963: General circulation experiments with the primitive equations. *Mon. Wea. Rev.*: **91,** 99–164.

Smith, W. L, W. F. Feltz, R. O. Knuteson, H. E. Revercomb, H. B. Howell, and H. M. Woolf, 1999: The retrieval of planetary boundary layer structure using ground-based infrared spectral radiance measurements. *J. Atmos. Oceanic Technol.,* **16,** 323-333.

Sorbjan, Z., 1996a: Numerical study of penetrative and "solid lid" nonpenetrative convective boundary layers. *J. Atmos. Sci.,* **53,** 101-112.

Sorbjan, Z., 1996b: Effects cause by varying the strength of the capping inversion based on a large eddy simulation model of the shear-free convective boundary layer. *J. Atmos. Sci.,* **53,** 2015-2024.

Sorbjan, Z., 2004: Large-eddy simulation of the baroclinic mixed layer. *Bound.-Layer Meteor.,* **112,** 57-80.

Stevens, B., 2002: Entrainment in stratocumulus-topped mixed layers. *Quart. J. Roy. Meteor. Soc.,* **128,** 2663-2690.

Stevens, B., J. Duan, J. C. McWilliams, M. Muennich, and J. D. Neelin, 2002: Entrainment, Rayleigh friction, and boundary layer winds over the tropical Pacific. *J. Climate,* **15,** 30-44.

Stevens, B., D. H. Lenschow, G. Vali, H. Gerber, A. Bandy, B. Blomquist, J.-L. Brenguier, C. S. Bretherton, F. Burnet, T. Campos, S. Chai, I. Faloona, D. Friesen, S. Haimov, K. Laursen, D. K. Lilly, S. M. Loehrer, S. P. Malinowski, B. Morley, M. D. Petters, D. C. Rogers, L. Russell, V. Savic-Jovcic, J. R. Snider, D. Straub, M. J. Szumowski, H. Takagi, D. C. Thornton, M. Tschudi, C. Twohy, M. Wetzel, and M. C. van Zanten, 2003: Dynamics and chemistry of marine stratocumulus – DYCOMS-II. *Bull. Amer. Meteor. Soc.,* **84,** 579-593.

Stull, R. B., 1973: Inversion rise model based on penetrative convection. *J. Atmos. Sci.*, **30**, 1092-1099.

Stull, R. B., 1976a: The energetics of entrainment across a density interface. *J. Atmos. Sci.,* **33,** 1260-1267.

Stull, R. B., 1976b: Internal gravity waves generated by penetrative convection. *J. Atmos. Sci.,* **33,** 1279-1286.

Stull, R. B., 1976c: Mixed-layer depth model based on turbulent energetics. *J. Atmos. Sci.,* **33,** 1268-1278.

Stull, R. B., 1988: An introduction to boundary layer meteorology. *Kluwer Academic Publishers.* 670 pp.

Sullivan, P., C.-H. Moeng, B. Stevens, D. H. Lenschow, and S. D. Mayor, 1998: Structure of the entrainment zone capping the convective atmospheric boundary layer. *J. Atmos. Sci.,* **55,** 3042-3064.

Sykes, R. I., and D. S. Henn, 1989: Large-eddy simulation of turbulent sheared convection. *J. Atmos. Sci.,* **46,** 1106-1118.

Tennekes, H., 1973: A model for the dynamics of the inversion above a convective boundary layer. *J. Atmos. Sci.*, **30**, 558-567.

Tennekes, H., and A. G. M. Driedonks, 1981: Basic entrainment equations for the atmospheric boundary layer. *Bound.-Layer Meteor.,* **20,** 515-531.

Troen, I., and L. Mahrt, 1986: A simple model of the atmospheric boundary layer; sensitivity to surface evaporation. *Bound.-Layer Meteor.,* **37,** 129-148.

Turner, D. D., and J. E. M. Goldsmith, 1999: Twenty-four-hour Raman lidar water vapor measurements during the Atmospheric Radiation Measurement Program's 1996 and 1997 water vapor intensive observation periods. *J. Atmos. Oceanic Technol.*, **16,** 1062-1076.

D.D. Turner, W.F. Feltz, and R.A. Ferrare, 2000: Continuous water vapor profiles from operational active and passive remote sensors. *Bull. Amer. Meteor. Soc.*, **81,** 1301-1317.

Turner, J. S., 1965: The coupled turbulent transport sof salt and heat across a sharp density interface. *Int. J. Heat Mass Transfer,* **8,** 759-767.

Turner, J. S., 1968: The influence of molecular diffusivity on turbulent entrainment across a density interface. *J. Fluid. Mech.,* **33,** 639-656.

Turner, J. S., 1973: *Buoyancy Effects in Fluids*. Cambridge University Press, 367 pp.

VanZanten, M. C., P. G. Duynkerke, and J. W. M. Cuijpers, 1999: Entrainment parameterization in convective boundary layers. *J. Atmos. Sci.,* **56,** 813-828.

Weckwerth, T. M., D. B. Parsons, S. E. Koch, J. A. Moore, M. A. LeMone, B. B. Demoz, C. Flamant, B. Geerts, J. Wang, and W. F. Feltz, 2004: An Overview of the International H_2O Project (IHOP_2002) and Some Preliminary Highlights. *Bull. Amer. Meteor. Soc.,* **85,** 253–277.

Weisman, M. L., and J. B. Klemp, 1982: The dependence of numerically simulated convective storms on vertical wind shear and buoyancy. *Mon. Wea. Rev.,* **110,** 504-520.

Weisman, M. L., and J. B. Klemp, 1984: The structure and classification of numerically simulated convective storms in directionally varying wind shears. *Mon. Wea. Rev.,* 112, 2479-2498.

Weiss, C., 2004: *Variational Pseudo Multiple-Doppler Analyses of a Dryline Utilizing Very-High Resolution Mobile Doppler Radar Data.* Ph.D. dissertation, University of Oklahoma, Norman, Oklahoma.

White, A. B., and C. J. Senff, 1999: A comparison of mixing depths observed by ground-based wind profilers and an airborne lidar. *J. Atmos. and Oceanic Technol.,* **16,** 584-590.

Whiteman, D. N., S. H. Melfi, and R. A. Ferrare, 1992: Raman lidar system for the measurement of water vapor and aerosols in the Earth's atmosphere. *Applied Optics*, **31,** 3068-3082.

Willis, G. E. and Deardorff, J. W. 1974: A laboratory model of the unstable planetary boundary layer. *J. Atmos. Sci.*, **31**, 1297-1307.

Wu, J., 1973: Wind-induced turbulent entrainment across a stable density interface. *J. Fluid Mech.,* **61,** 275-287.

Wyngaard, J. C., and R. A. Brost, 1984: Top-down and bottom-up diffusion of a scalar in the convective boundary layer. *J. Atmos. Sci.,* **41,** 102-112.

Wyngaard, J. C., 1998: Experiment, numerical modeling, numerical simulation, and their roles in the study of convection. *Buoyant Convection in Geophysical Flows,* pp. 239-251, Kluwer Academic Publishers.

Xue, M., K. K. Droegemeier, and V. Wong, 2000: The advanced regional prediction system (ARPS)—a multi-scale nonhydrostatic atmospheric simulation and prediction model. Part I: Model dynamics and verification. *Meteorol. Atmos. Phys.,* **75,** 161-193.

Young, G. S., B. K. Cameron, and E. E. Hebble, 2000: Observations of the entrainment zone in a rapidly entraining boundary layer. *J. Atmos. Sci.,* **57,** 3145-3160.

Zeman, O., and H. Tennekes, 1977: Parameterization of the turbulent energy budget at the top of the daytime atmospheric boundary layer. *J. Atmos. Sci.*, **34**, 111-123.

Ziegler, C. L., and E. N. Rasmussen, 1998: The initiation of moist convection at the dryline: forecasting issues from a case study perspective. *Weather and Forecasting,* **13,** 1106–1131.

Zilitinkevitch, S. S., 1975: Comments on “a model for the dynamics of the inversion above a convective boundary layer”. *J. Atmos. Sci.,* **32,** 991-992.

Zilitinkevitch, S. S., 1991: *Turbulent Penetrative Convection*. Avebury Technical, Aldershot, 179 pp.

Zilitinkevitch, S. S., and D.V.Mironov, 1992: Theoretical model of the thermocline in a freshwater basin. *J. Phys. Oceanogr.*, **22**, 988-996.

Appendix A

Large Eddy Simulation model equations

Basic Model Equations

The large eddy simulation (LES) equations can be derived by starting with a generalized form of the Navier-Stokes equations as in Kundu (1990) but in a rotating reference frame:

$$\rho\frac{Du_i}{Dt} = -\rho g\delta_{i3} - \frac{\partial p}{\partial x_i} + 2\rho\Omega_k u_j \varepsilon_{ijk} - \frac{2}{3}\frac{\partial}{\partial x_i}\left(\mu\nabla\cdot\vec{u}\right) + 2\frac{\partial}{\partial x_j}\left(\mu S_{ij}\right), \tag{A1}$$

$$\frac{1}{\rho}\frac{D\rho}{Dt} + \frac{\partial u_i}{\partial x_i} = 0. \tag{A2}$$

where $S_{ij} = \frac{1}{2}\left(\frac{\partial u_i}{\partial x_j} + \frac{\partial u_j}{\partial x_i}\right)$ is the strain tensor. We apply the Boussinesq approximation to the fluid:

1) The continuity equation is replaced by $\nabla\cdot\vec{u} = 0$.
2) Density is constant everywhere except when it is coupled with gravity.
3) The viscosity, thermal diffusivity, and specific heat of the fluid are regarded as constants.

Dividing by the constant density, ρ_0, and defining $f = 2\Omega\sin\phi$ (only a vertical component), we arrive at the following:

$$\frac{\partial u_i}{\partial t} = -\frac{\partial u_i u_j}{\partial x_j} - \frac{\rho}{\rho_0} g\delta_{i3} - \frac{1}{\rho_0}\frac{\partial p}{\partial x_i} + f u_j \varepsilon_{ij3} + 2\frac{\partial}{\partial x_j}\left(\nu S_{ij}\right). \tag{A3}$$

We then allow for the cancellation of terms that occurs for hydrostatic and geostrophic balance. These states are defined as follows:

$$\begin{aligned} &\frac{\partial p_{gh}}{\partial z} = -\rho_0 g, \\ &u_{g,j} = \varepsilon_{ij3}\frac{1}{\rho_0 f}\frac{\partial p_{gh}}{\partial x_i}, \end{aligned} \tag{A5}$$

where p_{gh} is the pressure that corresponds to the geostrophic and hydrostatic balance. Then, defining $\pi = \frac{p - p_{gh}}{\rho_0}$, and approximating $-\frac{(\rho - \rho_0)}{\rho_0}$ by $\frac{\theta_v - \theta_{v0}}{\theta_{v0}}$, the equations change to the following form:

$$\frac{\partial u_i}{\partial t} = -\frac{\partial u_i u_j}{\partial x_j} + g\frac{\theta_v - \theta_{v0}}{\theta_0}\delta_{i3} - \frac{\partial \pi}{\partial x_i} + f\left(u_j - u_{g,j}\right)\varepsilon_{ij3} + 2\frac{\partial}{\partial x_j}\left(\nu S_{ij}\right). \tag{A6}$$

LES does not have the resolution to solve the equation in this particular form. Instead, the equation must be filtered to be consistent with the grid spacing. The filter has the following form:

$$\widetilde{u_i}(x) = \frac{1}{\Delta x}\int_{x-\frac{\Delta x}{2}}^{x+\frac{\Delta x}{2}} u_i(x')B_{\Delta x}(x - x')dx', \tag{A7}$$

where overbars represent filtered quantities, Δx is the grid cell size, and $B_{\Delta x}$ is the filter function. In LES used in the present study, $B_{\Delta x}$ is the top hat filter:

$$B_{\Delta x} = \begin{cases} \frac{1}{\Delta x} & \left(x - \frac{\Delta x}{2} \le x' \le x + \frac{\Delta x}{2}\right) \\ 0 & \left(x' < x - \frac{\Delta x}{2}; x' > x + \frac{\Delta x}{2}\right) \end{cases}. \tag{A8}$$

As such, the filter does not specifically appear in the LES code. After filtering, the equations are:

$$\frac{\partial \widetilde{u_i}}{\partial t} = -\frac{\partial \widetilde{u_i u_j}}{\partial x_j} + g\frac{\widetilde{\theta_v} - \theta_{v0}}{\theta_{v0}}\delta_{i3} - \frac{\partial \widetilde{\pi}}{\partial x_i} + f\left(\widetilde{u_j} - u_{g,j}\right)\varepsilon_{ij3} + \frac{\partial}{\partial x_j}\left[\nu\left(\frac{\partial \widetilde{u_i}}{\partial x_j} + \frac{\partial \widetilde{u_j}}{\partial x_i}\right)\right] \quad \text{(A9)}$$

The nonlinear term is problematic, as it cannot be represented as a filtered product of two unfiltered variables, but rather, it can only be represented as a product of two filtered variables. The problem is handled in LES by splitting the filtered product into a product of filtered variables and a subgrid stress term.

$$\tau_{ij}^s = \widetilde{u_i u_j} - \widetilde{u_i}\widetilde{u_j}$$

$$\begin{aligned}\frac{\partial \widetilde{u_i}}{\partial t} = &-\frac{\partial \widetilde{u_i}\widetilde{u_j}}{\partial x_j} + g\frac{\widetilde{\theta_v} - \theta_{v0}}{\theta_{v0}}\delta_{i3} - \frac{\partial \widetilde{\pi}}{\partial x_i} + f\left(\widetilde{u_j} - u_{g,j}\right)\varepsilon_{ij3} \\ &+ \frac{\partial}{\partial x_j}\left[\nu\left(\frac{\partial \widetilde{u_i}}{\partial x_j} + \frac{\partial \widetilde{u_j}}{\partial x_i}\right) - \tau_{ij}^s\right]\end{aligned} \quad \text{(A10)}$$

The reader is referred to Piomelli and Chasnov (1996) for a detailed discussion of subgrid modeling as it is used in LES. The subgrid stress term is assumed to have the same form as it has when deriving the Navier-Stokes equations from the Cauchy equation:

$$\tau_{ij}^s = -p^s\delta_{ij} + \sigma_{ij}^s, \quad \text{(A12)}$$

where the superscript *s* designates the term as a subgrid term. The filtering operation above is assumed to be analogous to the averaging operation in the RANS, in which $\widetilde{u_i u_j} = \widetilde{u_i}\widetilde{u_j} + \widetilde{u_i' u_j'}$. In this case, the subgrid stress term, τ^s, is analogous to $\widetilde{u_i' u_j'}$. The sum of the *i*=*j* terms, $\widetilde{u_i' u_i'}$, is exactly twice the subgrid turbulence kinetic energy (STKE), *E*.

Using $p = -\frac{1}{3}\tau_{\alpha\alpha} = -\frac{2}{3}E$ (analogous to the equality specified in deriving the Navier-Stokes equations), we have:

$$\tau_{ij}^{s} = \frac{2}{3}E\delta_{ij} + \sigma_{ij}^{s}, \tag{A13}$$

Since the E term is analogous to pressure, it is grouped with the pressure term, and we redefine pressure as $\Pi = \bar{\pi} + \frac{2}{3}E$. Finally, the subgrid deviatoric stress tensor is assumed to have the form:

$$\sigma_{ij}^{s} = -K_m\left(\frac{\partial \widetilde{u_i}}{\partial x_j} + \frac{\partial \widetilde{u_j}}{\partial x_i}\right), \tag{A14}$$

where K_m is the subgrid momentum exchange coefficient. With these assumptions, the LES momentum equations become:

$$\begin{aligned}\frac{\partial \widetilde{u_i}}{\partial t} = &-\frac{\partial \widetilde{u_i}\widetilde{u_j}}{\partial x_j} + g\frac{\widetilde{\theta_v} - \theta_{v0}}{\theta_{v0}}\delta_{i3} - \frac{\partial \Pi}{\partial x_i} + f\left(\widetilde{u_j} - u_{g,j}\right)\varepsilon_{ij3} \\ &+ \frac{\partial}{\partial x_j}\left[\left(K_m + \nu\right)\left(\frac{\partial \widetilde{u_i}}{\partial x_j} + \frac{\partial \widetilde{u_j}}{\partial x_i}\right)\right].\end{aligned} \tag{A15}$$

For most practical purposes, $K_m >> \nu$, but ν is retained in the code for modeling small scale flows, in which $K_m >> \nu$ may no longer hold. Everything in the equation is in a resolved form, except for K_m, which is the final subgrid term that must be parameterized to close the problem.

The derivation of the thermodynamic equation proceeds in an analogous manner, but only with advection and diffusion terms with fewer terms. The thermodynamic equation is:

$$\frac{\partial \widetilde{\theta_v}}{\partial t} = -\frac{\partial \widetilde{u_i}\widetilde{\theta_v}}{\partial x_i} + \frac{\partial}{\partial x_i}\left[\left(K_h + \nu_H\right)\frac{\partial \widetilde{\theta_v}}{\partial x_i}\right]. \tag{A16}$$

The resolved continuity equation is of the form:

$$\frac{\partial \widetilde{u_i}}{\partial x_i} = 0. \tag{A17}$$

Subgrid closure

Subgrid closure is based on the balance of subgrid scale turbulence kinetic energy, hereafter denoted as STKE. The STKE equation, as written by Piomelli and Chasnov (1996), is as follows:

$$\frac{\partial E}{\partial t} = -\frac{\partial}{\partial x_j}\left(E\widetilde{u_j}\right) - \tau_{ij}^s \widetilde{S_{ij}} + \beta Q_3 - \frac{1}{2}\frac{\partial}{\partial x_j}\left(\widetilde{u_i u_i u_j} - \widetilde{u_i}\widetilde{u_i}\widetilde{u_j}\right) - \frac{\partial}{\partial x_j}\left(\widetilde{pu_j} - \widetilde{p}\widetilde{u_j}\right) \tag{A18}$$

(I) (II) (III) (IV) (V) (VI)

$$-\nu\left(\widetilde{\frac{\partial u_i}{\partial x_j}\frac{\partial u_i}{\partial x_j}} - \frac{\partial \widetilde{u_i}}{\partial x_j}\frac{\partial \widetilde{u_i}}{\partial x_j}\right),$$

(VII)

where $\beta = \frac{g}{T_0}$ and Q_3 is the vertical potential temperature flux. Term I is the local rate of change and term II is advection. Terms III and IV are the major source terms, with III being the mechanical production of STKE that occurs as energy cascades from larger scales into the subgrid scale. Term IV is the buoyancy production of turbulence. This term can be a source in the convective boundary layer but diminishes STKE in stable conditions. Terms V and VI are transport due to subgrid turbulent motions and subgrid pressure fluctuations, respectively. Finally, term VII is the dissipation of STKE.

Lilly-Smagorinsky closure

The Lilly-Smagorinsky subgrid closure scheme (Smagorinsky 1963; Lilly 1967) is based on an equilibrium assumption. Subgrid scale motions are assumed to have a time scale much smaller than resolved motions, and they adjust to perturbations much more rapidly than do resolved motions. Therefore, with respect to the time scales of resolved motions, the adjustment of subgrid motions is considered instantaneous. Under this assumption, all terms in the subgrid energy equation drop out except for III and VII. These terms are assumed to be in balance, with cascade of energy from the smallest resolved scales to the subgrid scale (III) instantly being converted to viscous dissipation (VII) within the subgrid domain.

The quantity inside the parentheses of Term VII is an unknown, but since VII is a viscous dissipation term, the relation of Batchelor (1953) is applied. Under this relation, viscous dissipation scales to the cube of the velocity scale divided by the length scale of the motions:

$$\nu\left(\widetilde{\frac{\partial u_i}{\partial x_j}\frac{\partial u_i}{\partial x_j}}-\frac{\partial \widetilde{u}_i}{\partial x_j}\frac{\partial \widetilde{u}_i}{\partial x_j}\right)=\varepsilon_\nu \sim \frac{u_l^3}{l}. \tag{A19}$$

The subgrid stress in term III takes on the form

$$\sigma_{ij}^s=-2K_m\widetilde{S_{ij}}=-K_m\left(\frac{\partial \widetilde{u}_i}{\partial x_j}+\frac{\partial \widetilde{u}_j}{\partial x_i}\right). \tag{A20}$$

Substituting this expression for τ_{ij}^s into Term III of the subgrid energy balance equation (A18), and with the assumption in (A19) above, we have:

$$\left(K_m 2\widetilde{S_{ij}}\right)\widetilde{S_{ij}} \sim \frac{u_l^3}{l}. \tag{A21}$$

Finally, eddy viscosity can be thought of as the product of a length scale and a velocity scale, so that it can be written in the form $K_m = u_l l$, and therefore, K_m / l can be substituted for u_l. The only remaining unknowns in the equation are then the eddy viscosity, K_m (for which we are solving the equation), and the length scale, l. Since the greatest energy-containing motions within the subgrid volume are at the largest scales, and these largest scales are approximately the size of the grid cell, it can be assumed that l is proportional to the local grid cell dimension, defined as $\Delta = \left(\Delta x \Delta y \Delta z\right)^{1/3}$ (the LES code in this study has constant Δ). Finally, to turn these proportionalities into equalities, the Smagorinsky coefficient, C_s, is introduced. The proportionality constant is chosen such that $l=C_s\Delta$, and with these substitutions, the solution for eddy viscosity becomes

$$K_m = \left(C_s \Delta\right)^2 \sqrt{2\widetilde{S_{ij}}\,\widetilde{S_{ij}}}. \tag{A22}$$

C_s can be evaluated using the technique in Lilly (1967). Although many LES studies use different values for this coefficient, its value is close to C_s=0.18, which is used in this study.

In the convective boundary layer, the turbulent heat exchange coefficient has a value approximately three times the turbulent exchange coefficient for momentum. In stable atmospheric layers, the heat exchange coefficient is approximately the same as the momentum exchange coefficient. The *subgrid* heat exchange coefficient in LES is therefore parameterized as, K_h =3K_m. when $\frac{\partial \tilde{\theta}}{\partial z} \le 0$, and and K_h =K_m when $\frac{\partial \tilde{\theta}}{\partial z} > 0$.

Deardorff Closure

Deardorff (1980) closure involves the calculation of subgrid energy at each time step in the model run. The STKE equation used is:

$$\frac{\partial E}{\partial t}+\frac{\partial \widetilde{u_i} E}{\partial x_i}=2K_m\widetilde{S_{ij}}\widetilde{S_{ij}}+\beta Q_3+\frac{\partial}{\partial x_i}2K_m\frac{\partial E}{\partial x_i}-\varepsilon. \tag{A23}$$

I II III IV V VI

As in the general STKE equation above, term I is the local rate of change and term II is advection by the resolved flow. Term III is the shear production term rewritten in terms of strain tensor, as in the derivation of the Smagorinsky closure. Term IV is the same form of the buoyancy production in the general STKE equation. In Deardorff closure, the pressure and turbulent redistribution of turbulence are combined into a single distribution term (V), and term VI is dissipation.

The subgrid exchange coefficients for heat and momentum are:

$$K_m=0.12l\sqrt{E} \text{ and } K_h=\left(1+\frac{2l}{\Delta}\right)K_m. \tag{A24}$$

The relationship between l and Δ is a little more complicated than with Smagorinsky closure:

$$l=\begin{cases}\Delta, & \dfrac{\partial\tilde{\theta}}{\partial z}\le 0;\\ \min\left\{\Delta,\dfrac{0.5\sqrt{E}}{\sqrt{\beta\dfrac{\partial\tilde{\theta}}{\partial z}}}\right\} & \dfrac{\partial\tilde{\theta}}{\partial z}>0.\end{cases} \tag{A25}$$

Finally, the dissipation term is parameterized as:

$$\varepsilon = f_c\left(0.19 + 0.51\frac{l}{\Delta}\right)\frac{E^{3/2}}{l}, \tag{A26}$$

where f_c is a correction multiplier that varies with distance z_w from a wall according to:

$$f_c = 1 + \frac{2}{\left(\frac{z_w}{\Delta z_w} + 1.5\right)^2 - 3.3}, \tag{A27}$$

where Δz_w is the size of the first near-wall grid cell.

We now have a complete set of equations for LES, as well as two choices of subgrid closure.

Procedure for Integrating the Equations

The integration of the equations of motion begins with evaluation of the advection terms on the staggered grid. This follows with the evaluation of the buoyancy, Coriolis, and diffusion terms. The integration appears as follows (time is in differential form):

$$\frac{\widetilde{u_{i,p}} - \widetilde{u_{i,m}}}{2\Delta t} = \left\{-\frac{\partial \widetilde{u_i}\widetilde{u_j}}{\partial x_j} + g\frac{\tilde{\theta} - \theta_0}{\theta_0}\delta_{i3} + f\left(\widetilde{u_j} - u_{g,j}\right)\varepsilon_{ij3} + \frac{\partial}{\partial x_j}\left[\left(K_m + \nu\right)\left(\frac{\partial \widetilde{u_i}}{\partial x_j} + \frac{\partial \widetilde{u_j}}{\partial x_i}\right)\right]\right\} - \frac{\partial \Pi}{\partial x_i} \tag{A28}$$

Only the terms in the large brackets have been evaluated to this point, and the pressure term remains uncalculated. The time integration is next carried forward, and then the divergence is taken, so that

$$\frac{\partial \widetilde{u_{i,p}}}{\partial x_i} =$$

$$2\Delta t \frac{\partial}{\partial x_i}\left\{-\frac{\partial \widetilde{u_i}\widetilde{u_j}}{\partial x_j} + g\frac{\tilde{\theta}-\theta_0}{\theta_0}\delta_{i3} + f\left(\widetilde{u_j} - u_{g,j}\right)\varepsilon_{ij3} + \frac{\partial}{\partial x_j}\left[\left(K_m+\nu\right)\left(\frac{\partial \widetilde{u_i}}{\partial x_j} + \frac{\partial \widetilde{u_j}}{\partial x_i}\right)\right]\right\}. \quad \text{(A29)}$$

$$-2\Delta t \frac{\partial^2 \Pi}{\partial x_i^2}$$

The $u_{i,m}$ term has dropped out because it is non-divergent (its non-divergence was enforced during the previous time step). At this point, the continuity equation, $\frac{\partial \overline{u}_{i,p}}{\partial x_i} = 0$, is enforced, so (z) becomes

$$\frac{\partial^2 \Pi}{\partial x_i^2} = \frac{\partial}{\partial x_i}\left\{-\frac{\partial \widetilde{u_i}\widetilde{u_j}}{\partial x_j} + g\frac{\tilde{\theta}-\theta_0}{\theta_0}\delta_{i3} + f\left(\widetilde{u_j} - u_{g,j}\right)\varepsilon_{ij3} + \frac{\partial}{\partial x_j}\left[\left(K_m+\nu\right)\left(\frac{\partial \widetilde{u_i}}{\partial x_j} + \frac{\partial \widetilde{u_j}}{\partial x_i}\right)\right]\right\}. \quad \text{(A30)}$$

This equation is then solved with a Fast Fourier Transform in the horizontal direction and a tridiagonal matrix solver in the vertical. The resulting pressure is then used to correct the velocity.

$$\widetilde{u_{i,p}} = \widetilde{u_{i,p}} - 2\Delta t \frac{\partial \Pi}{\partial x_i}. \quad \text{(A31)}$$

The integration then proceeds to the next time step.

Appendix B

Effect of the Asselin Filter on Spectra

Amplitude Errors

The Asselin filter reduces the second-order leapfrog time-differencing scheme to first order in time, which makes it significantly dissipative. The filter acts in time, so the damping occurs as the local velocity changes from one time step to the next. The more sudden the change, the more the filter damps the change. Thus, in order for any wave or eddy to be affected by the filter, it must be moving through the grid, since local time derivatives for a stationary wave are zero. Also, for the same phase speed and amplitude, shorter waves are affected more than larger waves, since shorter waves will have larger local time derivatives.

The derivation of the equations in this section follows the techniques described in Durran (1996). The analysis begins with a stability analysis of the advection equation using the leapfrog scheme with the Asselin filter. The resulting amplitude errors are then used to calculate phase speed errors in the finite difference form of the advection equation. The advection equation is written

$$u_i^{n+1} = \widetilde{u_i^{n-1}} - \mu\left(u_{i+1}^n - u_{i-1}^n\right), \tag{B1}$$

where $\mu = c\Delta t / \Delta x$ (c is the phase speed of the advected wave). The superscripts refer to the time step in the finite difference equation, and the subscripts refer to grid points. Overbars denote filtered quantities. The filter is applied in the following form:

$$\widetilde{u_i^n} = u_i^n + \varepsilon\left(u_i^{n+1} - 2u_i^n + \widetilde{u_i^{n-1}}\right). \tag{B2}$$

ε is typically chosen to be 0.25. We convert (B2) to be written in terms of u_i^{n-1}, using λ as an amplitude error that occurs during the time integration:

$$\widetilde{\lambda u_i^{n-1}} = \lambda u_i^{n-1} + \varepsilon\left(\lambda^2 u_i^{n-1} - 2\lambda u_i^{n-1} + \widetilde{u_i^{n-1}}\right). \tag{B3}$$

Unfortunately, (B3) does not fully separate filtered and non-filtered quantities, and this makes the derivation very difficult. Fortunately, it can be shown that [see Durran (1996) for details] that at sufficiently large *n* (number of time steps) and sufficiently small ε,

$$\widetilde{\lambda u_i^{n-1}} \cong \lambda \widetilde{u_i^{n-1}},$$

so we can rearrange (B3) into the following form:

$$\left(\lambda + \varepsilon\right)\widetilde{u_i^{n-1}} = \lambda\left[\left(1 - 2\varepsilon\right) + \lambda\varepsilon\right]u_i^{n-1}. \tag{B4}$$

With $u_i^n = \lambda u_i^{n-1}$ and $u_i^{n+1} = \lambda^2 u_i^{n-1}$ (amplitude errors associated with each time step), we can rearrange (B1) to the following form:

$$\widetilde{u_i^{n-1}} = \lambda\left[\lambda u_i^{n-1} + \mu\left(u_{i+1}^{n-1} - u_{i-1}^{n-1}\right)\right] \tag{B5}$$

Substituting (B5) into (B4), we have

$$\lambda^2 + \left[-2\varepsilon + 2i\mu\sin\left(k\Delta x\right)\right]\lambda + \left[\left(2\varepsilon - 1\right) - \varepsilon 2i\mu\sin\left(k\Delta x\right)\right] = 0, \tag{B6}$$

whose solutions are

$$\lambda_{\pm} = -ia + \varepsilon \pm \sqrt{\left(1-\varepsilon\right)^2 - a^2}, \tag{B7}$$

where $a = \mu \sin(k\Delta x)$. The stability requirement is $\mu \le 1 - \varepsilon$, meaning the time step is more restrictive than the leapfrog equation without the Asselin filter. The absolute value of the amplitude error is (provided the stability constraint is met)

$$|\lambda_+| = \sqrt{\mu^2 \sin^2(k\Delta x) + \left(\varepsilon + \sqrt{(1-\varepsilon)^2 - \mu^2 \sin^2(k\Delta x)}\right)^2} . \quad \text{(B8)}$$

This solution as a function of wavenumber is plotted in Figure B.1. The solution is calculated for several different μ (~time step), ranging from a maximum stable time step to a time step one quarter of the maximum stable time step. Note that the error is worst for the $4\Delta x$ wave, and no amplitude error occurs for the $2\Delta x$ wave. This is because, as shown next, the phase speed of the $2\Delta x$ wave is zero.

Phase Speed Errors

The phase speed errors can be calculated from the amplitude errors (B7) for the equation. We define ω_a as the frequency of the analytical solution to the advection equation and ω_d as the frequency of the finite-difference form of the advection equation and ω_{dR} and ω_{aI} as the real and imaginary components of ω_d (ω_a only has a real component). Assuming the analytical wave at a local point behaves over a single time step as

$$\lambda_a = e^{-i\omega_a \Delta t} = |\lambda_a| e^{i\theta_a \Delta t}, \quad |\lambda_a| \equiv 1 , \quad \text{(B9)}$$

and the finite difference wave behaves as

$$\lambda_d = e^{-i(\omega_{dR} + i\omega_{dI})\Delta t} = e^{\omega_{dI}\Delta t} e^{-i\omega_{dR}\Delta t} = |\lambda_d| e^{i\theta_d \Delta t} , \quad \text{(B10)}$$

the phase change over one time step is therefore defined as

$$\theta_d \equiv \tan^{-1}\left[\frac{\mathrm{Im}(\lambda_d)}{\mathrm{Re}(\lambda_d)}\right]. \tag{B11}$$

Thus, for a given wavenumber, k, the phase speeds of the analytical and finite difference waves can be compared:

$$\frac{\theta_d}{\theta_a} = \frac{-\omega_{dR}\Delta t}{-\omega_a \Delta t} = \frac{kc_d}{kc_a} = \frac{c_d}{c_a}. \tag{B12}$$

For the analytical solution, the phase angle only has a real component:

$$\theta_a = -\omega_a \Delta t = -c_a k \Delta t = -\mu k \Delta x. \tag{B13}$$

The finite difference solution has a physical and a computational mode. It can be shown that the solution pertaining to λ_- is the computational mode and is 100% damped by the Asselin filter when $\varepsilon = 0.25$. Thus, to look at the phase speed errors of the physical solution, we use

$$\theta_d = \tan^{-1}\left[\frac{-a}{\varepsilon + \sqrt{(1-\varepsilon)^2 - a^2}}\right], \tag{B14}$$

with the square root term always being real if the stability constraint is met. Therefore, the phase speed of the finite difference solution relative to the analytical solution is

$$\frac{c_d}{c_a} = \frac{\theta_d}{\theta_a} = \frac{\tan^{-1}\left[\dfrac{-a}{\varepsilon + \sqrt{(1-\varepsilon)^2 - a^2}}\right]}{-\mu k \Delta x}. \tag{B15}$$

This solution is plotted in Figure B.2 along with the phase speed errors for the unfiltered leapfrog scheme. One sees that the $2\Delta x$ wave is stationary, and the best resolved waves have phase speeds that are nearly equal to the phase speed of the analytical solution. Looking at Figure B.1, a smaller time step increases the phase speed error, and if the time

step is right at its maximum, the phase speed can be slightly greater than the analytical phase speed. One does occasionally observe stationary $2\Delta x$ disturbances in LES, but these are generally limited to situations, in which the subgrid eddy viscosity does not damp them well (in non-turbulent regions) or if there is reflection (in local areas with $w<0$ close to the bottom surface).

LES Tests

To test the results presented in (B8) and (B15), experiments can be performed on the spectra output from LES. In LES, the time step is limited by a stability constraint, which is a combination of the stability constraints for the advection and diffusion finite difference equations. This constraint is more restrictive than the constraint of either equation alone. Additionally, the time step is determined by picking the grid point that has the most restrictive combined stability constraint. Therefore, in most locations in the LES grid, μ (~time step) is less than its maximum stable value. In fully turbulent NS regimes, the diffusion term (with eddy viscosity) becomes the dominant term in the LES equations and determines the time step, which is small compared to the maximum stable time step of the advection equation. Therefore, in most places in the grid, the amplitude error of the Asselin-filtered leapfrog scheme for the advection equation is not severe, and the spectra are relatively well simulated. In the GC case, the advection term is much larger if the grid is in the same frame of reference as the ground. Thus, the LES time step is mostly limited by the stability constraints of the advection equation, and the actual time step used is much closer to the maximum stable time step. The amplitude errors are, therefore, more severe, and the errors are worst for the $4\Delta x$ disturbance.

In the experiment, vertical velocity spectra output from the NS case was taken and "hit" a number of times with the amplitude error (B8) as a function of the wavenumber to see how it looked compared to the GC spectra. Figure 8.10 shows the results of this experiment, which was performed on spectra from the NS cases with $\partial\theta/\partial z = 0.010$ K/m and $Q_s = 0.30$ Km/s. The NS spectra are shown with a thick black line, and the thin black lines indicate the GC spectra. The NS spectra were taken and "hit" 20 times with the amplitude error in (B8). The resulting "hit NS" spectra are plotted in blue. They line up extremely well with the GC spectra, providing strong evidence that the Asselin filter is responsible for the much of the deviation of the GC spectra from the $k^{-5/3}$ law. In the range between $4\Delta x$ and $2\Delta x$, the "hit NS" does not match the GC spectrum. The thinking is that, in this wavenumber range, the subgrid eddy viscosity takes care of the remaining small portion of energy in this wavenumber range. The effect of subgrid closure was not included when calculating the "hit NS" spectrum. Such tails in the spectra are sensitive to the subgrid scheme, and they are discussed at greater length in Otte and Wyngaard (2001).

The grid in the GC cases can then be run in the frame of reference of the mean CBL flow, reducing the grid-relative advection to a level comparible with that of the NS case. As is shown in Figure 8.9, this resulted in a GC vertical velocity spectrum that matched the NS vertical velocity spectrum in the high wavenumber range. This essentially provides a smoking gun regarding the effects of the Asselin filter on spectra.

The GC case was also run with a much smaller time step to see if some improvement in spectra occurred. Results (not shown) indicate some return to the $k^{-5/3}$ law, but the relatively small improvement is not worth the extra computational time required.

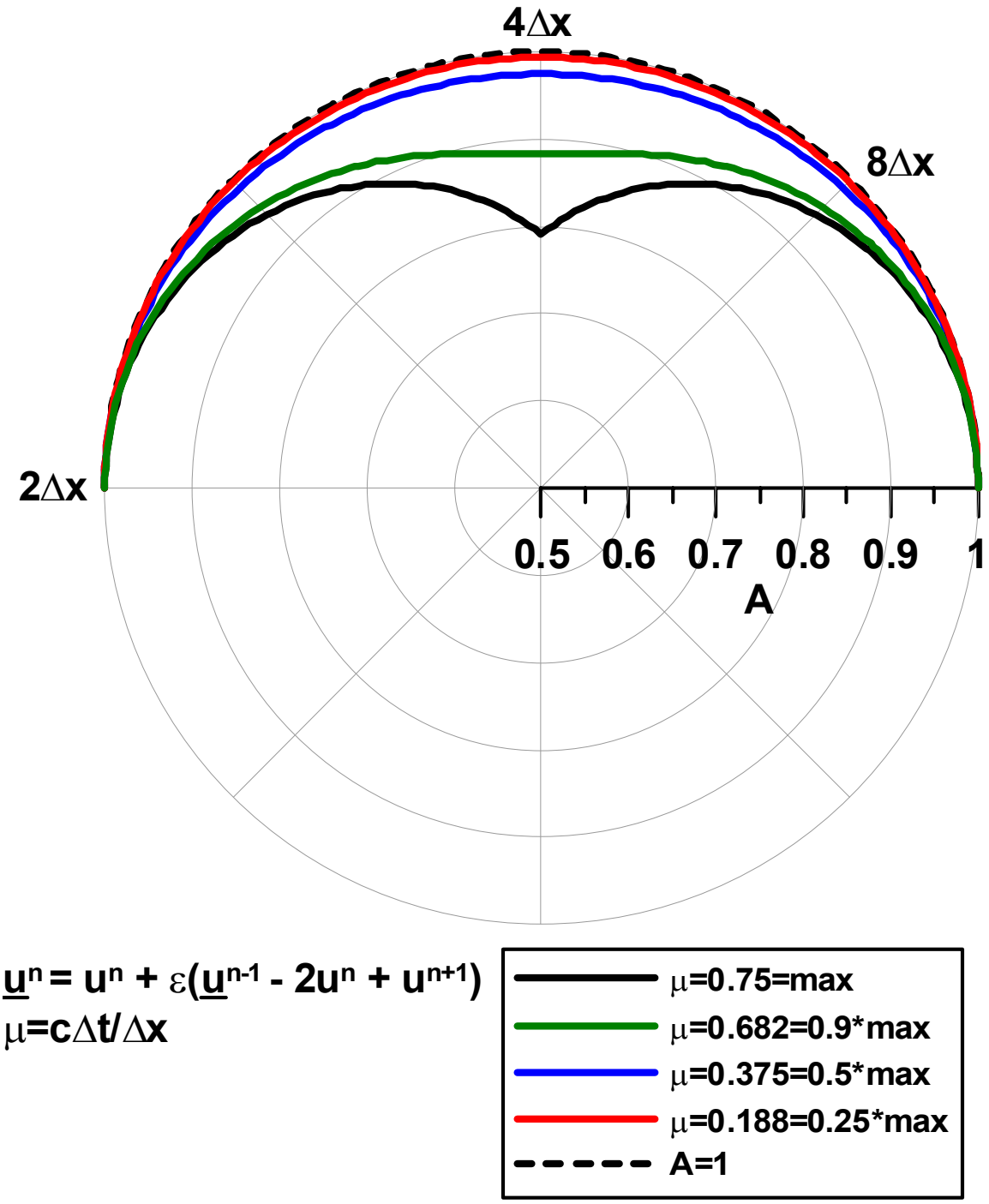

Figure B.1: *Relative amplitude, versus the analytical equation (λ_d/λ_a)*, for the advection equation using the Leapfrog scheme with an Asselin filter, ε=0.25.

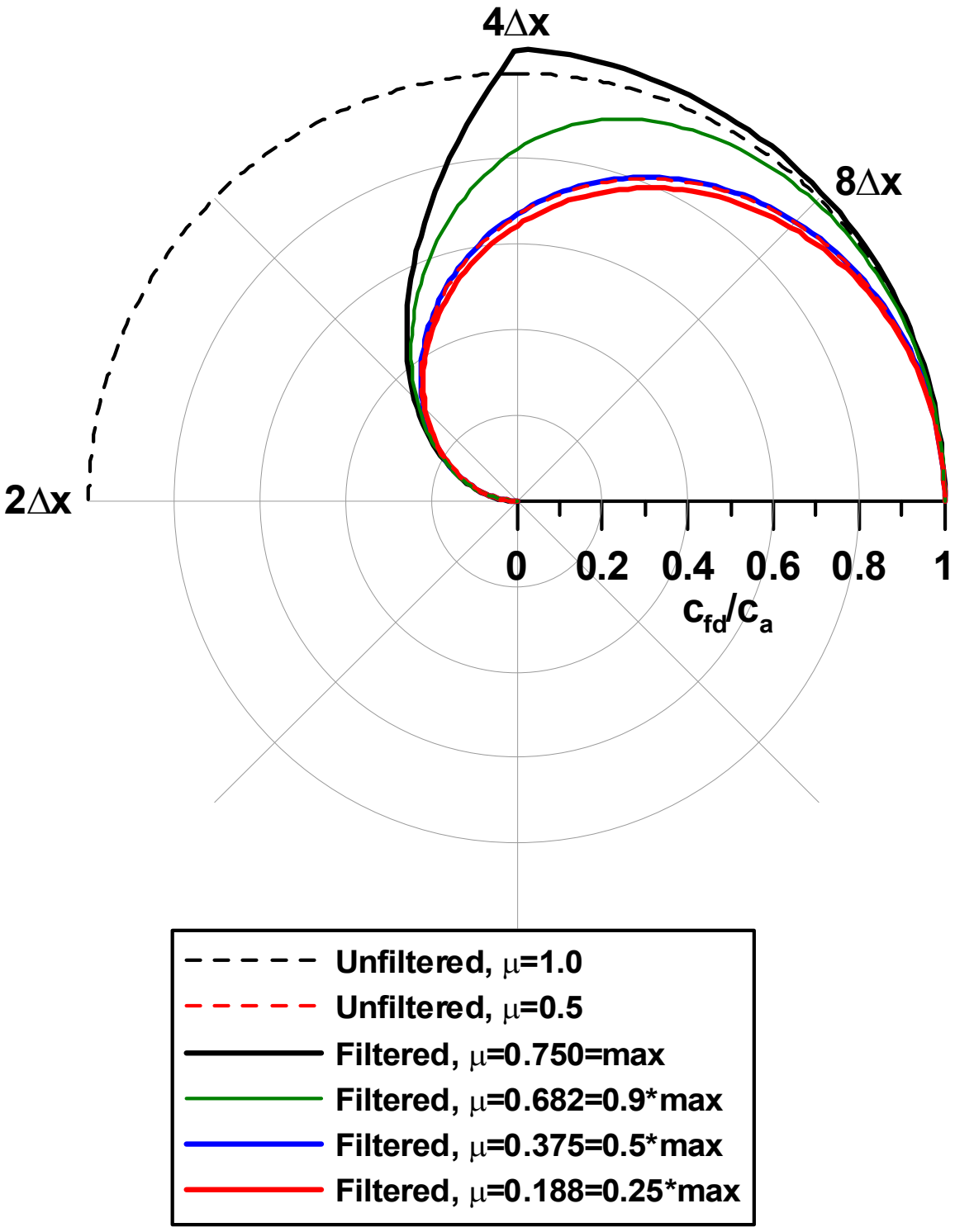

Figure B.2: Relative phase speed, versus the analytical equation (c_d/c_a), for the advection equation using the Leapfrog scheme with an Asselin filter, ε=0.25.